



UNIVERSITÀ DEGLI STUDI ROMA TRE
Dipartimento di Fisica “Edoardo Amaldi”
Dottorato di ricerca in fisica - XV ciclo

**Complete Angular Distributions
of the $\gamma d \rightarrow pn$ Reaction
in the Few GeV Region**

Federico Ronchetti

Coordinatore

prof. Filippo Ceradini

Tutore

prof. Enzo De Sanctis

Aprile 2003

Contents

1	Physical Motivations	1
1.1	Introduction	1
1.2	The Low Energy Region	1
1.2.1	Theoretical Interpretation	2
1.3	The High Energy Region	7
1.3.1	Theoretical Interpretation	8
1.3.2	The Origin of Cross Section Scaling	12
1.4	The Quark Gluon String Model	15
1.4.1	The Topological Expansion in QCD	15
1.4.2	Color Tube or Quark Gluon String	18
1.4.3	Non Perturbative Approach in the QGSM	19
1.4.4	QCD Content of Regge Trajectories	21
1.5	Quark Hadron Reactions in the QGSM	23
1.5.1	Transition Probabilities and Transition Amplitudes	23
1.6	Deuteron Photo-disintegration in the QGSM	27
1.6.1	Nonlinear Nucleon Regge Trajectories	30
1.7	Predictions for the $\gamma d \rightarrow pn$ Differential Cross Section	31
1.8	Summary	32
2	Experimental Apparatus	33
2.1	The Jefferson Lab Accelerator Facility	33
2.2	The CEBAF Hall B	34
2.2.1	Hall B Photon Production and Tagging	37
2.2.2	Photon Beam Position and Profile	37
2.2.3	Photon Energy and Timing	38
2.2.4	Photon Beam Flux	40
2.3	The CEBAF Large Angle Spectrometer (CLAS)	42
2.3.1	Target	43
2.3.2	Start Counter	45
2.3.3	Torus Magnet	45
2.3.4	Drift Chambers	46
2.3.5	Cerenkov counters	47
2.3.6	Time of Flight Scintillators	47
2.3.7	Electromagnetic Calorimeters	49
2.4	Trigger System and Data Acquisition	51
2.4.1	Trigger System	51

2.4.2	Data Acquisition	51
2.5	Summary	55
3	Event Reconstruction	
	and Data Analysis	57
3.1	Introduction	57
3.2	Running Conditions	57
3.3	Event Reconstruction	59
3.3.1	Physics Data	59
3.3.2	Simulated Data	61
3.4	Event Selection	62
3.4.1	Interaction Vertex	68
3.4.2	Energy Loss	68
3.5	Photon Flux Normalization	69
3.5.1	Validation of the Photon Flux Normalization	74
3.6	Data Quality Check	75
3.6.1	Data Stability	80
3.7	Momentum Corrections	84
3.8	Proton Detection Efficiency	93
3.8.1	Introduction	93
3.8.2	GEANT Simulation	93
3.8.3	Proton Detection Efficiency Evaluation using GSim	93
3.8.4	Check of the GSim Evaluation Results	95
3.8.5	Fiducial Cuts and Detector Acceptance	103
3.9	Background Subtraction	107
3.10	Evaluation of the Systematic Errors	113
3.11	Summary	114
4	Results	115
4.1	Introduction	115
4.2	The Differential Cross Section	115
4.2.1	Uniformity of the Six CLAS Sectors	116
4.2.2	The Energy Dependence of the Cross Section	118
4.2.3	Angular Distributions	122
4.2.4	The Cross Section Scaling	126
4.3	Summary and Conclusions	130
4.4	Tabulated Data	132
	References	143

List of Figures

1.1	Differential cross section angular distributions for the deuteron photo-disintegration process for selected incident photon energies below 0.8 GeV. Data points are from the following experiments: Bonn [8] (open squares), Frascati [9] (open crosses), MIT [10] (open triangles), LEGS [12] (open dots), and Mainz/DAPHNE [13] (solid dots). The curves belong to the following theoretical models: the Impulse Approximation [4] (dashed line), the Coupled Channel Approach [5] (up to 0.4 GeV) (continuous line), the Diagrammatic Approach [6] (dot dashed line), and the Modified Current Conservation [7] (dotted line). As can be seen from plots, the predictions of the theoretical models have problems in reproducing the data, starting from relatively low incident photon energies. (The plots are a courtesy of P. Pedroni - INFN, Pavia)	3
1.2	Legendre coefficients for the differential cross section. At the highest photon energy reached at Mainz (around 0.8 GeV), the A_1 and A_3 coefficients exhibit a small but significant deviation from the trend for the lowest energies. Data points are from the following experiments: Bonn [8] (open squares), Frascati [9] (open crosses), MIT [10] (open triangles), LEGS [12] (open dots), and Mainz/DAPHNE [13] (solid dots). The curves belong to the following theoretical models: the Impulse Approximation [4] (dashed line), the Coupled Channel Approach [5] (up to 0.4 GeV) (continuous line), the Diagrammatic Approach [6] (dot dashed line), and the Modified Current Conservation [7] (dotted line). (Courtesy of P. Pedroni - INFN, Pavia)	4
1.3	Total photo-disintegration cross section. In the energy region around 0.8 GeV the total cross section behavior is not a smooth decreasing function of the incident photon energy: this could be explained by the intermediate excitation of baryon resonances in the second resonance region which includes $P_{11}(1440)$, $D_{13}(1520)$, and $S_{11}(1535)$. Data points are from the following experiments: Bonn [8] (open squares), Frascati [9] (open crosses), MIT [10] (open triangles), LEGS [12] (open dots), and Mainz/DAPHNE [13] (solid dots). The curves belong to the following theoretical models: the Impulse Approximation [4] (dashed line), the Coupled Channel Approach [5] (up to 0.4 GeV) (continuous line), the Diagrammatic Approach [6] (dot dashed line), and the Modified Current Conservation [7] (dotted line). (Courtesy of P. Pedroni - INFN, Pavia)	5
1.4	Results from the NE8 experiment: the cross section shows scaling for incident photon energies larger than 1 GeV. The solid line represents a meson-nucleon description which do not account for the data starting from 0.5 GeV of incident photon energy.	7

1.5	Deuteron photo-disintegration differential cross section multiplied by s^{11} . Experimental data are from Mainz [13] (open/magenta circles), SLAC [17, 18] (open/green squares), Jlab Hall C [24, 25] (open/blue triangles), and Hall A [26] (open/black diamonds). Points are multiplied by s^{11} , and arrows indicate the expected threshold for the onset of the CCR scaling, where the momentum transfer to the proton, t is of the order of 1 GeV^2 [22]. Theoretical curves are described in the text.	9
1.6	Angular distributions for three incident photon energies: 1.6 (top plot), 1.9 (middle plot), and 2.4 GeV (bottom plot). The experimental data are from Refs [18, 24, 25, 26] while the curves represent the theoretical predictions of the QGSM [31] and the HRM [35]. Prediction from other models are not reported since they were not provided or could not be calculated. From the plots it is seen that the QGSM well describes the data. This model also predicts a forward to backward asymmetry. More data especially at very forward and backward angles are necessary to verify this prediction. . . .	11
1.7	Proton polarization transfers C_x (transverse in-plane, left panel) and C_z (longitudinal in-plane, right panel) in the deuteron photo-disintegration at $\theta_p^{\text{CM}} = 90^\circ$. The y -axis is perpendicular to the scattering plane, the z -axis is parallel to the scattered proton momentum and the x -axis is perpendicular to y and z . Experimental data are from [41] and have been corrected for spin rotation due to the LAB \rightarrow CM transformation. The solid/red curve represents the QGSM prediction for C_z [42]. The QGSM calculation for C_x is underway.	12
1.8	Asymmetry Σ for linearly polarized photons in the deuteron photo-disintegration at $\theta_p^{\text{CM}} = 90^\circ$ as a function of the incident photon energy. Experimental data are from Ref. [47]. The solid/red curve is the prediction of the QGSM [42].	13
1.9	Left panel: planar diagram for the reaction $ab \rightarrow cd$. Right panel: the same for the reaction $ab \rightarrow X$. Full lines denotes quarks, wavy lines, gluons. . .	16
1.10	Left panel: Cylinder type diagram. Right panel: cutting of these diagrams in the s -channel.	17
1.11	Topological diagram with one handle corresponding to the exchange of two Pomerons in the t -channel.	17
1.12	Hadron as a “bubble” in the vacuum.	18
1.13	Interaction and decay of a color tube.	19
1.14	Simple linear baryon Regge trajectories separated by $\Delta J = 2$ [70].	20
1.15	Color strings: (a) massless string, (b) homogeneous string connecting a $q\bar{q}$ couple, (c) inhomogeneous string with variable tension due to color vacuum polarization.	21
1.16	Total cross sections of the reactions $pp \rightarrow d\pi^+$ and $\bar{p}d \rightarrow p\pi^-$ as a function of the CM energy, and predictions of the QGS model.	23
1.17	Planar diagrams describing the binary reactions $\pi^0\pi^0 \rightarrow \pi^+\pi^-$ (a: left panel), $N\bar{N} \rightarrow \pi^+\pi^-$ (b: central panel), and $N\bar{N} \rightarrow N\bar{N}$ (c: right panel).	25
1.18	Diagrams describing three valence quark exchanges in the t -channel (left panel) and u -channel (right panel).	27
2.1	Schematic layout of the JLab Continuous Electron Beam Accelerator.	33

2.2	Left panel: Schematic view of the Hall B enclosure, including the CLAS metal supporting structures. The tagging spectrometer is shown at the entrance on the Hall, upstream with respect to the electron beam direction. Right panel: The CLAS detector magnified view showing the schematics for the detector subsystems.	35
2.3	Hall B beam-line, the CLAS detector, and associated equipment.	36
2.4	Hall B photon tagging system. Photons produced in the radiator continue toward the CLAS target following the same beam-line through the magnet yoke that is traversed by the electron beam when the tagger is not in use. The photon-tagging system can tag photons with energies between 20% and 95% of the incident electron energy, and is capable of operating with electron beam energies up to 6.1 GeV.	37
2.5	Tagger spectrometer electronics scheme. See the text for details.	39
2.6	Hall B Total Absorption Counter (TAC). The TAC is essentially 100% efficient allowing for the efficiency of the different elements of the tagger hodoscope to be determined. Due to counting pile-up problems, the TAC can only be operated at beam currents up to 100 pA, and must be retracted from the beam-line under normal running conditions.	40
2.7	A schematic top view of the CLAS detector cut along the beam line. Typical photon, electron and proton tracks (from top to bottom) from an interaction in the target are shown (the photon track through the CLAS drift chamber system is drawn only to guide the eye).	42
2.8	Unpolarized cryogenic target cooling system (from Ref. [97]).	44
2.9	The start counter assembly is a set of scintillators surrounding the target with the same geometric acceptance of the CLAS returning the time at which a charged particle has left the target region.	45
2.10	Left panel: Contours of constant magnetic field for the main CLAS toroid in the mid-plane between two coils (see also Fig. 2.7). Right panel: Magnetic field vectors for the CLAS toroid transverse to the beam direction in a plane centered on the target. The six coils are shown in cross-section.	46
2.11	Left panel: Portion of a region three drift chamber, showing the layout of its two super-layers. The high-lighted drift cells have fired at a charged particle passing by. Right panel: Section of the whole region 3 drift chamber.	46
2.12	Coverage of one CLAS sector by the time-of-flight scintillators.	48
2.13	Scheme of the electronic setup for a TOF counter. Each counter consists of single scintillator bar with a PMT at each end. The timing resolution of the scintillators varies from 80 ps for the shorter counters to 160 ps for the longer ones.	48
2.14	Upper panel: schematic view of one module of the forward electromagnetic calorimeter. The expanded view shows the three layers of lead and scintillator (conventionally referred as u , v , and w) making up the calorimeter sandwich structure. Lower panel: the large angle calorimeter tapered geometry (up-left), its lead-scintillator sandwich structure (up-right), and granularity (bottom-center).	50
2.15	Event rate and integrated events accumulated by the CLAS data system vs. time for a three year period.	52

2.16	Data flow schematic for CLAS, with the primary stream using the ET1 shared memory. Also shown are a variety of monitoring processes accessing data on other shared memory (ET2, ET3) managed by the ET system. See text for additional details.	54
3.1	Top pictures: Schematic view of the experimental setup used during the g2 run period. From left to right: electron beam, radiator, the tagger spectrometer, the photon beam-line, the deuteron target (TGT), the CLAS detector, and the down-stream photon flux normalization components. For the present experiment, the hadronic events generated in the target volume are detected in CLAS using the time-of-flight system, in coincidence with a tagged photon trigger and a start counter signal. Bottom pictures: the Level 1 trigger and the data acquisition system. Only the charged trigger scheme is indicated since the neutral trigger is not used in the current analysis.	58
3.2	Block diagram of the off-line data processing. The raw data files (simulated -left panel- or measured -right panel-) are converted into reconstructed files and processed by CLAS applications or user written code to obtain standard n-tuple files.	60
3.3	The tracking procedure in the CLAS drift chambers system. Left panel: a charged particle passing through a super-layer. The field wires are indicated by the open dots while crosses indicate the sensitive wires which collect the released charge. The drift times are associated to distances of closest approach (DOCAs) represented by the dotted lines. Right panel: two different values for the distance of closest approach of the particle from the sense wire can be defined, giving origin to a loss of spatial resolution. See text for details.	62
3.4	Typical missing mass spectra calculated for the six CLAS sectors from Eq. 3.5 for an incident photon energy of $E_\gamma = 1.05$ GeV and a forward proton scattering angle $\theta_p^{\text{LAB}} = 25^\circ$. The peak corresponding to the neutron rest mass can be clearly identified, and the shape of the distributions is well reproduced by a Gaussian plus an exponential fitting function. The red/dotted arrows shown in the panels represent the $(-3\sigma, 3\sigma)$ interval defining the width of the neutron peak, being σ the Gaussian function standard deviation.	64
3.5	Example of missing mass spectra calculated for the six CLAS sectors from Eq. 3.5 for an incident photon energy of $E_\gamma = 1.05$ GeV and a backward proton scattering angle $\theta_p^{\text{LAB}} = 115^\circ$. The distribution is less pronounced compared to the one obtained at forward angles since the momentum resolution of the CLAS is worse in the backward direction. Nevertheless the neutron signal is clearly evident and the shape of the distributions is well reproduced by a Gaussian plus an exponential fitting function. Again, the red/dotted arrows represent the $(-3\sigma, 3\sigma)$ interval defining the width of the neutron peak, being σ the Gaussian function standard deviation.	65
3.6	Behavior of the missing mass cuts as a function of the proton scattering angle θ_p^{CM} for four incident photon energies around 1 GeV. The solid horizontal line represents the value of the neutron rest mass, while the different dotted lines represents the missing mass cuts for the six CLAS sectors	66

3.7	Behavior of the missing mass cuts as a function of the proton scattering angle θ_p^{CM} for four incident photon energies around 2.95 GeV. The solid horizontal line represents the value of the neutron rest mass, while the different dotted lines represents the missing mass cuts for the six CLAS sectors. In this case, the cuts are wider than those calculated for lower photon energies nevertheless the missing mass distributions are still peaked enough for the fitting procedure to be applied.	67
3.8	Distribution of the vertex z -component for proton events originating in the target volume. The distribution shape reflects the target dimensions (10 cm length). The small peak on the left is the contribution of a target support structure and is eliminated by a cut on the vertex z -coordinate. The information on the interaction vertex and the x and y positions of the beam is contained in the MVRT bank in the case of multi-track events. The solid line represents a fit to the distribution defining the effective target length.	68
3.9	TDC timing spectrum of a single T-counter. The peak which caused the trigger and the accidental background can be clearly identified. Utilizing the accidental hits in the tagger, the normalization method determines the number of tagged photons from each T-counter. This is done by measuring the number of accidental hits of each T-counter in a given time interval τ , which is called the out-of-time window.	69
3.10	Schematic representation of a normalization run: the electron beam current is lowered to 100 pA and the total absorption counter is inserted into the beam-line, downstream of the CLAS. The trigger is formed only by the tagger master OR (MOR). This setup allows for a direct measurement of the photon flux from the total absorption counter (composed by a set of four lead-glass blocks with a detection efficiency close to 100%).	71
3.11	Behavior of the tagging efficiency for the tagger spectrometer T-counters for different runs (indicated by the different symbols). The tagging efficiency is defined as the number of tagged photons per energy interval divided by the total number of counts observed in the tagging counter defining that interval. The knowledge of this quantity is very important because it directly affects the determination of the photo-reaction cross sections and strongly depends on the beam setup.	72
3.12	Variation of the tagging efficiency with respect to the mean value for some tagger spectrometer T-counters. As can be seen the variation is around 3-4%.	73
3.13	Distribution of the z -component of the interaction vertex for the proton events (normalized to the number of incident photons) between a full (blue line) and empty target (black line) run. The difference between the two distributions (red line) is seen to be less than 1% in the interval $(-15 \leq z \leq -10)$ cm, confirming the validity of the photon normalization procedure.	74

3.14	Behavior of the normalized number of protons as a function of time for the “August” run period characterized by the tagger spectrometer in the prescale ON configuration. Top plot: for each run several files are analyzed (represented by the single points) and the normalized proton yield is seen to be constant in time. Bottom Plot: Overall distribution of the normalized proton yield fitted with a Gaussian function. The ratio between the standard deviation σ and the mean μ is less than 3%.	75
3.15	Distribution of the Λ values calculated for the normalized photo-disintegration proton yield N_E^i at an incident photon energy of 0.95 - 1.05 GeV (top plots) and 2.15 - 2.25 GeV (bottom plots). The horizontal lines represent the fiducial limits derived from the Chauvenet’s criterion. The distribution is practically flat and most of the runs yield values of Λ^i within the limits of the fiducial interval $(-\Delta_0, \Delta_0)$ represented by the two horizontal lines. Only two files have been discarded from the overall dataset.	78
3.16	Ratio of the normalized photo-disintegration proton yields from sectors 1 to 5 over sector 6 as a function of the run number. As it can be seen, all the distributions are flat and no time dependence on the run period is shown. The average values of uniformity are reported in table 3.3.	79
3.17	Normalized total proton yield per T-counter as a function of incident photon energy: the different symbols refer to different running conditions (tagger prescale ON or OFF and incident electron energy E_0). The behavior of the normalized proton yield per tagger T-counter does not show evident dependence on the experimental settings.	80
3.18	Distribution of the event time difference Δt between the tagger time and the start counter time for all outgoing charged particles (top plot), for proton events (middle plot), and for photo-disintegration events (bottom plot).	81
3.19	Level of accidental coincidences R shown as a function of the run number. The relatively flat behavior has two different levels: one is relative to the tagger prescale OFF configuration and has an average value around 1% while the other is relative to the tagger prescale ON configuration and is less than 2%.	83
3.20	Region of the kinematic plane where the momentum corrections could be calculated using two body kinematics.	84
3.21	Behavior of the ratio $\langle R_\phi \rangle$ as a function of ϕ in CLAS sector 1 for three values of the measured proton momentum P_0 : 0.55 GeV (top plot), 0.65 GeV (middle plot), and 0.75 GeV (bottom plot). In each ϕ -bin the ratio $R_\phi = P_\phi/P_0$ is calculated and its distribution is fitted using a Gaussian function to obtain the average value $\langle R_\phi \rangle$	86
3.22	missing mass distributions for $\gamma d \rightarrow pX$ events for sector 2 (top plot) and sector 3 (bottom plot) for two different proton momenta and scattering angles: $P=0.65$ GeV, $\theta = 115^\circ$ and $P=1.15$ GeV, $\theta = 15^\circ$, respectively. The missing mass distributions are sharper after the application of the correction procedure and their peak positions are closer to the neutron rest mass value.	87

3.23	Before the momentum correction. Ratio M_X/M_n (being M_n the nominal value for the neutron rest mass) plotted against the proton scattering angle in the LAB system separately for the six CLAS sectors and for the intermediate proton momentum of 1.05 GeV. The deviation from the unity affects practically all six CLAS sectors, and shows a dependence on the proton scattering angle. The maximum deviation is of the order of 3% in some sectors (specifically sector 4 and 6).	88
3.24	After the momentum correction. Ratio M_X/M_n (being M_n the nominal value for the neutron rest mass) plotted against the proton scattering angle in the LAB system separately for the six CLAS sectors and for the intermediate proton momentum 1.05 GeV. The situation is clearly improved compared to the one shown in Fig. 3.23 since the values obtained for M_X/M_n are of the order of 1 and the dependence on the proton scattering angle is removed by the correction.	89
3.25	Before the momentum correction. Distributions of the M_X values obtained from the missing mass distributions for $\gamma d \rightarrow pX$ events. The top plot shows the overall M_X distribution for the six CLAS sectors, while the remaining six plots show the contributions of the different sectors. It is seen that, the M_X distributions exhibit large widths which are different in the six CLAS sectors.	90
3.26	After the momentum correction. Distributions of the M_X values obtained from the missing mass distributions for $\gamma d \rightarrow pX$ events. The top plot shows the overall M_X distribution for the six CLAS sectors, while the remaining six plots show the contributions of the different sectors. After the application of the momentum correction procedure, the widths of the M_X distributions are reduced and are more uniform in the six sectors.	91
3.27	Position of the missing mass distribution peaks (associated with their RMS) before (solid/black squares) and after the correction (solid/red dots). The horizontal line represents the nominal value of the neutron rest mass.	92
3.28	The CLAS proton detection efficiency evaluated using GSim as a function of the azimuthal angle ϕ for $P_p^{\text{LAB}}=0.95$ GeV, $\theta_p^{\text{LAB}} = 45^\circ$, and with a ϕ binning of 5° . The shapes of the six CLAS sectors are reflected by the behavior of the proton detection efficiency and are clearly identified by the sudden decrease of the efficiency near the sector borders.	94
3.29	Behavior of the proton detection efficiency obtained from GSim shown as a function of the azimuthal and polar angles (on the abscissa and on the ordinates, respectively) of the generated protons for $P_p^{\text{LAB}}=0.95$ GeV. The quota represent the proton detection efficiency values and are shown in different colors/grays according to the scale indicated on the right side of the plot. The CLAS sectors are numbered from left to right. In each sector, a region of practically constant high efficiency (close to 95%) is clearly identified. The vertical low efficiency zones among sectors correspond the torus magnet coils. The horizontal gaps in the efficiency function (along θ) correspond to to out of work time-of-flight paddles or drift chambers wires taken into account in the simulation using the GPP tool.	95

- 3.30 Missing mass distribution for the event $\gamma d \rightarrow p\pi^- X$ at an intermediate proton momentum $P_p^{\text{LAB}} = 0.95$ GeV, an azimuthal angle $\phi = 10^\circ$ (corresponding to the center of sector 1), and for three different proton scattering angles θ_p^{LAB} : 10° (top), 40° (middle), and 70° (bottom). The curves superimposed to the plots are Gaussian plus straight line fitting functions calculated in the interval $(0.6 - 1.05)$ GeV. The background contamination is evaluated according to Eq. 3.23. 97
- 3.31 CLAS proton detection efficiency in CLAS evaluated from GSim (black/full dots) compared with the results measured from the $\gamma d \rightarrow p\pi^- p$ reaction (red/open dots) for $P_p^{\text{LAB}}=0.95$ GeV and $\theta_p^{\text{LAB}} = 45^\circ$. The resulting values for the proton detection efficiency are in good agreement. Note the different ϕ binning. The datum corresponding to a sector border azimuthal angle ϕ_B obtained from the $\gamma d \rightarrow p\pi^- p$ data is roughly the average of the GSim results at $\phi_B - 5^\circ$ and $\phi_B + 5^\circ$ 98
- 3.32 Proton detection efficiency in CLAS measured from the $\gamma d \rightarrow p\pi^- p$ reaction shown as a function of the proton azimuthal and polar angles for $P_p^{\text{LAB}}=0.95$ GeV. The quota represent the values of the proton detection efficiency in different colors/grays according to the scale indicated on the right side of the plot. The CLAS sectors are again numbered from left to right. The regions of constant high efficiency (close to 95%) can be clearly identified, even if the sampling rate $\Delta\phi = 10^\circ$ corresponds to a lower resolution. The vertical low efficiency regions among sectors are due to the presence the CLAS torus magnet coils. The horizontal gaps in the efficiency function (along θ) correspond to to out of work time-of-flight paddles and drift-chamber wires. 99
- 3.33 Final comparison between the results obtained from the GSim evaluation of the proton detection efficiency using the $\gamma d \rightarrow pn$ reaction (black/full dots) and the measurement from the data using the $\gamma d \rightarrow p\pi^- p$ reaction (red/empty dots). The points represent the weighted averages of the detection efficiency over proton momenta in the interval $(0.5 - 1.0)$ GeV for the sectors central region (defined by the interval $\Delta\phi = \pm 10^\circ$ assuming the sector azimuthal angle between $(-30^\circ, 30^\circ)$) and are shown as a function of the proton scattering angle θ_p^{LAB} . It is clearly seen that the GSim result is well matched by the $\gamma d \rightarrow p\pi^- p$ result. In addition, the actual detector status is well reproduced by the simulations: this is shown by the dips in the proton detection efficiency found at the same scattering angle θ_p^{LAB} in both results. 101
- 3.34 Distribution of the ratio $R = \frac{\epsilon_{\text{DATA}}}{\epsilon_{\text{GSIM}}}$ between the proton detection efficiency measured from $\gamma d \rightarrow p\pi^- p$ and simulated from $\gamma d \rightarrow pn$ (defined only in the kinematic bins ΔP_p^{LAB} and $\Delta\theta_p^{\text{LAB}}$ populated by both kind of data) for the sectors central region (defined by the interval $\Delta\phi = \pm 10^\circ$ assuming the sector azimuthal angle between $(-30^\circ, 30^\circ)$). The parameters representing the Gaussian fit are shown in the legend. It can be seen that the mean value of the distribution is of the order of the unity while the spread is about 8%. 102

3.35	An example of fiducial cuts in CLAS sector 2 for $P_p^{\text{LAB}}=1.15$ GeV. Upper panel: for $\theta_p^{\text{LAB}} = 15^\circ$. Lower panel: for $\theta_p^{\text{LAB}} = 65^\circ$. The horizontal shaded area shows the allowed variation band $\epsilon_0 \pm \delta\epsilon_0$ while the vertical lines delimit the fiducial region according to the behavior of the proton detection efficiency as a function of the azimuthal angles ϕ	104
3.36	Fiducial cuts in the CLAS sector 2 for $P_p^{\text{LAB}}=1.15$ GeV. The boundaries of the fiducial ϕ regions (along the abscissa) in the sector are shown for each proton scattering angle (along the ordinates). The mean values of the efficiency within the region are indicated by the color/gray code shown in the legend. The dip found at $\theta_p^{\text{LAB}} = 55^\circ$ is due to an out of work time-of-flight paddle, as shown also in Fig. 3.33	105
3.37	Result of the calculation of the efficiency-acceptance function for the six CLAS sectors. The abscissa report the proton momentum while the ordinates run on the proton scattering angle (both considered in the LAB system). Quotas identify regions of constant values of the efficiency-acceptance functions (numeric values can be obtained from the color/gray scale shown on the left). As can be seen from Fig. 3.37 the behavior of the six CLAS sectors is pretty uniform, except for the holes introduced by out of work channels in some sectors.	106
3.38	Missing mass distributions for the six CLAS sectors, for the intermediate energy $E_\gamma=0.95$ GeV, and a forward scattering angle $\theta_p^{\text{CM}} = 15^\circ$: the peak corresponding to the neutron rest mass is clearly identified. Each distribution is fitted with a Gaussian function plus exponential curve to take into account the continuous background. The red/dotted arrows identify a $(-3\sigma, 3\sigma)$ interval around the peak position, being σ the standard deviation of the Gaussian function.	108
3.39	Missing mass distributions for the six CLAS sectors for $\theta_p^{\text{CM}} = 125^\circ$ and for an energy incident photon energy $E_\gamma=0.95$ GeV. The distribution are wider and the neutron signal is less pronounced since at backward scattering angles the resolution of the CLAS spectrometer is lower. Nevertheless, the missing mass distributions are still well described by a Gaussian plus exponential function fit. The red/dotted arrows identify a $(-3\sigma, 3\sigma)$ interval around the peak position, being σ the standard deviation of the Gaussian function. . .	109
3.40	The behavior of the background contamination k as a function of the proton scattering angle for the six CLAS sectors and for the intermediate incident photon energy $E_\gamma=0.95$ GeV. The contribution is around 4% and is relatively flat for scattering angles less than 90°	110
3.41	Behavior of the background contamination k as a function of the incoming photon energy for the six CLAS sectors and for $\theta_p^{\text{CM}} = 35^\circ$. The last three data points, corresponding to the energy interval $1.8 \leq E_\gamma \leq 2.1$ GeV, are obtained averaging the contributions from all sectors and are identical in the plots shown. It is clearly seen that the data are well reproduced using a linear fit.	111

3.42	Behavior of the background contamination k as a function of the incoming photon energy for the six CLAS sectors and for $\theta_p^{\text{CM}} = 135^\circ$. The last three data points, corresponding to the energy interval $1.8 \leq E_\gamma \leq 2.1$ GeV, are obtained averaging the contributions from all sectors and are identical in the plots shown. At this proton scattering angles the background contribution is larger but it can still be extrapolated using a linear fit of the available points.	112
4.1	Distributions of the differences between the value of the cross section obtained in the individual sector and its average over the six sectors, divided by the average itself, as defined in Eq. 4.2 for each bin of proton scattering angle and incident photon energy. The result is shown separately for the six CLAS sectors (numbered from left to right and top to bottom). In each panel the statistical parameters of the distributions are shown and it can be seen that a systematic shift of the order of $2 \div 5\%$ is present in all sectors.	117
4.2	The CLAS results on the differential cross section $\frac{d\sigma}{dt}$ as a function of the total energy s (where t and s are the momentum transfer to the proton and the total energy in the Mandelstam notation) for proton scattering angles in the range $15^\circ \leq \theta_p^{\text{CM}} \leq 85^\circ$. As can be seen, the cross section decrease as a function of s is extremely steep and this behavior is enhanced as the scattering angle approaches 90° . The blue/solid line superimposed to the experimental results represents a power law fitting function proportional to s^n	119
4.3	The CLAS results on the differential cross section $\frac{d\sigma}{dt}$ as a function of the total energy s (where t and s are the momentum transfer to the proton and the total energy in the Mandelstam notation) for proton scattering angles in the range $95^\circ \leq \theta_p^{\text{CM}} \leq 155^\circ$. It can be seen that the cross section tendency to a fast decrease as a function of s , slows down going toward backward scattering angles. The blue/solid line superimposed to the experimental results represents a power law fitting function proportional to s^n	120
4.4	Exponents n obtained by the angular survey on the cross section. The data behavior is of the type $\frac{d\sigma}{dt} \simeq (\text{const})s^n$ as a function of the total energy s . It can be seen that the cross section decrease as a function of s follows different exponents n for different scattering angles. At very forward and backward angles (corresponding to the dominance of the t or u channel, and where u is the momentum transfer to the neutron) the exponent is of the order of -9 and -7 respectively. At more intermediate angles (around 90°), where both the t -dominance and u -dominance are suppressed, n drops around -13 . A clear asymmetry exist between forward ($n = -9$) and backward angles ($n = -7$). The errors on the data points are those given by MINUIT on the fitting parameter n	121

- 4.5 Angular distributions of the deuteron photo-disintegration cross section measured by the CLAS (solid/red dots) in the incident photon energy range 0.55 – 1.25 GeV. It can be seen that the CLAS data cover a broad range in the proton scattering angle: $15^\circ \leq \theta_p^{\text{CM}} \leq 155^\circ$. Results from Mainz [13] (open dots), SLAC [17, 18] (open squares), JLab Hall A [26] (open diamonds) and Hall C [24, 25] (open triangles) are included and are generally in agreement with the CLAS data. The angular dependence of the photo-disintegration cross section shows a pronounced asymmetry between the forward and backward proton scattering angles. For incident photon energies higher than 1 GeV, the solid line represents the non perturbative calculation of the QGSM [31] which well reproduces the data. In particular, the QGSM calculation accounts for the forward to backward asymmetry shown by the data. 123
- 4.6 Angular distributions of the deuteron photo-disintegration cross section measured by the CLAS (solid/red dots) in the incident photon energy range 1.35 – 2.05 GeV. Results from already published experiments such as SLAC [17, 18] (open squares), JLab Hall A [26] (open diamonds) and Hall C [24, 25] (open triangles) are included, where available. The cross section asymmetry between the forward and backward angles persists in this photon energy range. The QGSM [31] calculation (shown as a solid line) well reproduces the data behavior also in this energy range. 124
- 4.7 Angular distributions of the deuteron photo-disintegration cross section measured by the CLAS (solid/red dots) in the incident photon energy range 2.15 – 2.85 GeV. Results from SLAC [17, 18] (open squares), JLab Hall A [26] (open diamonds) and Hall C [24, 25] (open triangles) are included, where available. The angular distributions are well reproduced by the QGSM [31] calculation (shown as a solid line) which accounts for the data asymmetry between forward and backward scattering directions. 125
- 4.8 Deuteron photo-disintegration differential cross section expressed as $d\sigma/dt$ multiplied by s^{11} (being t the momentum transfer and s the total energy in the Mandelstam notation) in the angular range from $\theta_p^{\text{CM}} = 15^\circ$ up to $\theta_p^{\text{CM}} = 85^\circ$. The CLAS results are represented by the solid dots. Also shown are previously available data: SLAC [17, 18] data are represented by open squares, JLab Hall C [24, 25] data by open triangles, and JLab Hall A [26] data by open diamonds. The arrows in each panel, indicate the photon energies where the onset of the s^{-11} scaling is foreseen. This limit correspond to proton transverse momenta of 1 GeV/c. For the $\gamma d \rightarrow pn$ reaction the proton transverse momentum can be expressed $P_T^2 = \frac{1}{2} E_\gamma M_D \sin^2(\theta_p^{\text{CM}})$. According to the CCR, a constant behavior of the cross section as a function of the incident photon energy is expected when the limit for P_T is reached. The solid line represents the QGSM [31] non perturbative calculation for the cross section. This model, as discussed in the first Chapter of this thesis, gives a non perturbative description of the photo-disintegration cross section assuming that the scattering amplitude at very high energy is dominated by the exchange of three valence quarks in the t -channel. 127

4.9 Deuteron photo-disintegration differential cross section expressed as $d\sigma/dt$ multiplied by s^{11} (being t the momentum transfer and s the total energy in the Mandelstam notation) in the angular range from $\theta_p^{\text{CM}} = 95^\circ$ up to $\theta_p^{\text{CM}} = 155^\circ$. The CLAS results are represented by the solid dots. Also shown are previously available data: SLAC [17, 18] data are represented by open squares, JLab Hall C [24, 25] data by open triangles, and JLab Hall A [26] data by open diamonds. The arrows in each panel, indicate the photon energies where the onset of the s^{-11} scaling is foreseen. This limit correspond to proton transverse momenta of 1 GeV/c. For the $\gamma d \rightarrow pn$ reaction the proton transverse momentum can be expressed by $P_T^2 = \frac{1}{2}E_\gamma M_D \sin^2(\theta_p^{\text{CM}})$. According to the CCR, a constant behavior of the cross section as a function of the incident photon energy is expected when the limit for P_T is reached. It can be seen that the asymptotic behavior for the cross section is well established from $\theta_p^{\text{CM}} = 75^\circ$ up to $\theta_p^{\text{CM}} = 125^\circ$ while at backward angles, the cross section dependence on the photon energy follows powers of s different from -11 as shown in Fig. 4.4. The solid line represents the QGSM [31], a non perturbative calculation for the cross section. 128

List of Tables

2.1	Performance figures for the CEBAF RF super-conducting cells.	34
2.2	Characteristics of the total absorption counter (from Ref. [97]).	40
2.3	Summary of the CLAS detector characteristics.	55
3.1	Runs collected with the charged trigger used in the $\gamma d \rightarrow pn$ analysis. . . .	58
3.2	Normalization runs acquired during the “August” and “September” run periods.	73
3.3	Uniformity of the response of the CLAS sectors.	77
3.4	Numerical values of the missing mass distributions peaks and RMS before and after for the momentum correction procedure is applied in each sector, together with the standard deviations obtained fitting the corrected missing mass distributions.	92
3.5	Summary of the main contributions to the overall systematic uncertainty. .	113
4.1	Differential cross section data.	132

Abstract

The study of two body deuteron photo-disintegration is ideal for investigating the transition region from meson exchange to the Quantum Chromo Dynamics (QCD) regime because of its simplicity and amenability to calculation [1].

In the past years, the theoretical efforts have been focused in two different directions: extending at higher energies the models based on meson exchange, and improving the models inspired by QCD principles to extrapolate their predictions at lower energies, in order to find out the approach that best describes the experimental data and in which energy region the transition between the two descriptions takes place.

Discriminating among the available models is still difficult because data are relatively scarce and mainly cover a limited angular range.

The possibilities for a complete experimental investigation of the $\gamma d \rightarrow pn$ process are much improved since the availability of an intense (200 μA) electron beam of 6 GeV energy at the Jefferson Lab Continuous Electron Beam Accelerator Facility (CEBAF). In this new experimental context, a comprehensive study of the $\gamma d \rightarrow pn$ reaction was started in recent years, using complementary equipments:

- very high energy, high-intensity polarized and unpolarized *bremstrahlung* photon beams in conjunction with high resolution spectrometers of moderate angular acceptance for measurements at few scattering angles (JLab Halls “A” and “C”);
- high energy (unpolarized) tagged photon beam in conjunction with the large angular acceptance (nearly 4π) and good momentum resolution of the CLAS detector (JLab Hall “B”).

This thesis reports on the first, wide-ranging survey of the $\gamma d \rightarrow pn$ differential cross section, for incident photon energies between 0.5 and 3.2 GeV, characterized by the high statistics and large kinematic coverage obtained with the CEBAF Large Acceptance Spectrometer at Hall B (CLAS).

The subject is introduced from the physical motivation for the measurement together with an overview of the theoretical efforts made to describe the photo-disintegration process in the few GeV region. Then, the CLAS detector characteristics are briefly described in order to better illustrate the full data analysis procedure which, together with the final results and their theoretical interpretation, constitute the very original part of this work.

Chapter 1

Physical Motivations

1.1 Introduction

The study of high-energy two body deuteron photo-disintegration has received a renewed interest in recent years in the attempt to evidence quark related effects in nuclei. In fact, this reaction is well suited for studying the interplay of nuclear and particle physics while allowing the best possible separation between the known electromagnetic reaction mechanism and the nuclear system structure.

The physics interest deals with how and at what energy the transition takes place from the hadronic picture of the deuteron, established in the reaction at low energies (below 1 GeV), to the quark-gluon picture, which is expected to be correct for energies much higher than 1 GeV, where distances of the order of few tenths of Fermi play a role.

From the experimental point of view, the history of $\gamma d \rightarrow pn$ measurements has been characterized by large discrepancies among different datasets. The situation was complicated by the fact that the majority of the older experiments used *bremsstrahlung* photons and were subject to uncertainties due to the poor knowledge of the photon flux and energy. Moreover, large solid angle detectors were not widely available, leading to relatively small coverage in the proton scattering angle.

1.2 The Low Energy Region

The total photo-disintegration cross section data at incident photon energy below 1 GeV show a discrepancy up to 40% in the $\Delta(1232)$ resonance region. However, considering data from experiments performed with quasi mono-energetic photons or improved untagged *bremsstrahlung* techniques, a fair agreement (of order 8÷10%) is found especially above 300 MeV of photon energy [2, 3].

In this energy region the cross section data can be described with a number of theoretical models all based on the “traditional” nuclear picture of meson exchanges such as: the Impulse Approximation [4], the Coupled Channel Approach [5], the Diagrammatic Approach by [6], and the Modified Current Conservation [7].

The measured differential cross section is reproduced using a 4th order Legendre polynomial expansion:

$$\sum_{l=0}^4 A_l(E_\gamma) P_l(\cos \theta_p^{\text{CM}}) \quad (1.1)$$

and the total cross section can be computed using the relation: $\sigma_{tot} = 4\pi A_0$.

A selection from the measured angular distributions for the $\gamma d \rightarrow pn$ cross section in the photon energy range between 0.1 and 0.8 GeV is shown in Fig. 1.1 where the results are from the following experiments: Bonn [8], Frascati [9], MIT [10], LEGS [12], and Mainz/DAPHNE [13]. The overall dataset cover a relatively wide range in the proton scattering angle θ_p^{CM} , that is from 25° up to 160° .

The most significant contribution to the cross section data in this incident photon energy region is provided by the Mainz experiment, performed with a tagged photon beam in the energy range from 0.1 to 0.8 GeV in conjunction with the DAPHNE large-angle spectrometer. Results from this experiment are shown in Fig. 1.1 together with data points from Refs [14, 15, 16]. It can be seen that below 0.4 GeV the DAPHNE data better match the results of experiments carried out using a tagged photon beam such as Bonn and LEGS. This peculiarity is also reflected by the Legendre coefficients $A_1 - A_4$ plotted in the left panel of Fig. 1.2.

The consistency between the angular distributions provided by different experiments is better than that of the absolute cross section shown in Fig. 1.3. The DAPHNE results show a noticeable change in slope of the cross section, moving toward higher photon energies. The effects starts around 0.5 GeV and it is reflected in the shape of the Legendre polynomial coefficients shown in Fig. 1.2.

In this energy region, also the A_1 and A_3 coefficients exhibit a small but significant deviation from the trend for the lowest energies: this could be explained by the intermediate excitation of baryon resonances in the second resonance region which includes $P_{11}(1440)$, $D_{13}(1520)$, and $S_{11}(1535)$.

1.2.1 Theoretical Interpretation

Included in Figs 1.1, 1.2 and 1.3 are the results of four theoretical models based on meson-nucleon degrees of freedom.

The Impulse Approximation and the Coupled Channel Approach consider the nucleon internal degrees of freedom explicitly in the hamiltonian and the deuteron wave function is a superposition of different intrinsic configurations (NN , $N\Delta$, $\Delta\Delta$) containing also excited nucleons. These configurations are mutually coupled by non-diagonal transition potentials. The two models need some kind of phenomenological input and start on the same assumptions, but handle the resulting set of coupled equations differently: the Impulse Approximation is a perturbative solution in which only the NN ground configuration is retained while the isobar degree of freedom are only implicitly taken into account via the dispersive part of the $N - N$ potential. On the other hand, the Coupled Channel Approach gives the full solution for the $NN - \Delta\Delta$ coupled channel using custom models for the different potentials involved and for the Δ width. Its results includes only multipoles up to $L = 4$ while for scattering waves with $j \geq 4$ it still relies on the Impulse Approximation.

Figs 1.1 and 1.2 show that the Impulse Approximation reproduces the angular distributions up to 360 MeV even though it overestimates the total cross section. On the other hand, the Coupled Channel Approach gives a good description of

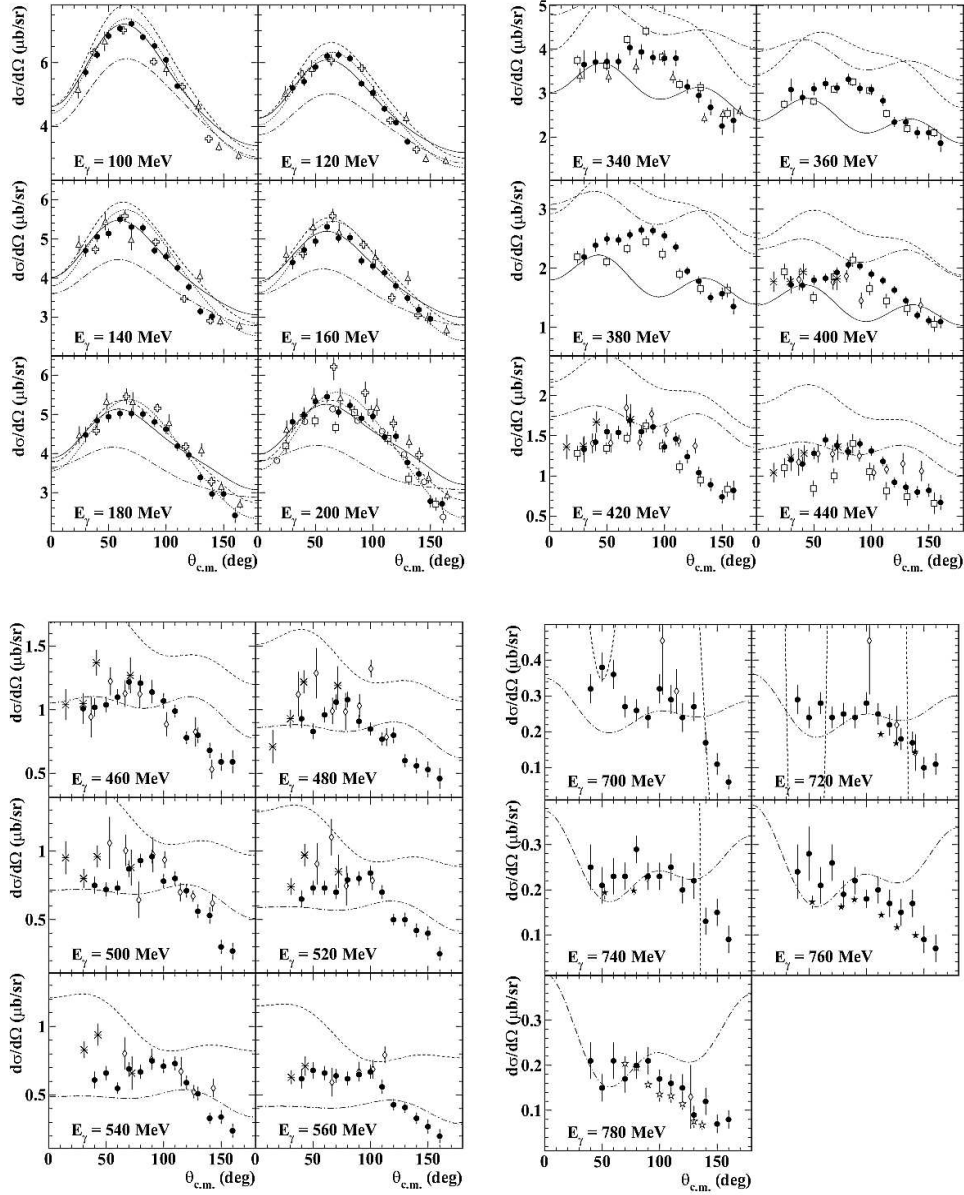


Figure 1.1: Differential cross section angular distributions for the deuteron photodisintegration process for selected incident photon energies below 0.8 GeV. Data points are from the following experiments: Bonn [8] (open squares), Frascati [9] (open crosses), MIT [10] (open triangles), LEGS [12] (open dots), and Mainz/DAPHNE [13] (solid dots). The curves belong to the following theoretical models: the Impulse Approximation [4] (dashed line), the Coupled Channel Approach [5] (up to 0.4 GeV) (continuous line), the Diagrammatic Approach [6] (dot dashed line), and the Modified Current Conservation [7] (dotted line). As can be seen from plots, the predictions of the theoretical models have problems in reproducing the data, starting from relatively low incident photon energies. (The plots are a courtesy of P. Pedroni - INFN, Pavia)

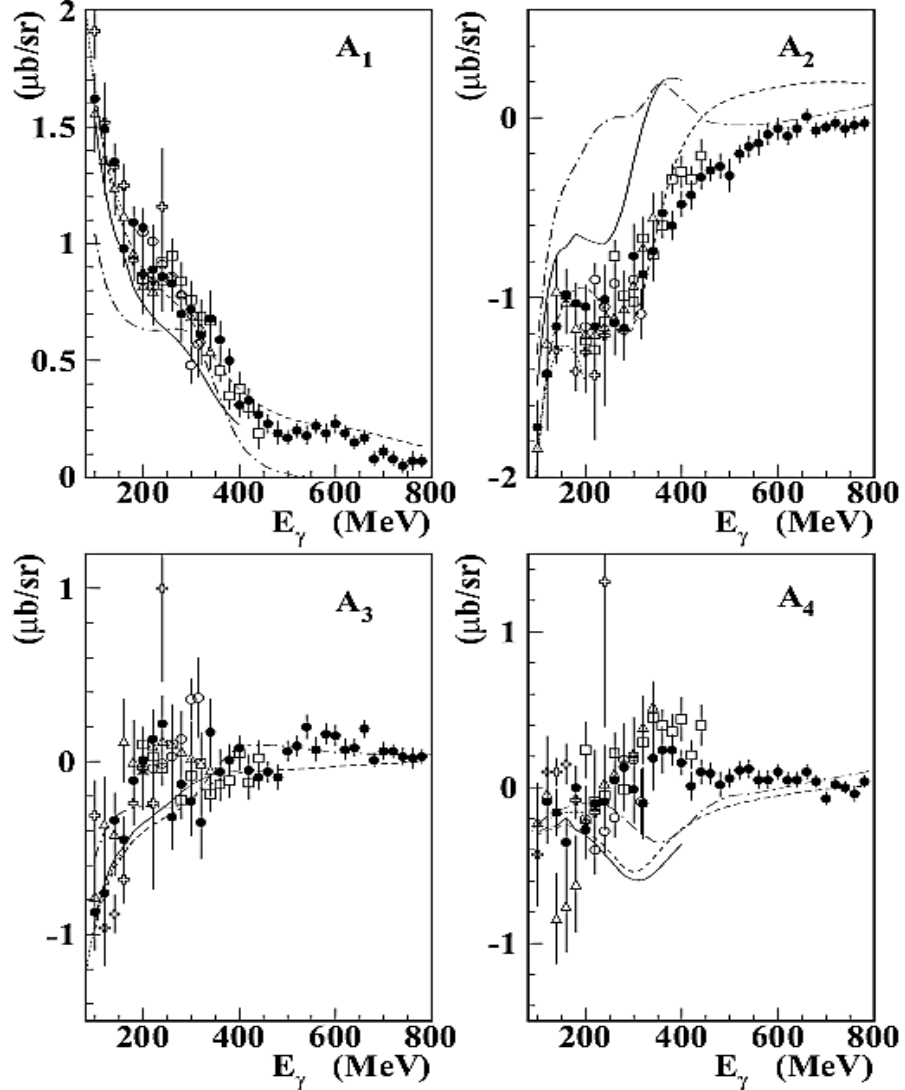


Figure 1.2: Legendre coefficients for the differential cross section. At the highest photon energy reached at Mainz (around 0.8 GeV), the A_1 and A_3 coefficients exhibit a small but significant deviation from the trend for the lowest energies. Data points are from the following experiments: Bonn [8] (open squares), Frascati [9] (open crosses), MIT [10] (open triangles), LEGS [12] (open dots), and Mainz/DAPHNE [13] (solid dots). The curves belong to the following theoretical models: the Impulse Approximation [4] (dashed line), the Coupled Channel Approach [5] (up to 0.4 GeV) (continuous line), the Diagrammatic Approach [6] (dot dashed line), and the Modified Current Conservation [7] (dotted line). (Courtesy of P. Pedroni - INFN, Pavia)

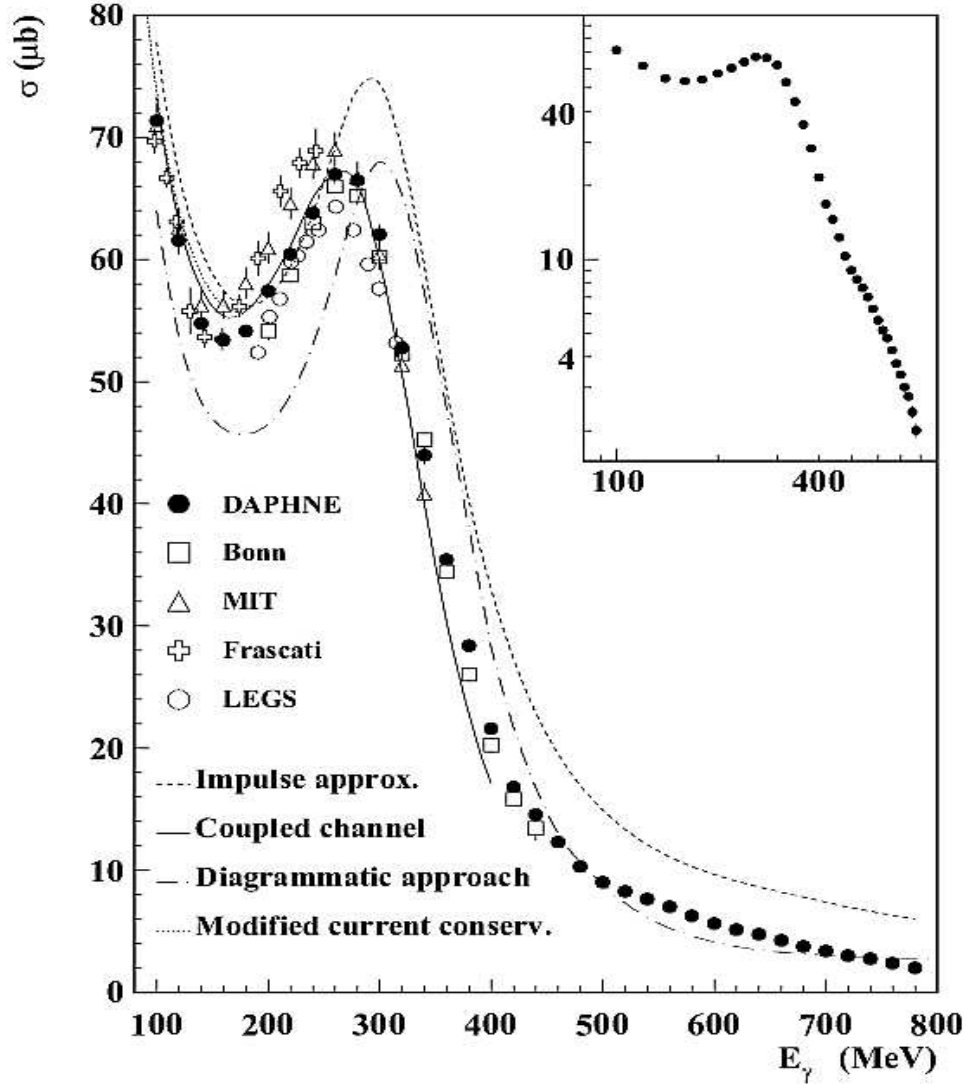


Figure 1.3: Total photo-disintegration cross section. In the energy region around 0.8 GeV the total cross section behavior is not a smooth decreasing function of the incident photon energy: this could be explained by the intermediate excitation of baryon resonances in the second resonance region which includes $P_{11}(1440)$, $D_{13}(1520)$, and $S_{11}(1535)$. Data points are from the following experiments: Bonn [8] (open squares), Frascati [9] (open crosses), MIT [10] (open triangles), LEGS [12] (open dots), and Mainz/DAPHNE [13] (solid dots). The curves belong to the following theoretical models: the Impulse Approximation [4] (dashed line), the Coupled Channel Approach [5] (up to 0.4 GeV) (continuous line), the Diagrammatic Approach [6] (dot dashed line), and the Modified Current Conservation [7] (dotted line). (Courtesy of P. Pedroni - INFN, Pavia)

the total cross section, but has some problems describing the shape of the angular distributions, since a dip is found at 90° which is not reflected by the data.

This feature appears also in the behavior of the A_2 coefficient shown in Fig. 1.2 (upper left) which determines the curvature of the angular distribution around 90° and which is strongly overestimated above 160 MeV. This anomalous behavior is produced by the $N\Delta$ configurations in higher partial waves [4, 5] with $j \geq 4$ which are important for the differential cross sections, but negligible for the total cross section.

In the Laget Diagrammatical Approach, the amplitude is expanded in a series of relevant interaction mechanisms. Each elementary transition amplitude is then determined starting from effective Lagrangians for the basic $N\pi$ and γN couplings. This model is again similar to the Impulse Approximation but predicts an incorrect energy for the Δ peak excitation. This discrepancy is due to dynamical effects on the Δ mass given by the corresponding $N - N$ and $N - \Delta$ channels that are not taken accounted for, so that the resulting energy for the Δ peak is shifted. This effect would be compensated by the $N - \Delta$ re-scattering, which is expected to shift back in place the Δ peak.

The approach of Jaus, Bofinger and Woolcock, calculates the multipole amplitude from an effective current density which takes into account convection, spin, and meson exchange currents. This procedure is based on an effective one-pion exchange current density which does not violate the current conservation law. The model allows for two adjustable parameters: the πNN coupling constant and the pion cut-off mass, which can be used to fit the existing experimental data below 200 MeV. This limit stems from the fact that only a limited number of multipole amplitudes have been considered and the finite Δ width has not been taken in to account. The calculations predict a total cross section which is very similar to the Coupled Channel result. Both methods agree with the Mainz cross section values up to about 120 MeV, but then between 120 and 180 MeV they both overestimate the experimental results.

1.3 The High Energy Region

For incident photon energies of the order of 1 GeV, the deuteron photo-disintegration differential cross section was measured for the first time by the SLAC NE8 experiment [17]. Results from the NE8 experiment are shown Fig. 1.4 for a proton scattering angle $\theta_p^{\text{CM}} = 90^\circ$. The data are multiplied by the s^{11} factor, where s is the square of the total energy in the usual Mandelstam notation.

Clearly, for $E_\gamma \geq 1$ GeV, the data shows a flat behavior. This represents the first evidence for the possibility of the so called *scaling* in the deuteron photo-disintegration cross section, suggesting that point-like constituents as quarks and gluons (*i.e.* the QCD degrees of freedom) could be the correct description for the process, in analogy to the Deep Inelastic Scattering (DIS). On the contrary, the traditional meson exchange description, discussed in the previous section to interpret the low energy data, breaks down.

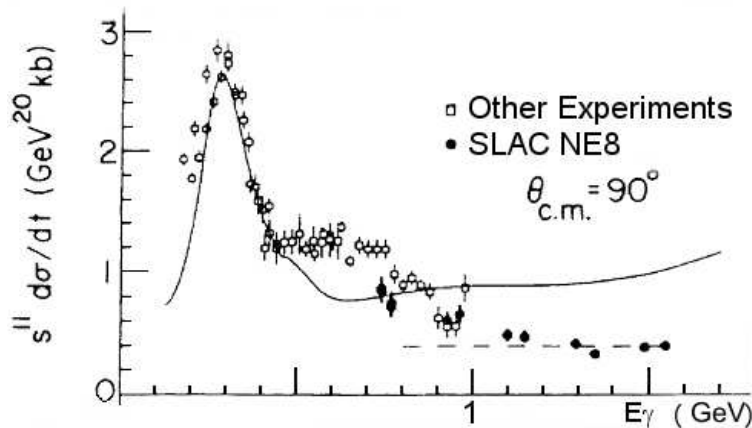


Figure 1.4: Results from the NE8 experiment: the cross section shows scaling for incident photon energies larger than 1 GeV. The solid line represents a meson-nucleon description which does not account for the data starting from 0.5 GeV of incident photon energy.

This striking result was supported and extended by another experiment subsequently performed at SLAC for photon energies up to 2.8 GeV [18].

The SLAC results have renewed the interest for the study of the deuteron photo-disintegration at high energy and as a consequence a vast physics program has been approved at Jefferson Lab. This program involves all the three JLab collaborations in a full investigation of the physics topics related to the deuteron photo-disintegration process:

- Hall A Collaboration: angular distributions at three medium energies and investigation of the polarization observables [19];
- Hall B Collaboration: nearly complete angular distributions from 0.5 to 3.0 GeV of photon energy [20];
- Hall C Collaboration: differential cross section at few angles and very high energy (up to 5.5 GeV) [21].

1.3.1 Theoretical Interpretation

The experimental data provided by SLAC, JLab Hall A, and Hall C are shown in Fig. 1.5 for the measured proton scattering angles. The cross section is again multiplied by s^{11} in order to evidence the possible scaling behavior.

In this energy region an asymptotic behavior could be expected on the basis of the simple model of the Constituent Counting Rules (CCR, [22]). This model considers the carriers of the currents within the hadrons as structureless and describable in terms of a renormalizable field theory, with the conditions of asymptotically scale invariance for the interactions among the constituents, and finiteness at the origin of the hadronic wave functions. Accordingly, applying dimensional counting to the minimum quark field component of a hadron accounts for many experimental consequences of its compositeness. The constituent counting rule prediction for exclusive scattering is:

$$\frac{d\sigma}{dt} = s^{(2-n)} f\left(\frac{t}{s}\right), \quad (1.2)$$

where $s \rightarrow \infty$ and t/s is fixed, where s , t (and u) are the usual relativistic invariants in the Mandelstam notation. Here n is the number of elementary fields in the initial and final states.

Considering the $\gamma d \rightarrow pn$ process it turns out that $n = 13$ since the initial state has one photon plus 6 quark fields while the final state has 6 quark fields which means that at high incident photon energy and intermediate angles, conventionally 90° , where both the t -dominance and u -dominance are suppressed the $\gamma d \rightarrow pn$ differential cross section is expected to scale as s^{-11} . As shown in Fig. 1.5, this prediction is well confirmed by the experimental data for $\theta_p^{\text{CM}} = 69^\circ$ and 89° .

The overall data behavior is less clear and may suggest a deviation from the predictions of the simple CCR scaling indicating, in turn, that pQCD itself is not plainly applicable.

In fact, the cross section at the forward angles $\theta_p^{\text{CM}} = 52^\circ$ and 36° falls off more slowly, with an $\simeq s^{-9}$ scaling at lower energies, until the onset of the s^{-11} behavior at about 3 and 4 GeV beam energy, respectively. However it results that an absolute pQCD calculation would not correctly predict the data. Further observations may be made for other photo-reactions, and it remains to be seen how this behavior arises and if pQCD is a genuine explanation for it.

In this case, a different approach have to be used and it seems very reasonable that a soft description for the process will have to be introduced.

This can be done following opposite strategies, such as the inclusion of QCD degrees of freedom in the low energy description or the extrapolation of the conventional $N - \pi$ interaction mechanisms to the higher energy region. It is also possible to merge suitable parts of this two techniques to obtain a hybrid description (for a full review see Ref. [23]). The curves shown in Fig. 1.5 represent the predictions of several theoretical models implementing the outlined strategies. In the Reduced Nuclear Amplitude (RNA) model [27, 28] the binding of the quarks inside the nucleons and the deuteron is taken into account with empirical form factors and the elementary cross section is computed assuming CCR scaling. This approach is able to describe the $\gamma d \rightarrow pn$ cross section with appropriate normalization factors for $\theta_p^{\text{CM}} = 89^\circ$ and 69° with $E_\gamma > 2$ GeV.

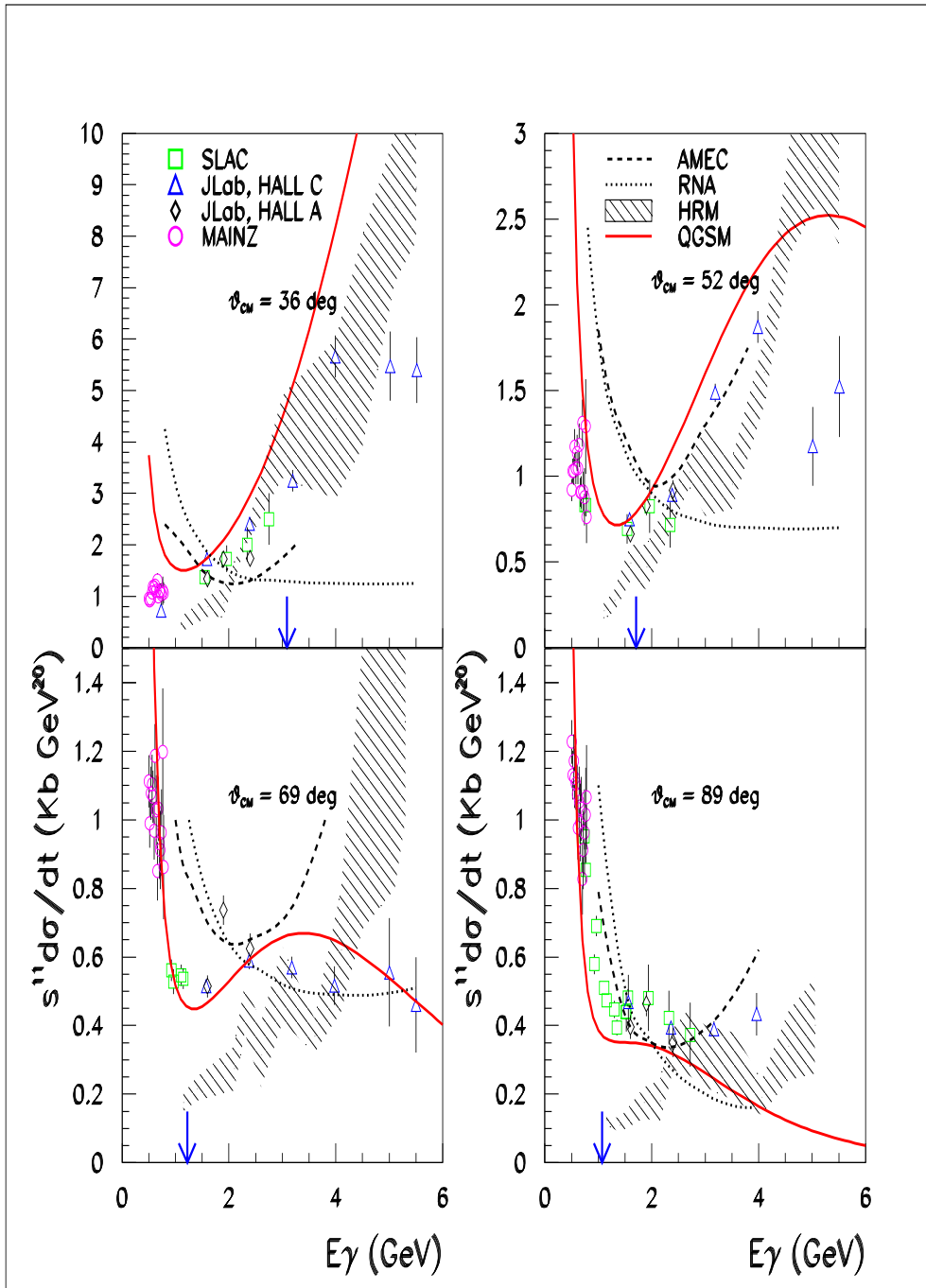


Figure 1.5: Deuteron photo-disintegration differential cross section multiplied by s^{11} . Experimental data are from Mainz [13] (open/magenta circles), SLAC [17, 18] (open/green squares), Jlab Hall C [24, 25] (open/blue triangles), and Hall A [26] (open/black diamonds). Points are multiplied by s^{11} , and arrows indicate the expected threshold for the onset of the CCR scaling, where the momentum transfer to the proton, t is of the order of 1 GeV^2 [22]. Theoretical curves are described in the text.

In the Hard quark Rescattering Model (HRM) [29], the elementary interaction consists of a quark exchange between the two nucleons. The incoming photon is absorbed by a quark of one nucleon which then gives up its momentum via a hard gluon exchange with a quark of the other nucleon. The model assumes that this rescattering mechanism is analogous, with some approximation, to the wide angle $p - n$ scattering which is also dominated by quark exchange. The limits for the applicability of the model are $E_\gamma > 2.5$ GeV and momentum transfer $t > 2$ GeV², but, under particular assumptions for the short distance $p - n$ interaction, they can be extended. However, the agreement with the data is poor, especially at higher energies where the uncertainty is large, due to the limited knowledge of the pn cross section for the actual kinematic conditions.

Even if traditional models based on the $N - \pi$ picture fail to reproduce the data at $E_\gamma > 1$ GeV, this approach can be extended, with the appropriate modifications, in the few GeV region. The Asymptotic Meson Exchange Current (AMEC) model [30], uses form factors to describe the $d - NN$ interaction vertex and an overall normalization factor fixed by fitting the experimental data at 1 GeV. The results reproduce the energy dependence of the cross section only for $\theta_p^{\text{CM}} = 89^\circ$.

It is worth noticing that this non QCD-based model provides a scaling law for the cross section, with an exponent depending on the scattering angle.

A non perturbative description of the photo-disintegration cross section data is given by the Quark Gluon String Model (QGSM) (Ref. [31]) This model assumes that the scattering amplitude at very high energy is dominated by the exchange of three valence quarks in the t -channel. The duality property of scattering amplitudes [32, 33] allows its extension at intermediate energies.

As shown in Fig. 1.5 the predictions of the QGSM are in good agreement with the available data in the full energy range at $\theta_p^{\text{CM}} = 89^\circ, 69^\circ$. At 52° the trend of the QGSM theoretical curve could be compatible with the last two points at the highest energies since their errors are quite large. At $\theta_p^{\text{CM}} = 36^\circ$ the situation is more delicate even if the QGSM curve has a better trend with respect to the other calculations.

A better insight and a more effective discrimination among the predictions of the competing theoretical models are obtained examining the angular distributions of the differential cross section [34].

Experimental data recently obtained from [26] for three different incident photon energies: $E_\gamma = 1.6, 1.9, \text{ and } 2.4$ GeV are shown in Fig. 1.6.

These angular distribution were measured only for the indicated energies and are not complete since the very forward and backward regions are not covered. Additional data from Refs [18, 24, 25] are also shown in Fig. 1.6 together with the curves representing theoretical predictions. The shaded area is the HRM [35] calculation which has an uncertainty of 15-20% while the QGSM prediction is represented by a dashed line. Other calculations are not shown since they were not provided (AMEC) or the model could not be applied in this case (RNA) since the curves for different angles have arbitrary normalizations.

Also in this case, the QGSM well reproduces the available distributions while the HRM (apart from a possible overall shift) show a different behavior at small and large angles.

From the experimental side, it is clear that the knowledge of the full angular distributions, including the points at very forward and backward angles and in a

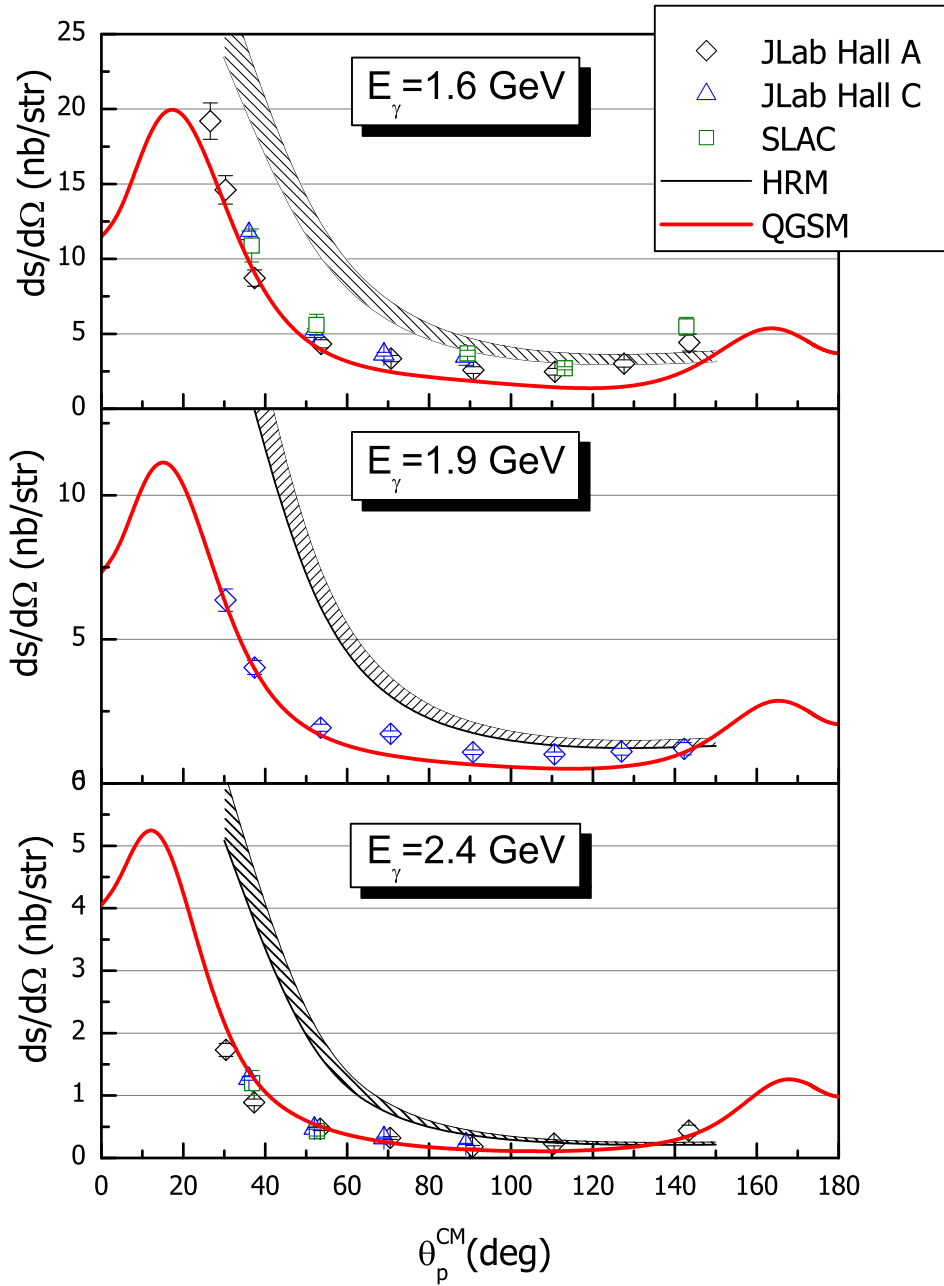


Figure 1.6: Angular distributions for three incident photon energies: 1.6 (top plot), 1.9 (middle plot), and 2.4 GeV (bottom plot). The experimental data are from Refs [18, 24, 25, 26] while the curves represent the theoretical predictions of the QGSM [31] and the HRM [35]. Prediction from other models are not reported since the were not provided or could not be calculated. From the plots it is seen that the QGSM well describes the data. This model also predicts a forward to backward asymmetry. More data especially at very forward and backward angles are necessary to verify this prediction.

wider incident photon energy range will be extremely helpful to better discriminate among the models and to further check the QGSM predictions.

1.3.2 The Origin of Cross Section Scaling

It has to be said that the applicability of the CCR at this incident photon energies is still an open question. In fact, this approach is based on the assumption that soft and hard contributions factorize [36] even if this hypothesis (relying on pQCD) may be valid only for very high momentum transfers which are not attained in the few GeV energy region where experimental data are available (see Refs [37, 38, 39, 40]). In order to clarify this point it is useful to consider the

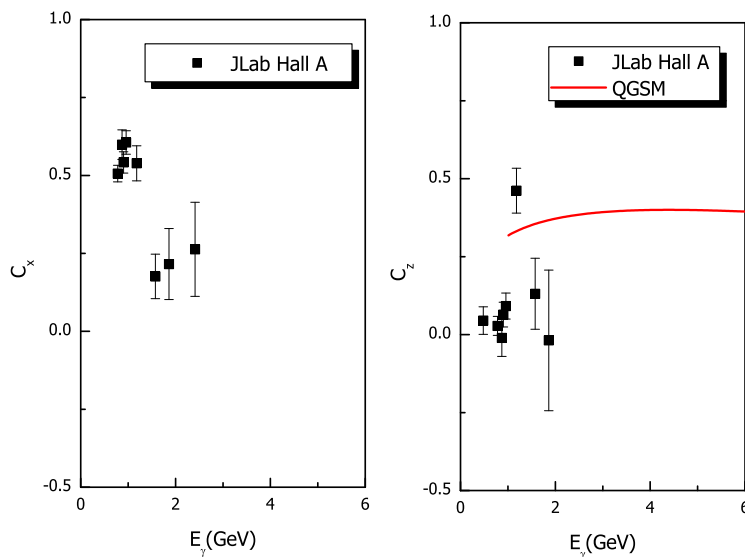


Figure 1.7: Proton polarization transfers C_x (transverse in-plane, left panel) and C_z (longitudinal in-plane, right panel) in the deuteron photo-disintegration at $\theta_p^{\text{CM}} = 90^\circ$. The y -axis is perpendicular to the scattering plane, the z -axis is parallel to the scattered proton momentum and the x -axis is perpendicular to y and z . Experimental data are from [41] and have been corrected for spin rotation due to the LAB \rightarrow CM transformation. The solid/red curve represents the QGSM prediction for C_z [42]. The QGSM calculation for C_x is underway.

complementary information to the differential cross section given by polarization observables. Significant data on this topic were recently provided by the JLab Hall A Collaboration [41] and are shown in Fig. 1.7 which gives the proton in-plane polarization transfers and the photon asymmetry as measured in the $\vec{\gamma}d \rightarrow \vec{p}n$ reaction for the proton angle $\theta_p^{\text{CM}} = 90^\circ$. In this case, the signature of pQCD effects rests in the so called Hadron Helicity Conservation (HHC) [36, 43, 44, 45]. HHC arises from the fact that vector interactions such as photon-quark or gluon-quark couplings conserve chirality, leading, in turn, to conservation of the sums of the components of the hadronic spins along their respective momentum directions.

If pQCD can be really invoked to explain the cross section scaling at $\theta_p^{\text{CM}} = 90^\circ$

it is expected that at the same angle the polarized observables will satisfy the pQCD based prediction of HHC of $C_x = C_z = 0$.

As shown in Fig. 1.7, for $E_\gamma \geq 1.5$ GeV the results on C_x seem not in agreement with the HHC prediction while the those on C_z are more difficult to interpret but the QGSM calculation for C_z has a reasonable trend with respect to the JLab data. A similar calculation for C_x is underway.

The problem with HHC lies in the limiting hypothesis of chirality conservation while the QGSM, being a non perturbative approach, is far from the chiral limit (characteristic of pQCD) and is able to introduce a chirality violation which may be reflected in the data.

For photon energies below 1.5 GeV the proton polarization transfers C_x and C_z show quasi-resonance structures at $\sqrt{s} = 2.7$ and 2.9 GeV, respectively. Such structures are conceptually out of the QGSM range of applicability [46].

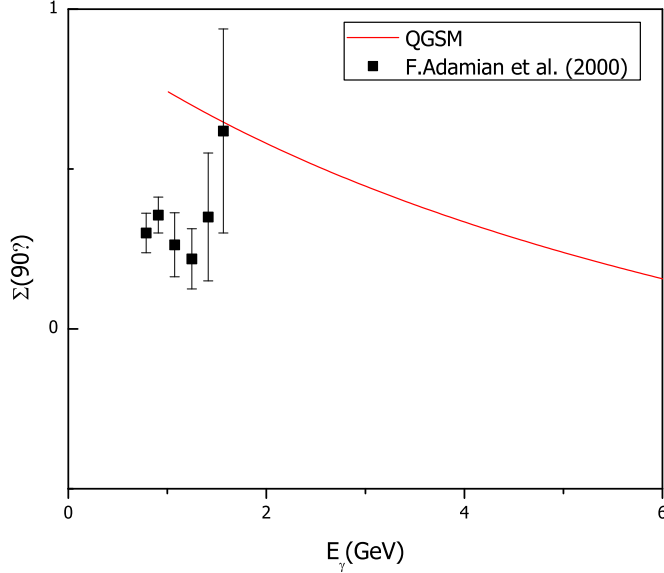


Figure 1.8: Asymmetry Σ for linearly polarized photons in the deuteron photo-disintegration at $\theta_p^{\text{CM}} = 90^\circ$ as a function of the incident photon energy. Experimental data are from Ref. [47]. The solid/red curve is the prediction of the QGSM [42].

Another observable carrying information on HHC predictions is the photon asymmetry, defined as

$$\Sigma(\theta_p^{\text{CM}}) = \frac{d\sigma_{\parallel} - d\sigma_{\perp}}{d\sigma_{\parallel} + d\sigma_{\perp}}, \quad (1.3)$$

for which the HHC prediction at $\theta_p^{\text{CM}} = 90^\circ$ is 1 (see Ref. [42]).

As can be seen from Fig. 1.8 most of the experimental data are limited to the incident photon energy region below 1.5 GeV where the perturbative regime may be not fully established, in any case the trend of the data does not seem to indicate that the HHC prediction is verified. In the higher energy region where $E_\gamma \geq 1.5$ GeV,

the QGSM predicts a slow decrease of $\Sigma(90^\circ)$ Unfortunately the overlap with the available data is quite limited so definite conclusions cannot be drawn yet.

Summarizing: at least for $\theta_p^{CM} = 90^\circ$ the cross section data and the in-plane polarization transfers results do not appear consistently described in a coherent perturbative picture.

This indicates that a non perturbative approach may be needed in order to fully describe the deuteron photo-disintegration process (polarized and unpolarized). The QGSM gives a non perturbative description of the process which reproduces fairly well the available data: for this reason the QGSM foundations will be given in the next Section.

1.4 The Quark Gluon String Model

Quantum chromodynamics is the fundamental theory of strong interactions. The asymptotic freedom of QCD implies that its coupling constant $\alpha_s(Q^2)$ becomes small at small distances (large Q^2) and this gives the possibility to use perturbation theory in processes with large momentum transfer. Experimental data for these processes are in good agreement with pQCD predictions. On the other hand, at large distances (of order $1/\Lambda_{QCD}$, where $\Lambda_{QCD} \simeq 0.3$ GeV) the coupling constant is not small anymore and non perturbative effects, which are responsible for confinement, come into play. The large distance dynamics is necessary to understand processes with small momentum transfer, which give dominant contributions to high energy hadronic interactions.

In this region a non perturbative approach should be used and there are not many ways to introduce non perturbative effects in QCD. One possibility is to consider lattice calculations [48], which are most directly related to the exact QCD results. This method, however, needs very large lattices to obtain accurate and reliable results and it is difficult to apply to complex phenomena as exclusive reactions at high energies. Another possibility is from the QCD sum rules [49] which express physical quantities in terms of several parameters such as vacuum correlators of gluonic and quark fields. As well as lattice calculations, this method has been applied mainly to *static* properties of hadrons. A third method, which will be briefly introduced in this overview, is the $1/N$ (or topological) expansion in QCD [50, 51, 52], where N is the number of colors or flavors. Dynamical content for this model will be drawn from the string (or color tube) models [53, 54, 55, 56, 57], which are closely related to the space-time picture of interaction in $1/N$ expansion. The string-like configuration of gluonic fields is confirmed by lattice calculations.

These ingredients form the basis for the Quark Gluon String Model (QGSM, [58, 59]) which then accounts for the confinement of quarks and can be considered a microscopic theory underlying the Regge phenomenology. As a result many relations between parameters of reggeon theory (based on analyticity and unitarity) can be established from the QGSM [60], since a quark-gluon string can be identified with a corresponding Regge trajectory. The QGSM has been applied to many different problems of strong interactions: hadronic mass spectrum [61], widths of resonances [62], relations between total cross sections, residues of Regge poles [63], behavior of hadronic form factors and, in recent years, to heavy ion collisions at high energy [64] and to the deuteron two body photo-disintegration [31].

1.4.1 The Topological Expansion in QCD

Large distance dynamics of QCD defines what is called soft process, *i.e.* when the value of the coupling constant $\alpha_s \simeq 1$ and cannot be used as a good expansion parameter. Since QCD has not yet been solved exactly, it is necessary to find out another parameter, which is small enough to allow a non perturbative expansion of amplitudes.

It is possible [50] to consider as a small parameter the quantity $1/N_c$, where N_c is the number of colors with corrections to the main term of order $1/N_c^2 \approx 0.1$. Another suitable parameter is $1/N_f$ where N_f is the number of flavors [51]. Soft processes involve only the light quark flavor (u, d, s) contributions, so that $N_f \approx 3$.

An intuitive justification for the use of these quantities, lies in the fact that these two parameters ($1/N_c, 1/N_f$) are the only dimensionless quantities in massless QCD, being the only suitable quantities to be used as expansion parameters in that limiting case. The formal limit of $N_c \rightarrow \infty$ [50] ($N_f/N_c \rightarrow 0$) shows many interesting properties and has been intensively studied since in this limiting case there is hope to obtain exact solution of the theory. However, this approximation is too far from the real world (for instance, all resonances are considered infinitely narrow ($\Gamma \approx 1/N_c$)). The case when the ratio ($N_f/N_c \rightarrow 1$) is fixed and the expansion of all amplitudes in $1/N_f$ or $1/N_c$ is carried out [51] is more realistic and is called topological expansion, since each term of the series corresponds to an infinite sets of Feynmann diagrams with definite topology. The $1/N$ expansion has a dynamical character which means that it can work better in some regions of the kinematical variables, while in some other regions its convergence can be worse. For example, in the case of a binary ($2 \rightarrow 2$) amplitude, which is a function of two variables (s, t), the $1/N$ expansion becomes more accurate as t increases in the positive t region [65], while for high energies additional terms have to be considered.

The topological classification of diagrams, in this scheme, starts from the amplitude for the binary reaction $ab \rightarrow cd$. Here, the main contribution is given by the “planar” diagrams, shown in figure Fig. 1.9 where planar means a class of diagrams where all lines lie on a plane without hard interactions inside the contour delimited by the external quark lines. These lines of valence quarks determine the *border* of the diagram.

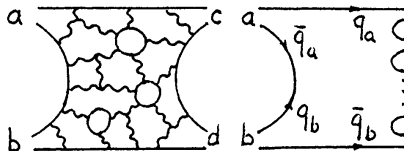


Figure 1.9: Left panel: planar diagram for the reaction $ab \rightarrow cd$. Right panel: the same for the reaction $ab \rightarrow X$. Full lines denotes quarks, wavy lines, gluons.

All planar diagrams give a contribution of the same order in $1/N$, taking into account that each color trace gives a factor N_c and each fermion loop a factor $-N_f$, and considering the limit of large N under the condition $g^2 N \approx 1$. It should be emphasized that the topological expansion can be applied only to colorless amplitudes. The unitarity content of the planar diagrams can be revealed cutting such a diagram in the s -channel as shown in right panel of Fig. 1.9. This operation gives the amplitude of multi-particle production, which is planar by itself.

Cutting of the diagram on the left panel in Fig. 1.9, either in the s or the t -channel, always contain a $q\bar{q}$ pair, which enters in the boundary of the diagram and determines the internal quantum numbers (charge, isospin, etc.) exchanged in the given channel. At high energies and small momentum transfers these planar diagrams are determined by exchange of Regge poles in the t -channel. Diagrams for elastic scattering (*i.e.* reactions without quantum numbers exchange in the t -channel), are shown in 1.10, where the valence quarks of the colliding hadrons are

conserved in the process of interaction.

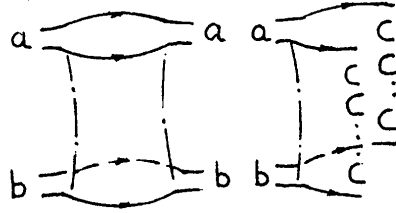


Figure 1.10: Left panel: Cylinder type diagram. Right panel: cutting of these diagrams in the s -channel.

These diagrams are of cylinder type and their s -channel cutting corresponds to the multi-particle production configurations. This is shown by the picture on the right of Fig. 1.10 which corresponds to the production of two chains of particles with the same structure as the one shown for the planar diagram cut of 1.9. From the t -channel point of view, the cylinder diagrams are due to gluon exchange in the t -channel, and they are usually assumed to give rise to a Pomeron pole. More complicated diagrams can be drawn, such the one shown in Fig. 1.11, which has two Pomeron exchange contribution, and one hole in the surface.

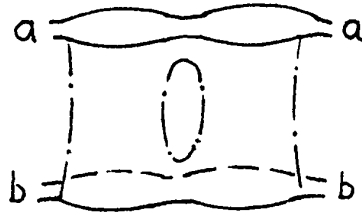


Figure 1.11: Topological diagram with one handle corresponding to the exchange of two Pomerons in the t -channel.

Holes in a diagram defines “handles”, so each topological class of surfaces is characterized by a given number of boundaries (n_b) and handles (n_h). The topological expansion allows a complete classification of diagrams based on the two parameters (n_b) and (n_h) and to determine their dependence on $1/N$.

All the diagrams belonging to a given topological class have the following dependence on $1/N$:

$$T(n_b, n_h) = \left(\frac{1}{N}\right)^{n_b+2n_h} \quad (1.4)$$

so that the contribution of planar diagrams ($n_b = 1, n_h = 0$) to the scattering amplitude is $1/N$, the cylinder diagram ($n_b = 2, n_h = 0$) contribution is $\sim (1/N)^2$ and that of the diagram of Fig. 1.11 ($n_b = 2, n_h = 1$) is $(1/N)^4$.

This equation is valid for 4-point amplitudes; amplitudes with a larger number of hadrons should take into account that each external hadronic state introduces a factor $1/\sqrt{N}$, due to the normalization of its wave function. The ratio of the cylinder to the planar diagram is $\sim 1/N$, however for amplitudes with vacuum quantum

numbers in the t -channel, the cylinder type diagrams will dominate at high energies. This because its relative contribution increases as $s^{\alpha_{P(0)} - \alpha_{R(0)}}$ as energy increases as it is implied by the dynamical character of the $1/N$ expansion. In many cases, the type of the process (and the number of boundaries) is fixed by the quantum numbers in the t -channel. In this case the expansion parameter depends only by the number of handles and, according to Eq. 1.4, is $(1/N)^2$.

1.4.2 Color Tube or Quark Gluon String

The topological expansion gives a useful classification of all QCD diagrams but needs a definite space time picture to become predictive. This picture is based on some assumptions on the properties of confinement which are related to the properties of the QCD vacuum. Many reasons suggest that QCD vacuum has a complicated structure and contains important large scale fluctuations of gluon and quark fields. These fluctuations generate vacuum correlations of gluon and quark fields which are not described by perturbation theory. In particular, the vacuum correlator of the square of gluonic field $G_{\mu\nu}^a$ has been found from the analysis of QCD sum rules [49]:

$$\frac{\alpha_s}{\pi} \langle 0 | G_{\mu\nu}^a | 0 \rangle \approx 0.012 (\text{GeV})^4 , \quad (1.5)$$

and it can be interpreted as a vacuum condensate connected to the energy density of the vacuum.

$$\varepsilon_\nu = -\frac{b}{32} \langle 0 | \frac{\alpha_s}{\pi} G_{\mu\nu}^a G_{\mu\nu}^a | 0 \rangle \quad \text{with } b = \frac{11}{3} N_c - \frac{2}{3} N_f . \quad (1.6)$$

Thus the energy density of the physical vacuum with the gluon condensate given by 1.5 is lower then for the "empty" vacuum. If the vacuum fluctuations will be broken in some region of space, then the energy of this region will be increased. Such a breaking of vacuum fluctuations in QCD (partial or complete) arises naturally inside hadrons, due to color fields induced by valence quarks. As a result, there will be two different states of vacuum condensate, one is the vacuum outside the hadrons and the other one inside the hadron. It is assumed that the chromo-electric field of quarks do not penetrate far into the ordinary vacuum medium since the gluons carry the color charge so that the flux lines attract each others. This behavior leads to the property of confinement, so that isolated states in the vacuum can exist only as "white" states with all color lines closed (see Fig. 1.12). In this picture a hadron can be considered as a bubble in a "vacuum liquid".

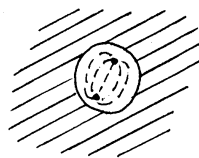


Figure 1.12: Hadron as a "bubble" in the vacuum.

The process of interaction of such bubbles at high energies (Fig. 1.13) leads to production of new objects: color tubes or strings (a string is a limiting case of a color tube with no transverse momentum distribution).

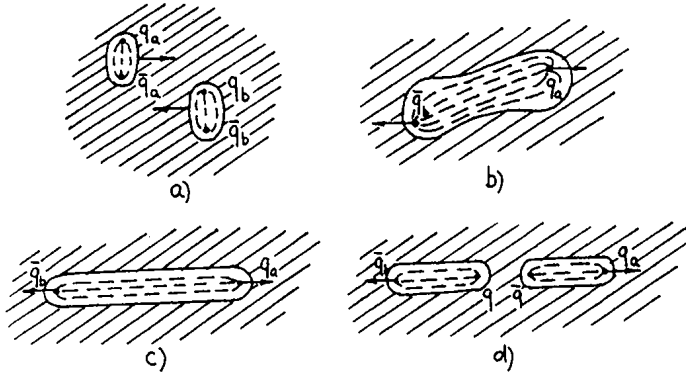


Figure 1.13: Interaction and decay of a color tube.

It is necessary to consider separately two cases.

- The processes with the annihilation of valence quarks of the colliding hadrons, corresponding to the planar diagrams of the $1/N$ expansion.
- The processes of the diffraction type, where the valence quarks are conserved, connected with cylinder type diagrams.

In the first case, after an interaction and annihilation of valence quarks the configuration shown in Fig. 1.13 (b), where the color lines connect the spectator quarks moving in opposite directions (in the CM system), is realized. As they move apart the region where the vacuum fluctuations are broken enlarges (Fig. 1.13 (c)) and the color tube or string is produced and this leads to an increase of the energy. At some point, the breaking of the color tube will be energetically favorable and the production of $q\bar{q}$ pairs from the vacuum (Fig. 1.13 (d)) will occur. This process repeats until many white bubbles or hadrons will be produced. The time needed for production of a hadron with momentum p and mass m is $\tau \sim \frac{p}{m^2}$, so in the CM system the fastest hadrons, which contain the spectator quarks q_a and \bar{q}_b , will be produced last. Each produced q and \bar{q} pair has a small relative momentum in their rest system which means a small rapidity difference. As a result of the Lorentz invariance, finally produced hadrons at high energy will be uniformly distributed in the rapidity and will have limited transverse momenta.

1.4.3 Non Perturbative Approach in the QGSM

The QGSM describes rather well the experimental data on exclusive and inclusive hadronic cross sections at high energy [61, 50, 51, 66] and gives new important insights into the Regge phenomenology. It can explain the quark-gluon content of different Reggeons, relate their residues, predict inclusive spectra of different particles in different kinematical regions, find the relations between exclusive and multiple production amplitudes through the unitary conditions. Concerning this

last topic, multiple production at high energy, the QGSM is very similar to the dual parton model [67].

The Regge pole analysis of the exclusive hadronic reactions [68] was formulated much before QCD and for this reason is very often seen as a dormant topic being so strongly identified with the pre-quark era of the S -matrix and dispersion relations approach to strong interactions. This point of view is not correct [69] since the description of high energy behavior in terms of singularities in the complex angular momentum plane of two body scattering amplitudes is completely general being based on the general principles of unitarity, analyticity and crossing symmetry. In recent years it has been resurrected by all the theories which aim to a string formulation for hadrons and the conjecture of Regge that high energy behavior of two body scattering amplitudes might be describable in terms of moving poles in the J -plane is *experimentally verified* and all hadrons do lie on trajectories which connects the particle mass with its total angular momentum (Fig. 1.14).

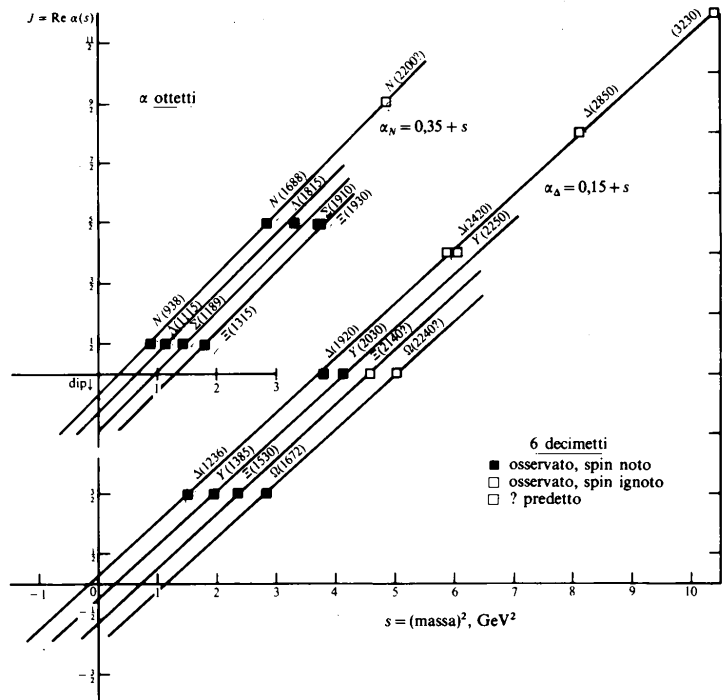


Figure 1.14: Simple linear baryon Regge trajectories separated by $\Delta J = 2$ [70].

Despite the very broad applications of such approaches to the different hadronic reactions and to the inclusive hadron-nucleus collisions at rather high energy they were poorly used in the description of exclusive reactions with nuclear targets. One of the main reason is apparently related to the fact that those approaches were originally introduced to describe high energy data, but data on exclusive reactions with nuclear targets have been limited, up to now, mainly to the intermediate energy region. Let us say something more on the region of validity in s and t of this approach. From the quantum mechanical point of view, high energy means that the wavelength of the photon is much smaller than the radius of the target nucleon which in QCD can be taken as the radius of confinement R_0 , which is about 1 Fm. Therefore, at

$E_\gamma \geq 1$ GeV, the necessary condition $E_\gamma R_0 \gg 1$ can be considered as fairly satisfied. In the Regge approach, high energy means $s \gg t_{char}$ where t_{char} is some characteristic value of t which is usually taken as $\simeq 1$ (GeV)². As the region of validity in t or u is concerned, there is a common convention that this is limited by $|t|$ or $|u| \leq 1$ (GeV/c)². This convention is based on the consideration that with increasing of $|t|$ or $|u|$ the secondary singularities in the complex angular momentum plane as daughter Regge trajectories or branch points [71] may also become important. However, this considerations cannot be formulated in a quantitative way because the residues of Regge poles and discontinuities of Regge cuts are usually parameterized and are different for different reactions. This means that at the phenomenological level, the description of data include contributions of some effective Regge trajectories which in turn may include the effects of secondary singularities.

A different philosophy is used in the QGSM since each graph in this model is classified according to its topology and the corresponding Regge singularity is fixed by the quark-gluon content of the graph itself. Therefore the corresponding amplitude can be considered for all values of s and t as an analytic functions of those variables. The QGSM gives the possibility to calculate parameters that before were considered only at the phenomenological level in the Regge theory and to establish a bridge between QCD and the Regge approach to strong interactions.

1.4.4 QCD Content of Regge Trajectories

There is experimental evidence and theoretical reasons that both meson and baryon states should be connected, on the J vs M^2 plane by an essentially non linear relation (trajectory) instead of the simple scheme shown in Fig. 1.14. In fact, the starting point for Regge's work was the partial wave expansion of the scattering amplitudes [71] but here we would like to reinterpret the original idea of Regge pole and trajectory using the modern QCD concepts and language to make evident that the Regge trajectories must contain some non linearity.

Let us consider a meson state composed of a $q\bar{q}$ pair connected by the color flux tube (Fig. 1.15).

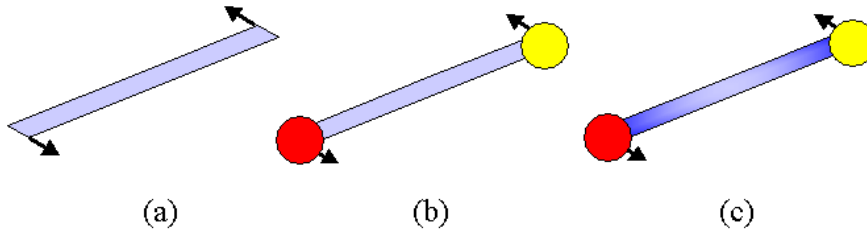


Figure 1.15: Color strings: (a) massless string, (b) homogeneous string connecting a $q\bar{q}$ couple, (c) inhomogeneous string with variable tension due to color vacuum polarization.

In a simple potential description the energy can be written as:

$$H = \sqrt{\vec{p}_1^2 + m_1^2} + \sqrt{\vec{p}_2^2 + m_2^2} + V(r) , \quad (1.7)$$

where $V(r) = \sigma r$ is a linear potential and $\sigma \simeq 400 \text{ (MeV)}^2$.

For a sake of simplicity, (Fig. 1.15 (a)) massless quarks will be considered. In the CM system the energy will be $H = 2p + \sigma r$ where the orbital angular momentum $\vec{\ell}$ will be $\vec{r} \times \vec{p}$ so that:

$$H(r) = 2\frac{\ell}{r} + \sigma r . \quad (1.8)$$

From the relation $\frac{\partial H}{\partial r} = -\frac{2\ell}{r^2} + \sigma = 0$ the minimum of H is found at $r_0 = \sqrt{\frac{2\ell}{\sigma}}$. If this position is chosen as the ground state of the system, the energy can be expressed as: $H(r_0) = E = 2\sqrt{2}\sqrt{\sigma\ell}$ or $E^2 = 8\sigma\ell$.

This relation gives the dependence of the angular momentum on the energy of the system: $\ell = \frac{1}{8\sigma}E^2$. Performing the substitutions $\alpha \Rightarrow \ell$ and $E^2 \Rightarrow t$:

$$\alpha(t) = \frac{1}{8\sigma}t , \quad (1.9)$$

so that the expression for a simple linear Regge trajectory can be readily recognized.

The choice of a massless $q\bar{q}$ system gives rise to a linear relation in the Mandelstam variable t . The exact calculation yields $\alpha(t) = \frac{1}{2\pi\sigma}t = \alpha't$ for our string with massless ends where $\alpha'(0) \sim 1 \text{ GeV}^2$.

This scheme can be generalized to a string connecting two massive quarks (Fig. 1.15 (b)). In this case a static tension is introduced on the color string, and an additional term is collected in the Regge trajectory:

$$\alpha(t) = \alpha(0) + \alpha'(0)t . \quad (1.10)$$

Another correction term can be obtained considering the screening effects introduced by the vacuum polarization in QCD which complicates the string structure. A distance dependent tension (Fig. 1.15 (c)) can account for this effects since the formation of $q\bar{q}$ pairs from the vacuum weakens the flux tube opening “holes” in the string. A possible form for such a potential due to $q\bar{q}$ loops comes from lattice QCD calculations (see Ref. [72]) and can be parametrized in terms of the screening length μ^{-1} :

$$V(r) = \left(-\frac{\alpha}{r} + \sigma r\right) \frac{1 - e^{-\mu r}}{\mu r} , \quad (1.11)$$

where $\alpha = 0.21 \pm 0.01 \text{ Fm}$.

This potential has the correct Coulomb behavior at small distances and approaches a constant at large distances. The ratio $\frac{\alpha}{\mu}$ represents the splitting energy of the $q\bar{q}$ pair, with $\mu^{-1} = 0.90 \pm 0.20 \text{ Fm}$.

As was shown in the simple model described above, it is expected that composite hadronic systems such mesons and baryons give rise to (slightly) non linear Regge trajectories. In the QGSM, the non linearity of baryon Regge trajectories is incorporated according to Refs [73, 74, 75, 76]. For small momentum transfers, the non linear part is negligible, but when $t \geq 1(\text{GeV}/c)^2$ effects introduced by the non linear part of the Regge trajectories become critical and must be considered.

1.5 Quark Hadron Reactions in the QGSM

The QGSM was originally developed to describe hadron-hadron collisions at high energy. In order to better define its extension to photo-reactions a brief review of its application and predictions for hadronic collisions will be given.

Reactions as $pp \rightarrow d\pi^+$ and $\bar{p}d \rightarrow p\pi^-$ are dominated by diagrams with three valence quark exchanges in the t -channel [77] in analogy to the deuteron photo-disintegration case (see Ref. [59] and Refs [78, 79]).

Fig. 1.16 shows the total cross section data for $pp \rightarrow d\pi^+$ [80]. It is seen that the QGSM very well reproduces the data with the single exception of the near threshold region. The QGSM describes quite well also the data from the $\bar{p}d \rightarrow p\pi^-$ reaction which have been obtained from the reversed channel $\pi^-p \rightarrow \bar{p}d$ [81, 82].

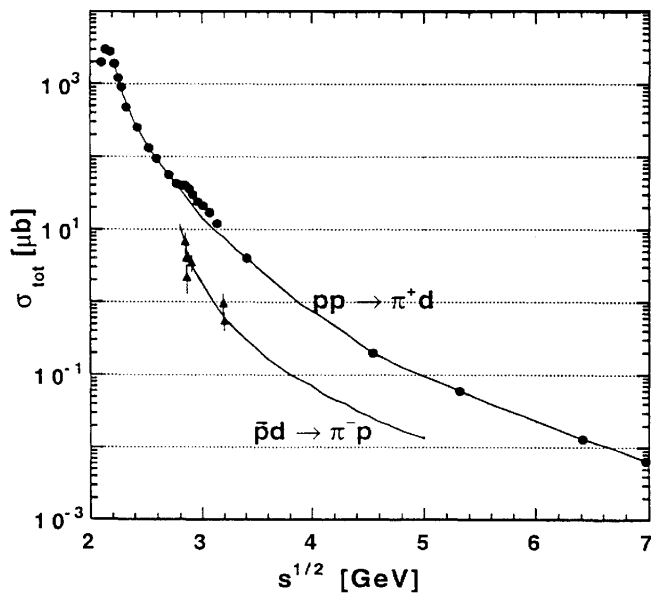


Figure 1.16: Total cross sections of the reactions $pp \rightarrow d\pi^+$ and $\bar{p}d \rightarrow p\pi^-$ as a function of the CM energy, and predictions of the QGS model.

1.5.1 Transition Probabilities and Transition Amplitudes

Each diagram of the topological expansion has a simple interpretation within the framework of the space-time pattern formulated in terms of a color string (see Refs [66, 83]). For instance, at high energy \sqrt{s} , the binary reaction shown in Fig. 1.17 (a) occurs due to a specific quark configuration in each pion, where (in the CM system) one quark (or anti-quark) takes almost the entire hadron momentum and plays the role of a spectator, while the valence anti-quark or quark is rather slow.

The difference in the rapidities Δy between the quark q and the anti-quark \bar{q} in each pion is

$$\Delta y = y_q - y_{\bar{q}} \simeq \frac{1}{2} \ln \frac{s}{s_0}, \quad (1.12)$$

with the scale $s_0 \simeq 1(\text{GeV})^2$.

When the two slow valence particles q and \bar{q} from the two initial π^0 s annihilate, the fast spectator quark and anti-quark continue to move in the previous directions and form a color string in the intermediate state. After that, the string breaks to produce $q\bar{q}$ -pairs from the vacuum and the formation of the $\pi^+\pi^-$ system takes place in the final state. The same space-time pattern holds also for the situation depicted in Fig. 1.17 (b) with the only difference, that the string is formed after the annihilation of a diquark anti-diquark pair from the $N\bar{N}$ system in the initial state. Correspondingly, the graph of Fig. 1.17 (c) shows the formation of the $q\bar{q}$ string due to annihilation of the valence diquark anti-diquark pair in the initial state and the production of a diquark anti-diquark pair as a consequence of the breaking of the string. The annihilation of the initial $q\bar{q}$ pair takes place, when a gap in rapidity of the valence q and \bar{q} is small and both interacting partons are almost at rest in CM system so that the relative impact parameter $\mathbf{b}_\perp - \mathbf{b}_{0\perp}$ is less than their interaction radius. It is possible to prove that the probability to find a valence quark with a rapidity y_q at impact parameter \mathbf{b}_\perp inside a hadron can be written as ([58, 61, 83])

$$w(y_q - y_0, \mathbf{b}_\perp - \mathbf{b}_{0\perp}) = \frac{c}{4\pi R^2(s)} \exp \left[-\beta(y_q - y_0) - \frac{(\mathbf{b}_\perp - \mathbf{b}_{0\perp})^2}{4R^2(s)} \right], \quad (1.13)$$

where c is a normalization constant, y_0 is the average rapidity, $\mathbf{b}_{0\perp}$ is the transverse coordinate in the CM system in the impact parameter representation. Furthermore, it is possible to relate the parameter β and the effective interaction radius squared $R^2(s)$ in 1.13 that specify the quark distribution inside a hadron, to the phenomenological parameters of a Regge trajectory $\alpha_i(t)$ which gives the dominant contribution to the amplitude for the considered planar graph. In this case one gets

$$R^2(s) = R_0^2 + \alpha'_i(y_q - y_0), \quad \beta = 1 - \alpha_i(0), \quad (1.14)$$

where $\alpha'_i = \alpha'_i(0)$ is the slope of the dominant Regge trajectory.

Due to the creation of a string in the intermediate state the amplitude of a binary reaction $ab \rightarrow cd$ has the s -channel factorization property, *i.e.* the probability for the string to produce different hadrons in the final state does not depend on the type of the annihilated quarks and it is only determined by the flavors of the produced quarks. The same independence also holds for the production of the color string in the intermediate state from the initial hadron configuration: it depends only on the type of the annihilated quarks. This s -channel factorization has been formulated in Refs [58, 61, 83] in terms of transition probabilities as defined in Eq. (1.13).

An example of this can be seen for the reactions shown in Fig. 1.17 as well as for the crossed reactions $\pi^+\pi^- \rightarrow \pi^0\pi^0$, $\pi^+\pi^- \rightarrow N\bar{N}$, and $N\bar{N} \rightarrow N\bar{N}$.

For large s values and finite values of the 4-momentum transfer squared t , these channels are described by planar diagrams with t -channel valence-quark exchanges as in Fig. 1.17, where the single and double solid lines correspond to valence quarks and diquarks, respectively (soft gluon exchanges are not shown). Introducing the hadron(γ)-quark and quark-hadron transition amplitudes, analytic expressions for the form factors have been found in the time-like region which admit continuation in the space-like region.

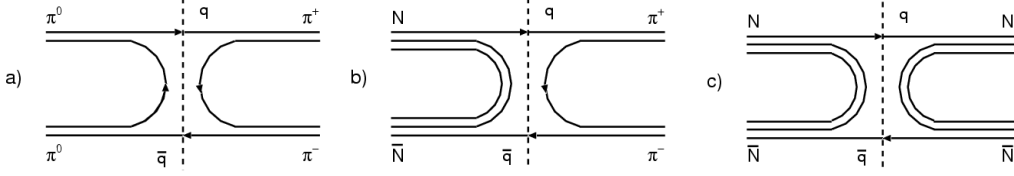


Figure 1.17: Planar diagrams describing the binary reactions $\pi^0\pi^0 \rightarrow \pi^+\pi^-$ (a: left panel), $N\bar{N} \rightarrow \pi^+\pi^-$ (b: central panel), and $N\bar{N} \rightarrow N\bar{N}$ (c: right panel).

This approach can be generalized [84] introducing the amplitudes $\tilde{T}^{ab \rightarrow q\bar{q}}(s, \mathbf{b}_\perp)$ and $\tilde{T}^{q\bar{q} \rightarrow cd}(s, \mathbf{b}_\perp)$, that describe the formation and the fission of an intermediate color string. The amplitude for the reaction $ab \rightarrow cd$ described by the planar graph can be written, using the s -channel factorization property, in the form of a convolution of two amplitudes:

$$A^{ab \rightarrow cd}(s, \mathbf{q}_\perp) = \frac{i}{8\pi^2 s} \int d^2 \mathbf{k}_\perp T^{ab \rightarrow q\bar{q}}(s, \mathbf{k}_\perp) T^{q\bar{q} \rightarrow cd}(s, \mathbf{q}_\perp - \mathbf{k}_\perp) \quad (1.15)$$

in momentum representation, or as the product

$$\tilde{A}^{ab \rightarrow cd}(s, \mathbf{b}_\perp) = \frac{i}{2s} \tilde{T}^{ab \rightarrow q\bar{q}}(s, \mathbf{b}_\perp) \tilde{T}^{q\bar{q} \rightarrow cd}(s, \mathbf{b}_\perp), \quad (1.16)$$

in the impact-parameter representation.

The solution for the quark-hadron transition amplitudes $T^{q\bar{q} \rightarrow \pi\bar{\pi}}(s, \mathbf{k}_\perp)$ and $T^{q\bar{q} \rightarrow N\bar{N}}(s, \mathbf{k}_\perp)$ at large invariant energy \sqrt{s} can be found using single Regge-pole parameterizations of the binary hadronic amplitudes $A^{\pi^0\pi^0 \rightarrow \pi^+\pi^-}$, $A^{N\bar{N} \rightarrow \pi\bar{\pi}}$ and $A^{N\bar{N} \rightarrow N\bar{N}}$

$$\begin{aligned} A^{\pi^0\pi^0 \rightarrow \pi^+\pi^-}(s, t) &= N_M \left(-\frac{s}{m_0^2} \right)^{\alpha_M(t)} \exp(R_{0M}^2 t), \\ A^{N\bar{N} \rightarrow \pi\bar{\pi}}(s, t) &= N_B \left(-\frac{s}{m_0^2} \right)^{\alpha_B(t)} \exp(R_{0B}^2 t), \\ A^{N\bar{N} \rightarrow N\bar{N}}(s, t) &= N_D \left(-\frac{s}{m_0^2} \right)^{\alpha_D(t)} \exp(R_{0D}^2 t). \end{aligned} \quad (1.17)$$

Here $\alpha_M(t)$, $\alpha_B(t)$ and $\alpha_D(t)$ are the dominant meson, baryon and diquark-antidiquark trajectories while N_M , N_B and N_D are normalization constants; $m_0^2 = s_0$ and R_{0i} is the interaction radius for the i -th trajectory. The following intercepts and slopes are found for the dominant Regge trajectories

$$\alpha_M(0) \simeq 0.5, \quad \alpha_B(0) \simeq -0.5, \quad \alpha_D(0) \simeq -1.5 \quad (1.18)$$

and

$$\alpha'_M(0) \simeq \alpha'_B(0) \simeq \alpha'_D(0) \simeq 1.0 \text{ GeV}^{-2}. \quad (1.19)$$

Using equations (1.16) and (1.17) the amplitudes $\tilde{T}^{q\bar{q}\rightarrow\pi\bar{\pi}}(s, \mathbf{b}_\perp)$ and $\tilde{T}^{q\bar{q}\rightarrow N\bar{N}}(s, \mathbf{b}_\perp)$ can be written as

$$\begin{aligned}\tilde{T}^{q\bar{q}\rightarrow\pi\bar{\pi}}(s, \mathbf{b}_\perp) &= N_M^{1/2} \frac{1}{2\sqrt{\pi}R_M(s)} \left(-\frac{s}{m_0^2}\right)^{(\alpha_M(0)+1)/2} \exp\left(-\frac{\mathbf{b}_\perp^2}{8R_M^2(s)}\right), \\ \tilde{T}^{q\bar{q}\rightarrow N\bar{N}}(s, \mathbf{b}_\perp) &= N_D^{1/2} \frac{1}{2\sqrt{\pi}R_D(s)} \left(-\frac{s}{m_0^2}\right)^{(\alpha_D(0)+1)/2} \exp\left(-\frac{\mathbf{b}_\perp^2}{8R_D^2(s)}\right),\end{aligned}\tag{1.20}$$

where $R_M(s)$ and $R_D(s)$ are the effective interaction radii given by

$$\begin{aligned}R_M^2(s) &= R_{0M}^2 + \alpha'_M(0) \ln\left(-\frac{s}{m_0^2}\right), \\ R_D^2(s) &= R_{0D}^2 + \alpha'_D(0) \ln\left(-\frac{s}{m_0^2}\right).\end{aligned}\tag{1.21}$$

The substitution of the amplitudes (1.20) into the factorization formula (1.16) gives:

$$\begin{aligned}\tilde{A}^{N\bar{N}\rightarrow\pi\bar{\pi}}(s, \mathbf{b}_\perp) &= \\ (N_M N_D)^{1/2} \frac{1}{4\pi R_D(s) R_M(s)} \left(-\frac{s}{m_0^2}\right)^{\frac{1}{2}(\alpha_D(0)+\alpha_M(0))} &\exp\left[-\mathbf{b}_\perp^2 \left(\frac{1}{8R_M^2(s)} + \frac{1}{8R_D^2(s)}\right)\right].\end{aligned}\tag{1.22}$$

Consistency of Eqs. (1.22) and (1.17) requires the following relations between the Regge parameters and normalization constants ([61, 84, 58]):

$$2\frac{1}{R_B^2(s)} = \frac{1}{R_M^2(s)} + \frac{1}{R_D^2(s)},\tag{1.23}$$

$$2\alpha(0)_B = \alpha_D(0) + \alpha_M(0),$$

$$(N_M N_D)^{1/2} \frac{1}{R_D(s) R_M(s)} = N_B \frac{1}{R_B^2(s)}.\tag{1.24}$$

If only light u, d quarks are involved it can be assumed that ([61, 78, 84])

$$\alpha'_M(0) = \alpha'_B(0) = \alpha'_D(0) \equiv \alpha'(0),$$

$$R_{0M}^2(0) = R_{0B}^2(0) = R_{0D}^2(0) \equiv R_0^2(0),\tag{1.25}$$

$$(N_M N_D)^{1/2} = N_B.$$

Then the relations (1.23) and (1.24) can be fulfilled at all s . Otherwise, they can only be satisfied at sufficiently large s (Ref. [92]).

1.6 Deuteron Photo-disintegration in the QGSM

It is convenient start the description of the photo-disintegration reaction considering the amplitudes for spin-less constituents before going over to the case in which the photon spin is included.

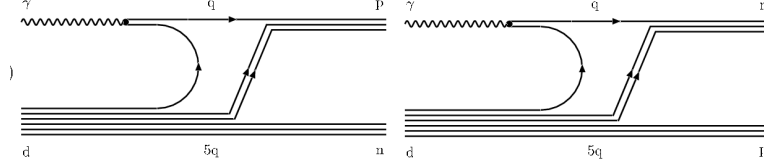


Figure 1.18: Diagrams describing three valence quark exchanges in the t -channel (left panel) and u -channel (right panel).

From Eq. 1.16 the transition amplitude corresponding to each quark diagram of Fig. 1.18 can be written as:

$$\tilde{A}^{\gamma d \rightarrow pn}(s, \mathbf{b}_\perp) = \frac{i}{2s} \tilde{T}^{\gamma d \rightarrow q(5q)}(s, \mathbf{b}_\perp) \tilde{T}^{q(5q) \rightarrow pn}(s, \mathbf{b}_\perp), \quad (1.26)$$

where the amplitudes $\tilde{T}^{\gamma d \rightarrow q(5q)}(s, \mathbf{b}_\perp)$ and $\tilde{T}^{q(5q) \rightarrow pn}(s, \mathbf{b}_\perp)$ are given by (cf. (1.20))

$$\begin{aligned} \tilde{T}^{\gamma d \rightarrow q(5q)}(s, \mathbf{b}_\perp) &= N_{M(6q)}^{1/2} \frac{1}{2\sqrt{\pi} R_{M(6q)}(s)} \left(-\frac{s}{m_0^2}\right)^{(\alpha_M(0)+1)/2} \exp\left(-\frac{\mathbf{b}_\perp^2}{8R_{M(6q)}^2(s)}\right), \\ \tilde{T}^{q(5q) \rightarrow pn}(s, \mathbf{b}_\perp) &= N_{D(6q)}^{1/2} \frac{1}{2\sqrt{\pi} R_{D(6q)}(s)} \left(-\frac{s}{m_0^2}\right)^{(\alpha_D(0)+1)/2} \exp\left(-\frac{\mathbf{b}_\perp^2}{8R_{D(6q)}^2(s)}\right). \end{aligned} \quad (1.27)$$

Here the effective interaction radii $R_{M(6q)}(s)$ and $R_{D(6q)}(s)$ are defined as

$$\begin{aligned} R_{M(6q)}^2(s) &= R_{0M(6q)}^2 + \alpha'_M(0) \ln\left(-\frac{s}{m_0^2}\right), \\ R_{D(6q)}^2(s) &= R_{0D(6q)}^2 + \alpha'_D(0) \ln\left(-\frac{s}{m_0^2}\right), \end{aligned} \quad (1.28)$$

where $R_{0M(6q)}^2$ and $R_{0D(6q)}^2$ are, in general, different from R_{0M}^2 and R_{0D}^2 in Eq. (1.21).

Since the photon possess an hadronic structure, a photo-reaction such as $\gamma d \rightarrow pn$ could be assimilated to a hadron-hadron collision. In this case, the photon spin must be taken into account since its transversal polarization leads to a non-trivial angular dependence of the residue of the amplitude [59]. Spin effects in the QGSM where first introduced using the s -channel factorization property of amplitudes, developed in Ref. [84] with respect to the description of the electromagnetic nucleon form factors F_1 and F_2 .

The resulting form factors for nucleons and pions comply well with the experimental data for both positive and negative values of q^2 (see Refs [85, 86, 87, 88, 89, 90]).

In the case of the deuteron photo-disintegration, the amplitude can be written in the form:

$$\begin{aligned} \langle p_3, \lambda_p; p_4, \lambda_n | \hat{T}(s, \mathbf{p}_{3\perp}) | p_2, \lambda_d; p_1, \lambda_\gamma \rangle = \\ \frac{i}{8\pi^2 s} \int d^2 \mathbf{k}_\perp \langle \lambda_p; \lambda_n | \hat{T}^{q(5q) \rightarrow pn}(s, \mathbf{k}_\perp) | \lambda_q; \lambda_{(5q)} \rangle \\ \langle \lambda_q; \lambda_{(5q)} | \hat{T}^{\gamma d \rightarrow q(5q)}(s, \mathbf{p}_{3\perp} - \mathbf{k}_\perp) | \lambda_d; \lambda_\gamma \rangle, \end{aligned} \quad (1.29)$$

where p_1, p_2, p_3 , and p_4 are the 4-momenta of the photon, deuteron, proton, and neutron, respectively, while λ_i is the s channel helicity of the i -th particle. Furthermore, making the simplifying assumption that the spin of the $(5q)$ state is $1/2$, the amplitude $\hat{T}^{\gamma d \rightarrow q(5q)}$ can be written as

$$\begin{aligned} \langle \lambda_q; \lambda_{(5q)} | \hat{T}(s, \mathbf{k}_\perp) | \lambda_d; \lambda_\gamma \rangle = \\ \bar{u}_{\lambda_q}(p_q) \hat{\epsilon}_{\lambda_\gamma} \left(\frac{-\hat{k} + m_q}{k^2 - m_q^2} \right) \hat{\epsilon}_{\lambda_d} v_{\lambda_{(5q)}}(p_{(5q)}) D^{\gamma d \rightarrow q(5q)}(s, \mathbf{k}_\perp), \end{aligned} \quad (1.30)$$

where ϵ_{λ_d} and $\epsilon_{\lambda_\gamma}$ are the deuteron and photon polarization vectors, $D^{\gamma d \rightarrow q(5q)}(s, \mathbf{k}_\perp)$ is the scalar amplitude and m_q is the quark mass. In analogy to $q\bar{q} \rightarrow N\bar{N}$, which was analyzed in Ref. [84], we can describe the spin structure of the amplitude $\hat{T}^{q(5q) \rightarrow pn}$ in terms of eight invariant amplitudes

$$\begin{aligned} \langle \lambda_p; \lambda_n | \hat{T}^{q+(5q) \rightarrow pn}(s, \mathbf{k}_\perp) | \lambda_q; \lambda_{(5q)} \rangle = \\ D_1(s, \mathbf{k}_\perp) \delta_{\lambda_p \lambda_q} \delta_{\lambda_n \lambda_{(5q)}} + D_2(s, \mathbf{k}_\perp) (\sigma_y)_{\lambda_p \lambda_q} \delta_{\lambda_n \lambda_{(5q)}} + \\ D_3(s, \mathbf{k}_\perp) \delta_{\lambda_p \lambda_q} (\sigma_y)_{\lambda_n \lambda_{(5q)}} + D_4(s, \mathbf{k}_\perp) (\sigma_x)_{\lambda_p \lambda_q} (\sigma_x)_{\lambda_n \lambda_{(5q)}} + \\ D_5(s, \mathbf{k}_\perp) (\sigma_y)_{\lambda_p \lambda_q} (\sigma_y)_{\lambda_n \lambda_{(5q)}} + D_6(s, \mathbf{k}_\perp) (\sigma_z)_{\lambda_p \lambda_q} (\sigma_z)_{\lambda_n \lambda_{(5q)}} + \\ D_7(s, \mathbf{k}_\perp) (\sigma_x)_{\lambda_p \lambda_q} (\sigma_z)_{\lambda_n \lambda_{(5q)}} + D_8(s, \mathbf{k}_\perp) (\sigma_z)_{\lambda_p \lambda_q} (\sigma_x)_{\lambda_n \lambda_{(5q)}}, \end{aligned} \quad (1.31)$$

where the z - and x -axes are directed along the photon momentum and the momentum transfer \mathbf{k}_\perp , respectively, and the y -axis is orthogonal to the scattering plane. Now the experimental data on the proton form factor are in agreement with the assumption that the dominant contribution stems from the amplitude corresponding to the conservation of the s -channel helicities ([84]). Here the same assumption is used, taking into account only the amplitude $D_1(s, \mathbf{k}_\perp)$. Thus:

$$\begin{aligned} \langle \lambda_p; \lambda_n | \hat{T}(s, \mathbf{p}_{3\perp}) | \lambda_d; \lambda_\gamma \rangle = \\ \frac{i}{8\pi^2 s} \int d^2 \mathbf{k}_\perp \bar{u}_{\lambda_p}(p_3) \hat{\epsilon}_{\lambda_\gamma} \left(\frac{-\hat{k} + m_q}{k^2 - m_q^2} \right) \hat{\epsilon}_{\lambda_d} v_{\lambda_n}(p_4) \\ \times D^{\gamma d \rightarrow q(5q)}(s, \mathbf{k}_\perp) D_1(s, \mathbf{p}_{3\perp} - \mathbf{k}_\perp). \end{aligned} \quad (1.32)$$

Furthermore, taking into account that at high energy $p_\gamma \gg \sqrt{s_0}$ and finite momentum transfer $t \simeq |\mathbf{p}_{3\perp}|^2 \simeq s_0$ the momentum k is almost transversal $k = (k_0, \mathbf{k}_\perp, k_z)$, where $k_0 \simeq k_z \simeq O\left(\frac{s_0}{2p_\gamma}\right)$ and $\int d^2\mathbf{k}_\perp \mathbf{k}_\perp(\dots) \sim \mathbf{p}_{3\perp}$, it is found the following representation for the spin structure of the $\gamma d \rightarrow pn$ amplitude:

$$\langle \lambda_p; \lambda_n | \hat{T}(s, \mathbf{p}_{3\perp}) | \lambda_d; \lambda_\gamma \rangle = \bar{u}_{\lambda_p}(p_3) \hat{\epsilon}_{\lambda_\gamma} (-A(s, t) \mathbf{p}_{3\perp} \cdot \boldsymbol{\gamma} + B(s, t) m) \hat{\epsilon}_{\lambda_d} v_{\lambda_n}(p_4), \quad (1.33)$$

where

$$A(s, t) = \frac{i}{8\pi^2 s} \int d^2\mathbf{k}_\perp \frac{\mathbf{k}_\perp \cdot \mathbf{p}_{3\perp}}{|\mathbf{p}_{3\perp}|^2} \frac{1}{k^2 - m_q^2} \times D^{\gamma d \rightarrow q(5q)}(s, \mathbf{k}_\perp) D_1^{q(5q) \rightarrow pn}(s, \mathbf{p}_{3\perp} - \mathbf{k}_\perp), \quad (1.34)$$

$$B(s, t) = \frac{i}{8\pi^2 s} \frac{m_q}{m} \int d^2\mathbf{k}_\perp \frac{1}{k^2 - m_q^2} \times D^{\gamma d \rightarrow q(5q)}(s, \mathbf{k}_\perp) D_1^{q(5q) \rightarrow pn}(s, \mathbf{p}_{3\perp} - \mathbf{k}_\perp), \quad (1.35)$$

and m is the nucleon mass. In the case of a Gaussian parametrization for $D^{\gamma d \rightarrow q(5q)}(s, \mathbf{k}_\perp)$ and D_1 (in Eqs. (24,25)) the ratio $R = A(s, t)/B(s, t)$ is a smooth function of t . Further on, it will be assumed that it is a constant and will be considered as a free parameter. The differential cross section for the reaction $\gamma d \rightarrow pn$ is then

$$\frac{d\sigma_{\gamma d \rightarrow pn}^I}{dt} = \frac{1}{64\pi s} \frac{1}{(p_\gamma^{\text{cm}})^2} [S_t |B(s, t)|^2 + S_u |B(s, u)|^2 + (-1)^{I+1} 2S_{tu} \text{Re}(B(s, t)B(s, u))], \quad (1.36)$$

where I is the isospin of the reaction, *i.e.* $I = 1$ (or 0) for isovector (or isoscalar) photons. The kinematical functions S_t , S_u , S_{tu} in (1.36) are given by

$$\begin{aligned} S_t &= \frac{1}{6} \sum_{\lambda_\gamma, \lambda_d} \text{Tr} \left[\hat{\epsilon}_{\lambda_\gamma} (R(\hat{p}_3 - \hat{p}_1) + m) \hat{\epsilon}_{\lambda_d} (\hat{p}_4 - m) \right. \\ &\quad \left. \times \hat{\epsilon}_{\lambda_d}^* (R(\hat{p}_3 - \hat{p}_1) + m) \hat{\epsilon}_{\lambda_\gamma}^* (\hat{p}_3 + m) \right], \\ S_u &= \frac{1}{6} \sum_{\lambda_\gamma, \lambda_d} \text{Tr} \left[\hat{\epsilon}_{\lambda_d} (R(\hat{p}_3 - \hat{p}_1) + m) \hat{\epsilon}_{\lambda_\gamma} (\hat{p}_4 - m) \right. \\ &\quad \left. \times \hat{\epsilon}_{\lambda_\gamma}^* (R(\hat{p}_3 - \hat{p}_1) + m) \hat{\epsilon}_{\lambda_d}^* (\hat{p}_3 + m) \right], \\ S_{tu} &= \frac{1}{6} \sum_{\lambda_\gamma, \lambda_d} \text{Tr} \left[\hat{\epsilon}_{\lambda_\gamma} (R(\hat{p}_3 - \hat{p}_1) + m) \hat{\epsilon}_{\lambda_d} (\hat{p}_4 - m) \right. \\ &\quad \left. \times \hat{\epsilon}_{\lambda_\gamma}^* (R(\hat{p}_3 - \hat{p}_1) + m) \hat{\epsilon}_{\lambda_d}^* (\hat{p}_3 + m) \right]. \end{aligned} \quad (1.37)$$

In order to fix the energy dependence of the amplitude $B(s, t)$ it is required that

$$\left. \frac{d\sigma}{dt} \right|_{\theta^{\text{CM}}=0} \sim \left(\frac{s}{s_0} \right)^{2\alpha_N(0)-2}. \quad (1.38)$$

Taking into account that $S_t \sim s$ for $s \gg s_0$ it is found that

$$B(s, t) \sim \left(\frac{s}{s_0} \right)^{\alpha_N(0)-1/2}. \quad (1.39)$$

Moreover, a good approximation for the energy dependence of $S_t(\theta^{CM} = 0)$ in the region $p_\gamma = 1 \div 7.5$ GeV is

$$S_t|_{\theta^{CM}=0} \approx C p_\gamma^2 \quad (1.40)$$

with $C = (36 \pm 3)$ GeV². Using this approximation $B(s, t)$ can be related to the Regge-pole exchange amplitude as

$$|B(s, t)|^2 = \frac{1}{C p_\gamma^2} |\mathcal{M}_{\text{Regge}}(s, t)|^2, \quad (1.41)$$

where

$$\mathcal{M}_{\text{Regge}}(s, t) = F(t) \left(\frac{s}{s_0} \right)^{\alpha_N(t)} \exp \left[-i \frac{\pi}{2} \left(\alpha_N(t) - \frac{1}{2} \right) \right]. \quad (1.42)$$

Here $\alpha_N(t)$ is the trajectory of the nucleon Regge pole and $s_0 = 4$ GeV² $\simeq m_d^2$.

1.6.1 Nonlinear Nucleon Regge Trajectories

According to the data on πN backward scattering (see *e.g.* the review [73]) the nucleon Regge trajectory has a nonlinearity of the form:

$$\alpha_N(t) = \alpha_N(0) + \alpha'_N(0) t + \frac{1}{2} \alpha''_N(0) t^2 K(t), \quad (1.43)$$

where $\alpha_N(0) = -0.5$, $\alpha'_N(0) = 0.9$ GeV⁻² are the intercept and slope of the Regge trajectory, and $\alpha''_N(0) = 0.20 \div 0.25$ GeV⁻⁴ is the coefficient of the nonlinear term. In (1.43) it is introduced also a cut-off function $K(t)$. Assuming that $K(t) = 1$ the amplitude will grow very fast with s at large t which would violate unitarity. To prevent this fast growth the exponential form

$$K(t) = \exp(-\beta t^2) \quad (1.44)$$

is chosen with $\beta = 0.008$ GeV⁻⁴. The small value of β does not destroy the parameterization of $\alpha(t)$ for $-t \leq 1.6$ GeV² derived from Ref. [73]. Note also that the phenomenological Regge trajectory (1.43) with a power-like or exponential cut-off is nonlinear only for moderate values of t ; at large t the quadratic term becomes small and the trajectory becomes essentially linear again.

On the other hand, the QCD motivated Regge trajectories as suggested by Brisudová, Burakovsky and Goldman (BBG) [83] show a different behavior at large t . As shown in the previous Section the screened quark-antiquark potential (Eq. 1.11) leads to nonlinear meson Regge trajectories. These trajectories can be parametrized on the whole physical sheet as

$$\alpha(t) = \alpha(0) + \gamma [T^\nu - (T - t)^\nu] \quad (1.45)$$

with $0 \leq \nu \leq 1/2$. The limiting cases $\nu = 1/2$ and $\nu \rightarrow 0$ ($\gamma\nu = \text{const}$) correspond to the square-root trajectory

$$\alpha(t) = \alpha(0) + \gamma \left[\sqrt{T} - \sqrt{T-t} \right], \quad (1.46)$$

and the logarithmic trajectory

$$\alpha(t) = \alpha(0) - (\gamma\nu) \ln \left(1 - \frac{t}{T} \right) \quad (1.47)$$

respectively. Such trajectories arise not only for heavy quarkonia, but also for light-flavor hadrons.

In order to find the possible forms of nonlinear Regge trajectories for mesons composed of light quarks, the analytical model shown in subsection 1.6.1 has to be considered. In this picture, the color flux tube is stretched between quark and antiquark at the tube ends. The varying string tension is introduced to simulate dynamical effects such as the weakening of the flux tube due to pair ($q\bar{q}$) creation. Within this framework it is possible to recover the form of the underlying potential for a given Regge trajectory. Potentials leading to “square-root” and “logarithmic” Regge trajectories have been taken from Ref. [83] where it was demonstrated that their effect is very similar to what is obtained by a screened potential in the unquenched lattice QCD. In addition, this approach is able to reproduce with very good accuracy all the available meson spectra.

From experimental data it is known that the slopes of meson and baryon Regge trajectories are almost the same $\alpha'_N \simeq \alpha'_\rho \simeq 0.9 - 1 \text{ GeV}^{-2}$ (see Ref. [66]). Since the slope is determined by the string tension which, in turn, depends on the color charges at the string ends, a baryon Regge trajectory can be described using the form suggested by the analytical string model for the meson. In the baryon case one of the quarks at the ends is substituted by a diquark ([91]).

1.7 Predictions for the $\gamma d \rightarrow pn$ Differential Cross Section

The dependence of the residue $F(t)$ on t can be written in the form (see [78, 79]):

$$F(t) = B \left[\frac{1}{m^2 - t} \exp(R_1^2 t) + C \exp(R_2^2 t) \right], \quad (1.48)$$

where the first term in the square brackets contains the nucleon pole and the second term accounts for the contribution of non-nucleonic degrees of freedom in the deuteron such as the **D** wave components and isobar contributions.

The set of parameter for the Regge trajectory is the same used in the phenomenological nonlinear trajectory [31]:

$$B = 4.01 \cdot 10^{-4} \text{ kb}^{1/2} \cdot \text{GeV}, \quad C = 0.7 \text{ GeV}^{-2}, \\ R_1^2 = 2 \text{ GeV}^{-2}, \quad R_2^2 = 0.03 \text{ GeV}^{-2}, \quad \alpha''_{N(0)} = 0.25 \text{ GeV}^{-4} \quad (1.49)$$

the ratio $R = A(s, t)/B(s, t)$ being equal to 1.

The QCD motivated logarithmic trajectory differs only for an overall normalization factor B taken as $1.8 \cdot 10^{-4} \text{ kb}^{1/2} \cdot \text{GeV}$ and for the ratio $R = A(s, t)/B(s, t)$ being equal to 2.

The free parameter T is fixed by comparison with the available experimental data. The QGSM predictions, based on the QCD motivated “logarithmic” trajectory of Eq. 1.47 were shown in Fig. 1.6 for $T = 1.7 \text{ GeV}^2$ taking into account the interference of the isovector and isoscalar components of the scattering amplitude. The forward-backward asymmetry arises from the interference of two amplitudes describing the contribution of isovector (ρ like) and isoscalar (ω like) photons, so that in this case the differential cross section can be written as

$$\begin{aligned} \frac{d\sigma_{\gamma d \rightarrow pn}^{\rho+\omega}}{dt} &= \frac{1}{64 \pi s} \frac{1}{(p_{\gamma}^{\text{cm}})^2} [S_t |B^{\rho}(s, t) + B^{\omega}(s, t)|^2 + \\ &S_u |B^{\rho}(s, u) - B^{\omega}(s, u)|^2 \\ &+ 2S_{tu} \text{Re}(B^{\rho}(s, t) + B^{\omega}(s, t))^* (B^{\rho}(s, u) - B^{\omega}(s, u))] , \quad (1.50) \end{aligned}$$

having used the vector dominance model in the form:

$$B^{\omega}(s, t) = B^{\rho}(s, t)/\sqrt{8}, \quad B^{\omega}(s, u) = B^{\rho}(s, u)/\sqrt{8}. \quad (1.51)$$

1.8 Summary

The study of the deuteron photo-disintegration at photon energies higher than 1 GeV can shed light on the reaction mechanisms at work in the transition from the nuclear to the QCD picture of the deuteron.

To this aim, the world cross section data on the deuteron photo-disintegration have been reviewed, both at low ($E_{\gamma} \leq 1 \text{ GeV}$) and high ($1 \leq E_{\gamma} \leq 5.5 \text{ GeV}$) incident photon energies. In the high energy region a new phenomenon emerges: the cross section scaling. According to a simple interpretation it could be a consequence of perturbative QCD. The scaling appears at different energies for different angles corresponding to a perpendicular momentum transfer of approximately 1 GeV^2 . From a closer look at the photo-disintegration data for the differential cross section emerges that the pQCD description is not plainly applicable especially at intermediate momentum transfers.

The complementary information derived from polarization observables suggests that non perturbative physics could be at work even at relatively high momentum transfers so that soft mechanism could mimic the scaling behavior. Some non perturbative quark models well describe the experimental data. Among the various models, the Quark Gluon String model stands out since it gives a good description of both cross section and proton in-plane polarization transfers data.

For this reason, the theoretical foundations and predictions of the QGSM have been fully illustrated.

From the experimental point of view, the possibility to further check the theoretical predictions and to discriminate among the different models requires the knowledge of the differential cross section in a wide range of photon energies and for very forward and backward angles.

Chapter 2

Experimental Apparatus

2.1 The Jefferson Lab Accelerator Facility

The Continuous Electron Beam Accelerator (CEBAF) at JLab uses a high power electron beam with energies up to 6 GeV and 100% duty cycle. A schematic layout of the accelerator and experimental halls is shown in Fig. 2.1. The machine design, based on a race-track configuration, has the advantage of limiting the length and cost of the accelerating sections by recirculating the beam several times into the linacs while keeping low the energy loss due to *bremsstrahlung* in the curvature parts of the tracks. The injection system consists of a 45 MeV linac inserting electrons

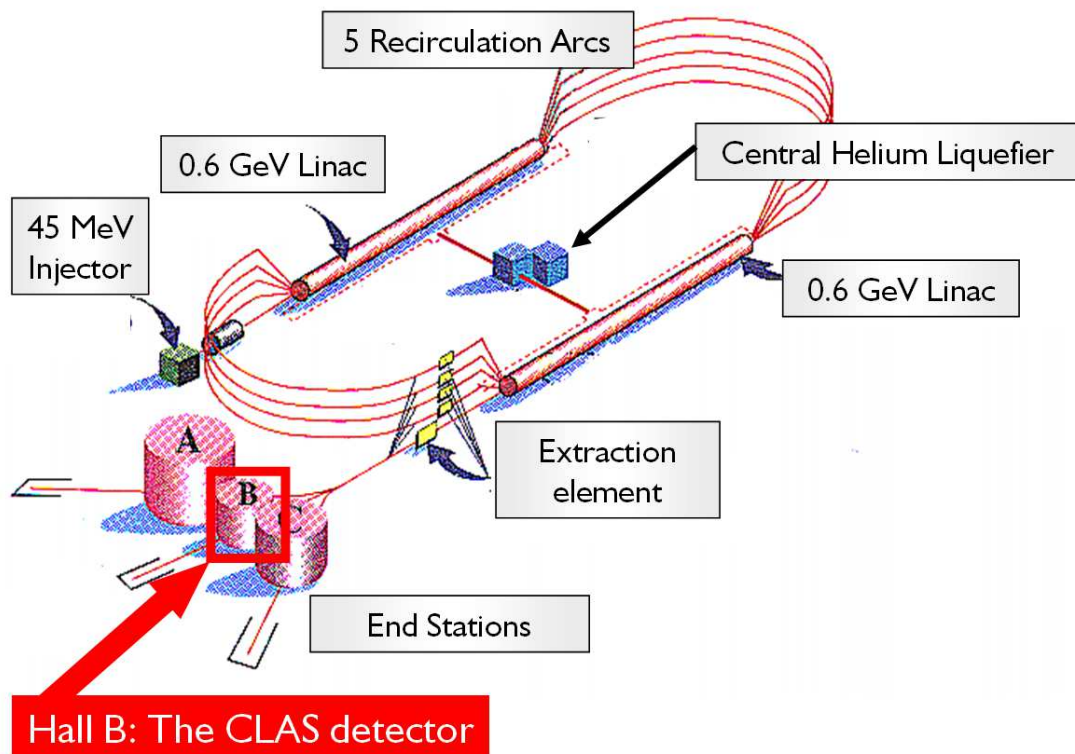


Figure 2.1: Schematic layout of the JLab Continuous Electron Beam Accelerator.

into the main accelerator. The different beams can coexist in the linacs, but must occupy different arcs. At the heart of the machine are the 8 five-cell niobium superconducting radio frequency (RF) cavities per cryo-module having an high average gradient (see Tab. 2.1) and operating at 1.5 GHz. Once into the main accelerator,

	Gradient	Quality Factor
Design specs	5.0 MeV/m	$2.4 \cdot 10^9$
Average performance	9.56 MeV/m	$7.0 \cdot 10^9$
Best performance	18.0 MeV/m	$9.0 \cdot 10^9$

Table 2.1: Performance figures for the CEBAF RF super-conducting cells.

the beam enters the north linac and gains an additional boost of 600 MeV of kinetic energy and then is bent through 180° and sent to the south linac where it is boosted once again by 600 MeV. At this point, the beam could be sent to an experimental hall or recirculated through the north linac. The beam can be further recirculated up to 4 times, picking 1200 MeV each time is sent around the accelerator.

The primary electron beam delivered by the accelerator can be separated to be sent to the experimental areas, Halls A, B, and C, for simultaneous experiments. The electron packet structure has a frequency of 1.5 GHz and can reach a bunch-to-bunch intensity modulated with a periodicity of 3, in order to deliver beam to the different Halls with variable intensity and energy so that beams in the three Halls can have either the same energy or energies multiples of $1/5$ of the end-point energy.

The experimental equipment in the Halls is complementary, addressing a wide range of physics issues. Hall A has two identical focusing high-resolution spectrometers with a maximum momentum of 4 GeV/c [93]. Hall C has two symmetric focusing spectrometers: one featuring acceptance of high-momentum particles, the other a short path length for the detection of decaying particles [94].

Hall B houses the CEBAF Large Acceptance Spectrometer, CLAS, designed for operation with both electron and tagged-photon beams and described in more detail in the next section.

2.2 The CEBAF Hall B

The Hall B facility is devoted to experimental studies of electro and photo-reactions requiring the detection of several only loosely correlated particles in the hadronic final state and measurements at limited (for the JLab standards) luminosities. In order to achieve high detection efficiency for multi-particle final states a large-acceptance detection is required. In addition, a large-acceptance detector may compensate for various restrictions limiting the experimental operation to moderate luminosities. For example, in experiments using a tagged *bremsstrahlung* photon beam, a lower luminosity is required to keep down accidental coincidences.

A view of the Hall B layout is shown in Figs 2.3 and 2.2 where the electron-photon beam line, the tagging spectrometer for photon beam operations, the large angle spectrometer CLAS and its associated equipments are represented. Also, solid-state polarized targets can only be operated at lower beam currents, corresponding to low luminosity. A high detection efficiency for multi-particle events and a useful event

rate at limited luminosity both require a detection system with a large acceptance. The instantaneous intensity of a tagged photon beam produced by the Hall B tagging spectrometer is limited to approximately 10^7 tagged γ /s by accidental coincidences, typically resulting in relatively low background rates in a large-acceptance detector.

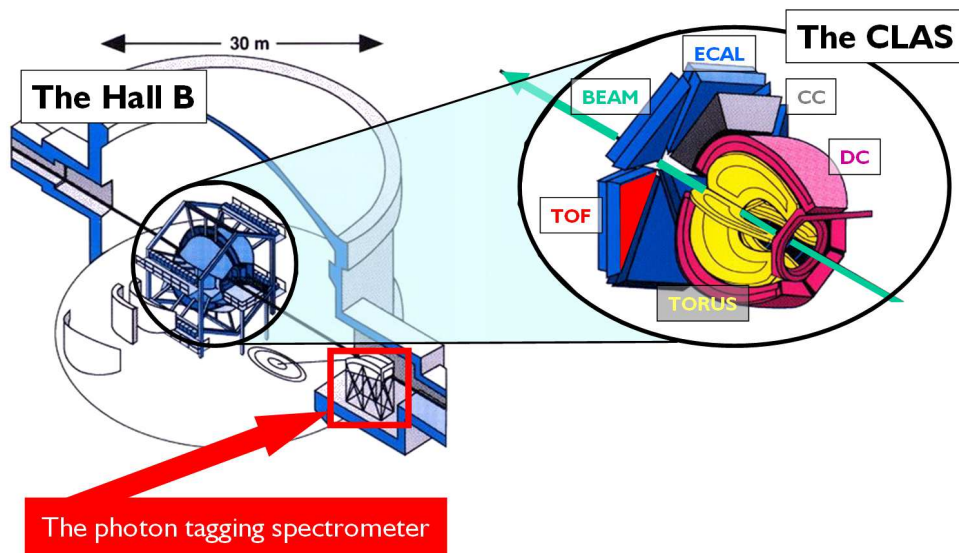


Figure 2.2: Left panel: Schematic view of the Hall B enclosure, including the CLAS metal supporting structures. The tagging spectrometer is shown at the entrance on the Hall, upstream with respect to the electron beam direction. Right panel: The CLAS detector magnified view showing the schematics for the detector subsystems.

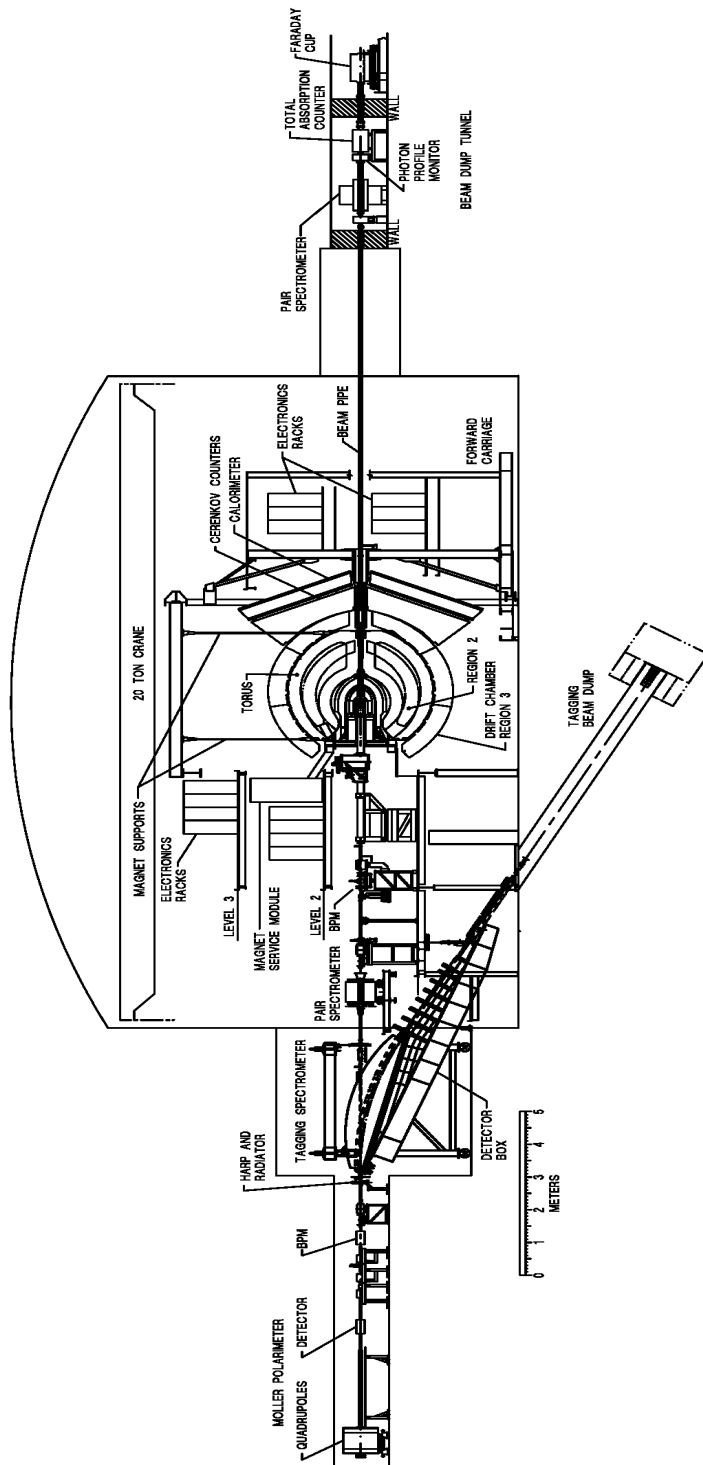


Figure 2.3: Hall B beam-line, the CLAS detector, and associated equipment.

2.2.1 Hall B Photon Production and Tagging

Electrons from the CEBAF accelerator strike a thin target (the "radiator") just upstream from a magnetic spectrometer [95] (the "tagger"). Photons produced in the radiator continue toward the CLAS target following the same beam-line through the magnet yoke that is traversed by the electron beam when the tagger is not in use. The *bremsstrahlung* tagging technique for direct measurement of the incident photon energy in photo-nuclear interactions is well established [96]. The JLab system is the first photon tagger in the multi GeV energy range to combine high resolution ($\simeq 10^{-3}E_0$) with a broad tagging range (20% – 95%) of E_0 .

There are three modes of operation for photon beams in Hall B: a normal non-polarized mode, a circularly polarized mode, and a linearly polarized mode. These are governed by the polarization state of the incident electron beam, and by the nature of the photon radiator.

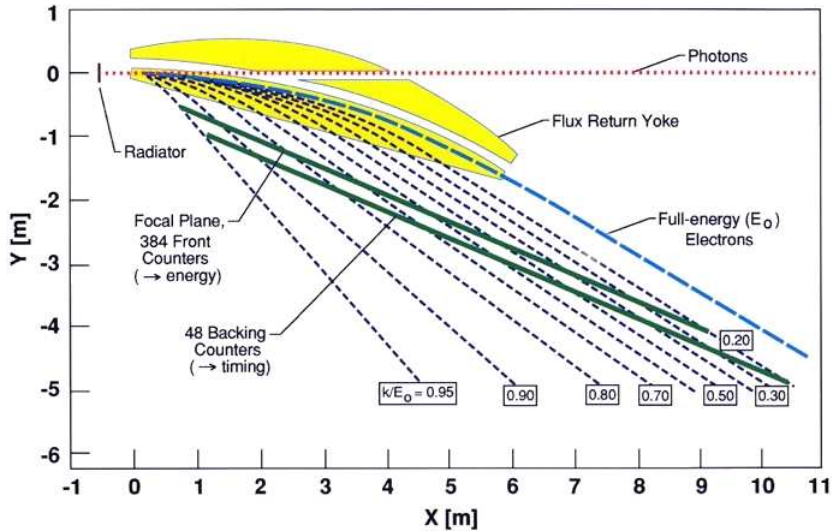


Figure 2.4: Hall B photon tagging system. Photons produced in the radiator continue toward the CLAS target following the same beam-line through the magnet yoke that is traversed by the electron beam when the tagger is not in use. The photon-tagging system can tag photons with energies between 20% and 95% of the incident electron energy, and is capable of operating with electron beam energies up to 6.1 GeV.

2.2.2 Photon Beam Position and Profile

The electron beam used in photon experiments is monitored up to a point just before the radiator by RF cavities providing a good determination of both the production point and initial direction of the photon beam. Then, downstream of the tagging magnet, the photon beam passes through a collimator.

In the present experiment, the collimator has a 0.861 cm diameter hole in a cylindrical nickel block 25 cm long. This collimator is located approximately 14 m from the radiator, and restricts the diameter of the photon beam at the CLAS target to less than 3 cm. A magnet placed just downstream from the collimator sweeps aside low energy secondary charged particles created in the collimator.

The photon beam position and size are monitored by a fixed array of crossed scintillator fibers located 20 m behind the CLAS target. The scintillators respond to the electron-positron pairs produced by photons in the CLAS target, in the atmosphere between the target and the hodoscope, or within the scintillating fibers themselves.

2.2.3 Photon Energy and Timing

The photon-tagging system can tag photons with energies between 20% and 95% of the incident electron energy E_0 , and is capable of operating with electron beam energies up to 6.1 GeV. The field setting of the tagger magnet is matched to the incident beam energy so that those electrons that do not radiate will follow a circular arc just inside the edge of the pole face, and will be directed into a secondary shielded beam dump below the floor of Hall B with a maximum capacity of 800 W.

An electron that radiates a *bremsstrahlung* photon has lower momentum, and consequently smaller radius of curvature in the tagger dipole field, so that it emerges from the magnet along the open edge of the pole gap. A scintillator hodoscope along the flat focal plane downstream from this straight edge detects this electron, and thereby allows for the determination of the energy and timing of the radiated photon.

The overall geometry of this arrangement may be seen in Fig. 2.4. The tagger dipole is topologically a C-magnet with a full-energy radius of curvature of 11.80 m, a full-energy deflection angle of 30° , and a gap width of 5.7 cm. The required magnetic field in the gap is 1.13 T for a beam energy of 4 GeV.

The focal plane hodoscope consists of two separate planes of scintillator detectors. The first detector plane (called the E-plane for energy) is composed of 384 plastic scintillators 20-cm long and 4-mm thick. Their widths (along the dispersion direction) range from 6 to 18 mm in order to subtend approximately constant momentum intervals of $0.003 \cdot E_0$. Each counter optically overlaps its adjacent neighbors by one third of their respective widths, thus creating 767 separate photon energy bins that provide an energy resolution of $0.001 \cdot E_0$.

The second detector plane (called T-plane for timing) lies 20 cm downstream of the E-plane and contains 61 counters, 2-cm thick, which are read out using PMTs attached by solid light guides at both ends (transverse to the particle direction) of each scintillator. The RMS timing resolution of these counters is 110 ps.

A schematic of the electronics of the tagger focal plane can be seen in Fig. 2.5. A scattered electron first encounters an E-counter and then passes a T-counter producing signals in both devices that are processed in separate electronic chains and participate in the construction of the tagger “event”.

The signal coming from the E-counter single PMT is sent to an ADML board, amplified and discriminated to produce an ECL logic pulse. In turn, this pulse is then sent to an E-T mapping module which performs appropriate coincidences according to E and T geometries in order to reduce the production of accidental triggers. The same ECL pulse acts as a start for the E-counter TDC which stop will be given by the CLAS trigger. To produce a tagger event, an ECL signal from the hit T-counter must be in coincidence with the E-counter signal so that both signals can be interpreted in term of a definite electron trajectory. To this aim, the output of the E-T mapping module is elongated using a discriminator so that the discriminated T-counter signal determines the timing. Thus, a three-fold coincidence is required

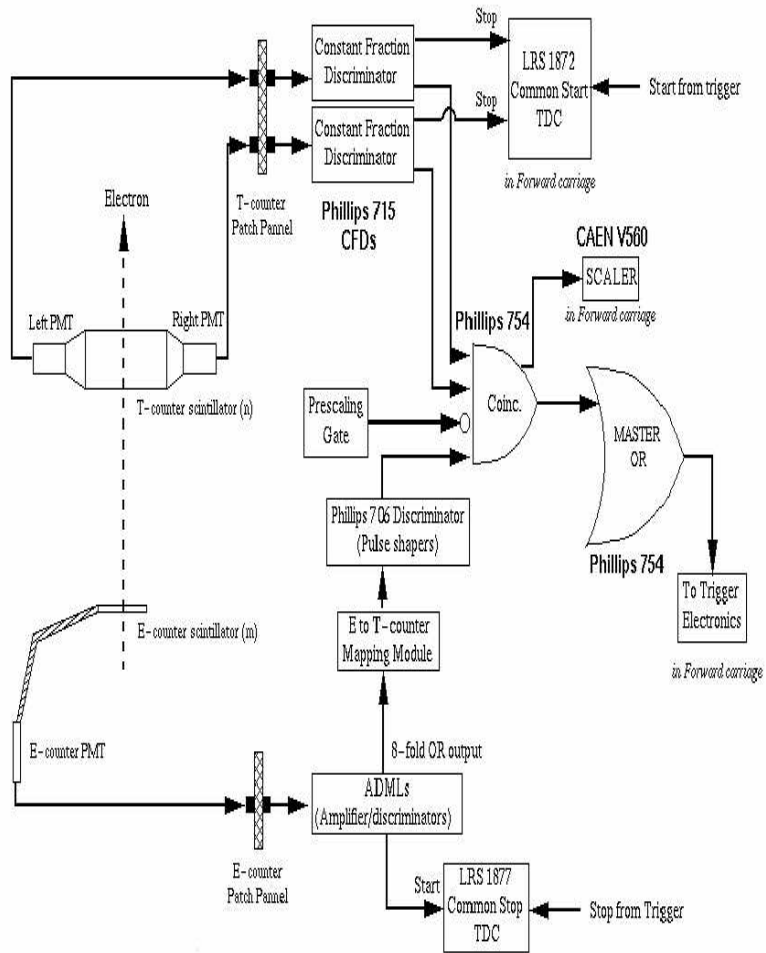


Figure 2.5: Tagger spectrometer electronics scheme. See the text for details.

between the “left” and “right” signals from the two sides of a T-counter scintillator bar and a geometrically matched E-counter signal. For the timing measurement, the output of each T-counter discriminator is sent to one multi-hit FASTBUS TDC, in common start mode, with 50 ps per channel resolution. The signal for the TDC start comes from the CLAS trigger while the stop from the T-counter. Since the tagger has 61 T-counters, there are 61 possible pulses which are sent through a cascade of logic modules set in OR mode (referred as “Master OR”, MOR).

2.2.4 Photon Beam Flux

The absolute photon flux is determined at very low flux rates by inserting a large lead-glass total absorption shower counter (TAC) into the photon beam. The

Property	Specs
Glass composition	55%Pb + 45%SiO ₂
Effective Z	48.9
Radiation Length	2.36 cm
Moliere Radius	3.1 cm
Refraction index	1.67
Cerenkov angle	34.3°
Density	4.08 g/cm ³
Effective length	17 RL
Energy resolution	16% at $E_\gamma = 300$ MeV
Timing resolution	4 ns
Efficiency	99%

Table 2.2: Characteristics of the total absorption counter (from Ref. [97]).

TAC is essentially 100% efficient (see Tab. 2.2), allowing for the efficiency of the different elements of the tagging hodoscope to be determined. Due to counting pile-up problems, the TAC can only be operated at beam currents up to 100 pA, and must be retracted from the beam-line under normal running conditions. Thus, a

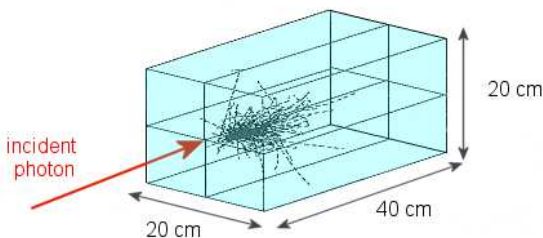


Figure 2.6: Hall B Total Absorption Counter (TAC). The TAC is essentially 100% efficient allowing for the efficiency of the different elements of the tagger hodoscope to be determined. Due to counting pile-up problems, the TAC can only be operated at beam currents up to 100 pA, and must be retracted from the beam-line under normal running conditions.

secondary monitor, linear in flux over a wide range, is cross-calibrated against the

TAC at low rates and then used to monitor the flux at higher intensities. More details on the photon flux normalization will be given in the next Chapter.

2.3 The CEBAF Large Angle Spectrometer (CLAS)

The CLAS is nearly 4π spectrometer based on a toroidal magnetic field. The primary requirements driving this choice were the ability to measure charged particles with good momentum resolution, provide geometrical coverage of charged particles to large angles in the laboratory, and keep a magnetic-field-free region around the target to allow the use of dynamically polarized targets. A view of the CLAS detector and its ancillary equipment (such as the photon tagging spectrometer and the downstream photon flux normalization devices) is shown in Fig. 2.7. A spherical co-

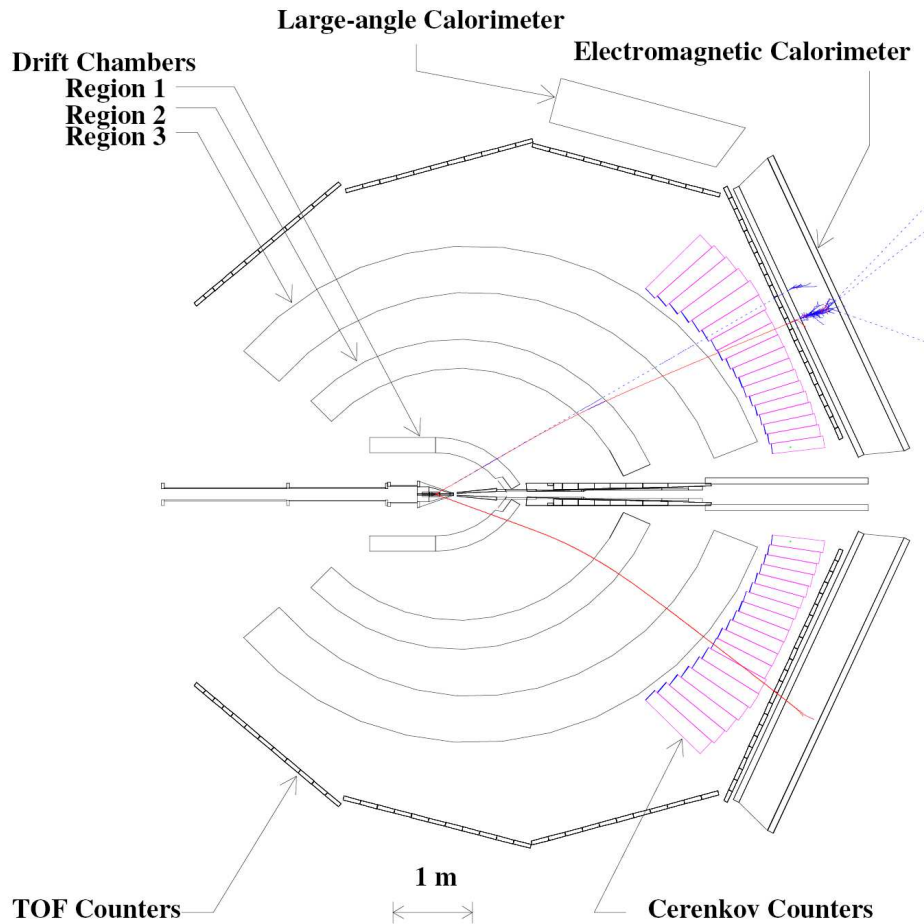


Figure 2.7: A schematic top view of the CLAS detector cut along the beam line. Typical photon, electron and proton tracks (from top to bottom) from an interaction in the target are shown (the photon track through the CLAS drift chamber system is drawn only to guide the eye).

ordinate system is used in all of the descriptions. The z -axis is taken to lie along the beam direction, with B as the polar (scattering) angle, and ϕ as the azimuthal angle. The x and y directions are then, respectively, horizontal and vertical in the plane normal to the beam. The CLAS magnetic field is generated by six superconducting coils arranged around the beam line to produce a field pointing primarily in the ϕ -direction. The particle detection system consists of drift chambers (DC) [98, 99, 100]

to determine the trajectories of charged particles, gas Cerenkov counters (CC) [101] for electron identification, scintillation counters [102] for measuring time of flight (TOF), and electromagnetic calorimeters (EC) [103, 104] to detect showering particles (electrons and photons) and neutrons by induced ionization.

The six segments are individually instrumented to form six independent magnetic spectrometers with a common target, trigger and data acquisition system (DAQ). A two-level trigger system is used to begin data conversion and readout. The Level-1 trigger can make use of the fast information from the time-of-flight counters, the Cerenkov counters, and the electromagnetic calorimeters. A Level-2 trigger adds crude track finding using hit patterns in the drift chambers. The data acquisition system collects the digitized data and stores the information for off-line analysis.

In the following sections, each of the CLAS subsystems and the Hall B ancillary equipment are briefly described.

2.3.1 Target

A variety of targets have been used to date, with dimensions adapted to the particular needs of either electron or photon running. The most common target used has been liquid H_2 . However, reactions have also been studied using liquid D_2 (as in the present case), ^3He , and ^4He ; solid ^{12}C , Al, Fe, Pb, and CH_2 ; and polarized NH_3 and ND_3 targets. All targets are positioned inside CLAS using support structures, inserted from the upstream end, and are independent of the detector itself (Fig. 2.8). Unpolarized targets have commonly been positioned inside CLAS at the center of curvature of the inner toroidal coil.

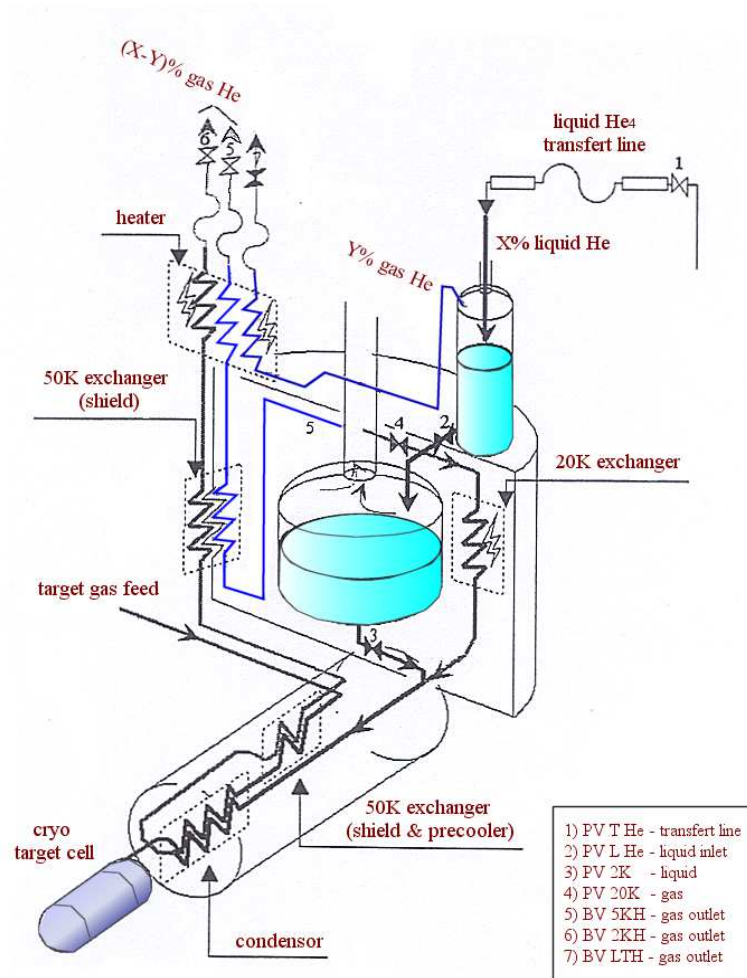


Figure 2.8: Unpolarized cryogenic target cooling system (from Ref. [97]).

2.3.2 Start Counter

The start counter (ST, see Ref. [105]) is a set of scintillators surrounding the target with the same geometric acceptance of the CLAS returning the time at which a charged particle has left the target region. This information, combined with time-of-flight information, determines the time needed to a charged particle to pass across the CLAS in tagged-*bremsstrahlung* experiments. The timing resolution relies on the

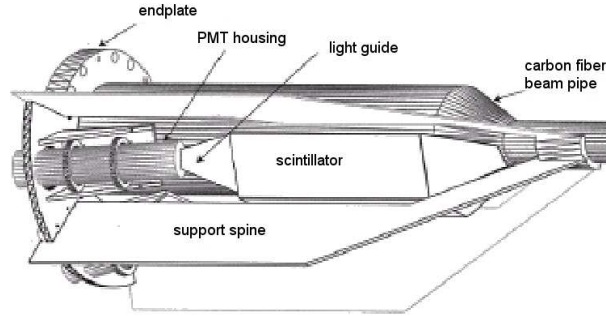


Figure 2.9: The start counter assembly is a set of scintillators surrounding the target with the same geometric acceptance of the CLAS returning the time at which a charged particle has left the target region.

determination of the charged particle impact point along the start counter scintillator panels. For this reason, light readout is done at both ends of the panels. To save space, in the forward direction two sectors of the start counter panels are merged in one scintillator. This scintillator is bent in the forward polar angle such that both ends of the panel are in the upstream direction allowing for a placement of a single photomultiplier tube. The start counter timing resolution is of 260 ps.

2.3.3 Torus Magnet

The magnetic field for the momentum analysis of charged particles is generated by six superconducting coils arranged in a toroidal geometry around the electron beam line. There is no iron in the system, so the magnetic field is calculated directly from the current in the coils.

The kidney-shape of the coils results in a high field integral for forward-going particles (typically high momentum), and a lower field integral for particles emitted at larger angles. At the same time, this coil geometry preserves a central field-free volume for the operation of a polarized target.

At the maximum design current of 3860 A, the total number of amp-turns is $5 \cdot 10^6$. At this current the integral magnetic field $\int \vec{B} \cdot d\vec{l}$ reaches 2.5 Tm in the forward direction, dropping to 0.6 Tm at a scattering angle of 90° . The magnetic field is reversible: when magnets are turned on in the normal condition, positive particles are bent outward from the beam axis.

The main field component is in the ϕ -direction, however, there are significant deviations from a pure ϕ -field close to the coils. The effect of these deviations on the particle trajectories is minimized by the circular inner shape of the coil: particles coming from the target do not experience a significant deflection in ϕ when crossing the inner boundary of the coil.

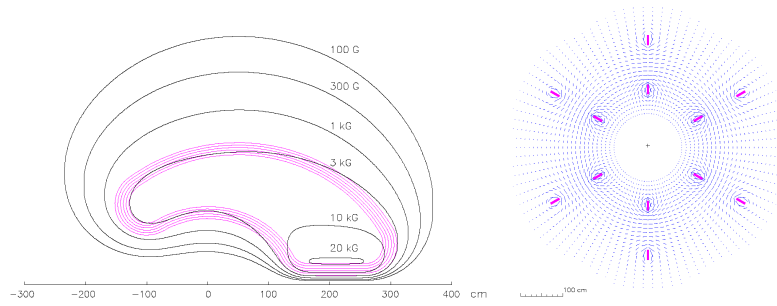


Figure 2.10: Left panel: Contours of constant magnetic field for the main CLAS toroid in the mid-plane between two coils (see also Fig. 2.7). Right panel: Magnetic field vectors for the CLAS toroid transverse to the beam direction in a plane centered on the target. The six coils are shown in cross-section.

Routine operation has been limited to 88% (3376 A) of the maximum current to keep internal mechanical stresses within conservative limits.

2.3.4 Drift Chambers

The CLAS toroidal magnetic field bends charged particles toward or away from the beam axis but leaves the azimuthal angle essentially unchanged. The magnet coils naturally define the detector into six independent tracking areas or "sectors". To simplify detector design and construction, 18 separate drift chambers were built and located at three radial positions in each of the six sectors. These radial locations are referred to as "Regions". The six "Region One" chambers surround the target in an area of low magnetic field, the six "Region Two" chambers are situated between the magnet coils in an area of high field near the point of maximum track sagitta, while the six "Region Three" chambers are located outside of the magnet coils [98, 99, 100].

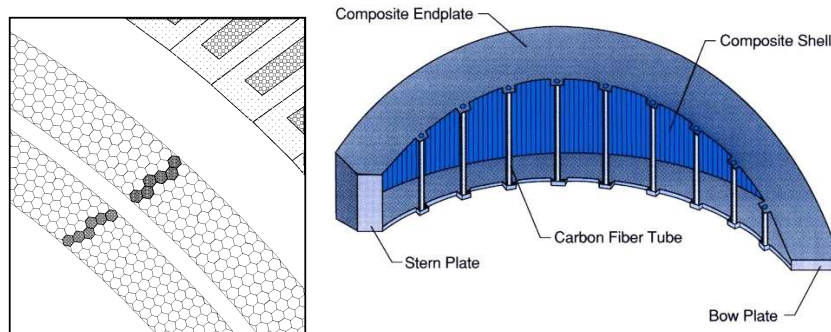


Figure 2.11: Left panel: Portion of a region three drift chamber, showing the layout of its two super-layers. The high-lighted drift cells have fired at a charged particle passing by. Right panel: Section of the whole region 3 drift chamber.

To optimally fill the sector volume, the chamber bodies were designed to support wires stretched between two end-plates, each parallel to its neighboring coil plane,

and thus tilted at 60° with respect to each other. This design provides maximum sensitivity to the track curvature since the wire direction is approximately perpendicular to the bend plane. The wire midpoints are arranged in "layers" of concentric (partial) circles, with the wire positions shifted by half the nominal wire spacing in successive layers. This pattern of wires in neighboring layers, with a repeating pattern of two field-wire layers and one sense-wire layer, results in a quasi-hexagonal pattern with six field wires surrounding one sense wire. The cell size increases uniformly with increasing radial distance from the target.

For pattern recognition and tracking redundancy, the wire layers in each chamber are grouped into two "super-layers" of six wire layers each, one axial to the magnetic field, and the other tilted at a 6° stereo angle to provide azimuthal information. The stereo super-layer of Region one is an exception to this rule, consisting of only four wire layers due to space constraints. A detail of the wire layout is shown in Fig. 2.11. The total number of sense wires in the drift chamber system is 35,148.

A high voltage system maintains the sense wires at a positive potential and the field wires at a negative potential whose absolute value is half that of the sense wires. A layer of guard wires surrounds the perimeter of each super-layer, with the high voltage potential adjusted to approximate the electric field configuration of an infinite grid. This three-voltage scheme minimizes the effects of nearby grounded surfaces such as the end-plate.

2.3.5 Cerenkov counters

The Cerenkov Counter (CC) [101] performs the dual function of triggering on electrons and separating electrons from pions. The design of the Cerenkov detector aims at maximizing the solid-angle coverage in each of the six sectors out to an angle $B = 45^\circ$ with the least possible amount of material (to prevent degradation of the energy resolution). This is achieved by placing the light collecting cones and photomultiplier tubes (PMTs) in the regions of ϕ that are already obscured by the magnet coils, and covering as much of the available space as possible with mirrors. Since charged-particle trajectories lie approximately in planes of constant ϕ , the placement of the PMTs in the shadows of the magnet coils does not affect the angular coverage. The light collection optics was designed to focus the light only in the ϕ direction, which preserves information on the electron polar angle. The Cerenkov radiator gas used in the detector is perfluorobutane (C_4F_{10}) having an index of refraction of 1.00153. This results in a high photon yield and a pion momentum threshold of 2.5 GeV/c.

2.3.6 Time of Flight Scintillators

The time-of-flight (TOF) counters [102] cover the polar angular range between 8° and 142° and the entire active range in azimuthal angle ϕ . The scintillators are located radially outside the tracking system and the Cerenkov counters but in front of the calorimeters. Their alignment and relative positioning with respect to the beam-line are shown in Fig. 2.12.

The scintillator thickness of 5.08 cm is uniform throughout, chosen to give a large signal for traversing minimum-ionizing particles. Each scintillator is positioned such that it is perpendicular to the average local particle trajectory. The width of each counter subtends about 1.5° of scattering angle. The forward counters (at polar

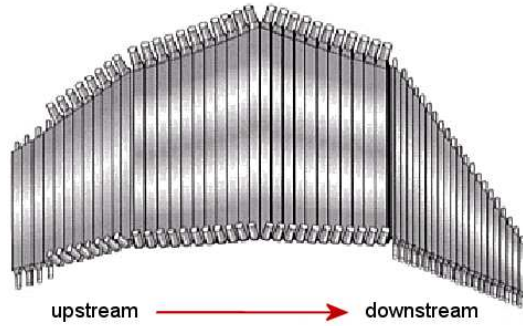


Figure 2.12: Coverage of one CLAS sector by the time-of-flight scintillators.

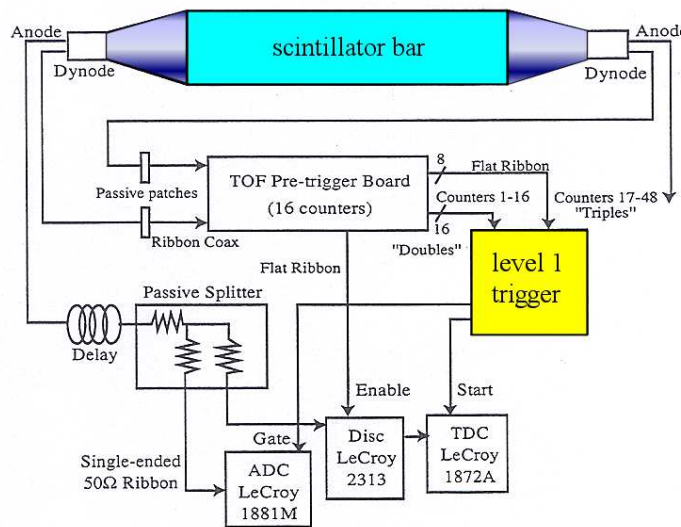


Figure 2.13: Scheme of the electronic setup for a TOF counter. Each counter consists of single scintillator bar with a PMT at each end. The timing resolution of the scintillators varies from 80 ps for the shorter counters to 160 ps for the longer ones.

angles θ less than 45°) are 15-cm wide, and the large-angle counters are 22-cm wide, in the polar angle direction.

Each TOF counter consists of a scintillator with a PMT at each end. The timing resolution of the scintillators varies from 80 ps for the shorter counters to 160 ps for the longer ones. The electronic readout of a single counter is shown in Fig. 2.13.

2.3.7 Electromagnetic Calorimeters

The forward region of the CLAS (polar angles from 8° to 45°) is equipped with an electromagnetic calorimeter segmented in six independent modules of triangular shape. Each module is composed by 13 units, and each unit consists of 3 layers of lead sheets 2 mm thick interleaved with scintillator bars of 10 cm length and thickness (top part of Fig. 2.14). Such a configuration provides the best compromise between energy resolution and neutron detection efficiency.

Each layer of scintillator is rotated by 120° with respect to the following layer to allow the stereo readout needed to resolve multiple hits into the calorimeter. The five units closest to the target are referred as the *inner* part of the calorimeter while the remaining units form the *outer* part. Inner and outer parts have independent electronic readout to sample the longitudinal shape of the showers developed within the calorimeter. The total thickness in terms of radiation lengths is 14.8 and the energy resolution of the forward calorimeter is $\sigma_E/E = 10\% \sqrt{E(\text{GeV})}$. The sampling fraction is approximately 0.3 for electrons of 3 GeV and greater, and for smaller energies, there is a monotonic decrease to about 0.25 for electrons of 0.5 GeV. The average RMS position resolution is 2.3 cm for electron showers with more than 0.5 GeV of energy deposited in the scintillator. The timing resolution for electrons averages 200 ps over the entire detector.

For two CLAS sectors the coverage is extended to polar angles of 75° by the Large Angle Calorimeter (LAC). The LAC is also a sampling calorimeter composed of two identical modules with a multi-layer structure of lead sheets and scintillator bars, similar to the forward calorimeter. A single LAC module consists of 33 layers, each composed of a 0.20 cm thick lead foil and 1.5 cm thick plastic scintillator bar [106].

The calorimeter geometry is projective, with scintillators of 10-cm average width. To avoid optical coupling, 0.2 mm thick Teflon sheets separate neighboring scintillators. Scintillator bars in consecutive layers are rotated by 90° to form a 40×24 matrix of roughly $10 \times 10 \text{ cm}^2$ cells (bottom part of Fig. 2.14).

To improve the e^-/π^- discrimination, the LAC modules are longitudinally divided into inner (17 layers) and outer (16 layers) regions with individual light readouts.

Each module is equipped with 256 photo-multiplier tubes [107]. The gain stability of each LAC photomultiplier is monitored with a precision of higher than 0.5% using a radioactive source of α -particles (^{241}Am) sealed within a YAP scintillator crystal [108]. Each LAC module corresponds to 12.9 radiation lengths and 1.0 hadronic absorption lengths and has an energy resolution of $\sigma(E)/E = 7.5\%/\sqrt{E(\text{GeV})}$.

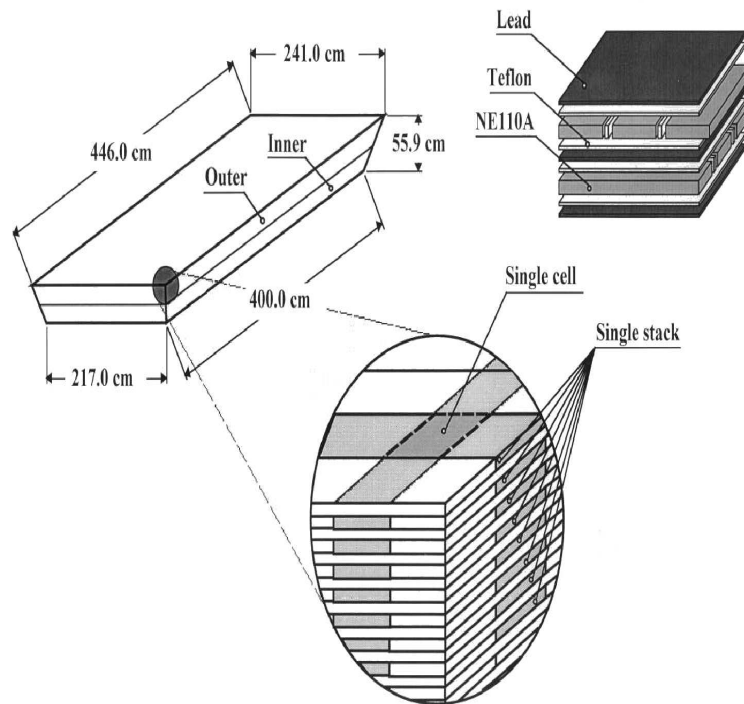
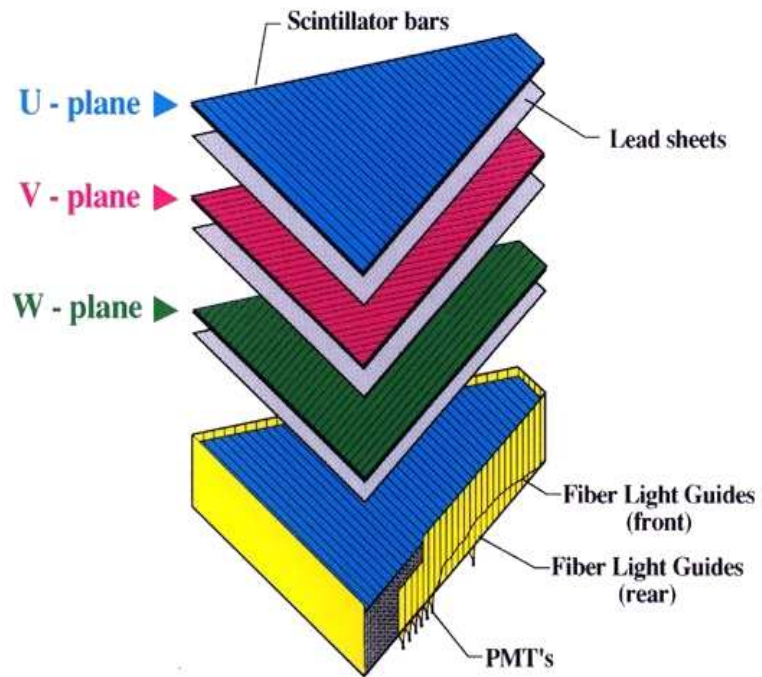


Figure 2.14: Upper panel: schematic view of one module of the forward electromagnetic calorimeter. The expanded view shows the three layers of lead and scintillator (conventionally referred as u , v , and w) making up the calorimeter sandwich structure. Lower panel: the large angle calorimeter tapered geometry (up-left), its lead-scintillator sandwich structure (up-right), and granularity (bottom-center).

2.4 Trigger System and Data Acquisition

Many of the CLAS detector subsystems use the same type of electronic modules for readout to minimize the complexity of the system and to simplify maintenance and integration. Initially, all analog signals were digitized using commercial FASTBUS modules. Recently, however, more electronic modules are available in VME, and are being integrated into the system.

The wire signals from the most complex CLAS subsystem, the drift chambers, are read out using LeCroy 1877 pipeline time-to-digital converters (TDCs) operated in common stop mode [98] with a least count of 0.5 ns.

For the PMT-based detectors, the signal times are digitized using LeCroy FASTBUS 1872A TDCs, and the pulse heights are converted using LeCroy FASTBUS 1881M analog-to-digital converters (ADCs). Most TDCs are fed from leading-edge LeCroy 2313 CAMAC discriminators set at a low threshold, typically 20 mV. The high-resolution TDCs, set to a nominal least count of 50 ps, are needed to achieve the required timing resolution for time-of-flight measurements. The ADC information is used to determine the energy deposition in each detector, as well as to correct to the TDC measurements for time walk.

The inputs to the Level 1 trigger are generated using custom electronics to sum appropriate groupings of PMT signals that can be used to generate fast signals with high efficiency. In order to study the trigger in software, these inputs are also recorded in the data stream with LeCroy 1877 FASTBUS pipeline TDCs along with all other trigger inputs.

2.4.1 Trigger System

To acquire events of interest while minimizing the dead-time, a two-level hierarchical trigger system was designed [109]. The Level 1 trigger is dead-timeless, processing all prompt PMT signals through a pipelined memory lookup within 90 ns. The resulting signals are sent to a trigger supervisor module, where they are used to gate the front-end electronics [110]. This custom board [111] takes the Level 1 (and Level 2) inputs from the trigger system and produces all common signals, busy gates, and resets required by the detector electronics. The Level 2 trigger uses the fast-clear capability by clearing events that satisfied Level 1, but which have no tracks in the drift chambers.

2.4.2 Data Acquisition

The CLAS data acquisition (DAQ) system was designed for an event rate of 2 kHz. Continued development of the DAQ over five years resulted in routine operation at event rates between 3 and 4 kHz for the 2000/01 running period as can be seen from Fig. 2.15. The data from the various detector components are digitized in 24 FASTBUS and VME crates within the experimental hall and collected by the 24 VME Readout Controllers in these crates. These data arrays, or event fragments, are buffered and then transferred via fast Ethernet lines to the CLAS online acquisition computer in the control room. Three primary processes, the Event Builder (EB), Event Transport (ET), and Event Recorder (ER), comprise the main data-flow elements in the acquisition computer. The EB assembles the incoming fragments into complete events. The completed event is then labeled by a run and

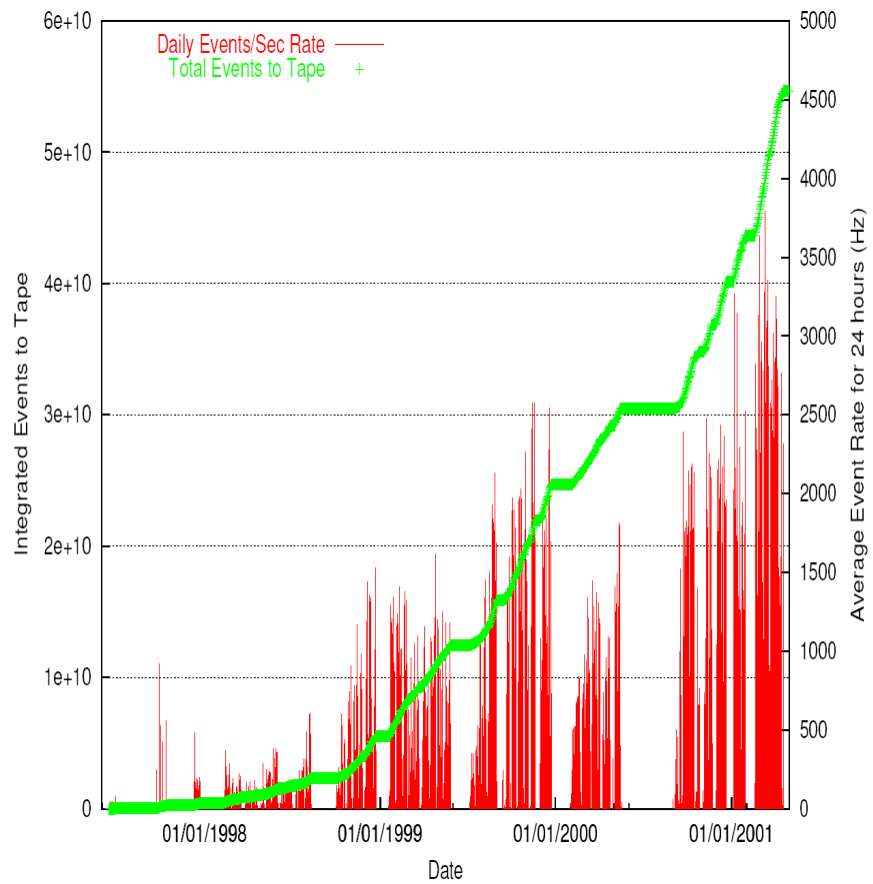


Figure 2.15: Event rate and integrated events accumulated by the CLAS data system vs. time for a three year period.

event number, an event type, and the trigger bits configuration. At this stage the event has the final format it needs for off-line analysis. The data flow is shown in Fig. 2.16: the EB passes the completed events to shared memory [112] on the CLAS on-line computer. The ET system manages this shared memory, allowing access by various event producer and consumer processes on the same or remote processor systems. The ER picks up all events for permanent storage.

Some events are transferred to remote ET systems, for raw data checks such as hit maps, status, and event displays, and for on-line reconstruction, analysis, and monitoring. The ER writes the data in a single stream to magnetic media. The output files are striped across an array of local RAID disks.

The CLAS data flow requires communication among some 100 processes running on a system of processors distributed around the detector in the experimental hall and linked to two Symmetric Multi-Processor (SMP) machines and a number of workstations in the control room. The framework for this organization is the CEBAF On-line Data Acquisition (CODA) system [113, 114]. The data runs are set up and performed by the CODA “Run Control” sequence, where a single run typically lasts for one or two hours.

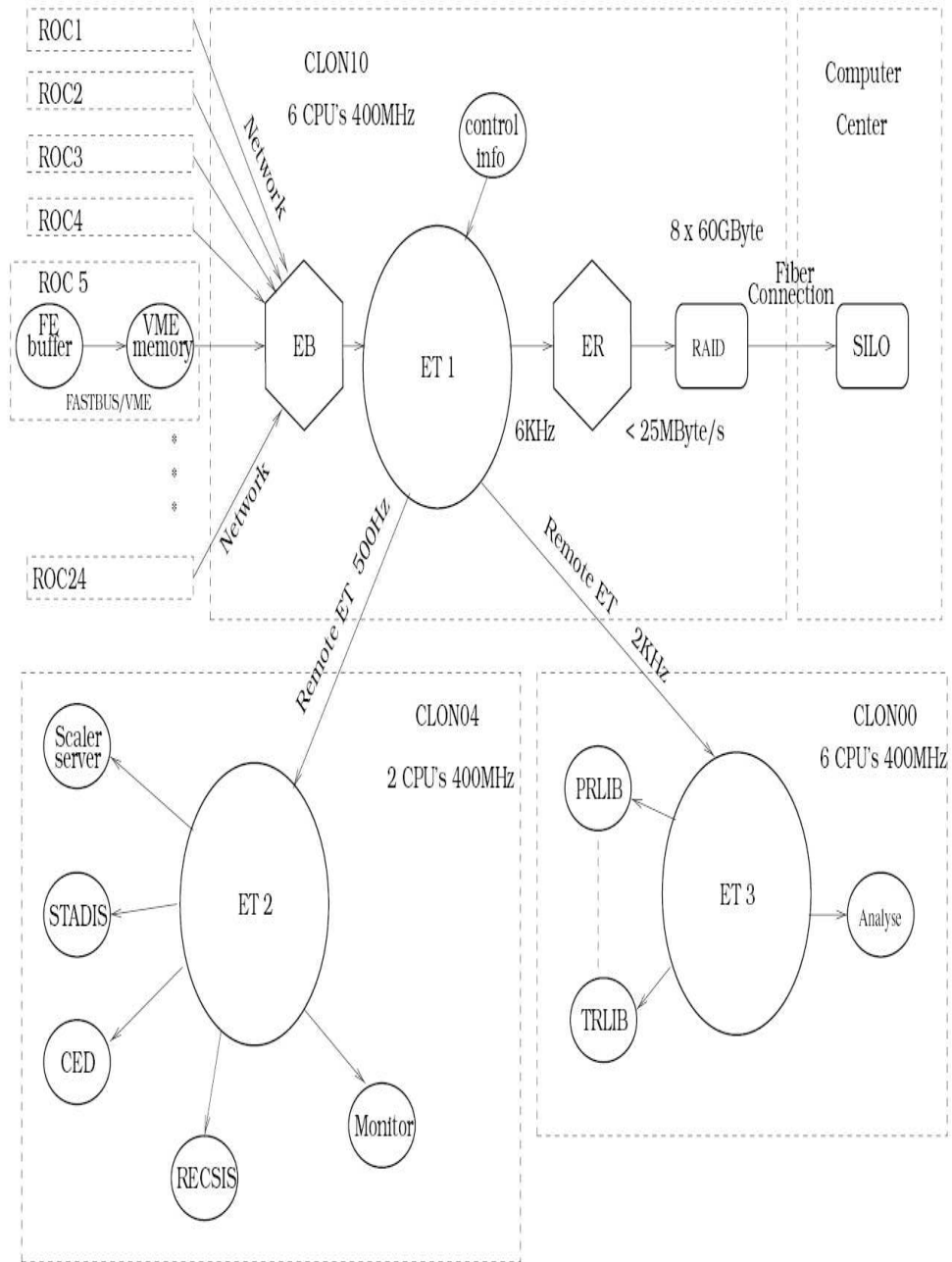


Figure 2.16: Data flow schematic for CLAS, with the primary stream using the ET1 shared memory. Also shown are a variety of monitoring processes accessing data on other shared memory (ET2, ET3) managed by the ET system. See text for additional details.

2.5 Summary

The Large Acceptance Spectrometer (CLAS) allows the study photo- and electro-induced nuclear and hadronic reactions by providing efficient detection of neutral and charged particles over a good fraction of the full solid angle. The detector capabilities (summarized in Tab. 2.3) are being used in a broad experimental program to study the structure and interactions of mesons, nucleons, and nuclei using polarized and unpolarized electron and photon beams and targets.

Capability	Quantity	Range
Coverage	charged particle angle	$8^\circ \leq \theta \leq 140^\circ$
	charged particle momentum	$p \geq 0.2 \text{ GeV}/c$
	photon angle (4 sectors)	$8^\circ \leq \theta \leq 45^\circ$
	photon angle (2 sectors)	$8^\circ \leq \theta \leq 75^\circ$
	photon energy	$E_\gamma \geq 0.1 \text{ GeV}$
Resolution	momentum ($\theta \lesssim 30^\circ$)	$\sigma_p/p \approx 0.5\%$
	momentum ($\theta \gtrsim 30^\circ$)	$\sigma_p/p \approx (1-2)\%$
	polar angle	$\sigma_\theta/\theta \approx 1 \text{ mrad}$
	azimuthal angle	$\sigma_\phi/\phi \approx 4 \text{ mrad}$
	time (charged particles)	$\sigma_t \approx (100-250) \text{ ps}$
	photon energy	$\sigma_E/E \approx 10\%/\sqrt{E}$
Particle ID	π/K separation	$p \leq 2 \text{ GeV}/c$
	π^+ /p separation	$p \leq 3.5 \text{ GeV}/c$
	π^- misidentified as e^-	$\leq 10^{-3}$
Luminosity	electron beam	$L \approx 10^{34} \text{ nucleon cm}^{-2}\text{s}^{-1}$
	photon beam	$L \approx 5 \cdot 10^{31} \text{ nucleon cm}^{-2}\text{s}^{-1}$
	data acquisition	event rate 4 kHz
	data rate	25 MB/s
Polarized target	magnetic field	$B_{\max} = 5 \text{ T}$

Table 2.3: Summary of the CLAS detector characteristics.

The CLAS, in conjunction with the associated photon tagging spectrometer represents an ideal experimental setup to measure the deuteron photo-disintegration differential cross section. In fact, it provides both large coverage in the proton scattering angle (from $\theta_p^{\text{LAB}} = 8^\circ$ to 140°) and an high energy (up to 3 GeV) tagged photon beam.

Chapter 3

Event Reconstruction and Data Analysis

3.1 Introduction

The $\gamma d \rightarrow pn$ differential cross section has been measured using the Hall B tagged photon beam in the energy range between 0.5 – 2.95 GeV and the CLAS large acceptance spectrometer. The various CLAS production runs are organized by “run periods” where experiments sharing common running conditions take data simultaneously. In this experiment (JLab E93-017, a part of the g2 run period experiments, where g2 stands for “ γ on a deuteron target”) a high-statistics dataset has been collected using a loose trigger requiring only one charged hadron in the final state in coincidence with a tagger counter. Four weeks of beam time have been used to accumulate approximately 2.4 billion valid triggers in two different periods during the August (18 days) and September (14 days) months of the year 1999.

3.2 Running Conditions

The E93-017 experiment is characterized as follows:

- Energy of the incident electron beam: $E_0=2.5$ GeV (“August”) and $E_0=3.1$ GeV (“September”). The electron beam was impinging upon a gold radiator of 10^{-4} radiation lengths;
- Tagger spectrometer settings: full focal plane $(0.2 - 0.95)E_0$ GeV, or *prescaling OFF* configuration for about 70% of the running time; high energy part of the focal plane $(0.35 - 0.95)E_0$ GeV (*prescaling ON* configuration) for the remaining time;
- Photon energy: 0.5 – 2.38 GeV (“August”) and 0.6 – 2.95 GeV (“September”);
- Current intensity: 10 – 13 nA;
- Photon intensity on the single tagger counter: $\simeq 7 \cdot 10^6$ tagged γ/s for *production* runs (standard current intensity reported above) and about 10^5 tagged γ/s for *normalization* runs (low current intensity runs $\simeq 100$ pA);

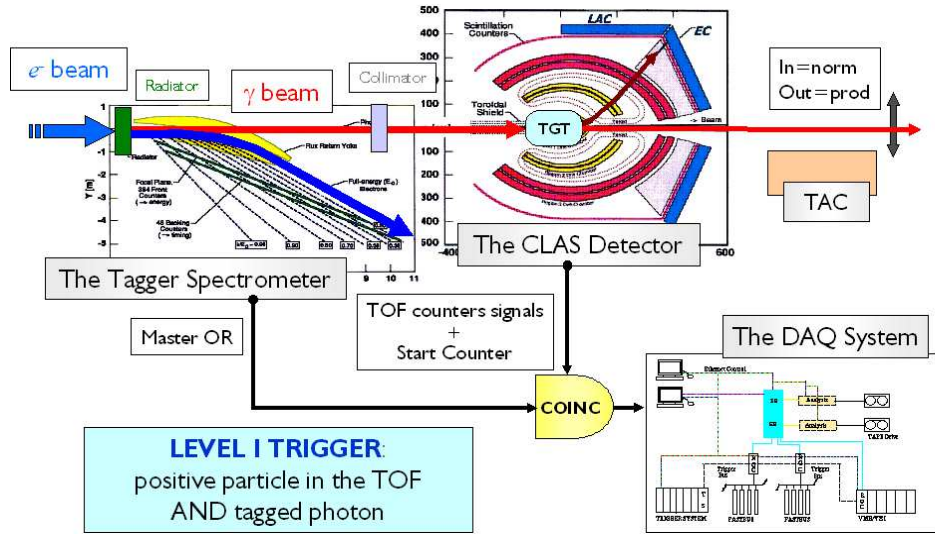


Figure 3.1: Top pictures: Schematic view of the experimental setup used during the g2 run period. From left to right: electron beam, radiator, the tagger spectrometer, the photon beam-line, the deuteron target (TGT), the CLAS detector, and the down-stream photon flux normalization components. For the present experiment, the hadronic events generated in the target volume are detected in CLAS using the time-of-flight system, in coincidence with a tagged photon trigger and a start counter signal. Bottom pictures: the Level 1 trigger and the data acquisition system. Only the charged trigger scheme is indicated since the neutral trigger is not used in the current analysis.

- Cryogenic target: mylar cylinder 4 cm in diameter and 10 cm long, filled with unpolarized liquid D_2 at 4 K of temperature;
- CLAS superconducting torus magnetic field: 3375 A (88% of the full field intensity) with positive particles out-bending (so called “normal” field configuration);
- Level 1 Trigger: coincidence between a signal in the tagger (Master OR) and either one charged track in the CLAS (80%) or 2 neutral hits (20%) in the electromagnetic calorimeters (the neutral trigger configuration is not used in the present analysis);

CHARGED TRIGGER RUNS
20086→20150
20188→20350
20584→20705
20741→20760

Table 3.1: Runs collected with the charged trigger used in the $\gamma d \rightarrow pn$ analysis.

The experimental setup is schematically shown in Fig. 3.1. Each data acquisition session is labeled by a *run number* so that, for the present experiment, run numbers go from 19,948 to 20,760. In addition to the basic dataset of 2.4 billion triggers,

additional 22 million empty target triggers have been taken mainly for background studies together with 178 million triggers at very low current intensity. These last data have been collected to measure the absolute photon flux and to study the photon tagger characteristics. In the present analysis, only the charged trigger runs have been used (shown in Tab. 3.1) for a total of 1,171 million of events.

3.3 Event Reconstruction

3.3.1 Physics Data

The event files collected during the on-line data acquisition (CODA) sessions are stored on tape silo system, to be retrieved in the off-line phase. These files contain information on the detector ADC/TDC readouts at the time the event was digitized in CLAS and are called *raw* data files. The final codification, in the form of standard n-tuples, of the physical quantities of interest requires a multi step procedure performed using both official software packages (developed by the CLAS collaboration) and custom (user-written) code. The logic flow chart of this procedure is shown in Fig. 3.2 (right side): files collected during the experimental run are processed by the reconstruction code (called “A1C”). The first step of the reconstruction process is the conversion of raw ADC/TDC hits from the detector readout electronics into physical quantities such as energy and time. This task is accomplished using appropriate constants (also called calibration constants), defined for each detector readout subsystem and run period. The whole set of calibration constants is stored into the CLAS database system which can be accessed from the off-line software packages and provides the information used for the reconstruction in the form of custom files (called *map* files) or via an on-line SQL-database server.

Using the calibration constants, the charged particle 4-momentum is determined from the time of flight and the track radius of curvature measured by the time-of-flight and drift chamber systems, respectively. Neutral particle momenta are basically reconstructed using the information coming from the electromagnetic calorimeters.

The procedure for the determination of the calibration constants is iterative: a preliminary reconstruction pass is performed on a relatively small fraction of the total collected raw files uniformly spaced through all the data taking period. During the preliminary pass, up-to-date pedestals constants for the various CLAS subsystems are used together with a “test” set of calibrations constants usually taken from a previous run period with similar experimental conditions. Then, the quality of the reconstructed data is monitored: if the result is not satisfying the constants are recalculated and successive passes of reconstruction are performed until the values of monitored quantities are acceptable. At this point the set of calibration constants is “frozen” into the database so that massive data reconstruction can be started (this process is referred as “cooking”). The output of the cooking process, is automatically screened by several data monitoring and filtering software utilities in order to check for possible problems or failures. For instance, diagnostic programs produce the status files containing the drift chambers occupancy and time-of-flight paddles status for the run period of interest.

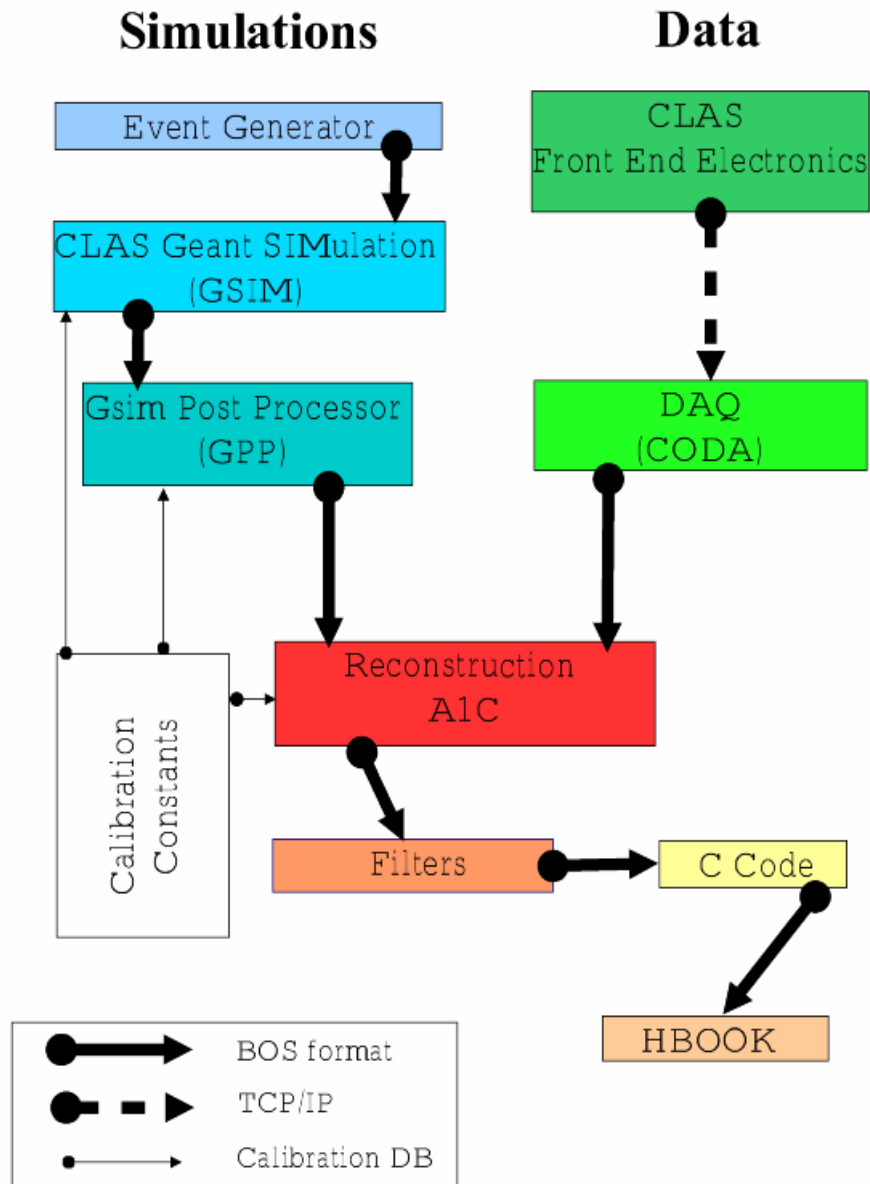


Figure 3.2: Block diagram of the off-line data processing. The raw data files (simulated -left panel- or measured -right panel-) are converted into reconstructed files and processed by CLAS applications or user written code to obtain standard n-tuple files.

In order to optimize the disk space requirements for the off-line analysis, a filtering package is run on the entire reconstructed dataset so that a set of reduced files (*skimmed* files) are produced for each (group of) physics channel(s) of interest. These reduced files only contain events belonging to the particular channel being analyzed, and only the banks strictly needed by the off-line analysis code.

The physical quantities characterizing the reconstructed events are organized in a sequence of numerical fields colloquially called *banks*. Banks are accessed and managed using a FORTRAN-based memory allocation system known as BOS (Basic Object System) [115]. Bank objects are addressed by capitalized 4-letters pointers.

3.3.2 Simulated Data

A similar reconstruction chain is used for data files resulting from the GEANT Simulation (GSim) of the CLAS detector. As shown on the left side of Fig. 3.2, the output of the GSim tool is processed by the same reconstruction program used for real data files, with the exception that a calibration procedure is not needed. In this case, the database system provides the “reverse” calibration constants needed by the GSim tool to produce the appropriate ADC/TDC hits for the generated particles in their simulated interaction with the CLAS. The complete simulation of the CLAS detector is performed in two steps: GEANT simulation and Post Processing.

In the first step, raw data files are created from the GSim tool considering the CLAS as an “ideal” detector where all the subsystems are working properly and the timing and spatial resolutions values are identical to the nominal ones.

On the contrary, the post processing phase introduces finite effects for the timing and spatial resolutions and takes into account possible problems affecting the actual detector setup. In fact, during the run period of interest, some detector subsystems may have out-of-work electronic channels and the drift-chambers may also have out of work wires.

An software package called GSim Post Processor (GPP) applies the necessary corrections to the GSim files using the information on the detector status (obtained from the diagnostic programs run after the reconstruction process) and takes into account the timing and spatial resolutions finite effects.

The introduction of the finite resolution effects is done defining a certain number of *smearing* factors for the time-of-flight and drift chambers subsystems.

The smearing factor f for the time-of-flight timing resolution is defined as follows:

$$\sigma_i = 2fR_i \tag{3.1}$$

where R_i is the ideal resolution of the TDC coupled to the time-of-flight scintillator paddle i .

For what concerns the spatial resolution of the drift chambers, the physical mechanism exploited to convert the drift time into distance is shown in the left panel of Fig. 3.3. A charged particle passing through a DC cell, releases a charge deposition on the sense wire that yields a drift time which is converted into a distance (DOCA, Distance Of Closest Approach) using pre-calculated functions.

On the other hand, the overall track, as defined by the reconstruction software, takes into account the time-distance information coming from all the cells crossed by the particle by means of a best fit procedure. In this case, the distance of closest

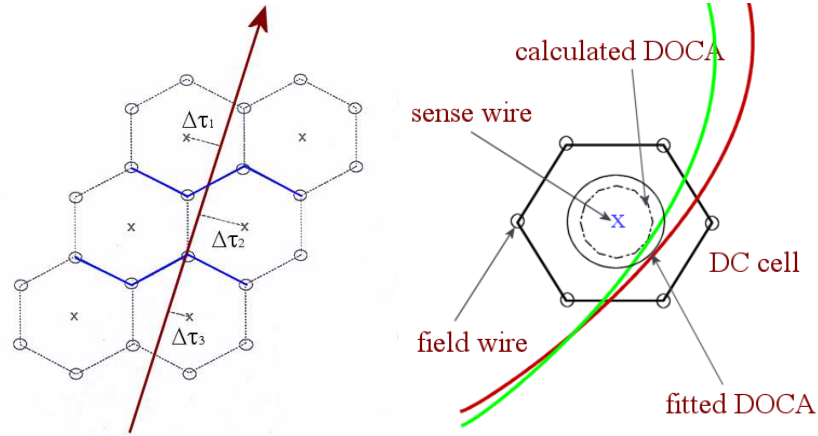


Figure 3.3: The tracking procedure in the CLAS drift chambers system. Left panel: a charged particle passing through a super-layer. The field wires are indicated by the open dots while crosses indicate the sensitive wires which collect the released charge. The drift times are associated to distances of closest approach (DOCAs) represented by the dotted lines. Right panel: two different values for the distance of closest approach of the particle from the sense wire can be defined, giving origin to a loss of spatial resolution. See text for details.

approach from the sense wire under consideration will be close to the calculated distance, but not exactly identical (right panel of Fig 3.3).

Inside each DC region the spatial residual is defined by the difference:

$$|\text{DOCA}_{\text{calc}}^{(j)}| - |\text{DOCA}_{\text{fit}}^{(j)}| \quad (3.2)$$

where $j = 1, 2, 3$ runs over the three DC regions. It turns out that spatial residual as a function of $\text{DOCA}_{\text{calc}}$ is almost constant. The resulting distribution can be fitted using a 5th-order polynomial:

$$S_j = \sum_{i=0}^5 p_i^{(j)} \text{DOCA}_{\text{calc}}^{i,(j)} \quad (3.3)$$

so that:

$$\sigma_j = \text{const} \cdot f_j \cdot S_j \quad (3.4)$$

where the quantities $f_{(1,2,3)}$ are the three spatial resolution smearing factors.

In order to introduce in the simulation the finite effects for the timing and spatial resolutions and the actual detector status, the GPP package is ran on the GSIM output files before they are processed by the reconstruction program.

3.4 Event Selection

In order to constrain the two body deuteron photo-disintegration events, the missing mass spectra have been calculated from the relation 3.5:

$$M_X^2 = (P_\gamma + P_d - P_p)^2 \quad (3.5)$$

where P_γ , P_d , and P_p are the 4-momenta obtained by the reconstruction software for the identified particles.

The resulting distributions exhibit a clear peak corresponding to the neutron rest mass. An example is shown in Figs 3.4 and Fig. 3.5 where the missing mass distributions are calculated for the intermediate incident photon energy of $E_\gamma = 1.05$ GeV and for proton scattering angles of $\theta_p^{\text{LAB}} = 25^\circ$ and $\theta_p^{\text{LAB}} = 115^\circ$, respectively. The different plots represent the contribution to the missing mass spectra from the six CLAS sectors. At forward angles, the neutron peak is quite sharp, the typical signal to noise ratio being of the order of $40 \div 60$ in this case. The shapes of the missing mass distributions are well reproduced using a Gaussian plus exponential fitting functions. The red/dotted arrows shown in the panels of Fig. 3.4 represent the $(-3\sigma, 3\sigma)$ interval (where σ is the standard deviation of the Gaussian fitting function) defining the width of the neutron peak. At backward proton scattering angles, the distributions peaks are less pronounced compared to those obtained at forward angles, since the momentum resolution of the CLAS is worse in the backward direction. Nevertheless, the neutron peak is still clearly evident.

In order to exclude $\gamma d \rightarrow pX$ events yielding mass values too far from the neutron rest mass the width σ of the Gaussian function is used to define $(-3\sigma, 3\sigma)$ cuts around the distribution peak.

These cuts are calculated, for each CLAS sector, as a function of the incident photon energy E_γ and of the proton scattering angle θ_p^{CM} . They have been used to define which proton events have to be associated to a two body photo-disintegration final state using also the information on the proton detection efficiency and detector fiducial cuts as explained in Sec. 3.8. An example of the behavior of the missing mass cuts as a function of θ_p^{CM} is shown in Fig. 3.6 for four incident photon energies around 1 GeV: the different dotted lines correspond to cuts in the six CLAS sectors. The missing mass cuts become wider at large scattering angles reflecting the behavior of the missing mass distributions shown in Fig. 3.4 and Fig. 3.5.

At higher incident photon energies the neutron peaks in the missing mass distributions become less defined since the resolution of the spectrometer decreases. In fact, the reconstruction of the momentum of straighter tracks left by protons of high momentum is less accurate and moreover the number of events is smaller since the cross section decreases very rapidly as a function of the incident photon energy.

An example of the behavior of the missing mass cuts as a function of the proton scattering angle θ_p^{CM} at incident photon energies around 2.9 GeV is shown in Fig. 3.7. In this case, for the reasons explained above, the cuts are wider than those calculated for lower photon energies even if the missing mass distributions are still peaked enough for the fitting procedure to be applied.

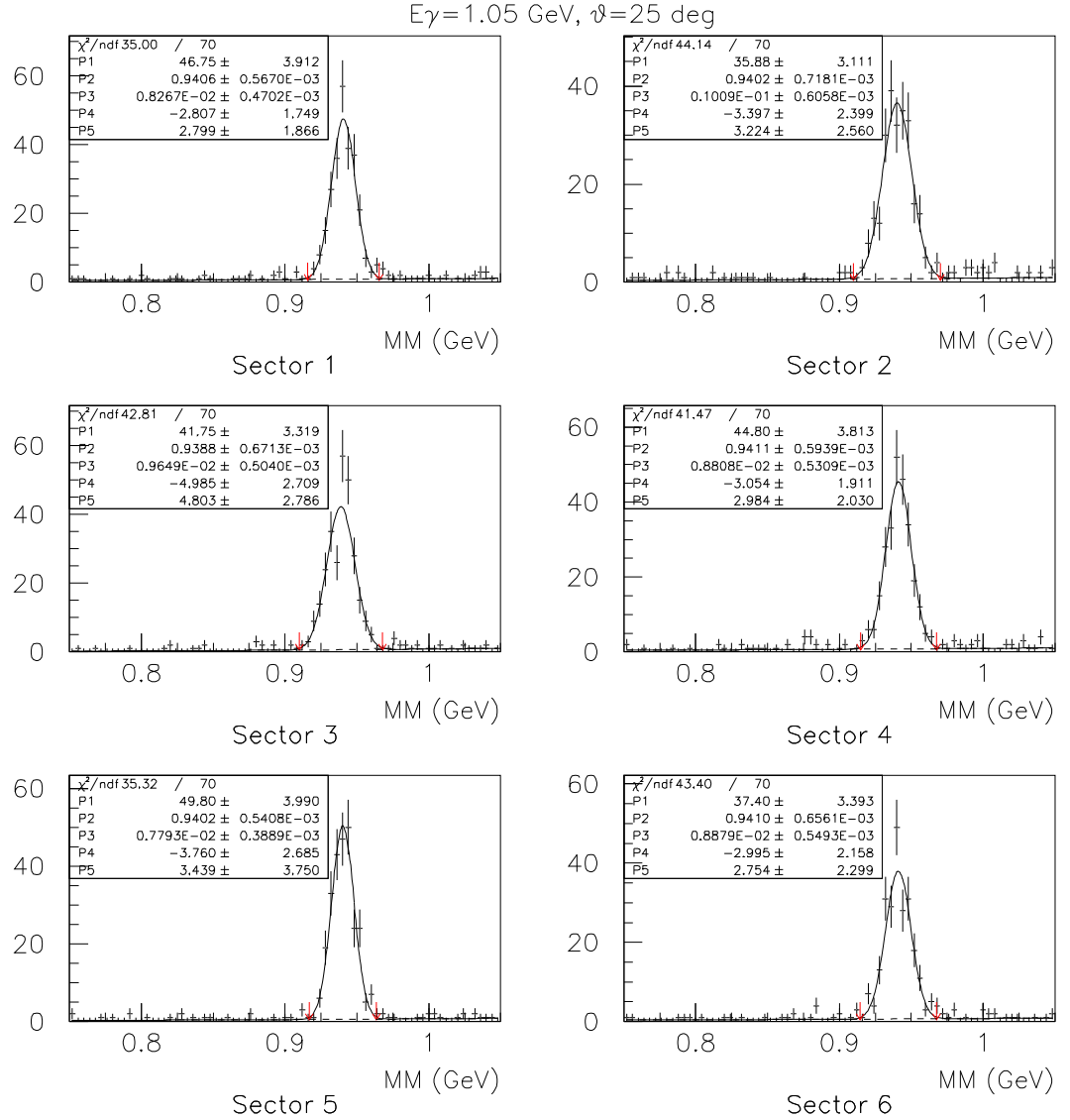


Figure 3.4: Typical missing mass spectra calculated for the six CLAS sectors from Eq. 3.5 for an incident photon energy of $E_\gamma = 1.05 \text{ GeV}$ and a forward proton scattering angle $\theta_p^{\text{LAB}} = 25^\circ$. The peak corresponding to the neutron rest mass can be clearly identified, and the shape of the distributions is well reproduced by a Gaussian plus an exponential fitting function. The red/dotted arrows shown in the panels represent the $(-3\sigma, 3\sigma)$ interval defining the width of the neutron peak, being σ the Gaussian function standard deviation.

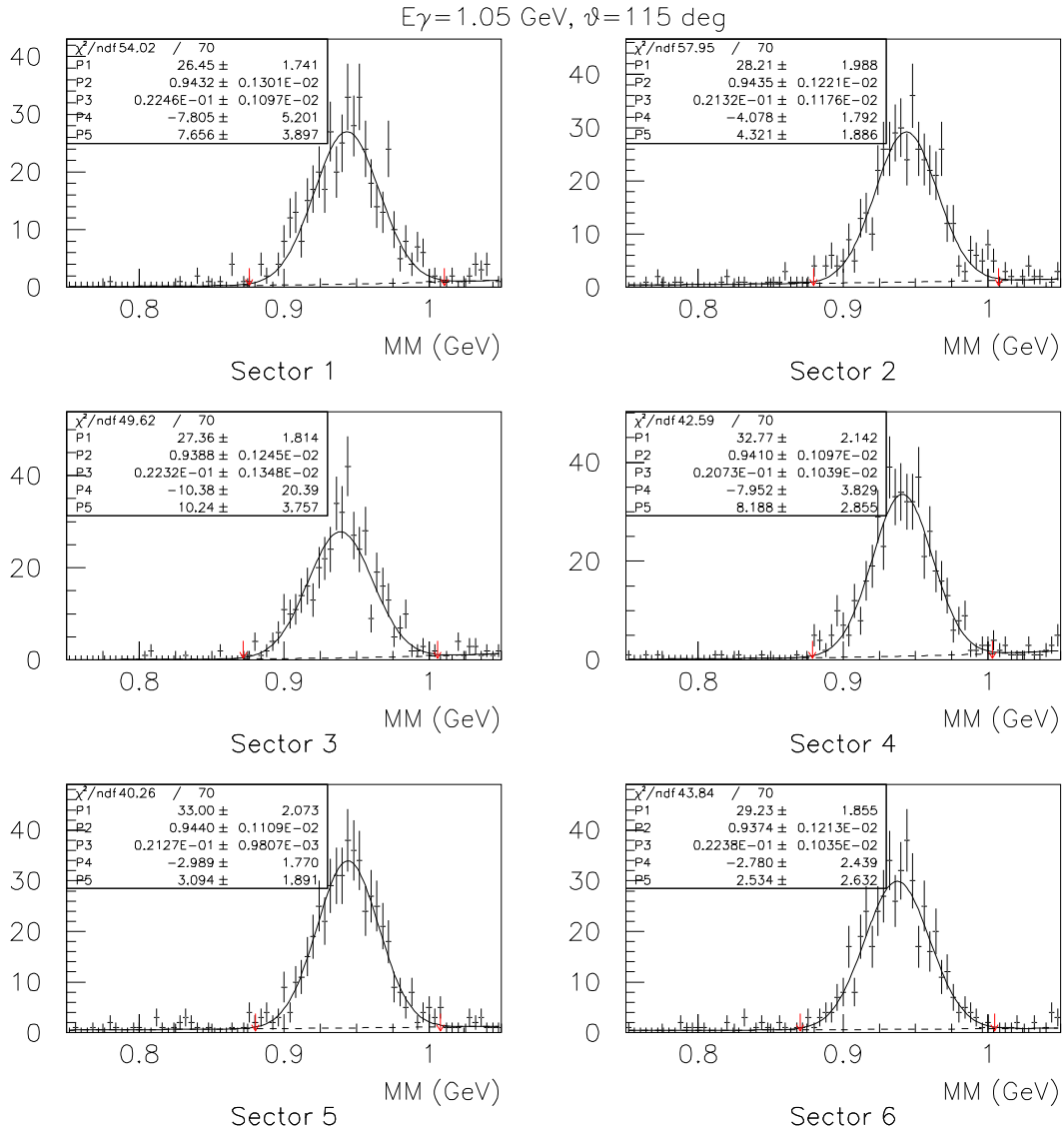


Figure 3.5: Example of missing mass spectra calculated for the six CLAS sectors from Eq. 3.5 for an incident photon energy of $E_\gamma = 1.05 \text{ GeV}$ and a backward proton scattering angle $\theta_p^{\text{LAB}} = 115^\circ$. The distribution is less pronounced compared to the one obtained at forward angles since the momentum resolution of the CLAS is worse in the backward direction. Nevertheless the neutron signal is clearly evident and the shape of the distributions is well reproduced by a Gaussian plus an exponential fitting function. Again, the red/dotted arrows represent the $(-3\sigma, 3\sigma)$ interval defining the width of the neutron peak, being σ the Gaussian function standard deviation.

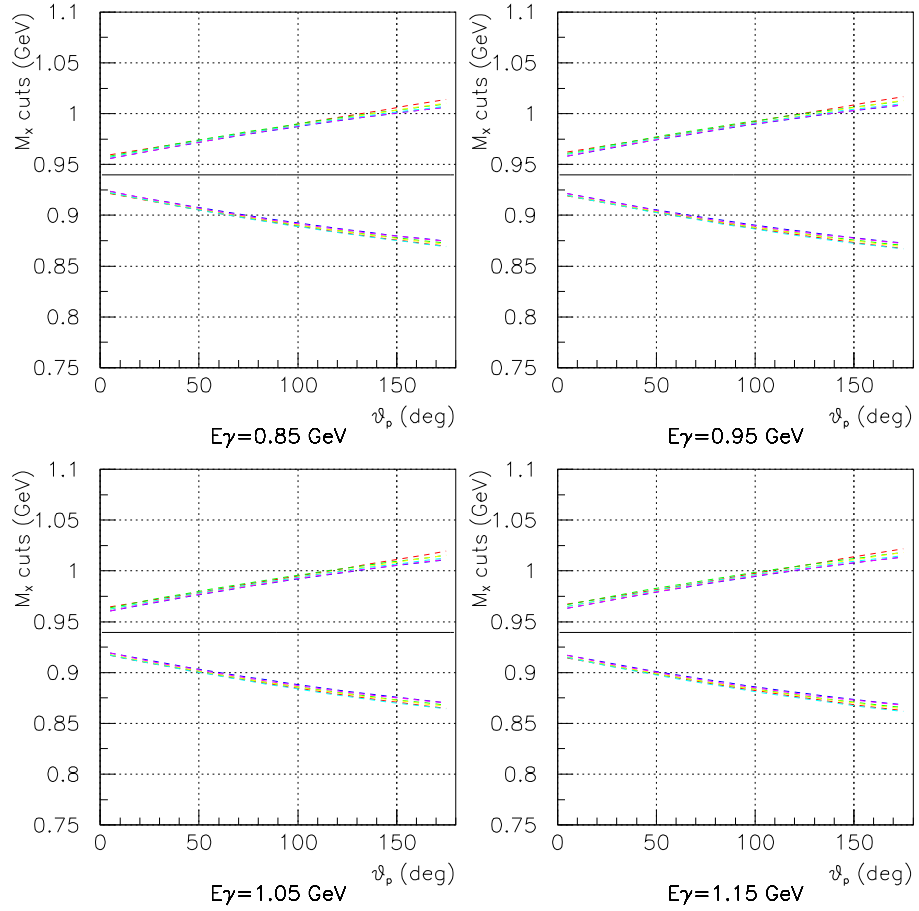


Figure 3.6: Behavior of the missing mass cuts as a function of the proton scattering angle θ_p^{CM} for four incident photon energies around 1 GeV. The solid horizontal line represents the value of the neutron rest mass, while the different dotted lines represents the missing mass cuts for the six CLAS sectors

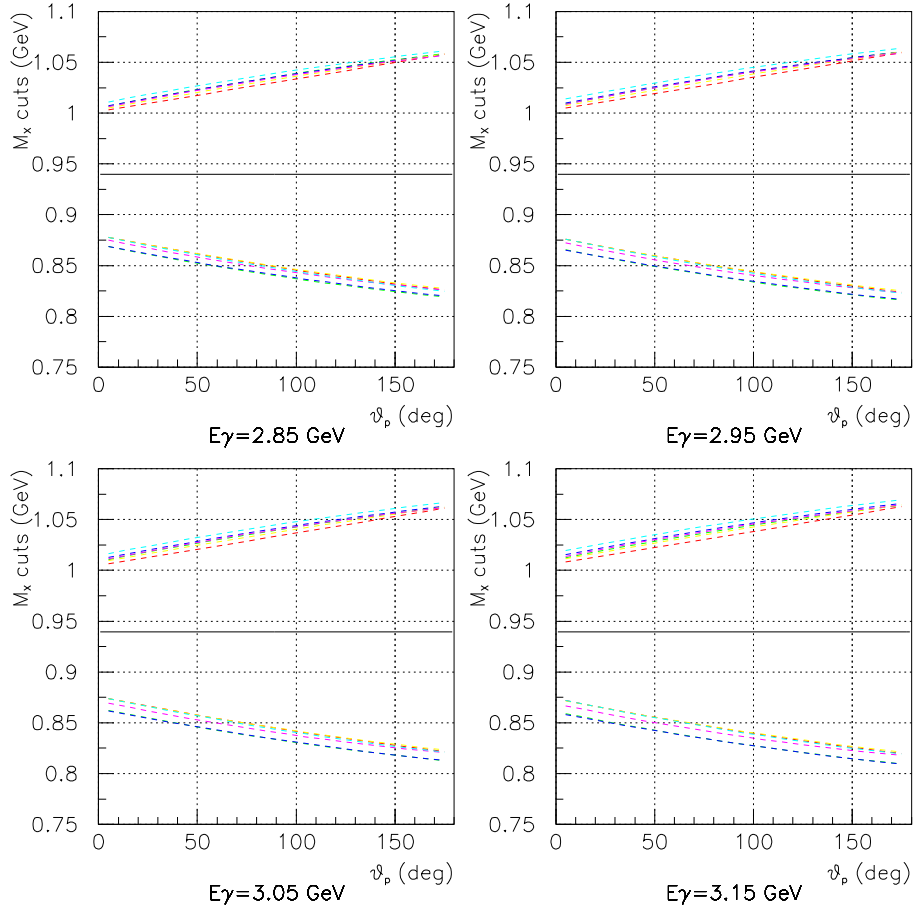


Figure 3.7: Behavior of the missing mass cuts as a function of the proton scattering angle θ_p^{CM} for four incident photon energies around 2.95 GeV. The solid horizontal line represents the value of the neutron rest mass, while the different dotted lines represents the missing mass cuts for the six CLAS sectors. In this case, the cuts are wider than those calculated for lower photon energies nevertheless the missing mass distributions are still peaked enough for the fitting procedure to be applied.

3.4.1 Interaction Vertex

The interaction vertex of the incident photon with a deuteron in the target volume is calculated from events with more than one charged particle in the final state using the intersection between the different tracks.

The distribution of the vertex z variable is shown in Fig. 3.8, where z is the direction of the incoming photon beam. As can be seen, the events are uniformly distributed along the 10 cm length target with a small contribution coming from a support structure located about 12 cm on the left of the target center. The solid line represents a fit to the distribution defining the effective target length.

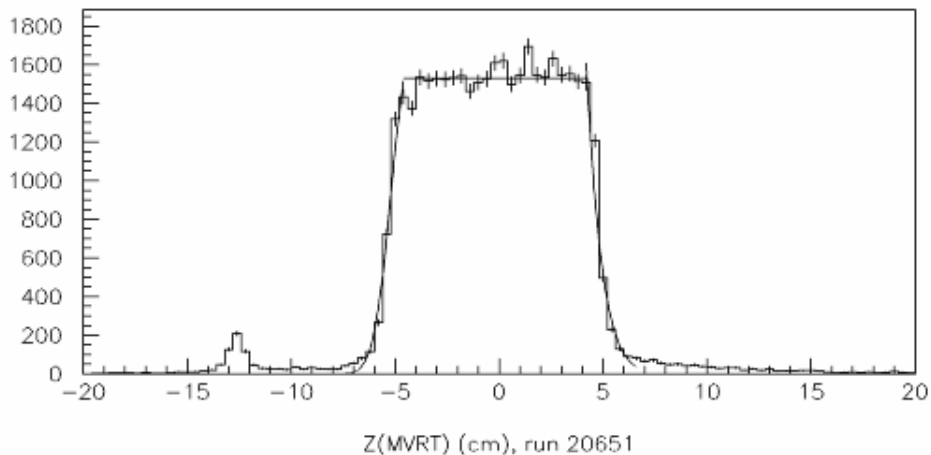


Figure 3.8: Distribution of the vertex z -component for proton events originating in the target volume. The distribution shape reflects the target dimensions (10 cm length). The small peak on the left is the contribution of a target support structure and is eliminated by a cut on the vertex z -coordinate. The information on the interaction vertex and the x and y positions of the beam is contained in the MVRT bank in the case of multi-track events. The solid line represents a fit to the distribution defining the effective target length.

In order to select events originating from the target volume containing liquid D_2 the following vertex cut is applied along the z -axis:

$$- 5.3 \leq z \leq 4.7 \text{ (cm)} , \quad (3.6)$$

where a displacement of -0.3 cm has been introduced to compensate for the shift of the center of the target from the origin of the z axis.

3.4.2 Energy Loss

The charged particles emitted in the target volume lose energy from ionization processes while traversing the liquid deuterium. The same effect occurs outside the target region when the charged hadron traverse the start counter scintillators. For these reasons a momentum correction has been introduced (Ref. [116]) in the reconstruction procedure to compensate for the energy lost by the outgoing charged particles in the target and start-counter regions.

3.5 Photon Flux Normalization

In order to calculate the cross section, the incident photon flux at the CLAS target must be known and the goal of the normalization procedure [117] is to determine it as a function of the energy. This is done using the information of the out-of-time photons by measuring the number of accidental hits of each T-counter in a given time interval τ , which is called the out of time window. Fig. 3.9 shows the histogram of the TDC timing spectrum for a single T-counter. The peak which caused the trigger and the accidental background can be clearly identified. Since the tagger TDCs operates in “common start” mode this peak implies that it was this T-counter which started all the other TDCs from the CLAS trigger associated to the hadronic event generated by this particular photon (electron). Most of the time the TDCs which were not involved with the trigger will just overflow. But other times an accidental hit occurs in a T-counter which did not produce the trigger. This occurs with probability $1 - \exp(-N_e^{(i)}(s) \cdot \tau)$ where $N_e^{(i)}(s)$ is the number of times the TDCs for each T-counter stop counting in the out of time window τ .

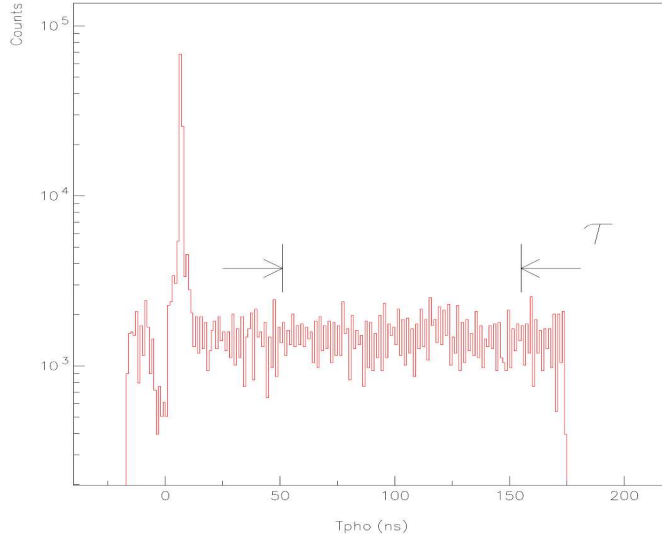


Figure 3.9: TDC timing spectrum of a single T-counter. The peak which caused the trigger and the accidental background can be clearly identified. Utilizing the accidental hits in the tagger, the normalization method determines the number of tagged photons from each T-counter. This is done by measuring the number of accidental hits of each T-counter in a given time interval τ , which is called the out-of-time window.

This measured electron rate is calculated “instantaneously” between each scaler dump in the DAQ, which is approximately every 10 sec. This procedure is based on the tagger T-counters and TAC TDCs information only (scaler-less).

The total number of measured electrons (or out-of-time photons) giving the photon flux $N_\gamma(E_\gamma^{(i)})$ at a the photon energy $E_\gamma^{(i)}$ is then determined from the sum:

$$N_\gamma(E_\gamma^{(i)}) = \epsilon_i^{\text{norm}} \cdot \sum_s N_e^{(i)}(s) \quad (3.7)$$

where:

- i is the T-counter number ($1 \div 61$);
- $N_e^{(i)}(s)$ is the number of measured electrons per T-counter per scaler interval corresponding to tagged photons not associated with an hadronic event in CLAS;
- ϵ_i^{norm} is the tagging efficiency for the i^{th} -tagger channel measured during a normalization run.

The live-time of the DAQ in this time interval, is multiplied to the measured electron rate to give the number of measured electrons on each T-counter. So the number $N_e^{(i)}(s)$ can be re-written as:

$$N_e^{(i)}(s) = R^{(i)}(s) \cdot K(s) \cdot \text{LT}(s) \quad (3.8)$$

where the DAQ live-time, indicated by $\text{LT}(s)$, is calculated on an event basis as:

$$\text{LT}(s) = \frac{\text{Accepted Triggers}}{\text{Total Triggers}} \quad (3.9)$$

where

$$K(s) = \frac{\text{TRGS}[0] \cdot \text{Clock}_{\text{RG}}(s)}{10KH_z} \quad (3.10)$$

is the gated clock for the run, and where $R^{(i)}(s)$ is the electron rate for each T-counter which can be written as:

$$R^{(i)}(s) = \frac{N_{\text{TDC}}^{(i)}(s)}{\tau \cdot [N_{\text{TAGR}}^{(i)}(s) - N_{\text{EP}}^{(i)}(s)]} \quad (3.11)$$

In Eq. 3.11 $N_{\text{TDC}}^{(i)}(s)$ is the number of TDC hits per T-counter and per scaler time interval, $N_{\text{TAGR}}^{(i)}(s)$ is the total number of events with successful tagger reconstruction from the TAGR bank and $N_{\text{EP}}^{(i)}(s)$ is the number of times per scaler interval where there is a TDC hit before the out-of-time window τ .

In the present calculation scheme, $N_{\text{TAGR}}^{(i)}(s) \cdot \tau$ represents the total time, during 10 s (scaler time interval), in which the TDC was open while $N_{\text{EP}}^{(i)}(s) \cdot \tau$ represents a dead time.

In order to calculate the photon flux, the tagging efficiency, which is defined as the number of tagged photons per energy interval divided by the total number of counts observed in the tagging counter defining that interval, must be measured. The knowledge of this quantity is very important because it directly affects the determination of the photo-reaction cross sections. The tagging efficiency strongly depends on the beam setup. For instance, it will be reduced whenever tight collimation is required on the photon beam.

The measurement of the tagging efficiency is performed during low intensity “normalization” runs (schematically shown in Fig. 3.10) at approximately 10% of

the production beam current with the total absorption counter placed in the beam-line. This setup allows for a direct measurement of the photon flux from the total absorption counter (composed by a set of four lead-glass blocks with a detection efficiency close to 100%). Since the total absorption counter cannot handle photon

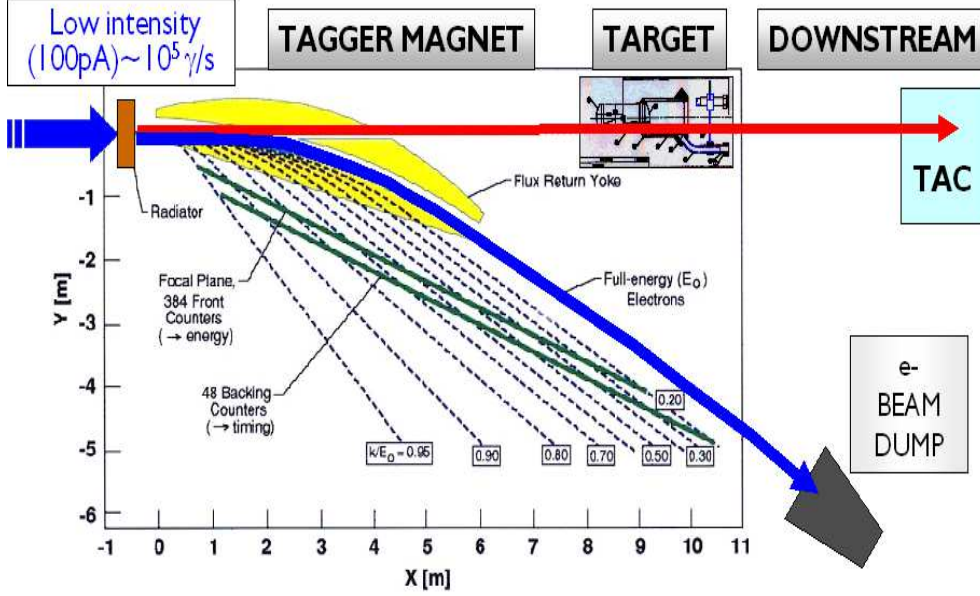


Figure 3.10: Schematic representation of a normalization run: the electron beam current is lowered to 100 pA and the total absorption counter is inserted into the beam-line, downstream of the CLAS. The trigger is formed only by the tagger master OR (MOR). This setup allows for a direct measurement of the photon flux from the total absorption counter (composed by a set of four lead-glass blocks with a detection efficiency close to 100%).

beam rates higher than 10^5 Hz without noticeable degradation it could not be inserted into the beam-line during the production runs to measure the photon flux directly.

During the data taking, normalization runs were performed at the end of each data acquisition session characterized by a group of production runs with common experimental conditions, such as trigger configuration and tagger prescaling settings.

Using this procedure, a total of 178 million normalization events have been collected. The relation giving the tagging efficiency for each tagger T-counter in a normalization run is:

$$\epsilon_i^{\text{norm}} = \frac{N_{\gamma}^{\text{TGT}}}{N_{e^-}^{\text{TAGR}}} = \frac{[T_i \cdot TAC]}{[T_i^{\text{RAW}}]_{\text{norm}}} \quad (3.12)$$

where $[T_i^{\text{raw}}]_{\text{norm}}$ counts the number of coincidences $T_{\text{left}} \cdot T_{\text{right}}$ while $[T_i \cdot TAC]$ is the number of those hits detected in coincidence with the TAC. A small correction is done ($\simeq 2 - 3\%$) to the tagging efficiency to account for the loss of photons from the target to the TAC [118].

The overall tagging efficiency as a function of the tagger spectrometer T-counter is shown in Fig. 3.11 for different runs. As can be seen also from Fig. 3.10 the higher numbered T-counters correspond to high energy electrons poorly deviated from the incident beam direction, so that their energy release ΔE_0 to the emitted photon is

small. According to the relation $\theta_\gamma \simeq m_e/\Delta E_0$ the photon emission angle is larger and for this reason the collimation of the low energy photons is poor. Thus, the loss in efficiency is due the larger fraction of photons cut out by the collimator. On the contrary, the dip in the efficiency in the very first part of the tagging range is due to background coming from the electron beam.

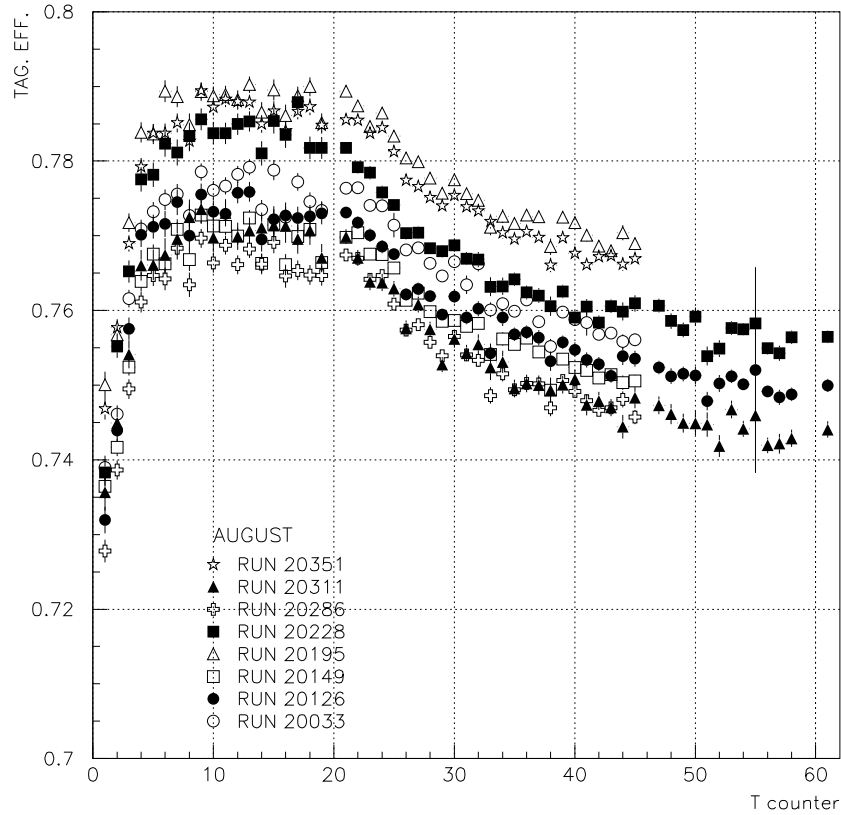


Figure 3.11: Behavior of the tagging efficiency for the tagger spectrometer T-counters for different runs (indicated by the different symbols). The tagging efficiency is defined as the number of tagged photons per energy interval divided by the total number of counts observed in the tagging counter defining that interval. The knowledge of this quantity is very important because it directly affects the determination of the photo-reaction cross sections and strongly depends on the beam setup.

A more detailed example of the stability of the tagging efficiency can be seen in Fig 3.12 where the variation of this quantity with respect to the mean value calculated for each run is shown for selected tagger counters. As it can be clearly seen, the tagging ratio is stable at level of $\simeq 3 \div 4\%$.

The normalization code have been used to process the normalization runs reported in Tab. 3.2. Since some T and E-counters were out-of-work, the procedure have been skipped for some of them, more precisely: T-counters: 20, 46, 59, 60 and E-counters: 66, 98, 101, 142, 214, 220, 222, 224, 239, 240, 285, 335, 337, 343, 380.

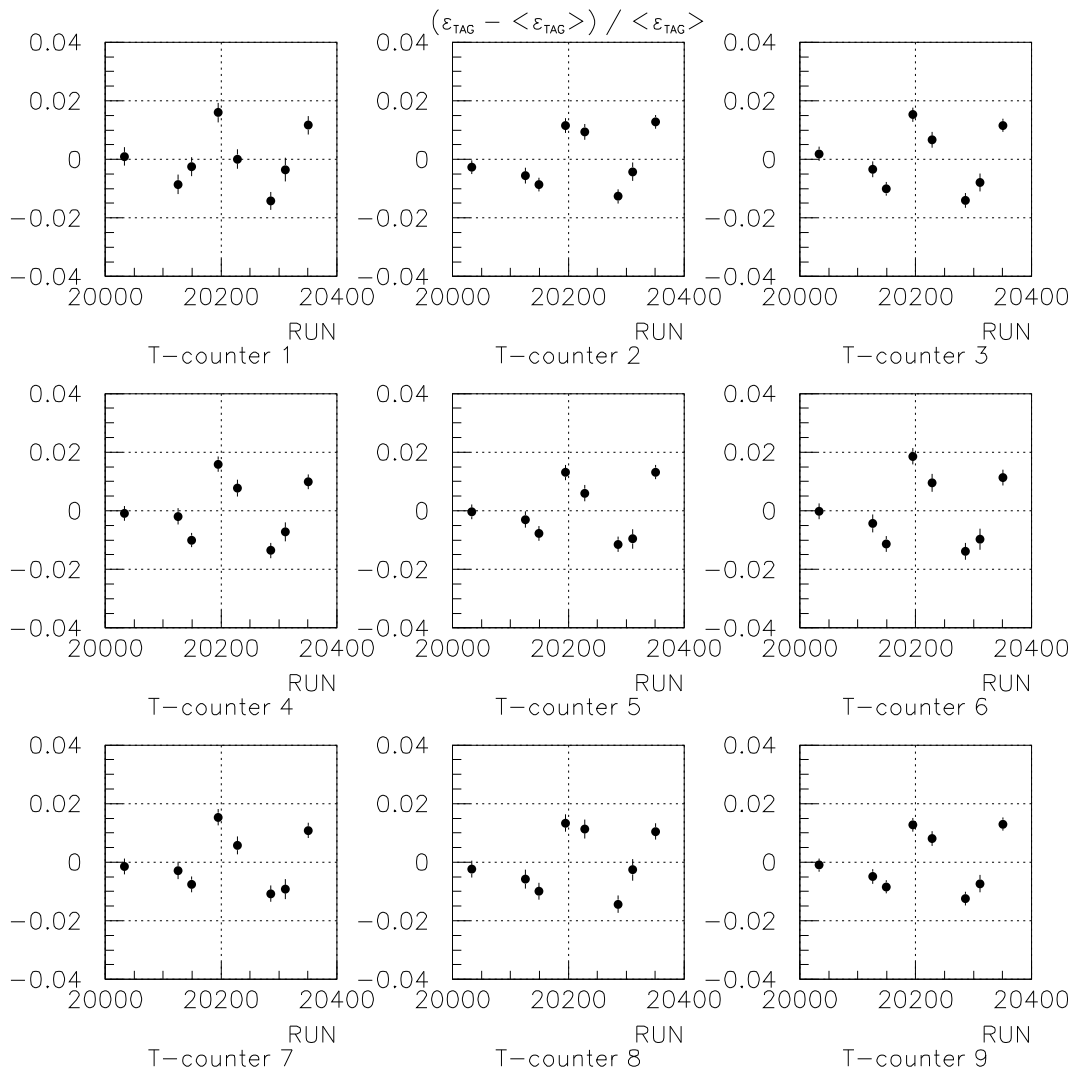


Figure 3.12: Variation of the tagging efficiency with respect to the mean value for some tagger spectrometer T-counters. As can be seen the variation is around 3-4%.

August	September
20033	20612
20126	20644
20149	20697
20195	20719
20228	20720
20286	20733
20311	20754
20351	20761
	20762

Table 3.2: Normalization runs acquired during the “August” and “September” run periods.

3.5.1 Validation of the Photon Flux Normalization

Empty target runs have been used to check the photon flux normalization results. The collected statistics is not enough to perform a complete check over the whole incident photon energy range and proton scattering angles. Nevertheless the photon flux normalization has been validated comparing the distribution of the z component of the interaction vertex for proton events (normalized to the number of incident photons) between a full and empty target run.

The distributions are shown in Fig. 3.13 where the empty target contribution (black line) exhibits two sharp peaks at $z = -5$ cm and $z = 5$ cm in addition to the one at $z = -12.5$ cm. These peaks are due to the interaction of the photon beam with the target cell entrance and exit windows. The smaller peak at $(-15 \leq z \leq -10)$ cm is due to a structure holding the target cell into place. The

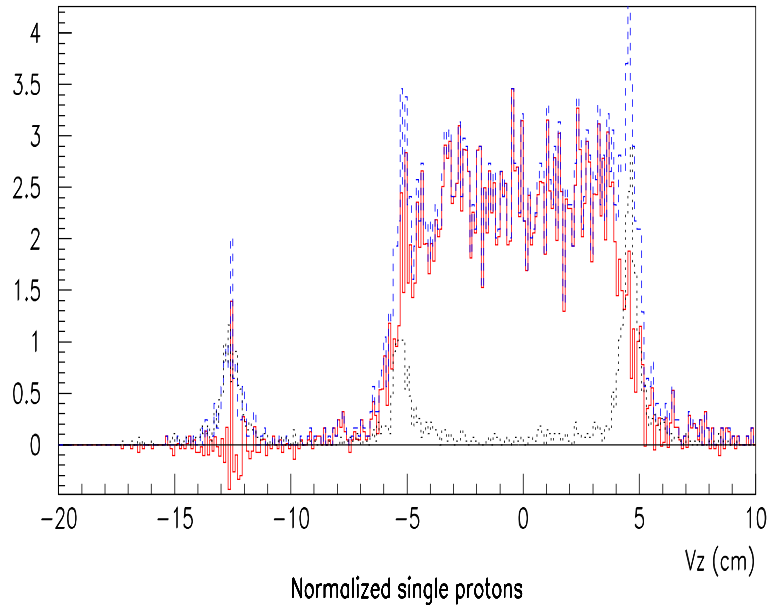


Figure 3.13: Distribution of the z -component of the interaction vertex for the proton events (normalized to the number of incident photons) between a full (blue line) and empty target (black line) run. The difference between the two distributions (red line) is seen to be less than 1% in the interval $(-15 \leq z \leq -10)$ cm, confirming the validity of the photon normalization procedure.

event distribution from the full target run, represented by the blue line of Fig. 3.13, has contributions from events originating in the enclosure contains the liquid D_2 . The difference between the full target and the empty target contributions is represented by the red line of Fig. 3.13. In order to validate the photon flux normalization result the number of events originating in the interval $(-15 \leq z \leq -10)$ cm has been considered in the two cases. If the photon normalization procedure is correct these two numbers must be very close. In fact, the difference $N_{\text{full}} - N_{\text{empty}}$ between the number of events in the chosen z interval is less than 1% since $N_{\text{full}} = 10.86 \pm 0.93$ and $N_{\text{empty}} = 10.94 \pm 0.63$, thus confirming the validity of the normalization procedure.

3.6 Data Quality Check

In order to select runs collected with stable running conditions, a given number of data quality checks have been performed on the reconstructed files used for the data analysis. The first quality checks have been performed during the “cooking” procedure where several run-based parameters, as the overall number of particles, the number of detected p , K^\pm , and π^\pm normalized to the incident photon flux in each CLAS sector, as well as the overall z vertex distribution (average value and width) are required to be constant at the few % level from run to run.

An example of the stability relative to the normalized number of protons as a function of time is shown in Fig. 3.14 for the “August” run period characterized by the tagger spectrometer in the prescale ON configuration. For each run several files are analyzed and the average normalized proton yield is seen to be constant in time at less than 3% level.

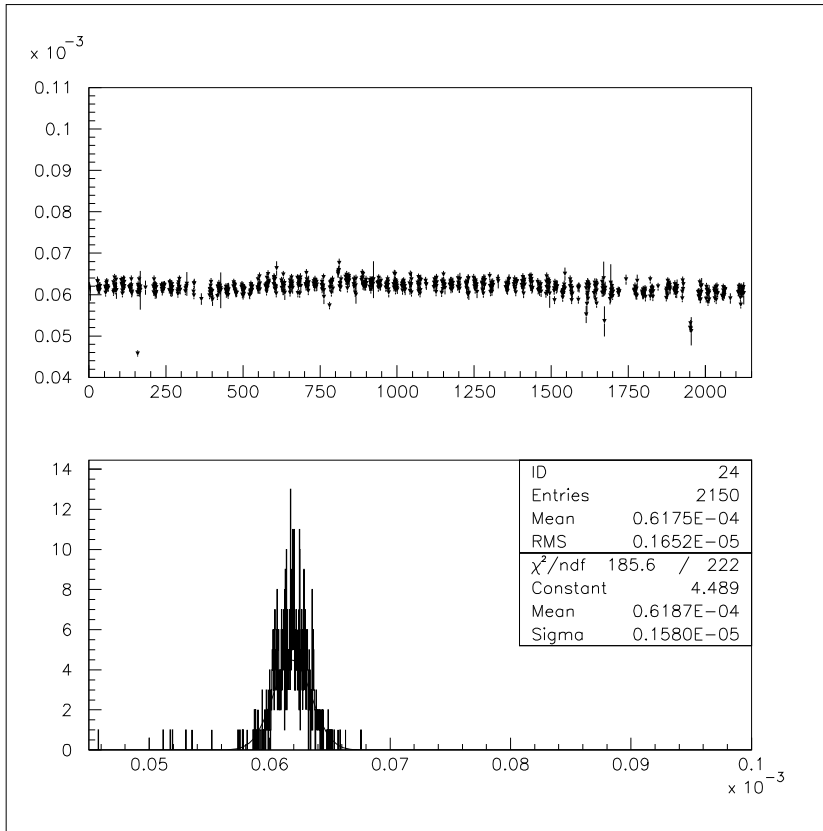


Figure 3.14: Behavior of the normalized number of protons as a function of time for the “August” run period characterized by the tagger spectrometer in the prescale ON configuration. Top plot: for each run several files are analyzed (represented by the single points) and the normalized proton yield is seen to be constant in time. Bottom Plot: Overall distribution of the normalized proton yield fitted with a Gaussian function. The ratio between the standard deviation σ and the mean μ is less than 3%.

After this first selection, a second more accurate quality check based on the deuteron two body photo-disintegration proton yield (normalized to the number of

incident photons) is performed to monitor the data quality for the present analysis. Significant file-based quantities have been considered:

- the number of events with at least one charged particle in the final state for each tagger T-counter, N_T^i ($T = 1 \div 61$);
- the number of photo-disintegration events per 100 MeV bin, N_E^i ($E = 1 \div 25$);
- the number of photo-disintegration events per sector, N_S^i ($S = 1 \div 6$);

where the index i runs over the number of collected data files N and each data file is considered a measurement of the above quantities. In order to define a criterion for rejecting the data files (measurements) which yield results are not compatible with the statistical fluctuations of the sample, the Chauvenet's criterion [119] has been applied. This criterion is based on hypothesis that one result may be rejected if it shows an “unusually large” deviation from the average of the results obtained from the remaining N measurements. The meaning of unusually large is defined using a Gaussian distribution function to calculate the probability that such a result will occur: if this probability is larger than $1/N$, the result is not considered anomalous, since it can be due to a statical fluctuation of the data sample. On the other hand, if the probability is much smaller than $1/N$, then it is very unlikely that the deviation of the result from the average is due to a fluctuation. In this case, the measurement is rejected and its unusually large deviation from the average of the remaining N measurements is considered as originating from a uncontrolled change in the experimental conditions or as the result of mistake which was not recorded in the experimental logbook. The “rule of thumb” used in the literature rejects a measurement if the probability of obtaining it is found to be less than $P_0 = \frac{1}{2N}$.

In order to apply the Chauvenet's criterion the mean values of N_T^i , N_E^i and N_S^i have been calculated according to the following relations:

$$\mu(A) = \frac{\sum_{i=1}^N \frac{A^i}{\sigma^2(A^i)}}{\sum_{i=1}^N \frac{1}{\sigma^2(A^i)}} \quad (3.13)$$

where $A^i = N_T^i$, N_E^i or N_S^i and $\sigma^2(A^i)$ is the related statistical error. The corresponding errors on the mean values are:

$$\sigma_\mu^2(A) = \frac{1}{\sum_{i=1}^N \frac{1}{\sigma^2(A^i)}} \quad (3.14)$$

where the sum index i runs over the total number of collected data files N . For each of the quantities A^i , the variable Λ can be defined as follows:

$$\Lambda^i(A) = \frac{\mu(A) - A^i}{\sigma(A^i)} \quad (3.15)$$

Under the hypothesis that the variables A^i follow a Gaussian distribution also the variable $\Lambda^i(A)$ is distributed according to a Gaussian curve with vanishing mean value and standard deviation equal to the unity.

The Chauvenet's limiting probability P_0 defines an interval of acceptability $(-\Delta_0, \Delta_0)$ for Λ^i such as:

$$P_0 = \frac{1}{\sqrt{2\pi}} \int_{-\Delta_0}^{\Delta_0} \frac{1}{\sigma(\Lambda_i)} e^{-\frac{1}{2} \left(\frac{\Lambda_i}{\sigma(\Lambda_i)} \right)^2} \quad (3.16)$$

so that in the present analysis data files yielding A^i values not satisfying the Chauvenet's criterion have been discarded.

An example of the Λ distribution obtained for $A^i = N_E^i$ (*i.e.* number of normalized photo-disintegration events) is shown in Fig. 3.15 for two different bins of incident photon energies since this quantity represents the most critical yield to be monitored in the present analysis. It can be seen that the distribution is practically flat and most of the data files yield values of Λ^i within the limits of the fiducial interval $(-\Delta_0, \Delta_0)$ represented by the two horizontal lines.

Only two data files have been found to yield Λ values out of the confidence interval defined according to the criterion illustrated above and have been excluded from the current analysis.

Another important parameter to be investigated is the uniformity of the response of the six CLAS sectors since they can be regarded as six independent spectrometers. The uniformity has been monitored considering the ratio between the normalized photo-disintegration protons yields from sectors 1 to 5 over those from sector 6, as a function of time (or run). The choice of using CLAS sector 6 as a reference sector has been done since from the proton detection efficiency study, sector six has shown the best response (more details will be given in Sec. 3.8).

As can be seen from Fig. 3.16, the distributions of the uniformity for sectors 1 to 5 with respect to sector 6 are flat and no time dependence is evident. The values of the overall uniformity are reported in table 3.3. The lower value of the uniformity for sector 3 can be understood taking into account that a certain number time-of-flight paddles were out of work, as will be shown in detail in Sec. 3.8.

Sector	Uniformity
S1/S6	0.97
S2/S6	0.97
S3/S6	0.91
S4/S6	0.99
S5/S6	1.01
Average	0.97 ± 0.01

Table 3.3: Uniformity of the response of the CLAS sectors.

In conclusion, data files not satisfying the data quality checks have been discarded and so forth excluded from the current analysis. Following the procedures discussed above, about 7% of the originally collected data have been excluded.

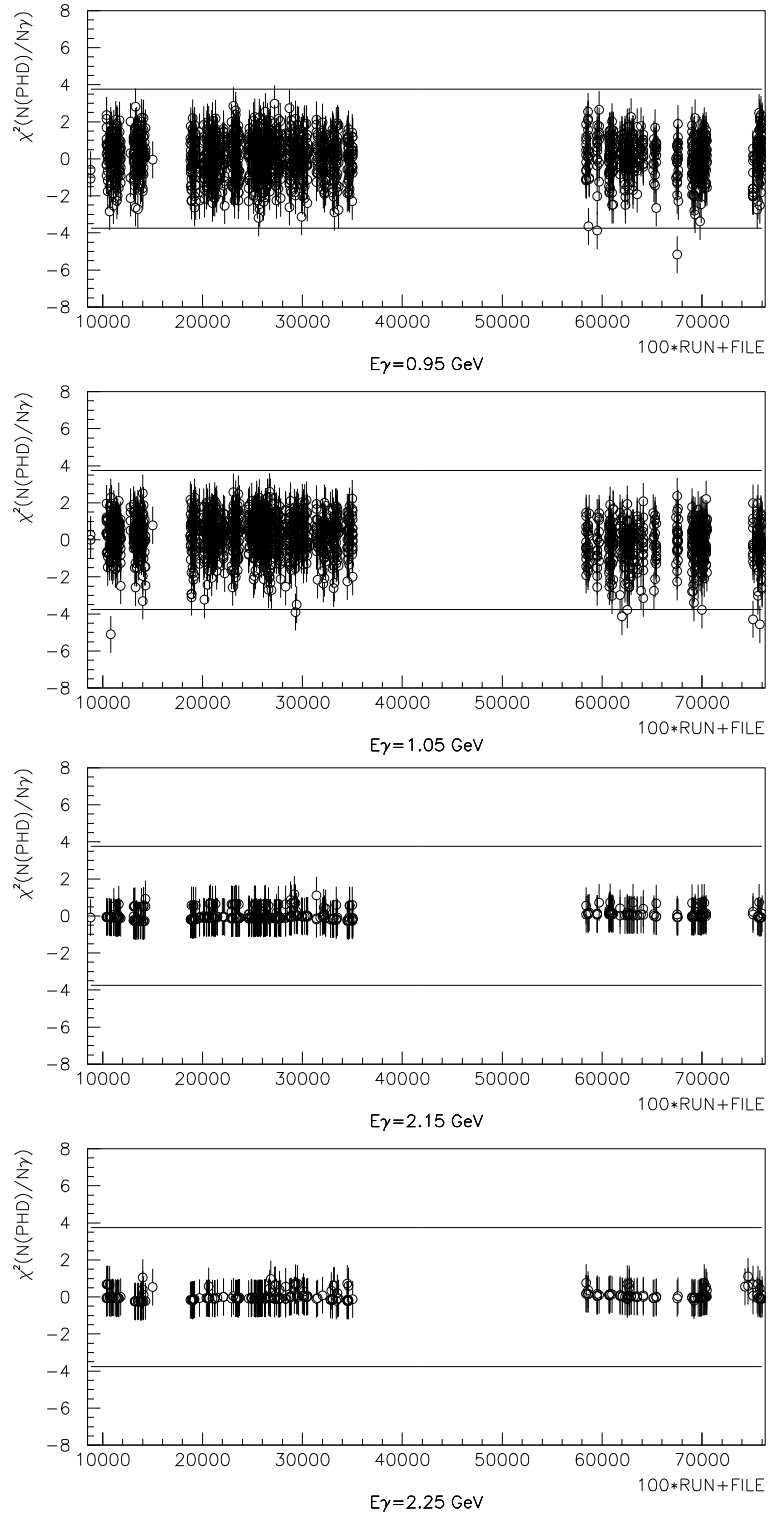


Figure 3.15: Distribution of the Λ values calculated for the normalized photo-disintegration proton yield N_E^i at an incident photon energy of 0.95 - 1.05 GeV (top plots) and 2.15 - 2.25 GeV (bottom plots). The horizontal lines represent the fiducial limits derived from the Chauvenet's criterion. The distribution is practically flat and most of the runs yield values of Λ^i within the limits of the fiducial interval $(-\Delta_0, \Delta_0)$ represented by the two horizontal lines. Only two files have been discarded from the overall dataset.

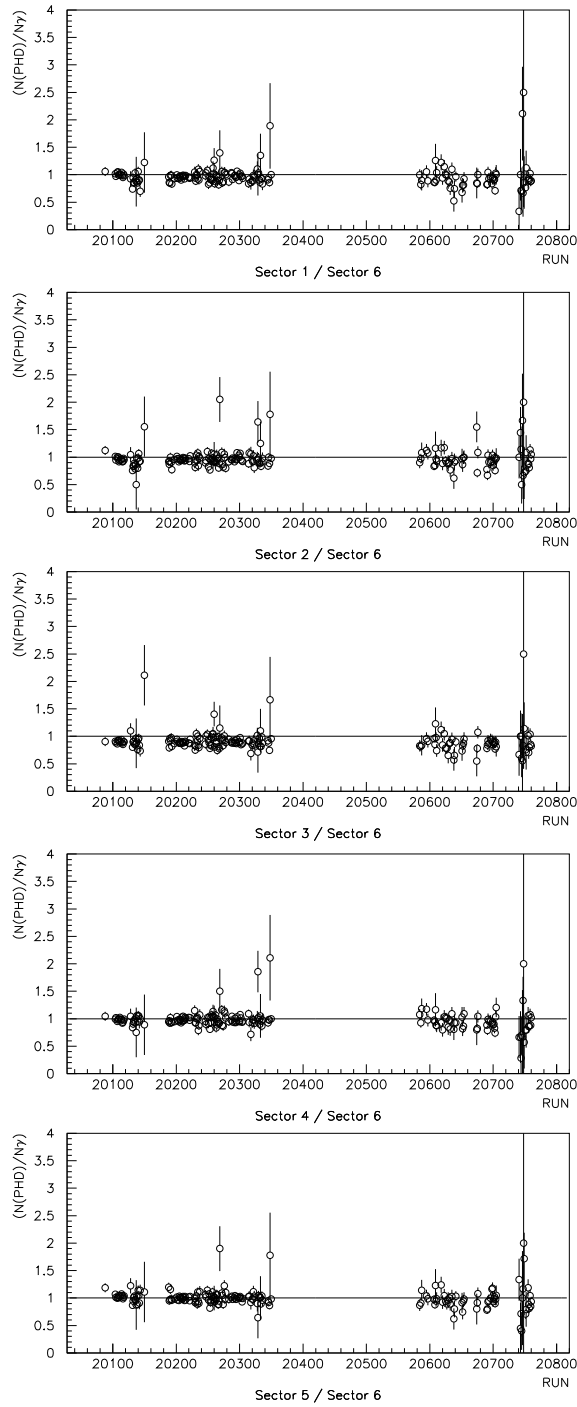


Figure 3.16: Ratio of the normalized photo-disintegration proton yields from sectors 1 to 5 over sector 6 as a function of the run number. As it can be seen, all the distributions are flat and no time dependence on the run period is shown. The average values of uniformity are reported in table 3.3.

3.6.1 Data Stability

The data files processed according to the quality checks described above have been additionally checked to make sure that the experimental conditions in place during their acquisition were stable.

Nevertheless, some experimental conditions must change since some runs have different requirements. For example, the maximum incident energy E_0 of the electrons may change as well as the tagger prescale settings.

For this reason, the data stability has been monitored using the total proton yield normalized to the incident photon flux and the rate of accidental coincidences, with different tagger prescale settings and different electron energies.

The typical behavior of the normalized proton yield per tagger T-counter as a function of the incident photon energy is shown in Fig. 3.17 for different prescale settings of the tagger spectrometer and for different initial electron energies E_0 . The overall normalized proton yield is proportional to the total photo-production cross section and is a decreasing function of the incident photon energy. On the

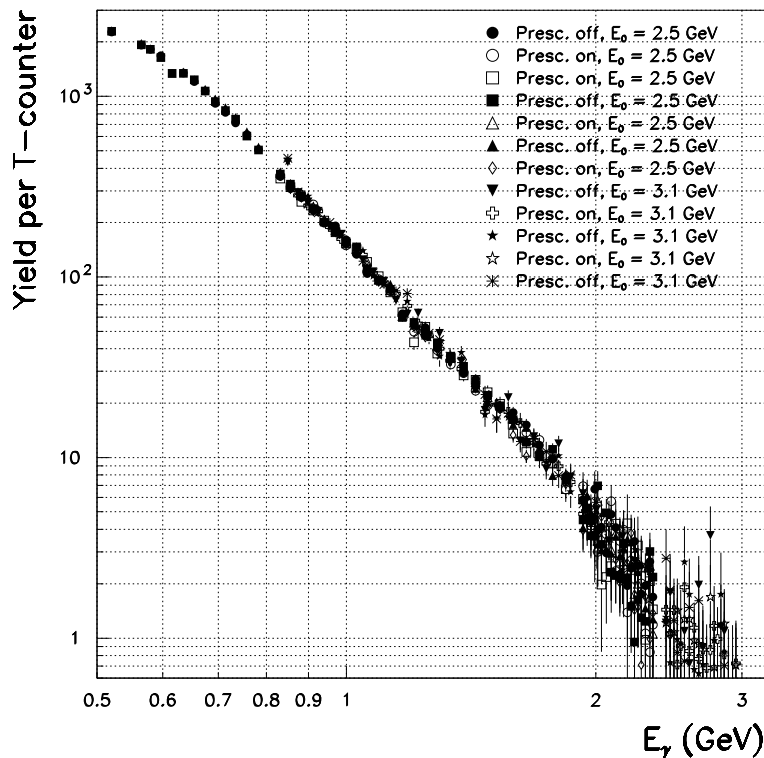


Figure 3.17: Normalized total proton yield per T-counter as a function of incident photon energy: the different symbols refer to different running conditions (tagger prescale ON or OFF and incident electron energy E_0). The behavior of the normalized proton yield per tagger T-counter does not show evident dependence on the experimental settings.

contrary, it does not show evident dependence on the experimental settings since the contributions of runs performed in different conditions (identified by the symbols shown in the legend of Fig. 3.17) all have a similar behavior as a function of the incident photon energy.

For what concerns the accidental coincidences, their contribution affects the data

taking since the total trigger for photo-production experiments in CLAS is given by the coincidence signals coming from the CLAS and the tagger spectrometer (Master OR).

The CLAS part of the trigger is formed when a charged particle, produced by an hadronic event in the target volume is detected in the near-by start counter scintillators, which seen from the target, cover the same solid angle as the time-of-flight system. The start counter signal has a time fluctuation of about $3 \div 4$ ns depending on production point of the particle in the target volume and impact position on the scintillators.

At the end of its flight path through the CLAS, the charged particle fires the time-of-flight scintillators so that a valid CLAS Level 1 trigger may be formed. The overall time fluctuation of the time-of-flight signal depends on several factors. The velocity of the outgoing particle gives rise to a time fluctuation which can be estimated considering the time difference between a fast (high momentum) and slow (low momentum) pions, which is $\simeq 30$ ns. Then, an additional $\simeq 15$ ns fluctuation is introduced by the impact position of the particle in the TOF scintillator. In order to guarantee a suitable overlap with the start counter signal which is only 12 ns wide the width of the TOF signal is chosen to be 100 ns wide. On the tagger

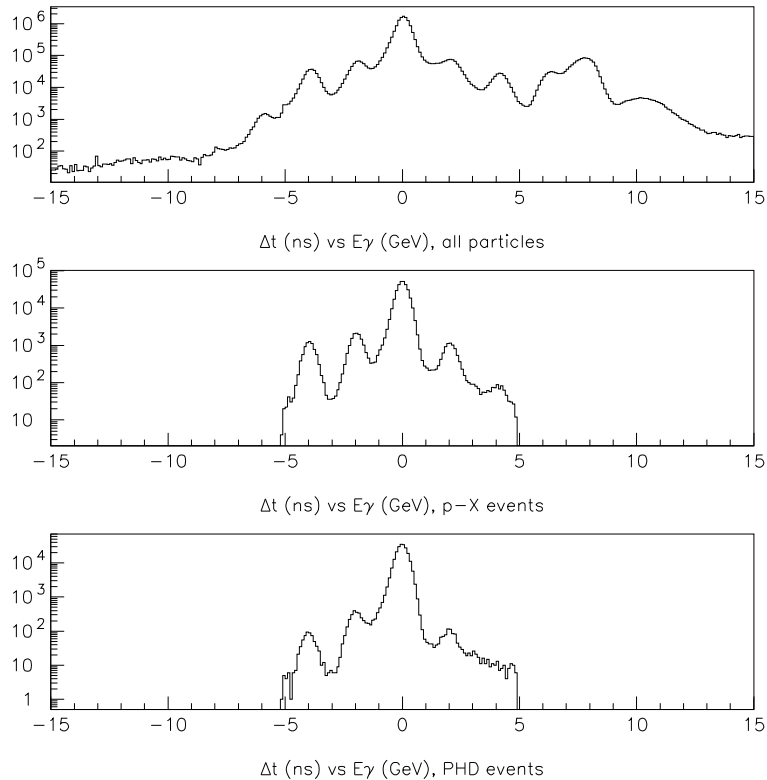


Figure 3.18: Distribution of the event time difference Δt between the tagger time and the start counter time for all outgoing charged particles (top plot), for proton events (middle plot), and for photo-disintegration events (bottom plot).

spectrometer side, each of the $7 \cdot 10^6$ γ /s flowing through the spectrometer can possibly produce a valid “good photon” trigger in one of the 121 T -counters so that

all the T-counters signals have to be aligned to produce a collective Master OR signal which is 15 ns wide. In this arrangement accidental coincidences are possible if, for example, multiple hits in the tagger have timings that can all be associated with a “good photon” pattern.

Another possibility is realized when a photon hits the target but its energy is not measured in the spectrometer being out of its tagging range (very low or extremely high energy photons). Such photons may produce an hadronic event which is detected in CLAS while this event is accidentally in coincidence with a “good photon” tagger pattern which did not produce it.

An example of the time difference distribution Δt between the tagger time and the start counter time is shown in Fig. 3.18 for all outgoing charged particles (top plot), for proton events (middle plot), and for photo-disintegration events (bottom plot). The ratio R of the number of events lying under time interval $(-1,1)$ ns to the average number of events under the two near by peaks gives the accidental coincidences level, that is:

$$R = \frac{\frac{1}{2}(N(-3, -1) + N(1, 3))}{N(-1, 1)} \quad (3.17)$$

The values of R as a function of the run number are shown in Fig. 3.19. It can be seen that the level of accidental coincidences has a relatively flat behavior as a function of the run number (time). On the contrary, two different levels are measured: one level is relative to the tagger prescale OFF configuration and has an average value around 1% while the other, relative to the tagger prescale ON configuration, is less than 2%.

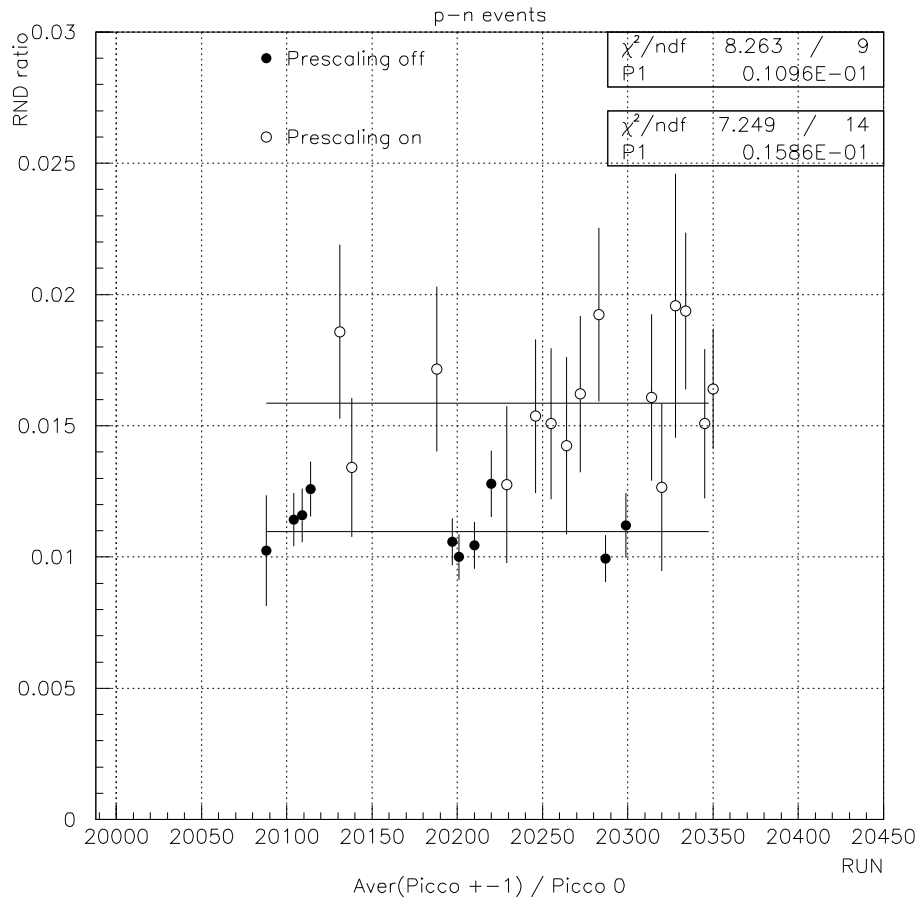


Figure 3.19: Level of accidental coincidences R shown as a function of the run number. The relatively flat behavior has two different levels: one is relative to the tagger prescale OFF configuration and has an average value around 1% while the other is relative to the tagger prescale ON configuration and is less than 2%.

3.7 Momentum Corrections

The missing mass distributions from $\gamma d \rightarrow pX$ events have been calculated over the whole range of incident photon energies and proton scattering angles and the resulting peak position has been found to be off with respect to the reference value given by the neutron rest mass. This shift is not very large (of the order of 3%, at maximum) nevertheless the distortion introduced in the missing mass distribution shape can reduce the number of identified photo-disintegration events.

A similar problem was found also in other CLAS experiments. For example, in the elastic ep scattering experiment the missing mass distribution peak for $ep \rightarrow eX$ events is shifted by the order of few % from the reference value of the proton rest mass [120]. This effect could be due to small misalignments of the drift chambers positions with respect to their nominal positions or to uncertainties in the magnetic field maps. Another possibility concerns the knowledge of the energy of the incoming photon which could be incorrect. Since it is not possible to disentangle between these two contributions, the shift of the missing mass peak is usually corrected introducing an empirical function $f(P_0, \theta_0, \phi_0)$ depending on the measured proton 3-momentum P_0 :

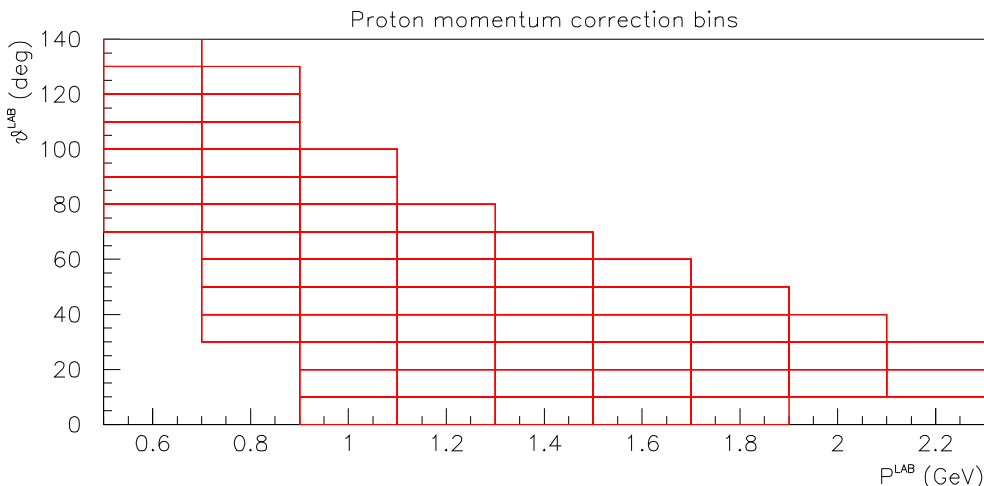


Figure 3.20: Region of the kinematic plane where the momentum corrections could be calculated using two body kinematics.

$$P' = P_0 f(P_0, \theta_0, \phi_0) \quad (3.18)$$

where P' is the corrected momentum and θ_0 and ϕ_0 are referred to measured proton angles in the LAB system. Assuming that angles and photon energy are correctly measured, the momentum correction function is factorized as follows:

$$P' = P_0 f_1(P'', \theta_0) f_2(P_0, \phi_0) \quad (3.19)$$

where P'' , f_1 , and f_2 are functions to be determined from the data according to the following procedure:

1. first, the proton momentum range is divided in 200 MeV bins;
2. in each bin of proton momentum, photo-disintegration events are selected from the $\gamma d \rightarrow pX$ distributions. In order to reduce background, a $(-2\sigma, 2\sigma)$ cut around the peak position is applied, where σ is the standard deviation obtained from a Gaussian fit of the missing mass distribution;
3. event by event the momentum expected on the base of two body kinematics is calculated as a function of photon energy E_γ and the proton scattering angle θ_0 , which are assumed correctly measured. An example of the region of the kinematic plane where this procedure has been applied is shown in Fig. 3.20.
4. Each bin of proton momentum is additionally divided in 5° wide bins of the azimuthal angle ϕ ;
5. in each ϕ -bin the ratio $R_\phi = P_\phi/P_0$ is calculated and its distribution is fitted using a Gaussian function to obtain the average value $\langle R_\phi \rangle$;
6. the behavior of $\langle R_\phi \rangle$ as a function of ϕ is reproduced using a 2^{rd} order polynomial (f_2 in Eq. 3.19). An example is shown in Fig. 3.21 for CLAS sector 1 and for three different values of proton momentum: P_0 : 0.55 GeV (top plot), 0.65 GeV (middle plot), and 0.75 GeV (bottom plot). Then, a first correction is applied to the measured momentum P_0 as a function of ϕ in the form $P'' = P_0 f_2(P_0, \phi_0)$
7. The procedure is repeated starting from point (4) and dividing each bin of proton momentum in 10° wide bins in the scattering angle θ . In this way, a second correction factor is calculated and applied to the measured momentum P_0 as a function of θ (f_1 in Eq. 3.19).

An example of the effect of the momentum correction procedure is shown in Fig. 3.22 for CLAS sector 3 (top plot) and sector 2 (bottom plot) for two different proton momenta and scattering angles: $P=0.65$ GeV, $\theta = 115^\circ$ and $P=1.15$ GeV, $\theta = 15^\circ$, respectively. The missing mass distributions are sharper after the correction procedure while the peak position (indicated by M_X) is closer to the neutron rest mass value.

In particular, Fig. 3.23 shows the overall situation before the application of the momentum correction procedure. As can be seen, the deviation from the unity of the ratio M_X/M_n , (being M_n the nominal value for the neutron rest mass) plotted against the proton scattering angle in the LAB system separately for the six CLAS sectors and for the intermediate proton momentum of 1.05 GeV, affects practically all sectors and shows a dependence on the proton scattering angle. The maximum deviation is of the order of 3% in some sectors (specifically sector 4 and 6). The same quantity, after introducing the momentum correction procedure is shown in Fig. 3.24. It can be seen that the deviation from the unity is greatly reduced in all sectors together with the dependence of M_X/M_n on the proton scattering angle.

The distributions of the M_X values obtained from the missing mass distributions for $\gamma d \rightarrow pX$ events before and after the application of the momentum correction procedure are shown in Figs. 3.25 and 3.26 respectively. The top plot shows the overall M_X distribution for the six CLAS sectors, while the remaining six plots show the contributions of the different sectors. As shown in Fig. 3.25 before the

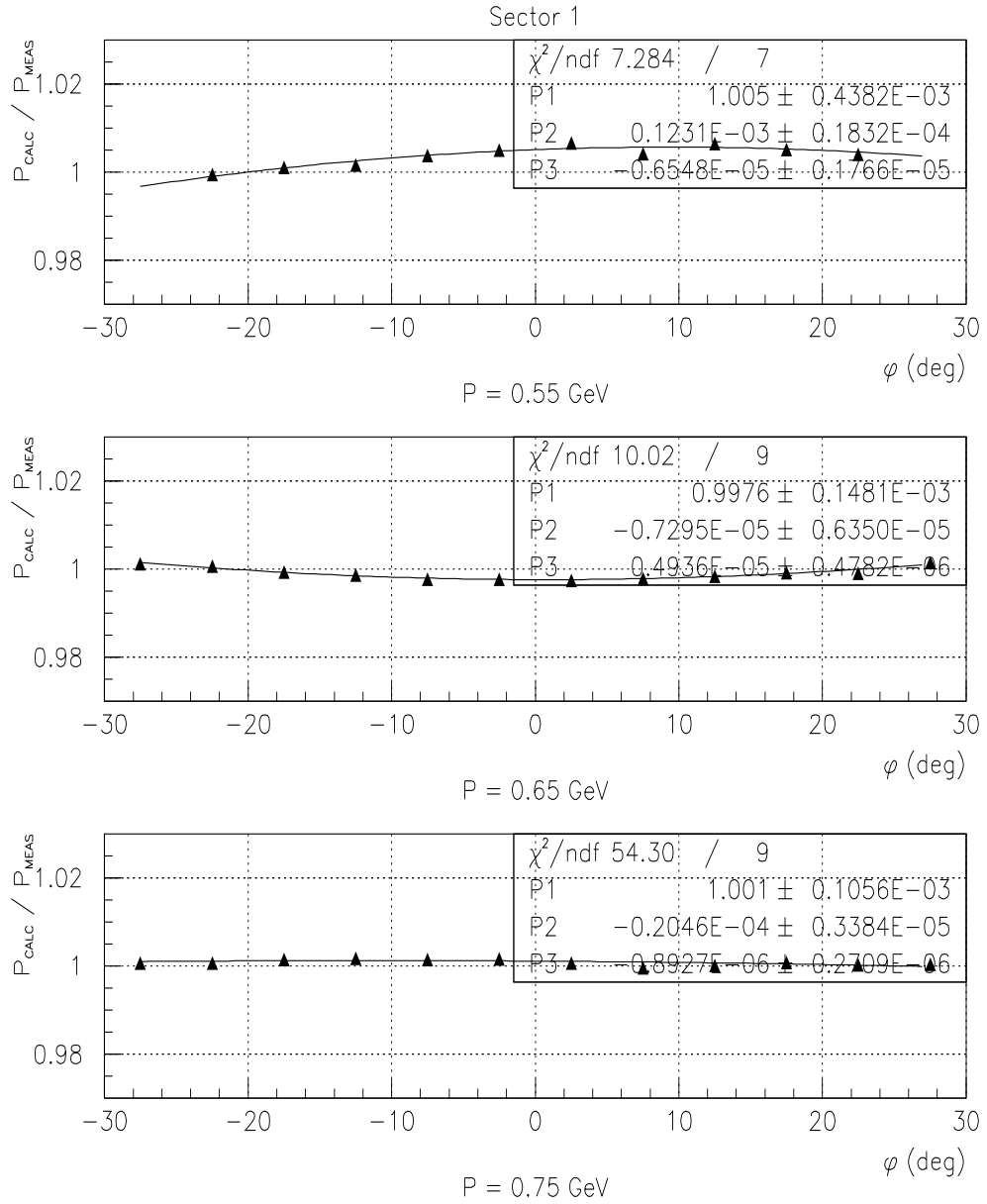


Figure 3.21: Behavior of the ratio $\langle R_\phi \rangle$ as a function of ϕ in CLAS sector 1 for three values of the measured proton momentum P_0 : 0.55 GeV (top plot), 0.65 GeV (middle plot), and 0.75 GeV (bottom plot). In each ϕ -bin the ratio $R_\phi = P_\phi/P_0$ is calculated and its distribution is fitted using a Gaussian function to obtain the average value $\langle R_\phi \rangle$.

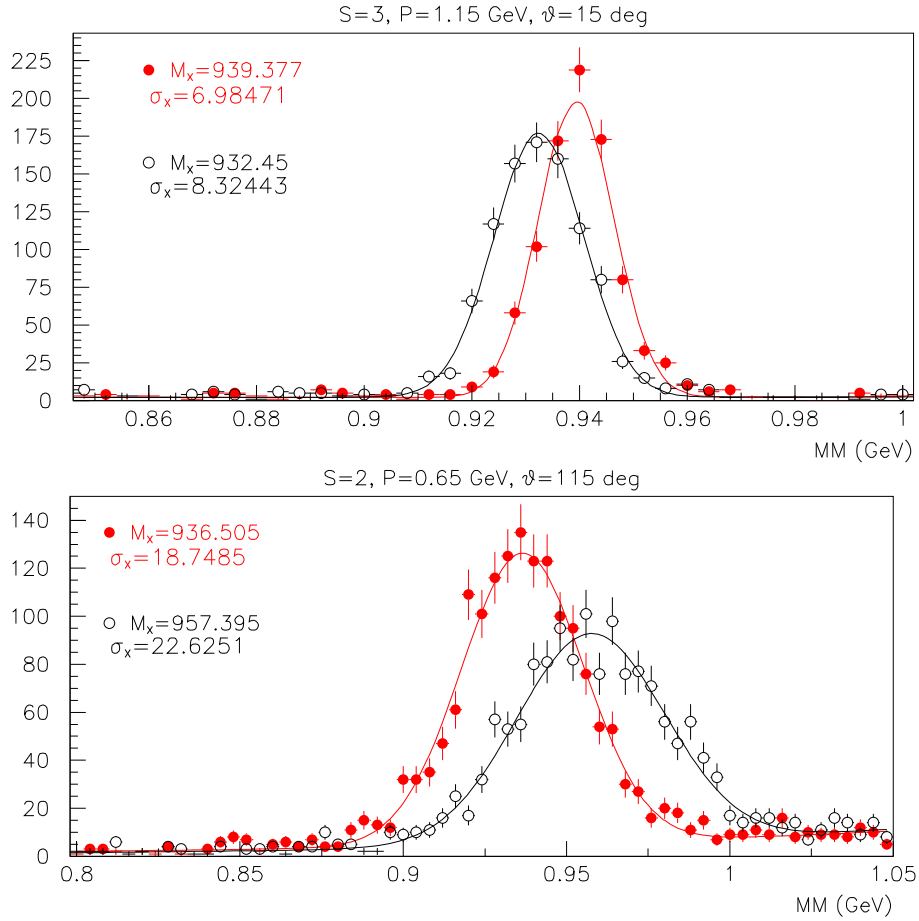


Figure 3.22: missing mass distributions for $\gamma d \rightarrow pX$ events for sector 2 (top plot) and sector 3 (bottom plot) for two different proton momenta and scattering angles: $P=0.65 \text{ GeV}$, $\theta = 115^\circ$ and $P=1.15 \text{ GeV}$, $\theta = 15^\circ$, respectively. The missing mass distributions are sharper after the application of the correction procedure and their peak positions are closer to the neutron rest mass value.

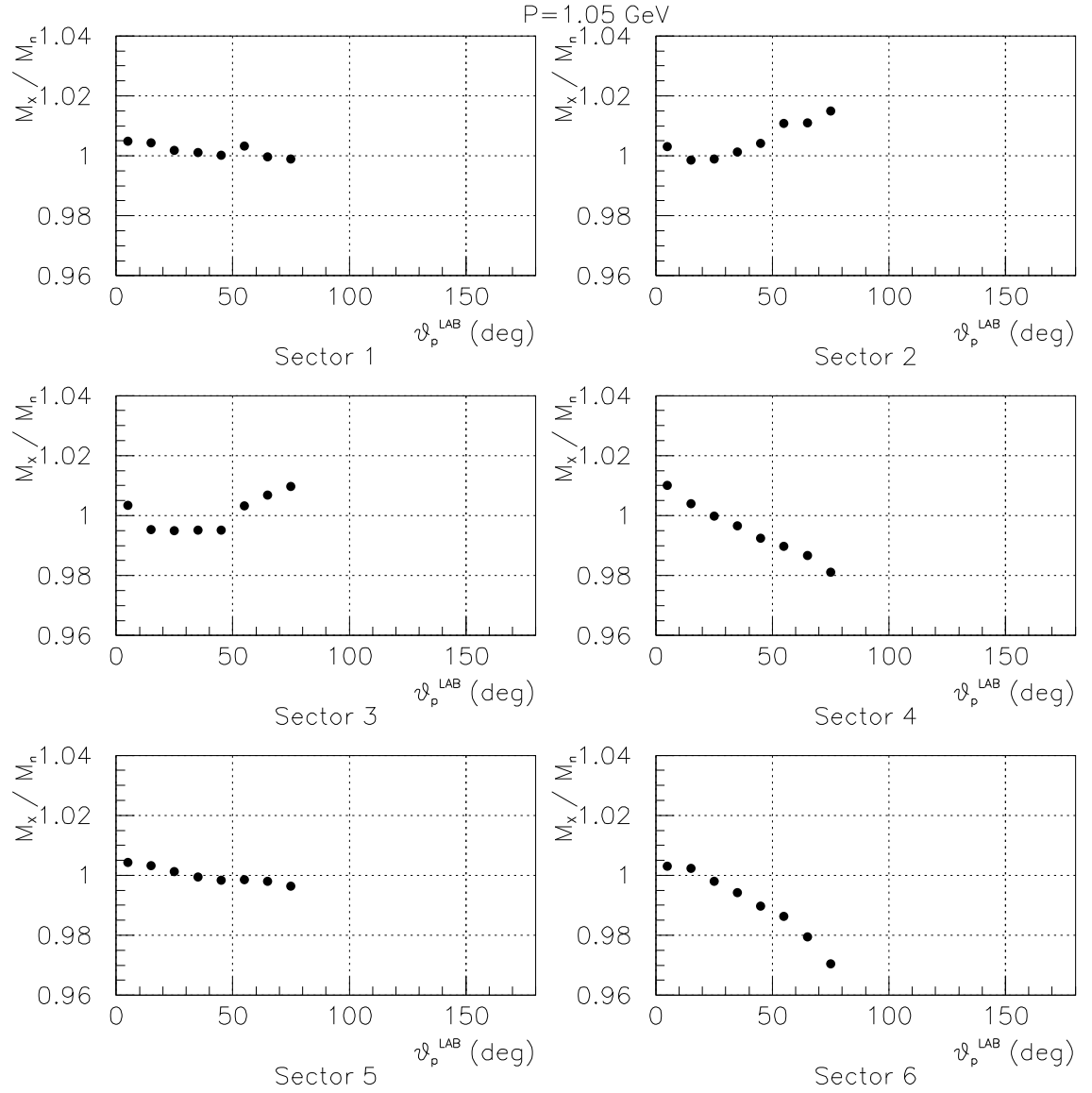


Figure 3.23: Before the momentum correction. Ratio M_X/M_n (being M_n the nominal value for the neutron rest mass) plotted against the proton scattering angle in the LAB system separately for the six CLAS sectors and for the intermediate proton momentum of 1.05 GeV. The deviation from the unity affects practically all six CLAS sectors, and shows a dependence on the proton scattering angle. The maximum deviation is of the order of 3% in some sectors (specifically sector 4 and 6).

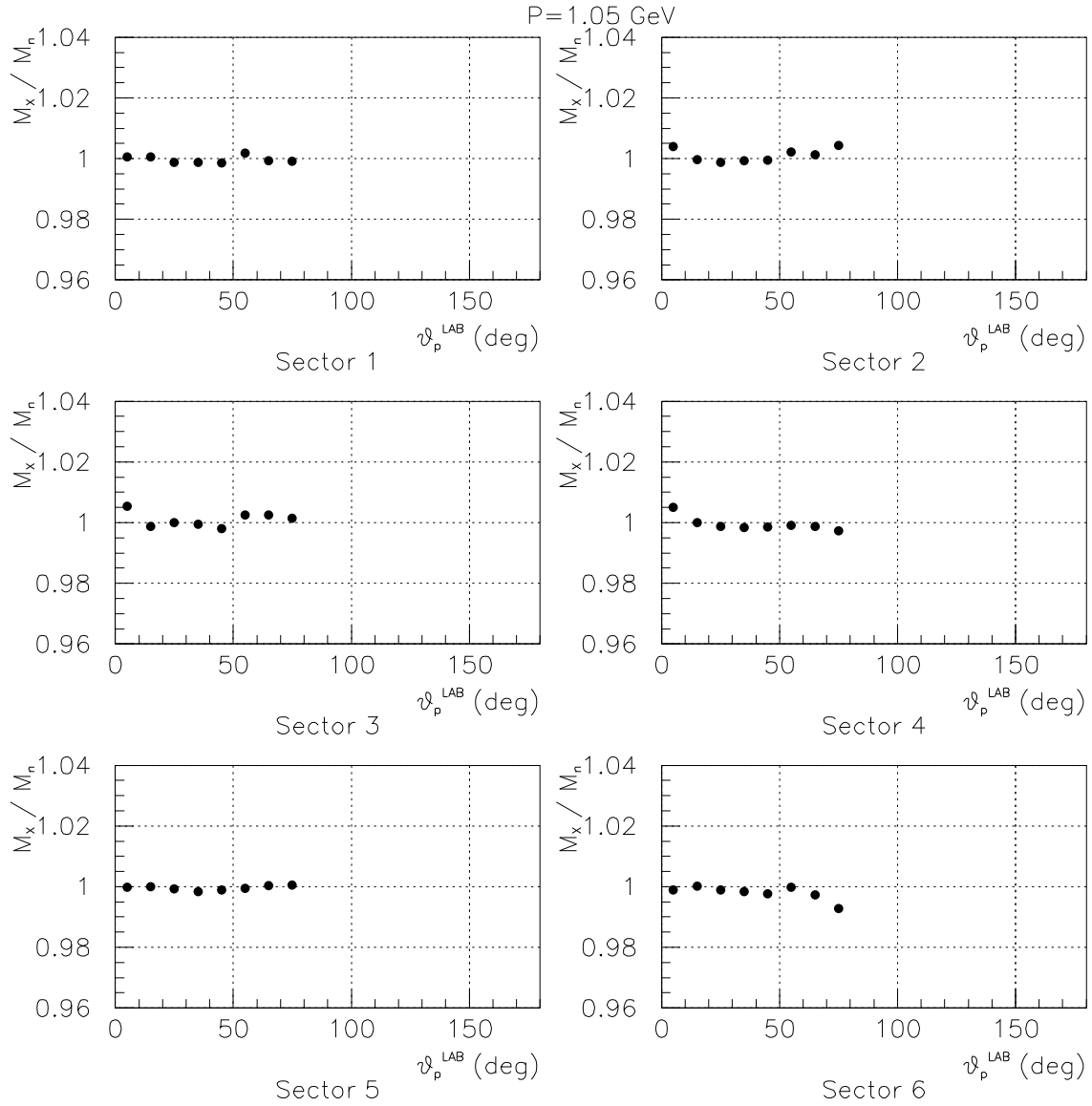


Figure 3.24: After the momentum correction. Ratio M_X/M_n (being M_n the nominal value for the neutron rest mass) plotted against the proton scattering angle in the LAB system separately for the six CLAS sectors and for the intermediate proton momentum 1.05 GeV. The situation is clearly improved compared to the one shown in Fig. 3.23 since the values obtained for M_X/M_n are of the order of 1 and the dependence on the proton scattering angle is removed by the correction.

momentum correction is applied, the M_X distributions have large widths which are quite different in the six CLAS sectors. On the contrary, after the application of the momentum correction procedure, the widths of the M_X distributions are reduced and are uniform in the six sectors, as shown in Fig. 3.26.

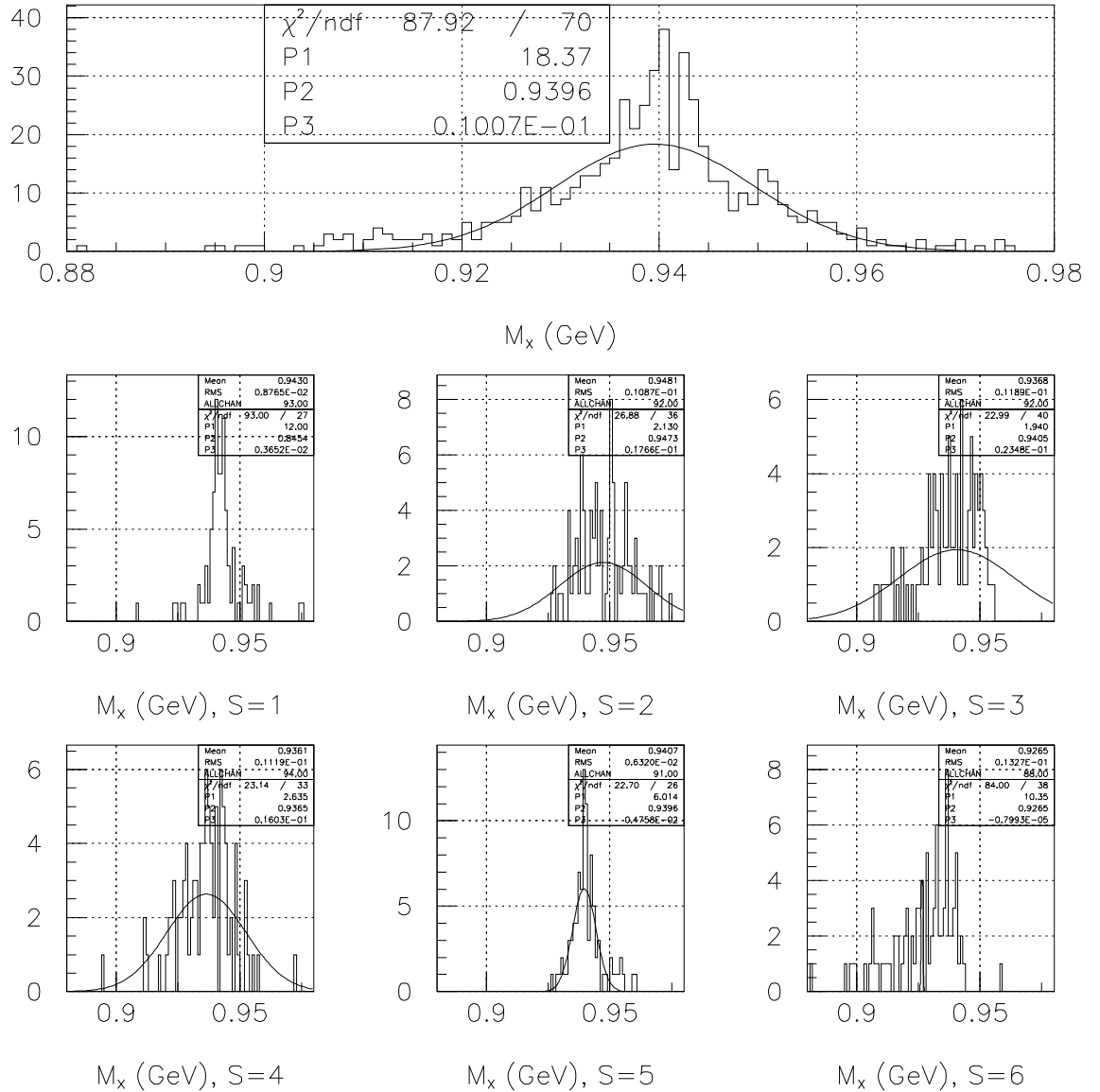


Figure 3.25: Before the momentum correction. Distributions of the M_X values obtained from the missing mass distributions for $\gamma d \rightarrow pX$ events. The top plot shows the overall M_X distribution for the six CLAS sectors, while the remaining six plots show the contributions of the different sectors. It is seen that, the M_X distributions exhibit large widths which are different in the six CLAS sectors.

A summary of the improvement in the momentum reconstruction introduced by the correction procedure is shown in Fig. 3.27. The plot shows the position of the missing mass distribution peaks (associated with their RMS) before (solid/black squares) and after (solid/red dots) the correction while the horizontal line represents

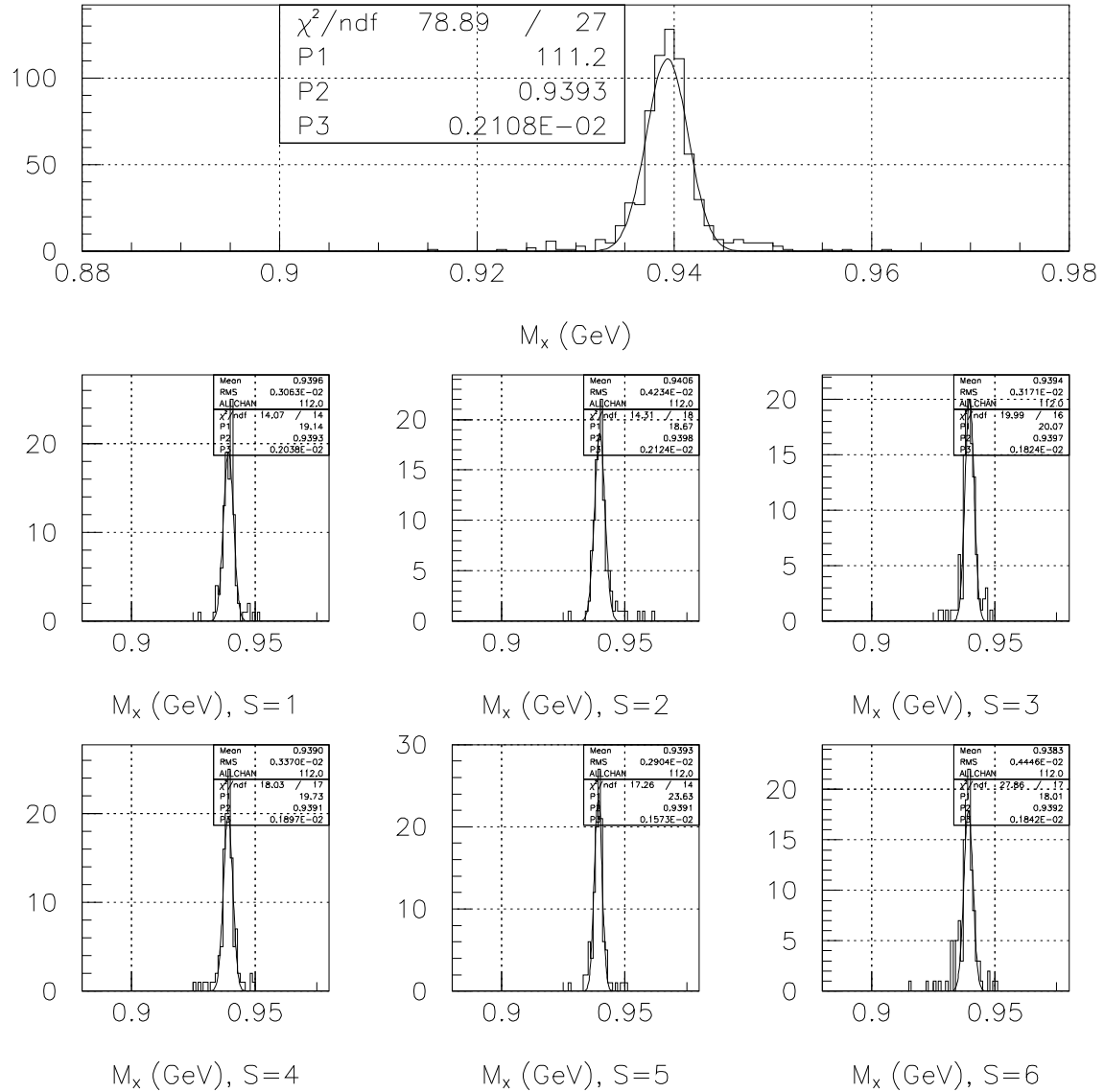


Figure 3.26: After the momentum correction. Distributions of the M_X values obtained from the missing mass distributions for $\gamma d \rightarrow pX$ events. The top plot shows the overall M_X distribution for the six CLAS sectors, while the remaining six plots show the contributions of the different sectors. After the application of the momentum correction procedure, the widths of the M_X distributions are reduced and are more uniform in the six sectors.

Sector	Peak Before	RMS	Peak After	RMS	σ fit
1	943.0	8.7	939.6	3.1	2.1
2	948.1	10.9	940.6	4.2	2.1
3	936.8	11.9	939.4	3.2	1.8
4	936.1	11.2	939.0	3.4	1.9
5	940.7	6.3	939.3	2.9	1.6
6	926.5	13.3	938.2	4.4	1.8
ALL	939.6		939.3		2.1

Table 3.4: Numerical values of the missing mass distributions peaks and RMS before and after for the momentum correction procedure is applied in each sector, together with the standard deviations obtained fitting the corrected missing mass distributions.

the nominal value of the neutron rest mass.

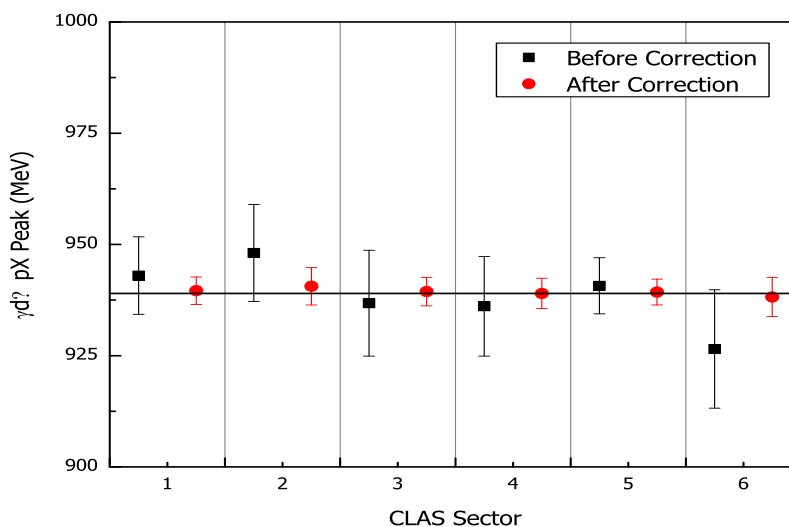


Figure 3.27: Position of the missing mass distribution peaks (associated with their RMS) before (solid/black squares) and after the correction (solid/red dots). The horizontal line represents the nominal value of the neutron rest mass.

For a more quantitative comparison, in Tab. 3.4 are given the numerical values of the missing mass distributions peak positions and RMS in each sector before and after for the correction together with the standard deviations obtained fitting the distributions after the correction procedure.

3.8 Proton Detection Efficiency

3.8.1 Introduction

The extraction of the photo-disintegration differential cross section requires the knowledge of the number of $\gamma d \rightarrow pn$ events produced in the selected bins of the outgoing proton momentum and scattering angle. In order to count these events correctly the proton detection efficiency in CLAS have to be evaluated.

The CLAS proton detection efficiency cannot be extracted from the photo-disintegration data because it also requires the detection of the photo-disintegration neutron in the CLAS. This procedure is not convenient since:

- neutrons are detected by the electromagnetic calorimeters, having a much smaller angular coverage ($\theta_p^{\text{LAB}} \leq 45^\circ$ or 70° for two CLAS sectors) than the time-of-flight scintillators which are used to detect protons;
- the neutron detection efficiency of the calorimeters is less than 50% (see Ref.[121]).

For the above reasons, to evaluate the single proton detection efficiency a GEANT simulation of the CLAS detector has been used.

3.8.2 GEANT Simulation

In order to simulate $\gamma d \rightarrow pn$ reaction in the CLAS, an appropriate number of events are produced using a simple Monte Carlo code. The events are generated uniformly in the CM system using an flat photon energy spectrum between 0.5 and 2.95 GeV and then Lorentz boosted in the LAB frame. Since the proton detection efficiency does not depend on the production mechanism, no cross section or background information is taken into account by the event generator.

In order to have statistical errors smaller than those introduced from other quantities entering in the final cross section calculation, about $20 \cdot 10^6$ photo-disintegration events have been generated.

3.8.3 Proton Detection Efficiency Evaluation using GSim

The proton detection efficiency calculated from the simulation is defined as the ratio between the number of generated events ($N_{\gamma d \rightarrow pn}^{\text{GEN}}$) in a certain kinematic bin ($\Delta P_p^{\text{LAB}}, \Delta \theta_p^{\text{LAB}}, \Delta \phi$) over the number of reconstructed events ($N_{\gamma d \rightarrow pn}^{\text{REC}}$) in the same kinematic bin:

$$\epsilon_{\text{GSIM}} = \frac{N_{\gamma d \rightarrow pn}^{\text{REC}}(\Delta P_p^{\text{LAB}}, \Delta \theta_p^{\text{LAB}}, \Delta \phi)}{N_{\gamma d \rightarrow pn}^{\text{GEN}}(\Delta P_p^{\text{LAB}}, \Delta \theta_p^{\text{LAB}}, \Delta \phi)} . \quad (3.20)$$

A binning in proton momentum and polar scattering angle of $\Delta P_p^{\text{LAB}} = 100$ MeV and $\Delta \theta_p^{\text{LAB}} = 10^\circ$ is chosen to match the one used in the final cross-section calculation. On the other hand, a binning of $\Delta \phi = 5^\circ$ is chosen to better investigate the azimuthal behavior of the CLAS proton detection efficiency. In fact, according to the CLAS toroidal geometry, the reconstruction is worse on the borders of the six sectors, since these regions are adjacent to the superconducting magnet coils.

The number of simulated photo-disintegration protons identified in CLAS (the numerator of Eq. 3.20) by the particle ID is sensitive to the quality of momentum reconstruction. In order to discard protons whose momentum is not correctly reconstructed, the differences between the angles of generated and reconstructed protons

$$\Delta\theta = \theta_p^{\text{GEN}}(P_p^{\text{LAB}}) - \theta_p^{\text{REC}}(P_p^{\text{LAB}}), \quad \Delta\phi = \phi_p^{\text{GEN}}(P_p^{\text{LAB}}) - \phi_p^{\text{REC}}(P_p^{\text{LAB}}) \quad (3.21)$$

have been obtained and the standard deviations $\sigma_{\Delta\theta}$ and $\sigma_{\Delta\phi}$ of the distributions have been calculated from a Gaussian fit.

The momentum dependence of $\sigma_{\Delta\theta}$ and $\sigma_{\Delta\phi}$ has been fitted using a polynomial function in the range ($0.5 \leq P_p^{\text{LAB}} \leq 3.2$) GeV to obtain a variable cut used to discard reconstructed protons having polar and azimuthal angles differences outside the $(-3\sigma, 3\sigma)$ interval, for θ and ϕ separately.

The result of the GSim evaluation of the proton detection efficiency in CLAS is shown in Fig. 3.28 as a function of the CLAS azimuthal angle ϕ , for $P_p^{\text{LAB}}=0.95$ GeV and $\theta_p^{\text{LAB}} = 45^\circ$. Each CLAS sector has a ϕ extension of 60° and it is sampled with a ϕ binning of 5° using the procedure described above. From Fig. 3.28 it is clear that the proton detection efficiency is almost constant (with an average value around 95%) in the central regions of each CLAS sector while it drops vertically near the sector borders.

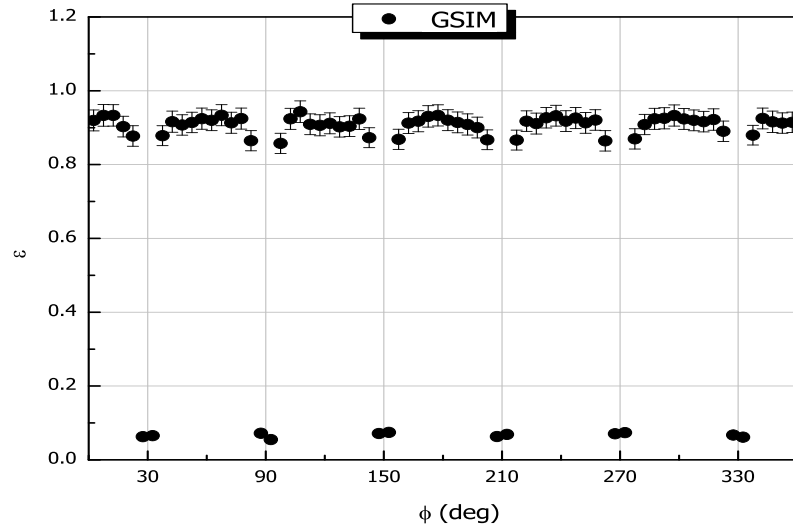


Figure 3.28: The CLAS proton detection efficiency evaluated using GSim as a function of the azimuthal angle ϕ for $P_p^{\text{LAB}}=0.95$ GeV, $\theta_p^{\text{LAB}} = 45^\circ$, and with a ϕ binning of 5° . The shapes of the six CLAS sectors are reflected by the behavior of the proton detection efficiency and are clearly identified by the sudden decrease of the efficiency near the sector borders.

The overall behavior of the proton detection efficiency as obtained from the GSim evaluation is shown in the contour plot of Fig. 3.29 as a function of the generated proton azimuthal and polar angles (running on the abscissa and on the ordinates, respectively) for a momentum $P_p^{\text{LAB}}=0.95$ GeV. The quota represent the proton

detection efficiency values and are shown in different colors/grays according to the scale indicated on the right side of the plot. The CLAS sectors are numbered in the plot from left to right and in each sector, a region of practically constant high efficiency (close to 95%) is clearly identified. The vertical low efficiency zones among sectors correspond to the decrease due to the presence of the torus magnet coils. The horizontal gaps in the efficiency function (along θ) correspond to out of work time-of-flight paddles or drift chambers wires introduced in the simulation by the GPP tool.

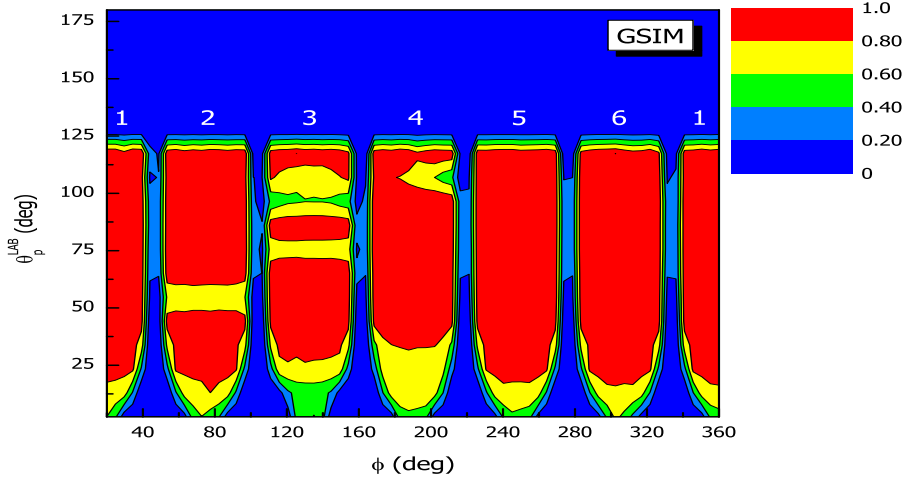


Figure 3.29: Behavior of the proton detection efficiency obtained from GSim shown as a function of the azimuthal and polar angles (on the abscissa and on the ordinates, respectively) of the generated protons for $P_p^{\text{LAB}}=0.95$ GeV. The quota represent the proton detection efficiency values and are shown in different colors/grays according to the scale indicated on the right side of the plot. The CLAS sectors are numbered from left to right. In each sector, a region of practically constant high efficiency (close to 95%) is clearly identified. The vertical low efficiency zones among sectors correspond the torus magnet coils. The horizontal gaps in the efficiency function (along θ) correspond to to out of work time-of-flight paddles or drift chambers wires taken into account in the simulation using the GPP tool.

3.8.4 Check of the GSim Evaluation Results

The proton detection efficiency in CLAS can also be measured from the g2 data using the $\gamma d \rightarrow p\pi^- p$ reaction. The definition of the efficiency in this case is different from the one given in Eq. 3.20 for the simulated events since the data does not convey any information on the “generated” particles. For this reason, the correct definition for the proton detection efficiency in CLAS in this case is the following:

$$\epsilon_{\text{DATA}} = \frac{N_{\gamma d \rightarrow p\pi^- p}^{\text{PID}}(\Delta P_p^{\text{LAB}}, \Delta \theta_p^{\text{LAB}}, \Delta \phi)}{N_{\gamma d \rightarrow p\pi^- X(p)}^{\text{MM}}(\Delta P_p^{\text{LAB}}, \Delta \theta_p^{\text{LAB}}, \Delta \phi) - K(\Delta P_p^{\text{LAB}}, \Delta \theta_p^{\text{LAB}}, \Delta \phi)} \cdot \quad (3.22)$$

The quantity $N_{\gamma d \rightarrow p\pi^- X(p)}^{\text{MM}}$ in Eq. 3.22 represents the number of protons identified

searching for a π^-p pair from the particle ID and then calculating the event missing mass according to the relation $X^2(p) = (P_\gamma + P_d - P_p - P_{\pi^-})^2$, where $P_{i=\gamma,d,p,\pi^-}$ indicates the particles 4-momenta.

On the contrary, $N_{\gamma d \rightarrow p \pi^- p}^{\text{PID}}$ is the number of $p\pi^-p$ events identified directly by the particle ID. Clearly, in this last case, the particle ID identifies both protons, and there is no reason to count one proton as “missing” and the other as “identified” so the calculation is repeated exchanging the proton labels.

The momenta of the identified particles in the final state have been compensated for the energy loss into the liquid D₂ target and the start counter scintillators but no momentum corrections such those described in Sec. 3.7 have been applied in this case.

The bins of the kinematic variables $(\Delta P_p^{\text{LAB}}, \Delta \theta_p^{\text{LAB}}, \Delta \phi)$ in Eq. 3.22 are always referred to the “missing” proton. The binning in proton momentum and scattering angle is identical to the one used in the simulation case. A different choice is done for the binning in the azimuthal angle ϕ chosen to be $\Delta \phi = 10^\circ$ since the proton detection efficiency in CLAS measured from the $\gamma d \rightarrow p\pi^-p$ reaction is mainly used to validate the simulation result and a full investigation of the CLAS proton detection capability in the ϕ coordinate is not necessary in this case.

Counting the number of protons identified by the event $\gamma d \rightarrow p\pi^-X$ (the first term in the denominator of Eq. 3.22) requires the knowledge of the event missing mass distributions in each bin of proton momentum and angles. These distributions have been calculated and fitted using a Gaussian curve and a straight line to identify the peak position (corresponding to the proton rest mass) and the background contribution K (second term in the denominator of Eq. 3.22) as:

$$K(\Delta P_p^{\text{LAB}}, \Delta \theta_p^{\text{LAB}}, \Delta \phi) = \int_{-3\sigma}^{3\sigma} (p_4 + p_5 M) dM \quad (3.23)$$

where the fit parameters p_4, p_5 identify the straight line and $\sigma = p_3$ represents standard deviation of the Gaussian fitting function. In order to count the number of protons associated with the exclusive event $\gamma d \rightarrow p\pi^-X(p)$ a $(-3\sigma, 3\sigma)$ cut around the peak of the missing mass distribution is applied.

Examples of the obtained $\gamma d \rightarrow p\pi^-X$ missing mass distributions are shown in Fig. 3.30 for an intermediate proton momentum $P_p^{\text{LAB}} = 0.95$ GeV, an azimuthal angle $\phi = 10^\circ$, and for three different proton scattering angles θ_p^{LAB} : 10° (top plot), 40° (middle plot), and 70° (bottom plot). The shape of the distributions is well reproduced by the Gaussian plus linear fitting function calculated in the interval $(0.6 - 1.05)$ GeV.

As in the reconstruction of the simulated proton tracks, the momentum determination is worse at the border of the six CLAS sectors since these regions are closer to the torus magnet coils. In order to discard protons which momentum is not correctly reconstructed, the differences between the angles of “identified” and “missing” protons

$$\Delta \theta = \theta_p^{\text{MM}}(P_p^{\text{LAB}}) - \theta_p^{\text{PID}}(P_p^{\text{LAB}}), \quad \Delta \phi = \phi_p^{\text{MM}}(P_p^{\text{LAB}}) - \phi_p^{\text{PID}}(P_p^{\text{LAB}}) \quad (3.24)$$

have been obtained and the standard deviations $\sigma_{\Delta \theta}$ and $\sigma_{\Delta \phi}$ of the distributions have been calculated from a Gaussian fit.

The momentum dependence of $\sigma_{\Delta \theta}$ and $\sigma_{\Delta \phi}$ has been calculated using a polynomial fit in the range $(0.4 \leq P_p^{\text{LAB}} \leq 2.3)$ GeV to obtain a variable cut used to

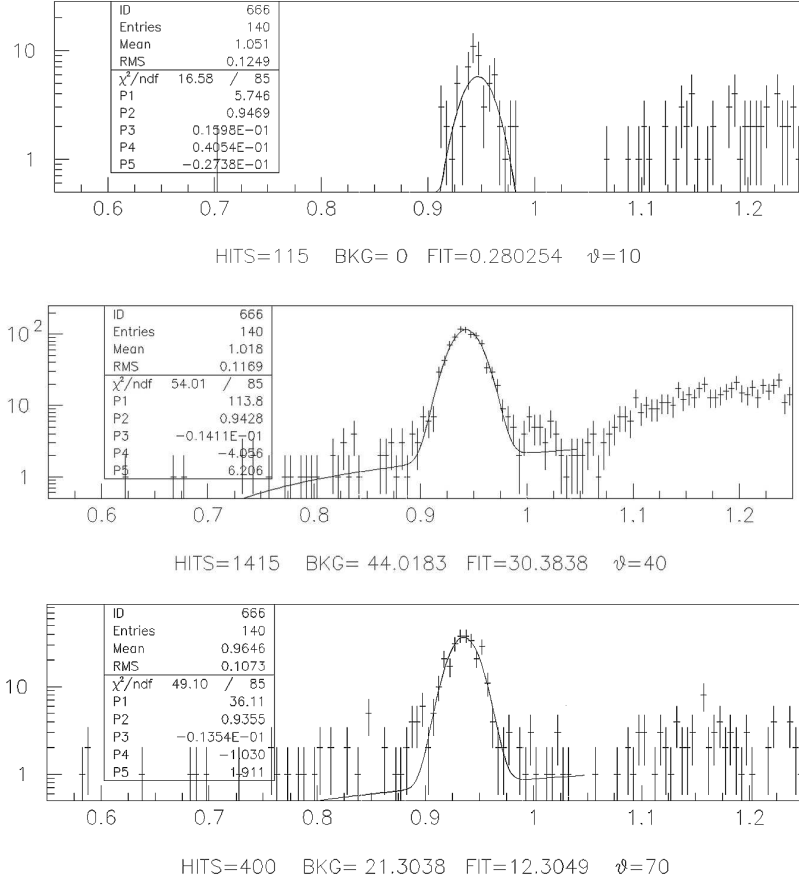


Figure 3.30: Missing mass distribution for the event $\gamma d \rightarrow p\pi^- X$ at an intermediate proton momentum $P_p^{\text{LAB}} = 0.95$ GeV, an azimuthal angle $\phi = 10^\circ$ (corresponding to the center of sector 1), and for three different proton scattering angles θ_p^{LAB} : 10° (top), 40° (middle), and 70° (bottom). The curves superimposed to the plots are Gaussian plus straight line fitting functions calculated in the interval (0.6 – 1.05) GeV. The background contamination is evaluated according to Eq. 3.23.

discard reconstructed protons having polar and azimuthal angles differences outside the $(-3\sigma, 3\sigma)$ interval, for θ and ϕ separately.

An example of the proton detection efficiency in CLAS measured from the $\gamma d \rightarrow p\pi^-p$ reaction is shown in Fig. 3.31 at the intermediate proton momentum $P_p^{\text{LAB}}=0.95$ GeV and $\theta_p^{\text{LAB}} = 45^\circ$. The black/full dots represent the GSim result for the proton detection efficiency while the red/open dots are the current result from the $\gamma d \rightarrow p\pi^-p$ data. As can be seen, the resulting efficiency values are in good agreement. It should be noted the different ϕ binning. The datum corresponding to a sector border azimuthal angle ϕ_B obtained from $\gamma d \rightarrow p\pi^-p$ data is roughly the average of the GSim results obtained at $\phi_B - 5^\circ$ and $\phi_B + 5^\circ$. The comparison between

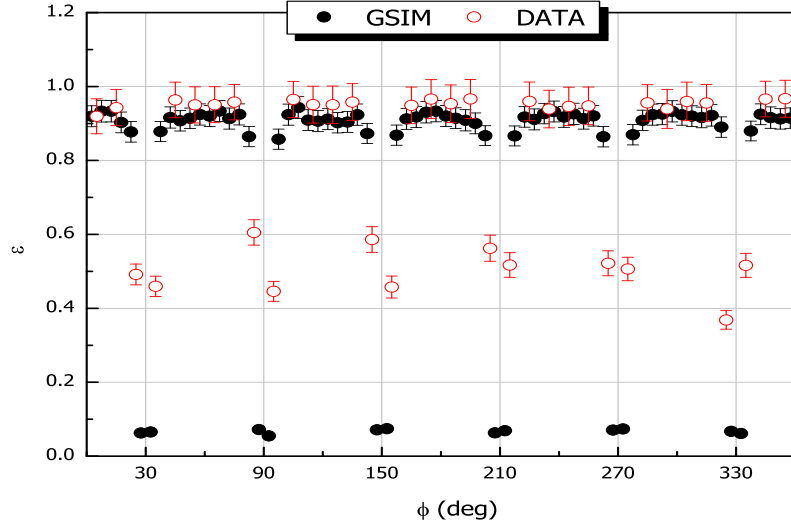


Figure 3.31: CLAS proton detection efficiency in CLAS evaluated from GSim (black/full dots) compared with the results measured from the $\gamma d \rightarrow p\pi^-p$ reaction (red/open dots) for $P_p^{\text{LAB}}=0.95$ GeV and $\theta_p^{\text{LAB}} = 45^\circ$. The resulting values for the proton detection efficiency are in good agreement. Note the different ϕ binning. The datum corresponding to a sector border azimuthal angle ϕ_B obtained from the $\gamma d \rightarrow p\pi^-p$ data is roughly the average of the GSim results at $\phi_B - 5^\circ$ and $\phi_B + 5^\circ$.

the results obtained using the two methods cannot be extended to all the momentum bins covered by the simulated $\gamma d \rightarrow pn$ events since the phase space available to the $\gamma d \rightarrow p\pi^-p$ reaction is smaller compared to the photo-disintegration case. This is clearly seen in Fig. 3.32 where the proton detection efficiency, measured from the $\gamma d \rightarrow p\pi^-p$ reaction, is shown as a function of the proton azimuthal and polar angles (on the abscissa and on the ordinates, respectively) for $P_p^{\text{LAB}}=0.95$ GeV. The comparison of this result with Fig. 3.29, evidently shows that in this case the proton is detected only up to $\theta_p^{\text{LAB}} = 90^\circ$ while in the photo-disintegration case, the angular coverage extends up to $\theta_p^{\text{LAB}} = 125^\circ$, for this value of proton momentum. The quota represent the values of the proton detection efficiency in different colors/grays according to the scale indicated on the right side of the plot. The CLAS sectors are numbered from left to right. The regions of constant high efficiency (close to 95%)

can be clearly identified. Note that the sampling rate $\Delta\phi = 10^\circ$ yields a lower resolution with respect to the GSim result (Fig. 3.29). The vertical low efficiency regions among sectors are due to the presence of the torus magnet coils. The horizontal gaps in the efficiency function (along θ) correspond to out of work time-of-flight paddles and drift chambers wires.

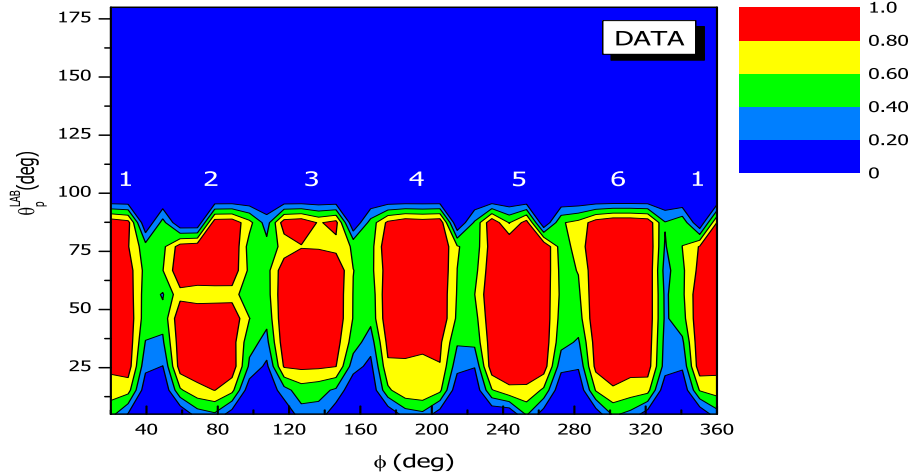


Figure 3.32: Proton detection efficiency in CLAS measured from the $\gamma d \rightarrow p\pi^-p$ reaction shown as a function of the proton azimuthal and polar angles for $P_p^{\text{LAB}}=0.95$ GeV. The quota represent the values of the proton detection efficiency in different colors/grays according to the scale indicated on the right side of the plot. The CLAS sectors are again numbered from left to right. The regions of constant high efficiency (close to 95%) can be clearly identified, even if the sampling rate $\Delta\phi = 10^\circ$ corresponds to a lower resolution. The vertical low efficiency regions among sectors are due to the presence the CLAS torus magnet coils. The horizontal gaps in the efficiency function (along θ) correspond to to out of work time-of-flight paddles and drift-chamber wires.

The result on the proton detection efficiency in CLAS measured from the $\gamma d \rightarrow p\pi^-p$ data is used, in the present analysis, to validate the GSim result in the appropriate kinematic range. In fact, the limitation in phase space coverage does not allow a full comparison between the final results nor the usage of the proton detection efficiency measured from the $\gamma d \rightarrow p\pi^-p$ data in the calculation the final photo-disintegration cross section.

The information obtained from the $\gamma d \rightarrow p\pi^-p$ data is used to define the final timing and spatial resolutions smearing factors to be introduced in the simulation in order to match the characteristics of the simulated detector with those of the real apparatus. The comparison is done iteratively, running partial reconstructions on the simulated files until the required resolution smearing factors are determined.

After this procedure, spatial and timing resolutions smearing factors equal to 1 have been applied to the simulation results for all proton scattering angles. An exception is done for very forward proton scattering angles $8^\circ \leq \theta_p^{\text{LAB}} \leq 10^\circ$, where a spatial resolution smearing factor equal to 2 has been used.

A final comparison between the results obtained from the GSim evaluation of the proton detection efficiency using the $\gamma d \rightarrow pn$ reaction (black/full dots) and the measurement from the data using the $\gamma d \rightarrow p\pi^-p$ reaction (red/empty dots) is shown Fig. 3.33 separately for the six CLAS sectors. The points represent the weighted averages of the proton detection efficiency in CLAS over proton momenta in the interval (0.5 – 1.0) GeV for the sectors central region (defined by the interval $\Delta\phi = \pm 10^\circ$ assuming the sector azimuthal between $(-30^\circ, 30^\circ)$) and are shown as a function of the proton scattering angle θ_p^{LAB} . It is clearly seen how the GSim result is well matched by the $\gamma d \rightarrow p\pi^-p$ result. In addition, the actual detector status is well reproduced by the simulations: this is shown by the dips in the proton detection efficiency found for the same scattering angle θ_p^{LAB} in both results (see, for instance, sector 3 for $\theta_p^{\text{LAB}} = 75^\circ$ and 95°).

In order to evaluate the uniformity between the two results, the distribution for the values of ratio $R = \frac{\epsilon_{\text{DATA}}}{\epsilon_{\text{GSIM}}}$ (defined only for the kinematic bins ΔP_p^{LAB} and $\Delta\theta_p^{\text{LAB}}$ populated by both kind of data) between the efficiency calculated with the two techniques is shown in Fig. 3.34 for proton momenta in the range (0.5 – 1.0) GeV. As can be seen from the legend, the mean value of the distribution is of the order of the unity while the spread is about 8%. The best agreement between the simulation and data is found for sector 6. This finding can be used to properly normalize cross section data from other sectors.

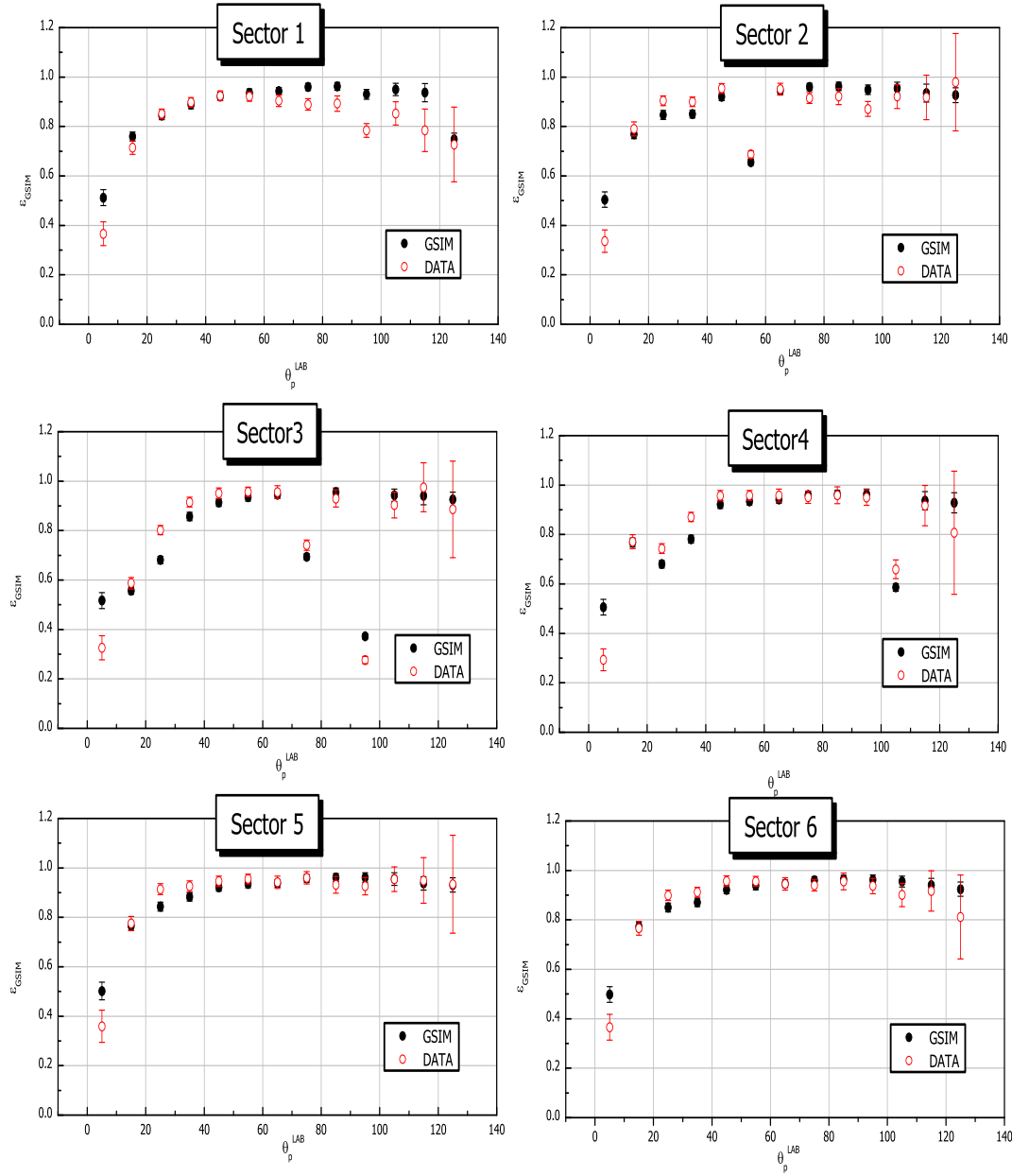


Figure 3.33: Final comparison between the results obtained from the GSiM evaluation of the proton detection efficiency using the $\gamma d \rightarrow pn$ reaction (black/full dots) and the measurement from the data using the $\gamma d \rightarrow p\pi^-p$ reaction (red/empty dots). The points represent the weighted averages of the detection efficiency over proton momenta in the interval $(0.5 - 1.0)$ GeV for the sectors central region (defined by the interval $\Delta\phi = \pm 10^\circ$ assuming the sector azimuthal angle between $(-30^\circ, 30^\circ)$) and are shown as a function of the proton scattering angle θ_p^{LAB} . It is clearly seen that the GSiM result is well matched by the $\gamma d \rightarrow p\pi^-p$ result. In addition, the actual detector status is well reproduced by the simulations: this is shown by the dips in the proton detection efficiency found at the same scattering angle θ_p^{LAB} in both results.

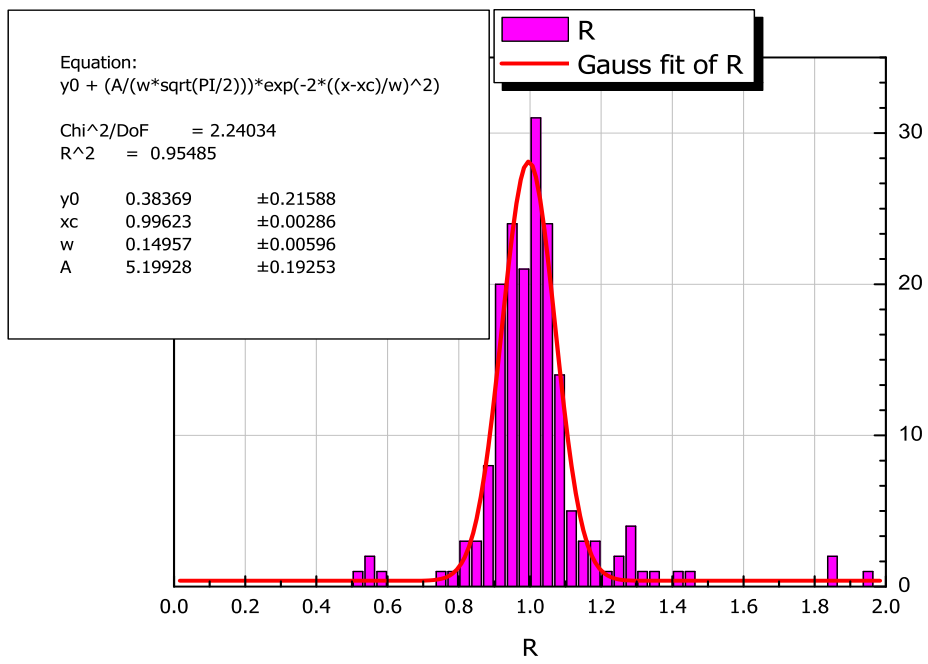


Figure 3.34: Distribution of the ratio $R = \frac{\epsilon_{DATA}}{\epsilon_{GSIM}}$ between the proton detection efficiency measured from $\gamma d \rightarrow p\pi^-p$ and simulated from $\gamma d \rightarrow pn$ (defined only in the kinematic bins ΔP_p^{LAB} and $\Delta\theta_p^{LAB}$ populated by both kind of data) for the sectors central region (defined by the interval $\Delta\phi = \pm 10^\circ$ assuming the sector azimuthal angle between $(-30^\circ, 30^\circ)$). The parameters representing the Gaussian fit are shown in the legend. It can be seen that the mean value of the distribution is of the order of the unity while the spread is about 8%.

3.8.5 Fiducial Cuts and Detector Acceptance

The information obtained from the simulated $\gamma d \rightarrow pn$ reaction in CLAS allows the determination of the so-called “fiducial” regions in the azimuthal angle ϕ . In fact, a fiducial region can be defined, for each sector S and each bin of proton momentum ΔP_p^{LAB} and scattering angle $\Delta\theta_p^{\text{LAB}}$, as the ϕ section of the CLAS detector characterized by a constant efficiency.

The procedure used to identify the fiducial regions requires the calculation of a reference value for the proton detection efficiency (indicated as ϵ_0) in each CLAS sector and for each bin of proton momentum and scattering angle. This reference value is obtained averaging the contributions of the most central regions of each sector. The corresponding indetermination associated to ϵ_0 is indicated by $\delta\epsilon_0$.

Then, in each CLAS sector (for each bin of proton momentum and scattering angle) the proton detection efficiency, ϵ_i , in the remaining i^{th} ϕ -bin on the left and on the right of the central region is investigated and the values of ϵ_i whose error bars $\delta\epsilon_i$ do not overlap with the band defined by the relation $\epsilon_0 \pm \delta\epsilon_0$ are rejected.

An example of this procedure is shown in Fig. 3.35 for sector 2, for a proton momentum $P_p^{\text{LAB}}=1.15$ GeV and the scattering angles $\theta_p^{\text{LAB}} = 15^\circ$ (top plot) and $\theta_p^{\text{LAB}} = 65^\circ$ (bottom plot).

The horizontal shaded area corresponds to the allowed variation band $\epsilon_0 \pm \delta\epsilon_0$ while the vertical lines mark the boundaries used to exclude efficiency data considered out from the allowed variation band according to the criterion outlined above. It can be seen that the procedure retains only the contributions from to the ϕ region where the efficiency behavior is constant.

An example of the resulting fiducial cuts in the CLAS sector 2 for $P_p^{\text{LAB}}=1.15$ GeV is shown in the contour plot of Fig. 3.36. The boundaries of the fiducial ϕ regions (along the abscissa) are shown for each proton scattering angle (along the ordinates). The mean values of the efficiency within the region are indicated by the color/gray code. The dip found at $\theta_p^{\text{LAB}} = 55^\circ$ is due to an out of work time-of-flight paddle, as shown also in Fig. 3.33

The procedure outlined above is applied in each CLAS sector and for each bin of proton momentum and scattering angle in order to derive the full set of fiducial cuts. This is needed to properly weight the number of photo-disintegration events entering in the final differential cross section calculation since it will be expressed as a function of the outgoing proton momentum, scattering angle, and sector.

For this reason, the ϕ information contained in the original proton detection efficiency ϵ_{GSIM} must be averaged over the CLAS sectors fiducial regions so to obtain the sector-based efficiency-acceptance function:

$$\eta_{\text{GSIM}}(\Delta P_p^{\text{LAB}}, \Delta\theta_p^{\text{LAB}}, S) = \frac{\sum_i w_i \epsilon_{\text{GSIM}}(\Delta P_p^{\text{LAB}}, \Delta\theta_p^{\text{LAB}}, \Delta\phi_i)}{\sum_i w_i} \quad (3.25)$$

where $1/w_i = (\delta\epsilon_{\text{GSIM}}(\Delta P_p^{\text{LAB}}, \Delta\theta_p^{\text{LAB}}, \Delta\phi_i))^2$ is the weight assigned to each datum from the original efficiency function, S stands for the CLAS sector, and the index i runs over the ϕ -bins of sector S for the given proton momentum and scattering angle.

The result of this calculation for the efficiency-acceptance function is shown in the contour plot of Fig. 3.37 for the six CLAS sectors. The abscissa report the proton momentum while the ordinates run on the proton scattering angle (both

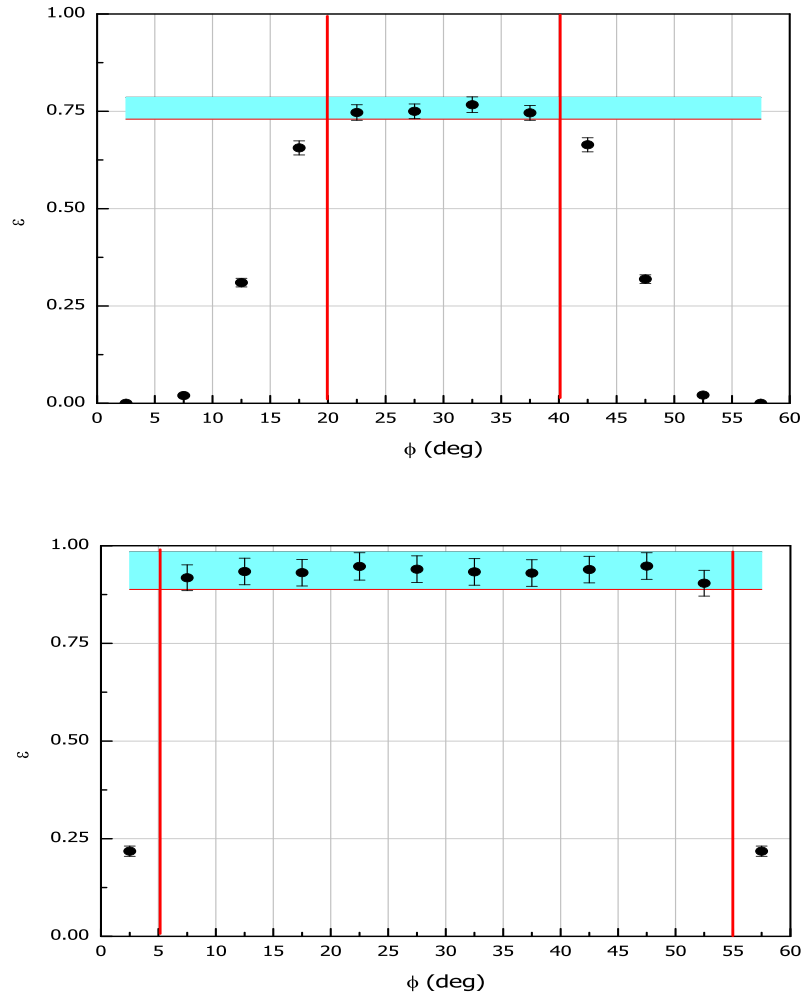


Figure 3.35: An example of fiducial cuts in CLAS sector 2 for $P_p^{\text{LAB}}=1.15$ GeV. Upper panel: for $\theta_p^{\text{LAB}} = 15^\circ$. Lower panel: for $\theta_p^{\text{LAB}} = 65^\circ$. The horizontal shaded area shows the allowed variation band $\epsilon_0 \pm \delta\epsilon_0$ while the vertical lines delimit the fiducial region according to the behavior of the proton detection efficiency as a function of the azimuthal angles ϕ .

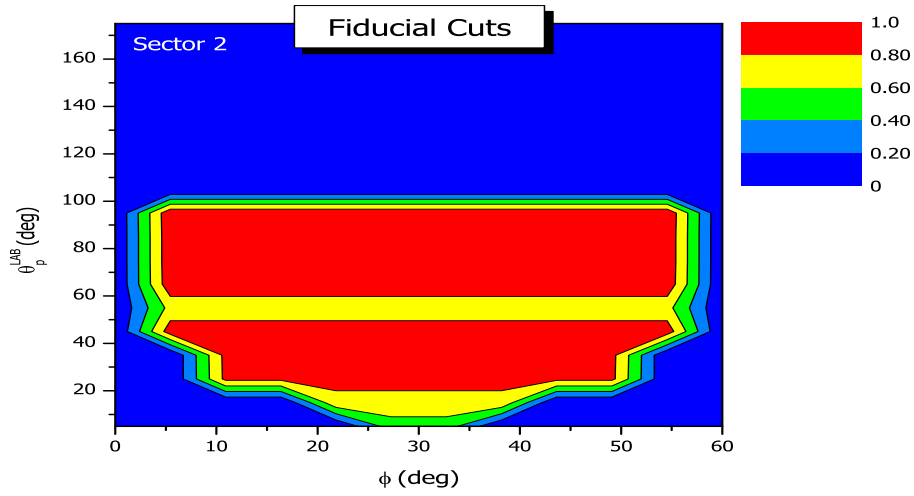


Figure 3.36: Fiducial cuts in the CLAS sector 2 for $P_p^{\text{LAB}}=1.15$ GeV. The boundaries of the fiducial ϕ regions (along the abscissa) in the sector are shown for each proton scattering angle (along the ordinates). The mean values of the efficiency within the region are indicated by the color/gray code shown in the legend. The dip found at $\theta_p^{\text{LAB}} = 55^\circ$ is due to an out of work time-of-flight paddle, as shown also in Fig. 3.33

considered in the LAB system). Quotas identify regions of constant values of the efficiency-acceptance functions (numeric values can be obtained from the color/gray scale shown on the left). As can be seen from Fig. 3.37 the behavior of the six CLAS sectors is pretty uniform, except for the holes introduced by out of work channels in some sectors.

CLAS efficiency-acceptance

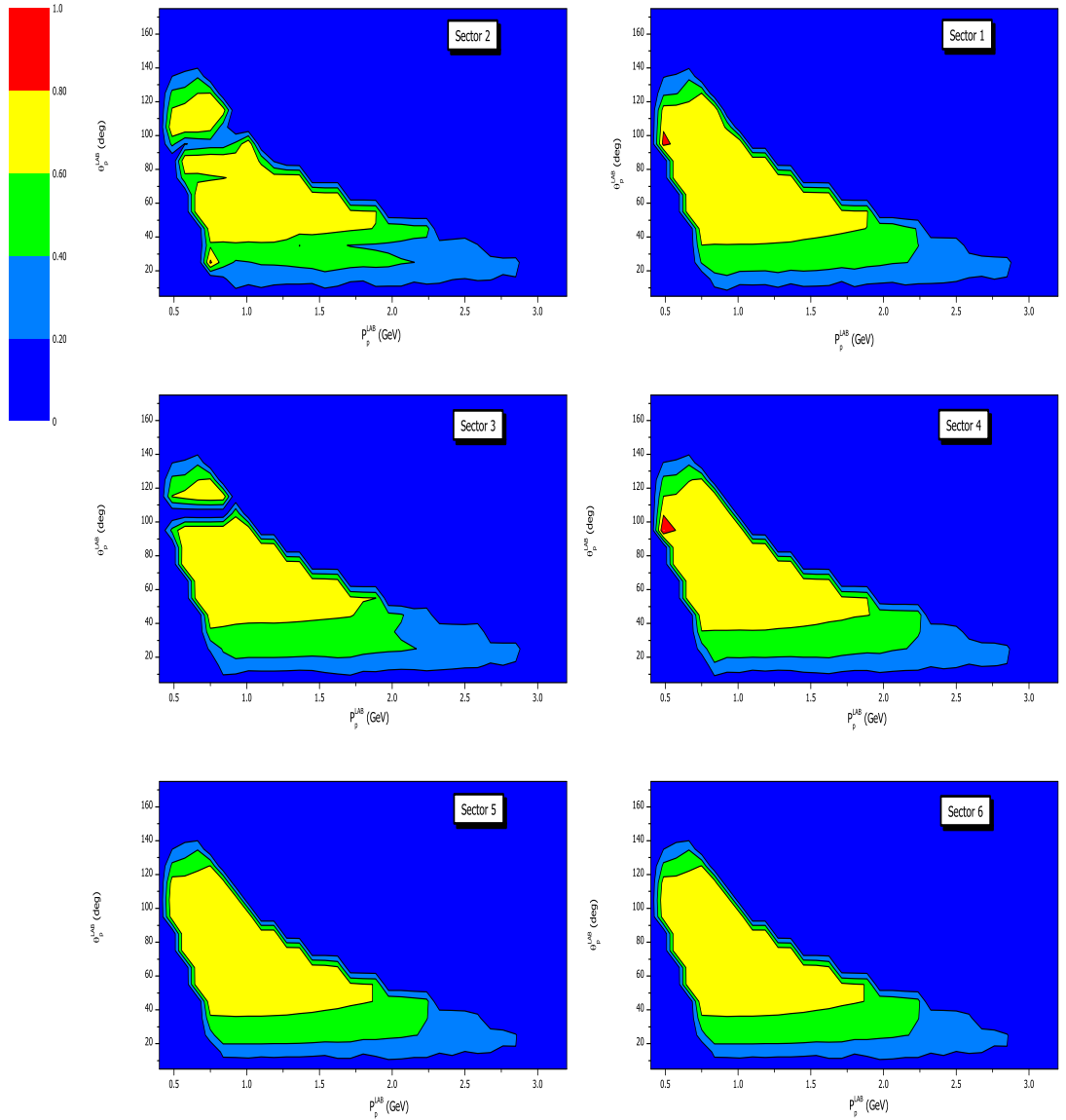


Figure 3.37: Result of the calculation of the efficiency-acceptance function for the six CLAS sectors. The abscissa report the proton momentum while the ordinates run on the proton scattering angle (both considered in the LAB system). Quotas identify regions of constant values of the efficiency-acceptance functions (numeric values can be obtained from the color/gray scale shown on the left). As can be seen from Fig. 3.37 the behavior of the six CLAS sectors is pretty uniform, except for the holes introduced by out of work channels in some sectors.

3.9 Background Subtraction

The determination of the number of “true” photo-disintegration events requires the knowledge of the contamination from background events. In fact, the missing mass distribution from $\gamma d \rightarrow pX$ events usually exhibits a peak in correspondence to the neutron rest mass value sitting over a continuous background mainly due to photo-production events originating from the target cell walls.

In the present analysis, the background contribution is evaluated from the data. Only the events detected in the fiducial regions of the CLAS, defined using the fiducial cuts obtained in the previous section, are taken into account. For each event, the missing mass is calculated and distributions are obtained for each bin of proton scattering angle θ_p^{CM} and incident photon energy E_γ .

Examples of the obtained missing mass distributions are shown in Fig. 3.38 for the six CLAS sectors, for the intermediate energy $E_\gamma=0.95$ GeV, and a forward scattering angle $\theta_p^{\text{CM}} = 15^\circ$: the peak corresponding to the neutron rest mass is clearly identified and each distribution is fitted with a Gaussian function plus exponential curve to take into account the continuous background.

At larger angles (for the same energy $E_\gamma=0.95$ GeV), the distribution are wider and the neutron signal is less pronounced, as shown in Fig. 3.39. Nevertheless, they are still well described by a Gaussian plus exponential function fit.

The contamination from background events under the missing mass distribution peak is calculated according to the relation:

$$k(\theta_p^{\text{CM}}, E_\gamma) = \frac{\int_{-3\sigma}^{3\sigma} e^{p_4+p_5M} dM}{N_{\text{peak}}} \quad (3.26)$$

where σ is the standard deviation of the Gaussian function, p_4 and p_5 are the parameters of the exponential function, and N_{peak} is the number of events under the $(-3\sigma, 3\sigma)$ interval around the peak position.

The behavior of the background contamination k as a function of the proton scattering angle is shown in Fig. 3.40 for the six CLAS sectors and for the intermediate incident photon energy $E_\gamma=0.95$ GeV. The contribution is around 5% and is relatively flat for scattering angles less than 90° . At larger angles the contamination is higher since the missing mass distributions get wider since the momentum resolution of the detector decreases.

A similar situation occurs at high incident energies (more than 2.1 GeV) where the background subtraction cannot be directly performed since the statistics is not enough to obtain a prominent neutron peak in the missing mass distributions. To overcome this limitation, the behavior of the background contamination has been studied as a function of the incoming photon energy and extrapolated up to 3 GeV using a linear fit. An example of the result is shown in Fig. 3.41 for the six CLAS sectors and for $\theta_p^{\text{CM}} = 35^\circ$. The last three data points, corresponding to the energy interval $1.8 \leq E_\gamma \leq 2.1$ GeV, are obtained averaging the contributions coming from all sectors since the statistics is not enough to have a clear neutron signal in the missing mass spectra, and are identical in the plots shown. It is clearly seen that the data are well reproduced using a linear fit.

At large proton scattering angles the background contamination k is larger but it can still be extrapolated using a linear fit of the available points. This can be seen from Fig. 3.42 for the six CLAS sectors and for $\theta_p^{\text{CM}} = 135^\circ$. In analogy to

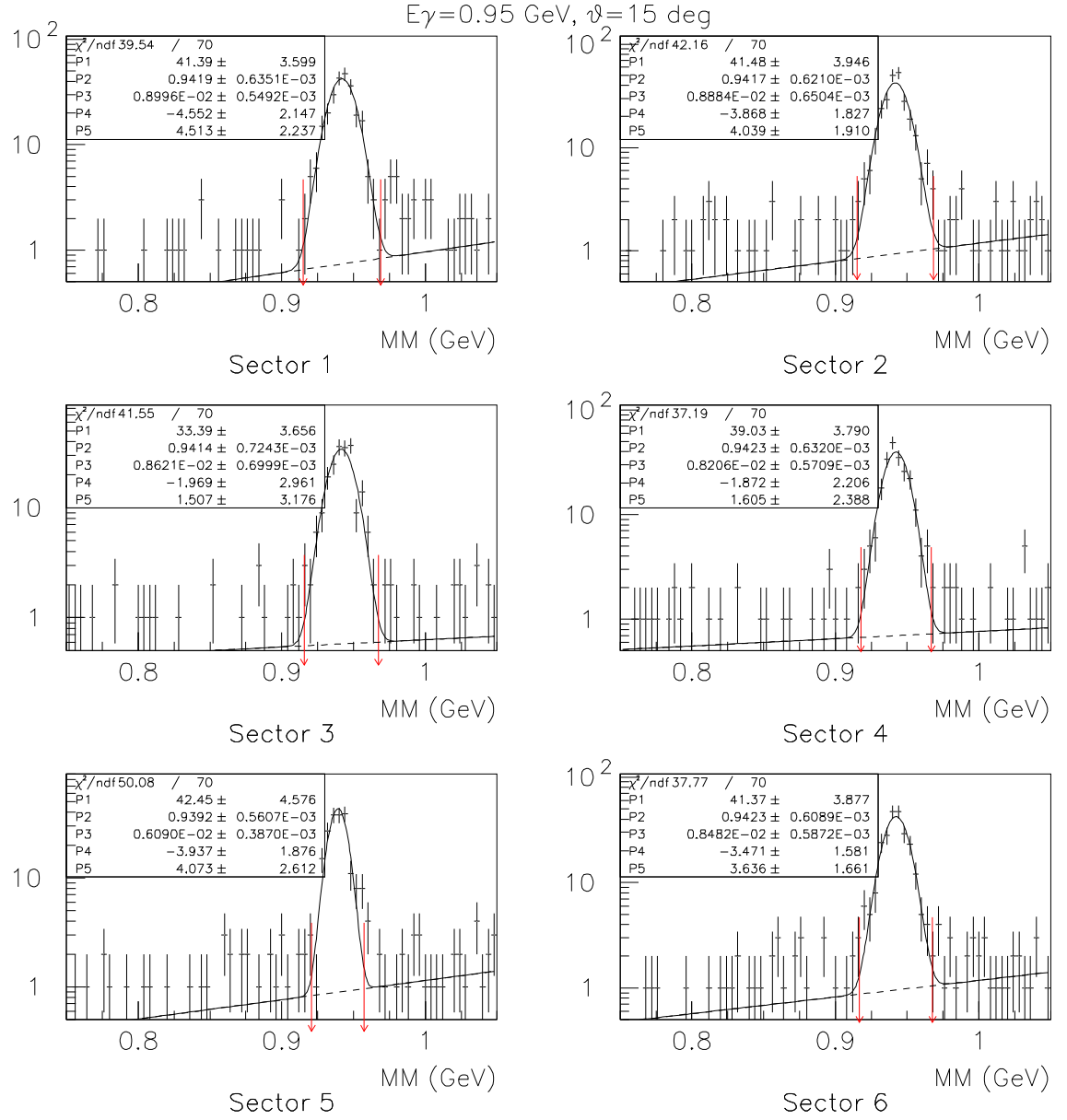


Figure 3.38: Missing mass distributions for the six CLAS sectors, for the intermediate energy $E_\gamma = 0.95 \text{ GeV}$, and a forward scattering angle $\theta_p^{\text{CM}} = 15^\circ$: the peak corresponding to the neutron rest mass is clearly identified. Each distribution is fitted with a Gaussian function plus exponential curve to take into account the continuous background. The red/dotted arrows identify a $(-3\sigma, 3\sigma)$ interval around the peak position, being σ the standard deviation of the Gaussian function.

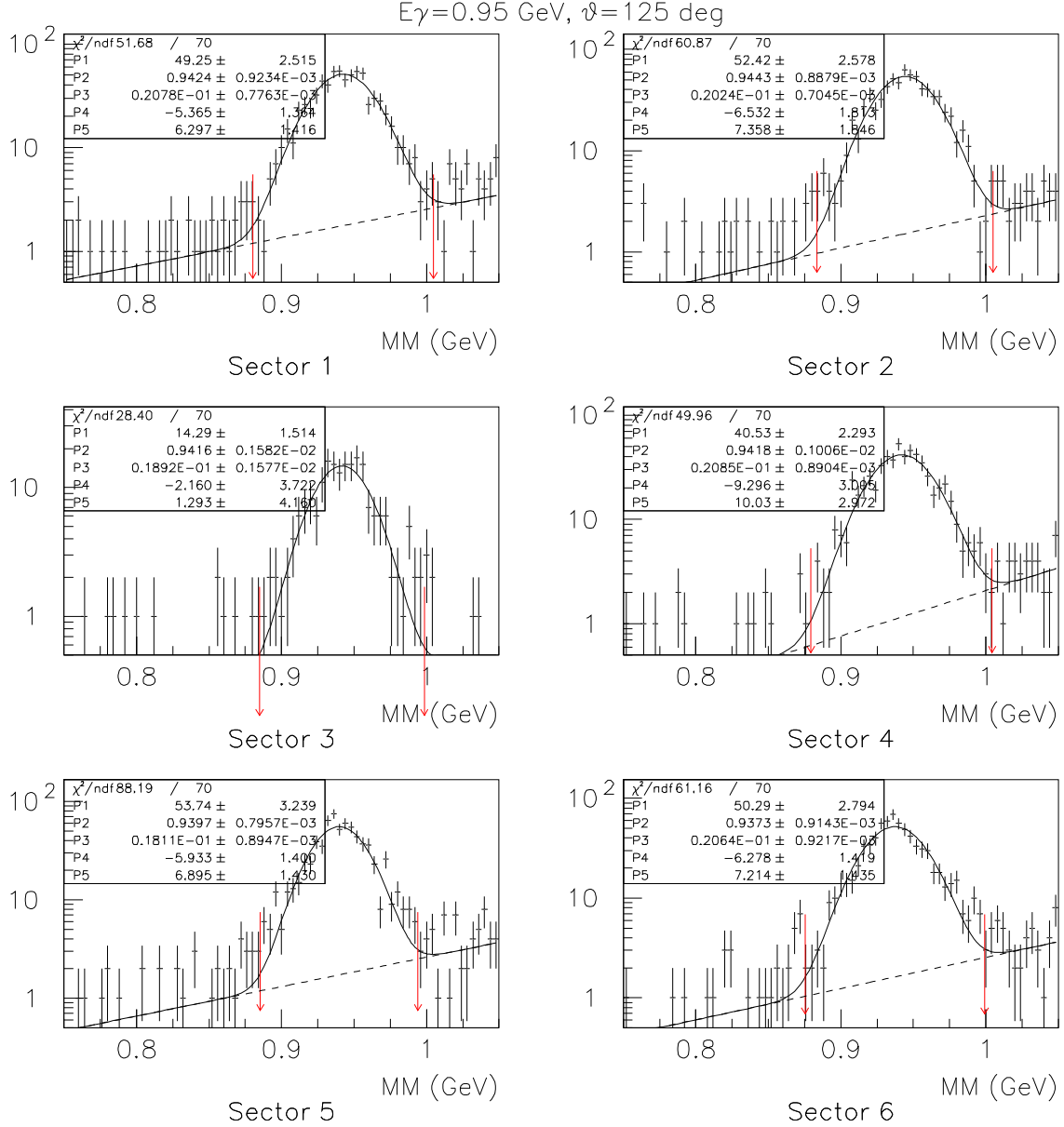


Figure 3.39: Missing mass distributions for the six CLAS sectors for $\theta_p^{\text{CM}} = 125^\circ$ and for an energy incident photon energy $E_\gamma = 0.95 \text{ GeV}$. The distributions are wider and the neutron signal is less pronounced since at backward scattering angles the resolution of the CLAS spectrometer is lower. Nevertheless, the missing mass distributions are still well described by a Gaussian plus exponential function fit. The red/dotted arrows identify a $(-3\sigma, 3\sigma)$ interval around the peak position, being σ the standard deviation of the Gaussian function.

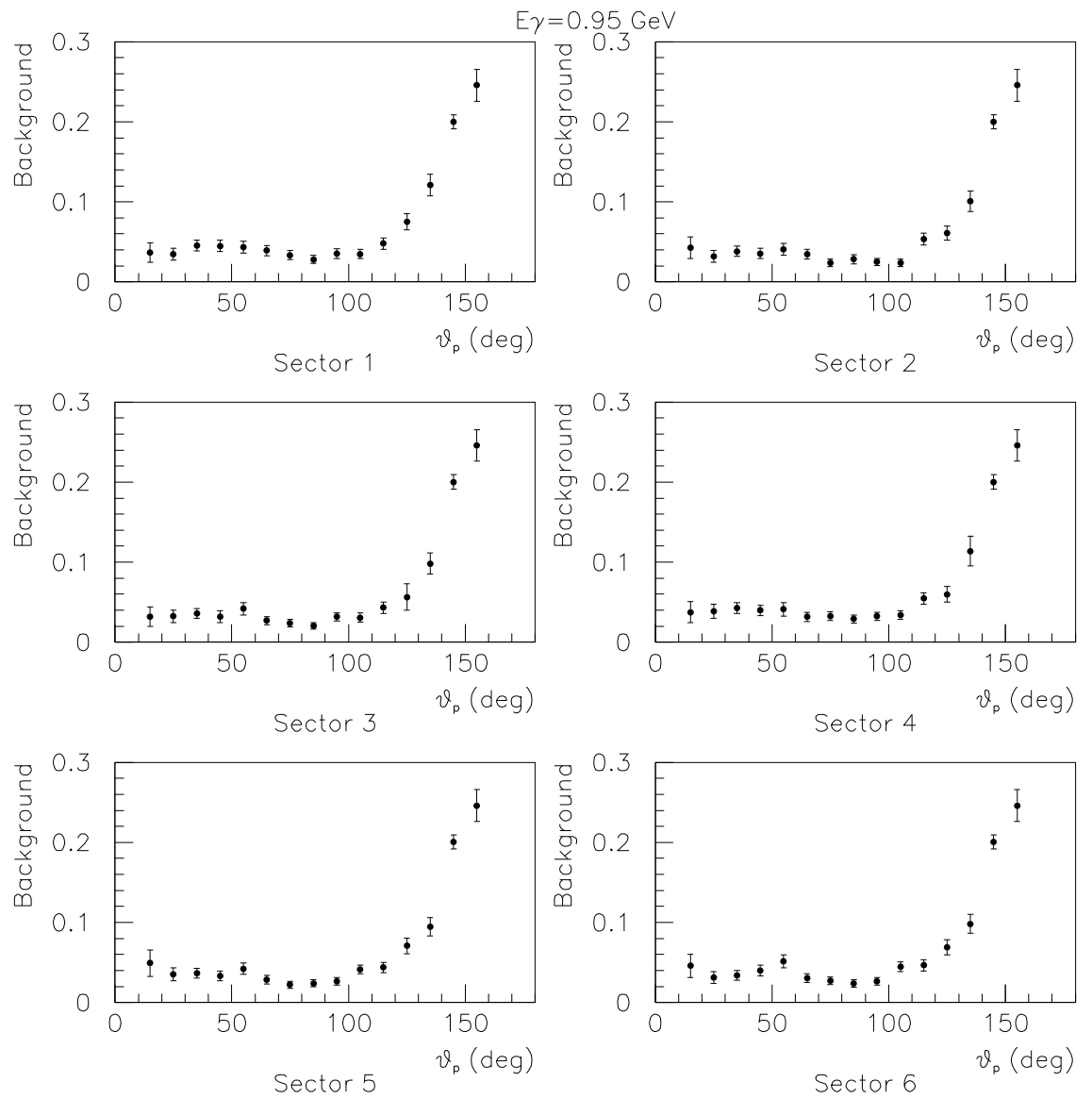


Figure 3.40: The behavior of the background contamination k as a function of the proton scattering angle for the six CLAS sectors and for the intermediate incident photon energy $E_\gamma = 0.95 \text{ GeV}$. The contribution is around 4% and is relatively flat for scattering angles less than 90° .

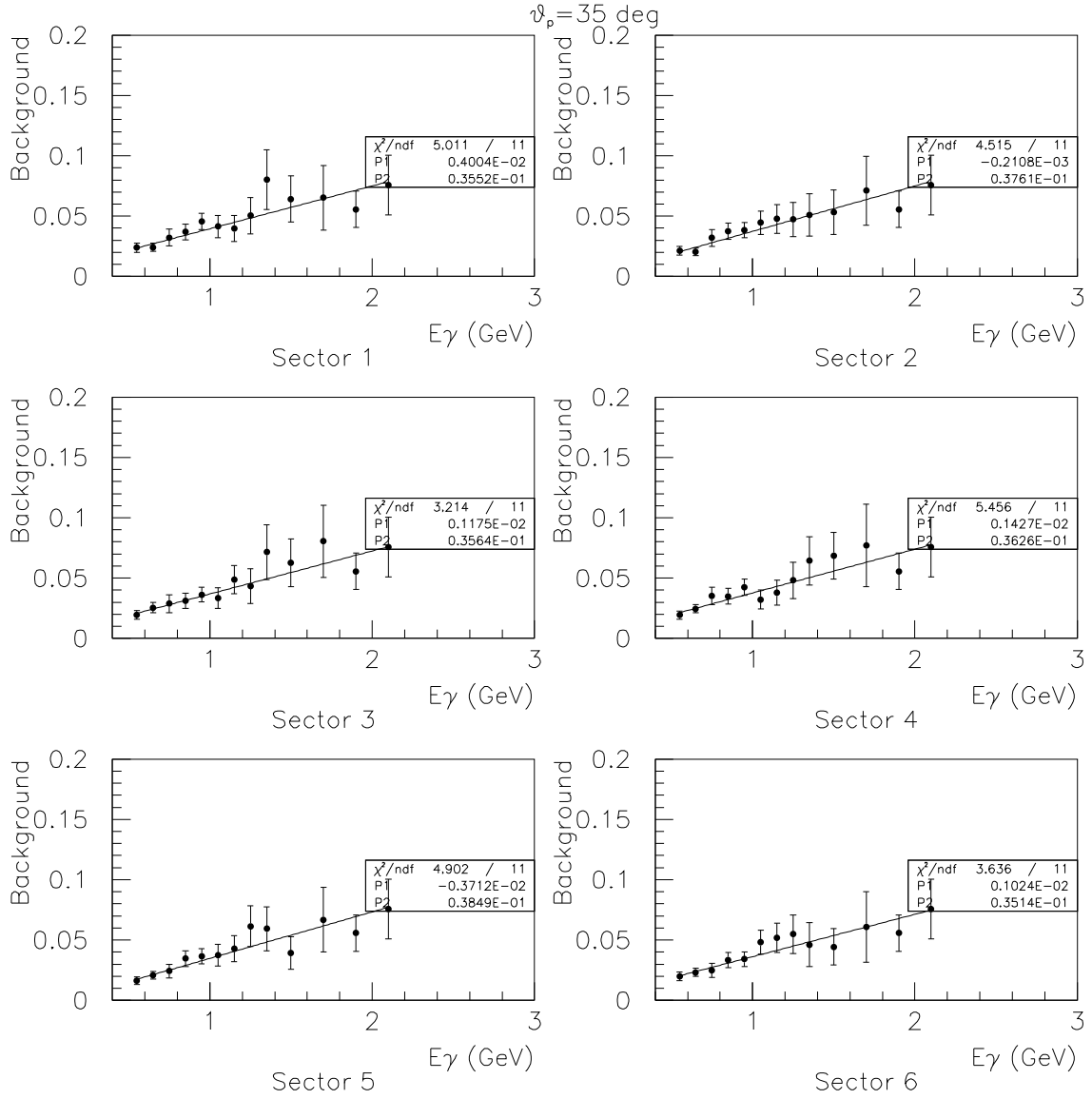


Figure 3.41: Behavior of the background contamination k as a function of the incoming photon energy for the six CLAS sectors and for $\theta_p^{\text{CM}} = 35^\circ$. The last three data points, corresponding to the energy interval $1.8 \leq E_\gamma \leq 2.1$ GeV, are obtained averaging the contributions from all sectors and are identical in the plots shown. It is clearly seen that the data are well reproduced using a linear fit.

the situation described in Fig. 3.41 the last three points are obtained averaging the contribution of all sectors.

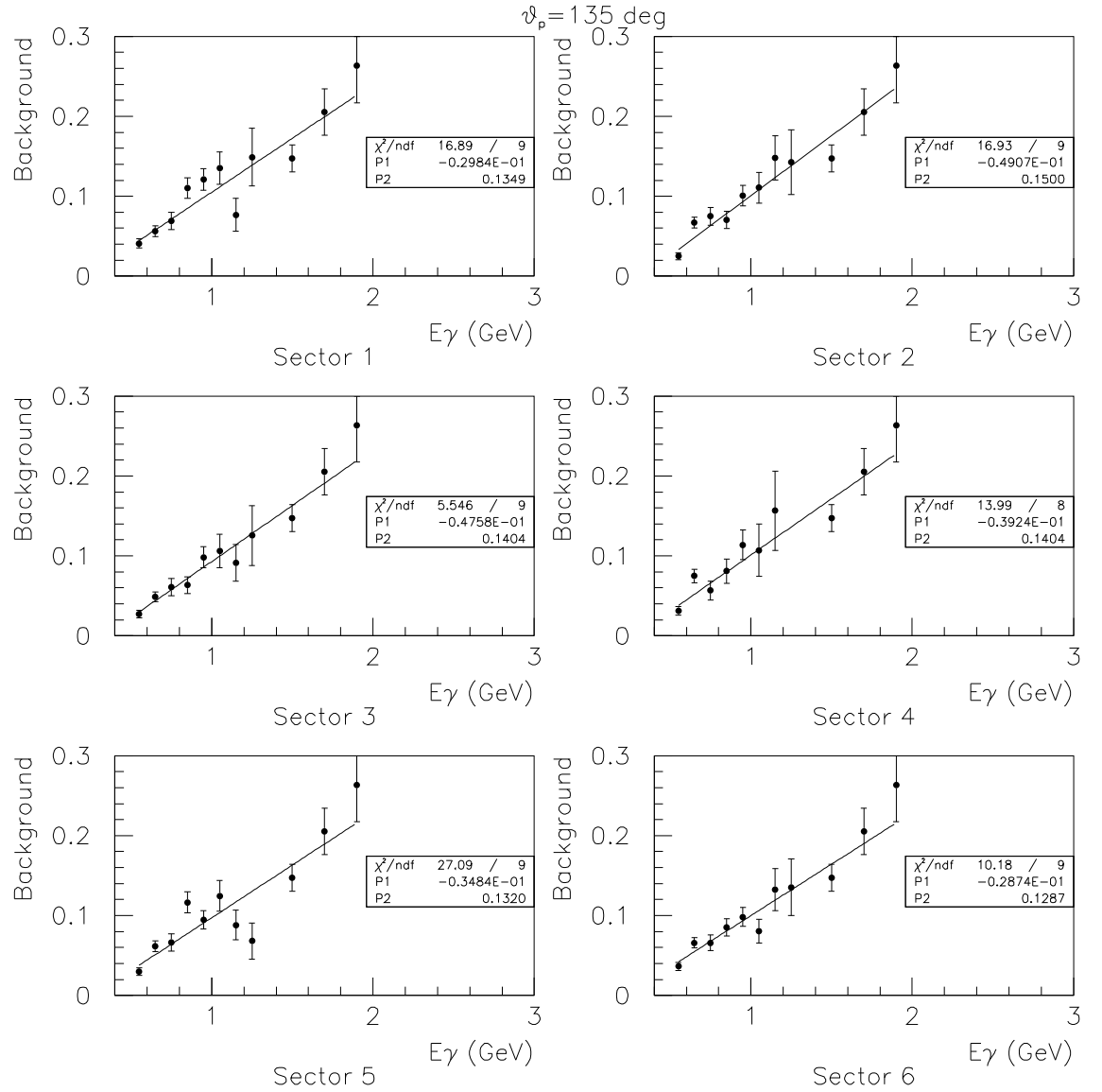


Figure 3.42: Behavior of the background contamination k as a function of the incoming photon energy for the six CLAS sectors and for $\theta_p^{\text{CM}} = 135^\circ$. The last three data points, corresponding to the energy interval $1.8 \leq E_\gamma \leq 2.1$ GeV, are obtained averaging the contributions from all sectors and are identical in the plots shown. At this proton scattering angles the background contribution is larger but it can still be extrapolated using a linear fit of the available points.

3.10 Evaluation of the Systematic Errors

Systematic errors may result from faulty calibration of the experimental equipment or from biased procedures used in the analysis of the data. These errors must be estimated from reconsidering the status of the experimental conditions and the techniques used to analyze the data.

In the present analysis, the main contributions to the overall systematic uncertainty come from the following procedures:

- determination of the number of incident photons;
- background subtraction;
- evaluation of the proton detection efficiency.

The evaluation of the systematic error on the photon flux normalization, is done using the information on the tagging efficiency as described in Sec. 3.5. As a consequence, it can be seen that the systematic uncertainties are estimated to be around 3 – 4%.

The background subtraction procedure introduces a systematic error of the order of 10% when repeated with different cuts while the proton detection efficiency in CLAS has been evaluated using two different techniques (as shown in Sec. 3.8).

The comparison between these results, in the full overlap of the kinematics of the two reactions introduces a systematic error of the order of 5%.

The different contributions are summarized in Tab. 3.5.

Procedure	systematic error
Photon flux normalization	3-4%
Background subtraction	8-10%
Proton detection efficiency	5-6%
Overall	10-12%

Table 3.5: Summary of the main contributions to the overall systematic uncertainty.

It should be underlined anyhow that a more accurate evaluation of the systematic uncertainties is still underway.

3.11 Summary

In this Chapter the various phases of the data analysis chain are fully described. First, the CLAS event format and the reconstruction procedure are introduced since these structures have been used to access and process the g2 data to perform all subsequent analysis.

Then, the data calibration procedure is briefly described followed by the definition of the photo-disintegration event. At this point, the photon flux normalization procedure has to be introduced since its needed to normalize the number of photo disintegration events used to calculate the final cross-section.

In order to obtain accurate results, data quality checks are performed using appropriate criteria and several corrections are introduced to improve the quality of the reconstruction.

The CLAS proton detection efficiency is evaluated both from a GEANT simulation of the detector and from the data itself in order to verify the consistency between the results. After this step, the fiducial regions of the detector are defined.

Then, the background contamination is evaluated from the data and the subtraction procedure is described.

Finally, an estimation of the overall systematic error has been given.

Chapter 4

Results

4.1 Introduction

This Chapter is devoted to the illustration of the final results on the deuteron photo-disintegration cross section obtained from the analysis of the full statistics of the data collected with the CLAS detector during the g2 data production period.

The CLAS data represent the first wide ranging survey of the deuteron photo-disintegration cross section in the few GeV region (0.55–3.0 GeV) of incident photon energy. The statistical uncertainties are of the order of 2 ÷ 5% below 1.5 GeV, and of the order of 10% for E_γ around 2.5 GeV.

The CLAS experimental results are discussed and compared to the published data. They give for the first time the possibility to study the photo-disintegration cross section as a function of the incident photon energy over the full range of proton scattering angles, thus expanding the view limited to four scattering angles ($\theta_p^{\text{CM}} = 36^\circ, 52^\circ, 69^\circ, \text{ and } 89^\circ$) investigated in the past years (as discussed in the first Chapter of the present thesis).

Then, the angular distributions of the cross sections, integrated over the CLAS azimuthal coordinate, are shown for incident photon energies from 0.5 to 3.0 GeV in 100 MeV bins. These data provide for the first time, the cross section at very forward ($\theta_p^{\text{CM}} = 15^\circ$) and backward proton scattering angles ($\theta_p^{\text{CM}} = 155^\circ$) allowing to test the available theoretical predictions in regions where the cross section behavior becomes steeper.

In addition, both the new CLAS results and the published angular distributions are compared to the non perturbative calculation of the Quark Gluon String Model (QGSM) since, as shown in the first Chapter of this thesis, this model describes rather well the data.

4.2 The Differential Cross Section

The photo-disintegration cross section is calculated weighting the number of protons ($N_{\gamma d \rightarrow pn}$) detected in the CLAS from photo-disintegration events in each bin of proton scattering angle and incident photon energy, by the effective number of deuteron targets, the absolute number of incident photons $N_\gamma(1-F)$, where F is the photon beam attenuation through the experimental target, the efficiency-acceptance function η_{QGSM} (Sec. 3.8) and taking into account the background contamination k

(as defined in Eq. 3.26), *i.e.*:

$$\frac{d\sigma}{d\Omega}(E_\gamma, \theta_p^{\text{CM}}) = \frac{A}{\rho x N_A} \frac{1}{(1-F) N_\gamma \Delta\Omega} \frac{N_{\gamma d \rightarrow pn}}{\eta_{\text{GSIM}}} (1 - k(E_\gamma, \theta_p^{\text{CM}})) , \quad (4.1)$$

where A is the target molecular weight, N_A is the Avogadro's number, and ρ and x (as defined in Sec. 3.4.1) the target density and effective length, respectively.

The CLAS cross section data are fully reported in Sec. 4.4 (at the end of the present Chapter) tabulated as a function of the incident photon energy (Tab. 4.1). For each energy bin, the values of the differential cross section as $d\sigma/d\Omega$, obtained summing the individual contributions of the six CLAS sectors, are reported as a function of the proton scattering angle in the CM system, together with their statistical uncertainties. The tables report also the values of $d\sigma/dt$ as a function of the proton scattering angle in the CM system, with their associated statistical uncertainties.

4.2.1 Uniformity of the Six CLAS Sectors

As stated in Chap. 2, the CLAS is composed of six independent sectors that can be considered as six similar spectrometers. This allows for the investigation of the uniformity of the final cross section results since the measurements are performed independently in each spectrometer (sector), and provides an estimate of the systematic uncertainty due to the CLAS detector efficiency.

The uniformity of the results has been evaluated considering the differences between the values of the cross section obtained in each bin of incident photon energy and proton scattering angle for each sector S (with $S = 1 \div 6$) and the related average over the six sectors, divided by the average itself, or:

$$V = \frac{\left(\frac{d\sigma}{d\Omega}\right)_S - \left\langle \frac{d\sigma}{d\Omega} \right\rangle}{\left\langle \frac{d\sigma}{d\Omega} \right\rangle} \quad (4.2)$$

The resulting distributions for the values of V are shown in Fig. 4.1 separately for the six CLAS sectors (numbered from left to right and top to bottom). In each panel the statistical parameters of the distributions are shown and it can be seen that a systematic shift of the order of $2 \div 5\%$ is present in all sectors.

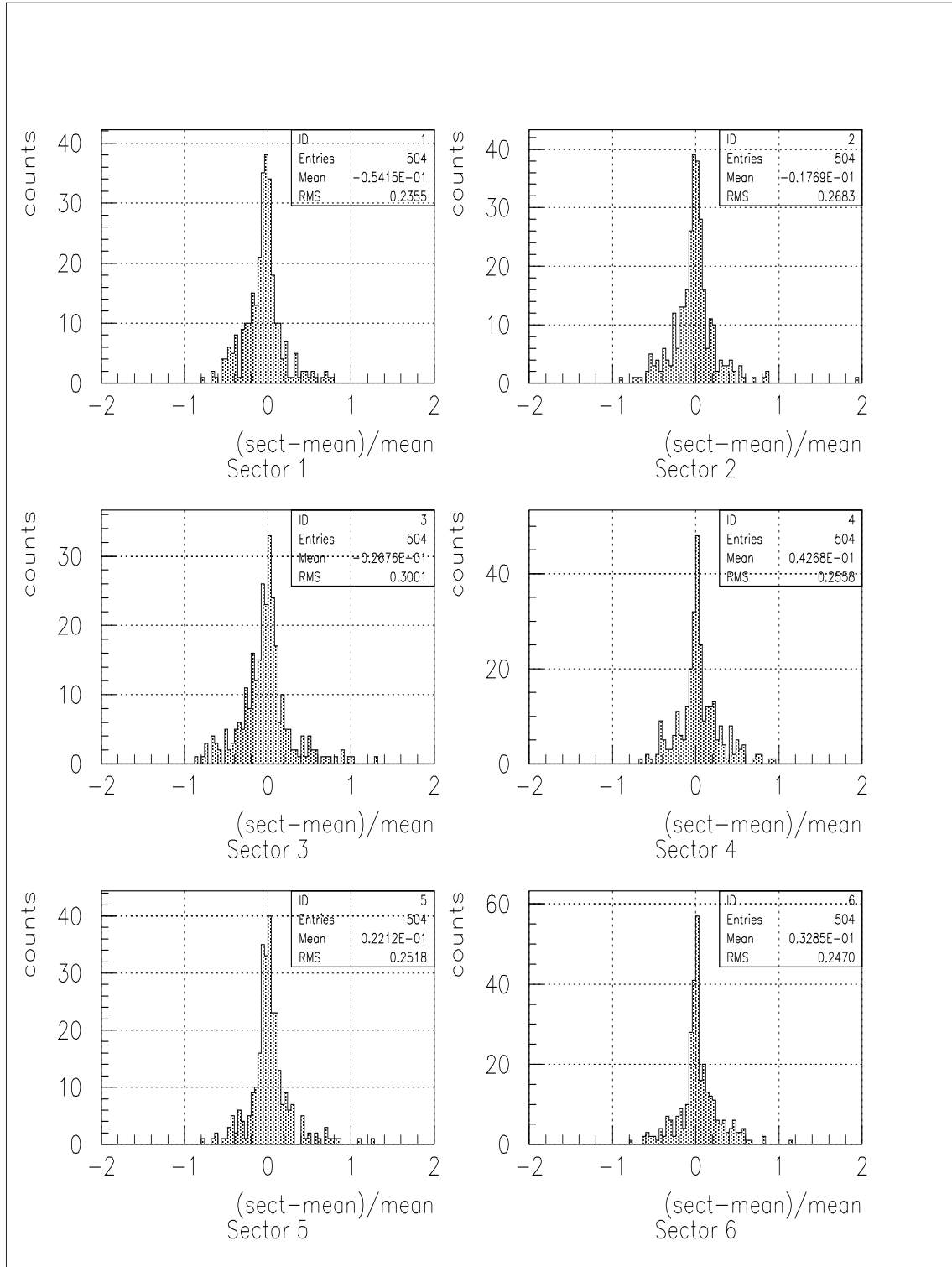


Figure 4.1: Distributions of the differences between the value of the cross section obtained in the individual sector and its average over the six sectors, divided by the average itself, as defined in Eq. 4.2 for each bin of proton scattering angle and incident photon energy. The result is shown separately for the six CLAS sectors (numbered from left to right and top to bottom). In each panel the statistical parameters of the distributions are shown and it can be seen that a systematic shift of the order of $2 \div 5\%$ is present in all sectors.

4.2.2 The Energy Dependence of the Cross Section

The new CLAS data give for the first time the opportunity to study the energy dependence of the deuteron photo disintegration differential cross section over the wide range of proton scattering angles covered with the CLAS detector and with a very good statistical accuracy.

The results on the differential cross section $\frac{d\sigma}{dt}$ are presented in Fig. 4.2 and Fig. 4.3 (solid/red dots) as a function of the total energy s (here t , u , and s are the momentum transfer to the proton, to the neutron and the total energy in the Mandelstam notation) for proton scattering angles in the range $15^\circ \leq \theta_p^{\text{CM}} \leq 155^\circ$. As can be seen from Fig. 4.2 and Fig. 4.3 the cross section decrease as a function of s is extremely steep and this behavior is enhanced for scattering angles around 90° . The blue/solid line superimposed to the experimental results represents a power law fitting function proportional to s^n .

The resulting exponents n obtained from the fits of the cross section for the various angles are plotted in Fig. 4.4. It can be seen that the cross section decrease as a function of s occurs according to different exponents n for the different scattering angles. At very forward and backward angles, corresponding to the dominance of the t or u channel, the exponent is of the order of -9 and -7 respectively. At more intermediate angles (around 90°), where both the t -dominance and u -dominance are suppressed, n drops around -13 . Moreover, one can also argue that an asymmetry exist between forward ($n = -9$) and backward angles ($n = -7$) and a local maximum can be identified for $\theta_p^{\text{CM}} = 155^\circ$.

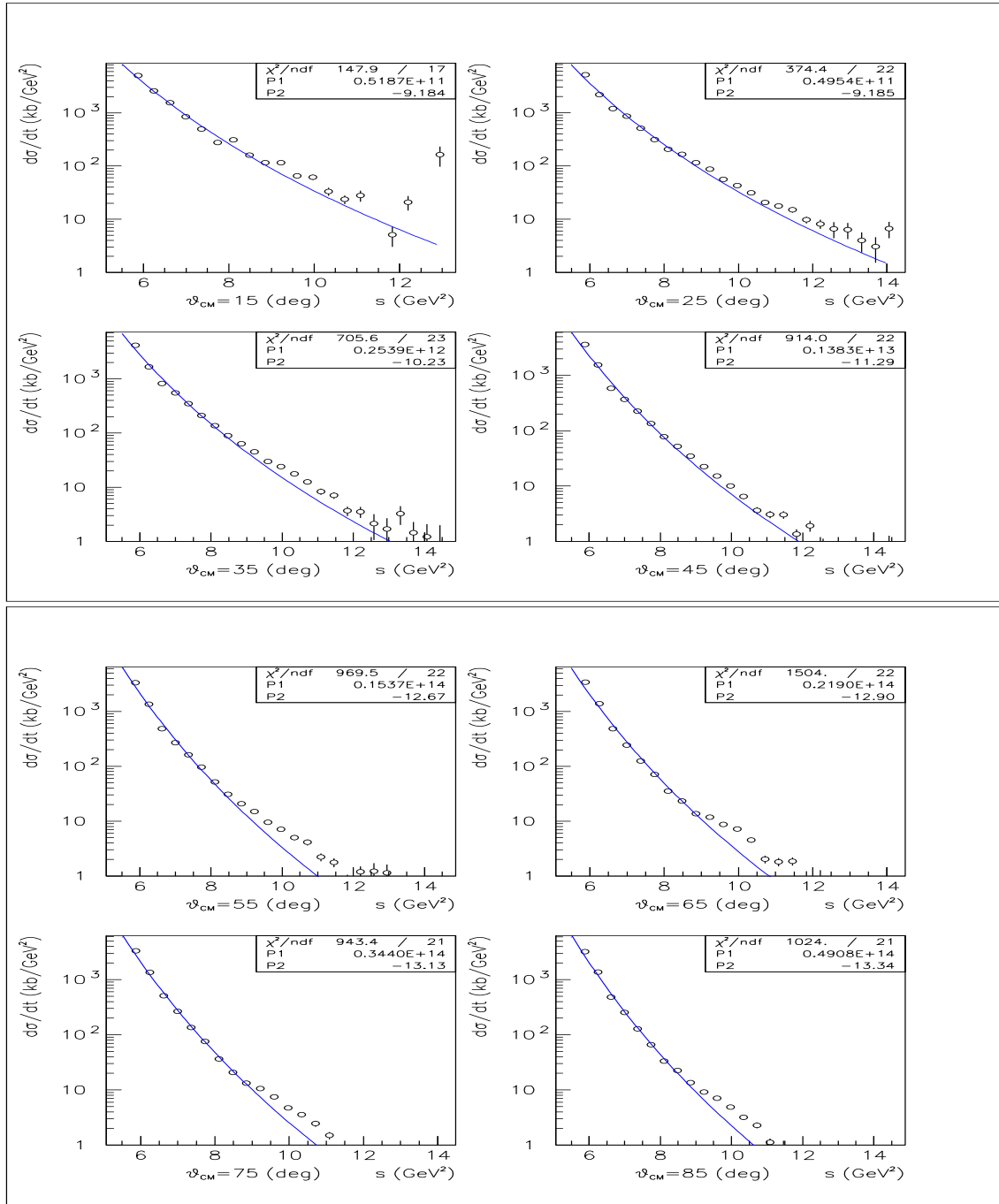


Figure 4.2: The CLAS results on the differential cross section $\frac{d\sigma}{dt}$ as a function of the total energy s (where t and s are the momentum transfer to the proton and the total energy in the Mandelstam notation) for proton scattering angles in the range $15^\circ \leq \theta_p^{\text{CM}} \leq 85^\circ$. As can be seen, the cross section decrease as a function of s is extremely steep and this behavior is enhanced as the scattering angle approaches 90° . The blue/solid line superimposed to the experimental results represents a power law fitting function proportional to s^n .

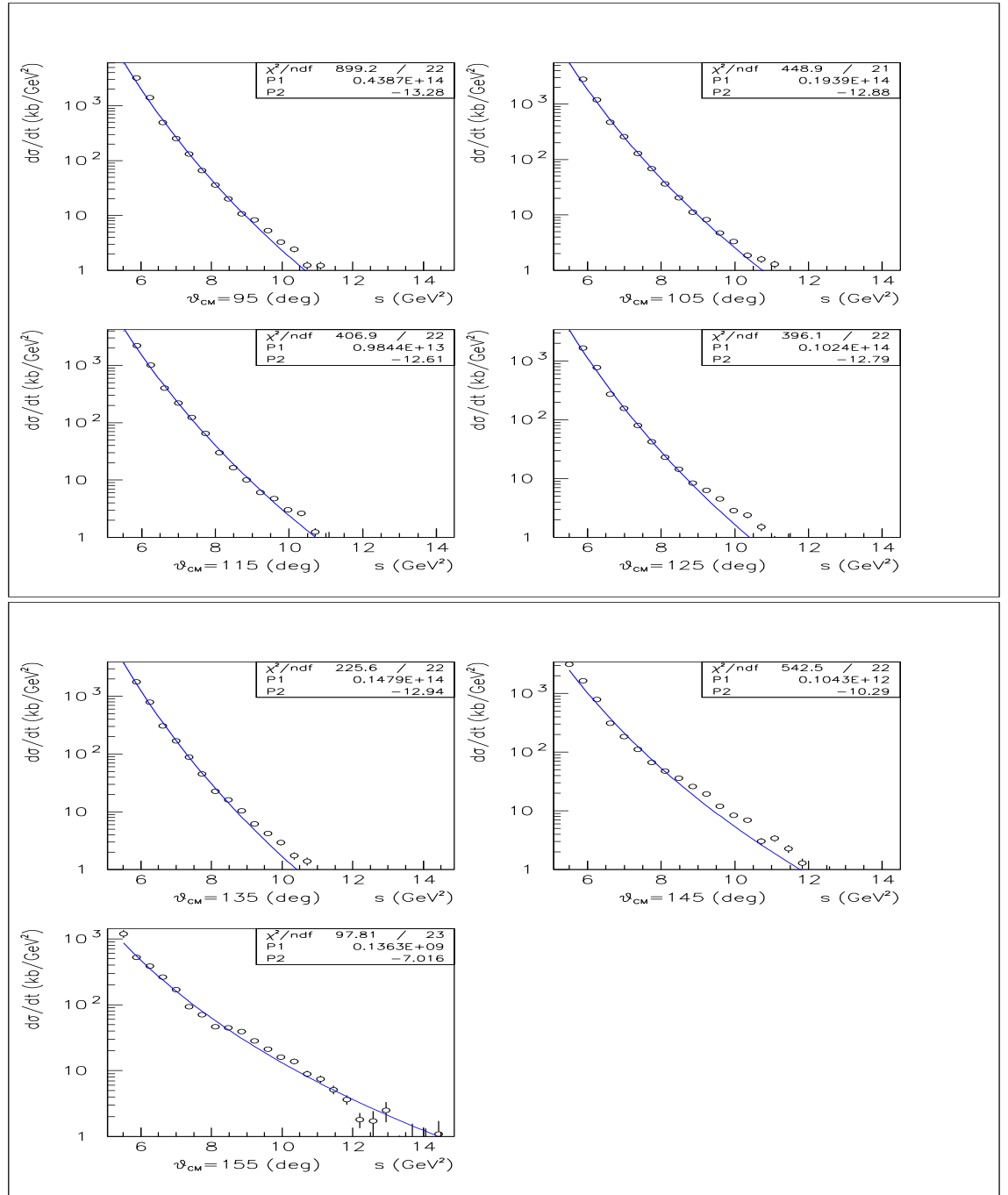


Figure 4.3: The CLAS results on the differential cross section $\frac{d\sigma}{dt}$ as a function of the total energy s (where t and s are the momentum transfer to the proton and the total energy in the Mandelstam notation) for proton scattering angles in the range $95^\circ \leq \theta_p^{\text{CM}} \leq 155^\circ$. It can be seen that the cross section tendency to a fast decrease as a function of s , slows down going toward backward scattering angles. The blue/solid line superimposed to the experimental results represents a power law fitting function proportional to s^n .

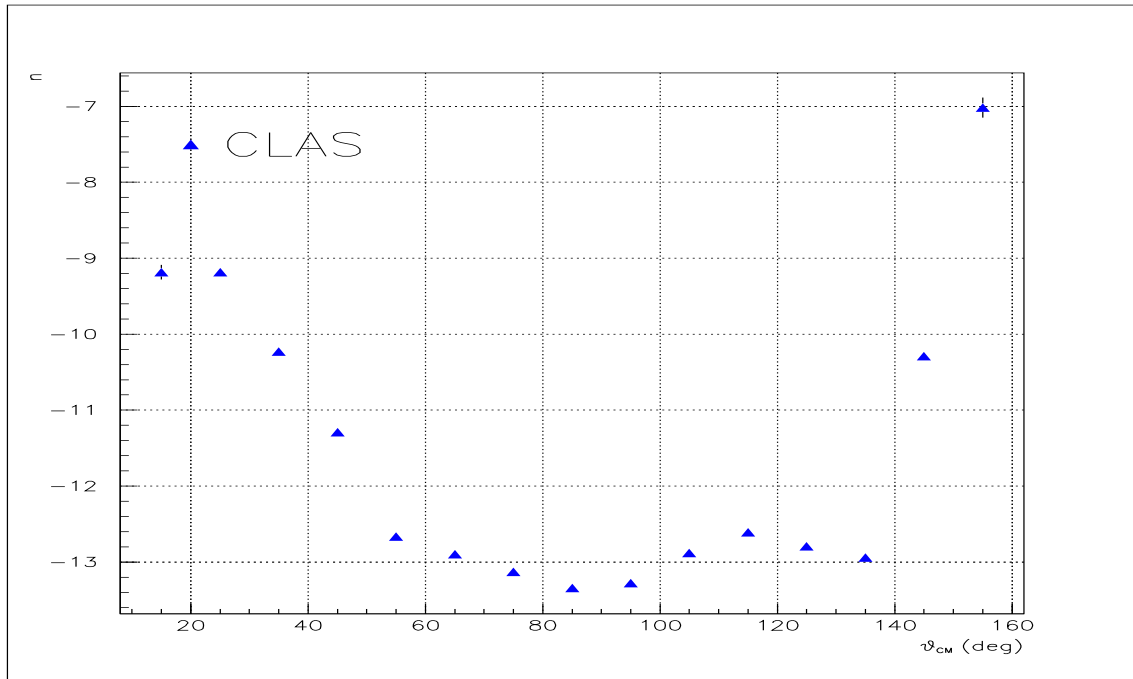


Figure 4.4: Exponents n obtained by the angular survey on the cross section. The data behavior is of the type $\frac{d\sigma}{dt} \simeq (\text{const})s^n$ as a function of the total energy s . It can be seen that the cross section decrease as a function of s follows different exponents n for different scattering angles. At very forward and backward angles (corresponding to the dominance of the t or u channel, and where u is the momentum transfer to the neutron) the exponent is of the order of -9 and -7 respectively. At more intermediate angles (around 90°), where both the t -dominance and u -dominance are suppressed, n drops around -13 . A clear asymmetry exist between forward ($n = -9$) and backward angles ($n = -7$). The errors on the data points are those given by MINUIT on the fitting parameter n .

4.2.3 Angular Distributions

The angular distributions derived using Eq. 4.1 are shown in Figs. 4.5, Fig. 4.6, and Fig. 4.7 for incident photon energy bins of 100 MeV, in the range from 0.55 up to 2.9 GeV. As seen from the figures, the data cover a broad range in the proton scattering angle: $15^\circ \leq \theta_p^{\text{CM}} \leq 155^\circ$ allowing for the first time to investigate the behavior of the cross section at very forward and backward scattering angles.

Results from published data are also included in the plots. More specifically, results in the highest energy bins obtained by the Mainz/DAPHNE [13] experiment overlap the CLAS data in the photon energy region $0.55 \leq E_\gamma \leq 0.75$ GeV. At higher photon energies, results from the SLAC [17, 18] experiments are shown together with the recent data from the JLab Hall C [24, 25] and Hall A [26] collaborations. As can be seen from Fig. 4.5, in the energy region below 1 GeV, the angular distributions still exhibit a trace of the excitation of baryon resonances in the second resonance region, which comprises $P_{11}(1440)$, $D_{13}(1520)$, and $S_{11}(1535)$. At $E_\gamma = 0.55$ GeV, the Mainz data are slightly higher than the CLAS data, mostly at intermediate scattering angles. This discrepancy is greatly reduced at forward and backward angles and also becomes less evident at higher photon energies where the two datasets are well compatible to each other within the total statistical uncertainties.

At $E_\gamma = 0.65$ GeV, both the angular dependence and the absolute value of the differential cross section of the CLAS data are in good agreement with the Mainz result. Starting from $E_\gamma = 0.75$ GeV the comparison can be extended also to the SLAC and JLab Hall C data. It turns out that, in general, the CLAS results well agree with data from these experiments.

For incident photon energies higher than 1 GeV the angular dependence of the photo-disintegration cross section changes, and a more pronounced asymmetry emerges between the forward and backward angles, as can be seen from the bottom plots of Fig. 4.5.

The angular distributions obtained in the energy range $1.35 \leq E_\gamma \leq 2.85$ GeV are shown in Figs 4.5 and 4.6. At $E_\gamma = 1.6$ GeV and $E_\gamma = 1.9$ GeV the CLAS results are compared with the angular distributions measured by the JLab Hall A collaboration which cover a few scattering angles in the range $26^\circ \leq \theta_p^{\text{CM}} \leq 143^\circ$. The CLAS results confirms the Hall A data and extends that result at the very forward and backward angular regions where the cross section increases. In general, the clear angular asymmetry shown by the CLAS data persists in the whole range of explored photon energies, as is confirmed by Fig. 4.7 which shows the results up to $E_\gamma = 2.85$ GeV.

At photon energies higher than 1 GeV, where the resonance contributions starts to fade, the predictions of the QGSM [31] are included in the plots. As shown in Figs 4.5, 4.6, and Fig. 4.7, the angular distributions are well reproduced by the QGSM calculation (shown as a solid line). This model accounts very well for the persistent forward to backward asymmetry seen in the data by invoking the interference of the iso-vector and iso-scalar components of the photon, which is constructive at forward angles and destructive in the backward direction.

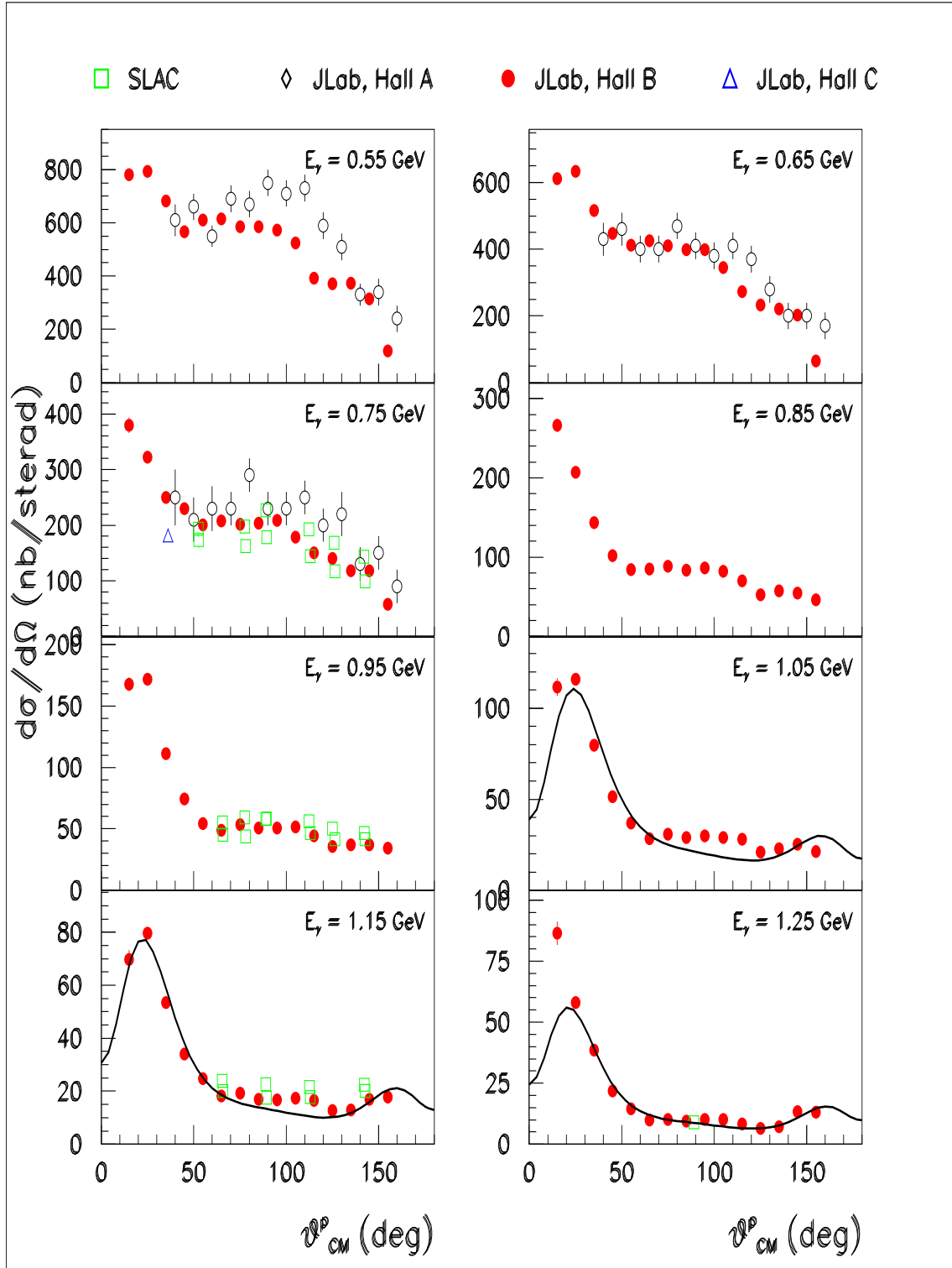


Figure 4.5: Angular distributions of the deuteron photo-disintegration cross section measured by the CLAS (solid/red dots) in the incident photon energy range 0.55 – 1.25 GeV. It can be seen that the CLAS data cover a broad range in the proton scattering angle: $15^\circ \leq \theta_p^{\text{CM}} \leq 155^\circ$. Results from Mainz [13] (open dots), SLAC [17, 18] (open squares), JLab Hall A [26] (open diamonds) and Hall C [24, 25] (open triangles) are included and are generally in agreement with the CLAS data. The angular dependence of the photo-disintegration cross section shows a pronounced asymmetry between the forward and backward proton scattering angles. For incident photon energies higher than 1 GeV, the solid line represents the non perturbative calculation of the QGSM [31] which well reproduces the data. In particular, the QGSM calculation accounts for the forward to backward asymmetry shown by the data.

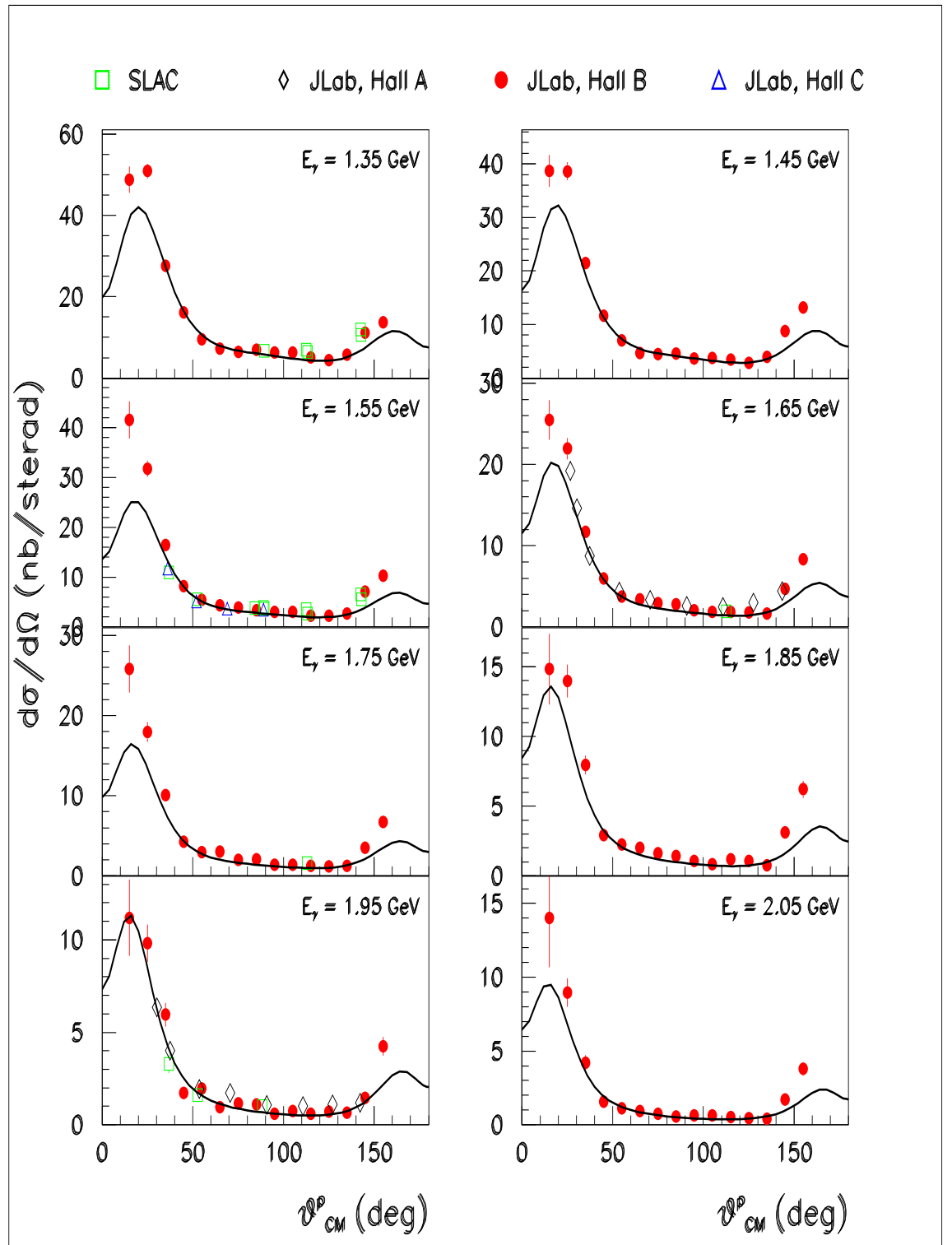


Figure 4.6: Angular distributions of the deuteron photo-disintegration cross section measured by the CLAS (solid/red dots) in the incident photon energy range 1.35 – 2.05 GeV. Results from already published experiments such as SLAC [17, 18] (open squares), JLab Hall A [26] (open diamonds) and Hall C [24, 25] (open triangles) are included, where available. The cross section asymmetry between the forward and backward angles persists in this photon energy range. The QGSM [31] calculation (shown as a solid line) well reproduces the data behavior also in this energy range.

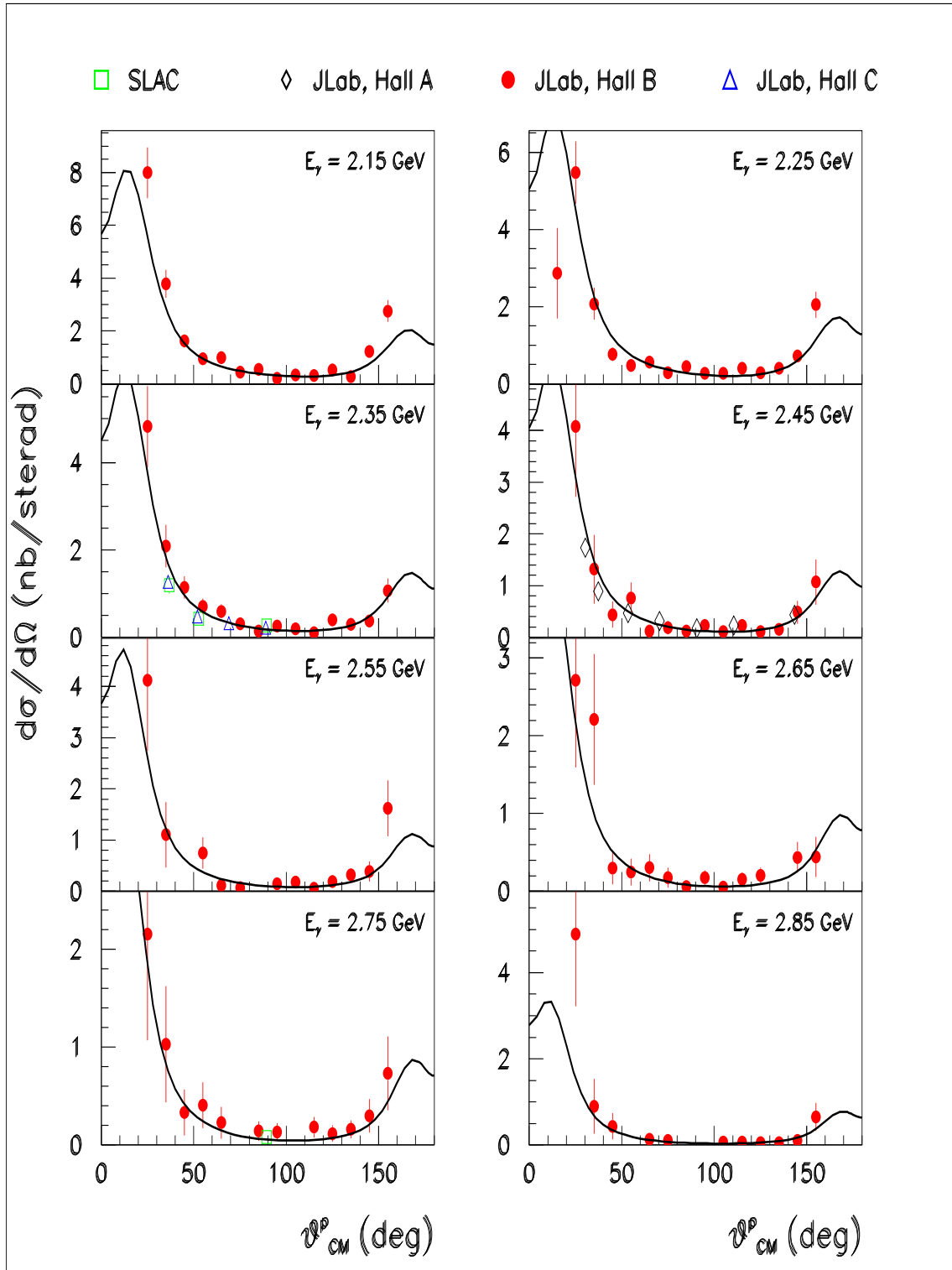


Figure 4.7: Angular distributions of the deuteron photo-disintegration cross section measured by the CLAS (solid/red dots) in the incident photon energy range 2.15 – 2.85 GeV. Results from SLAC [17, 18] (open squares), JLab Hall A [26] (open diamonds) and Hall C [24, 25] (open triangles) are included, where available. The angular distributions are well reproduced by the QGSM [31] calculation (shown as a solid line) which accounts for the data asymmetry between forward and backward scattering directions.

4.2.4 The Cross Section Scaling

As fully discussed in the opening Chapter of this thesis, the dependence of the differential cross section as a function of the incident photon energy has been often investigated in the past years to evidence the scaling behavior.

Such an effect is believed to show up in the cross section data when the proton transverse momentum

$$P_T^2 = \frac{1}{2} E_\gamma M_D \sin^2(\theta_p^{\text{CM}}), \quad (4.3)$$

being M_D the deuteron mass, is of the order of 1 (GeV/c)². In this case, the pQCD assumption that soft and hard contributions factorize may be realized.

In the case of deuteron photo-disintegration process, the cross section is expected to scale with a unique simple power law of the square of the total energy s

$$\frac{d\sigma}{dt} = f(\theta_p^{\text{CM}}) s^{-11} \quad (4.4)$$

according to the prediction of the Constituent Counting Rules (CCR). As can be seen from Eq. 4.4 the scaling law does not depend, apart from a constant factor, on the proton scattering angle.

As seen from the results shown in the previous paragraphs, the CCR prediction seems not in agreement, at the photon energies of interest here, with the obtained values for the exponent of the scaling law n as shown in Fig. 4.4.

This situation persists even at intermediate scattering angles (around 90°) where momentum transfer to the outgoing proton should be the highest possible and the perturbative regime is believed to be better established.

On the contrary, the present results indicate that pQCD is not plainly applicable to the description of the photo-disintegration process in the region of incident photon energy explored here.

In order to better underline this result, the CLAS differential cross section data, $d\sigma/dt$, multiplied by the s^{11} scaling factor, are shown in Figs 4.8 and 4.9 as a function of the incident photon energy in the range 0.55 – 3.0 GeV.

The s^{11} factor has been used to evidence possible deviations of the experimental data from the constant behavior expected on the basis of plain pQCD. In addition, it should be noticed that the CLAS data cover the incident photon energy range in fine steps of 100 MeV thus allowing for an unprecedented precision in sampling the cross section behavior in this energy region.

The panels of Fig. 4.8 and Fig. 4.9 show, from left to right and from top to bottom the calculated values for $s^{11} \frac{d\sigma}{dt}$ in the angular range from $\theta_p^{\text{CM}} = 15^\circ$ up to $\theta_p^{\text{CM}} = 155^\circ$. The CLAS data are represented by the solid/red dots, while the symbols relative to the data available in the literature are indicated in the legend found on the top of Fig. 4.8.

The arrows in each panel indicate the photon energies where $P_T = 1$ GeV/c. According to the CCR, a constant behavior of the s^{11} scaled cross section as a function of the incident photon energy is expected beyond that limit. As can be seen from Fig. 4.8 and Fig. 4.9 this situation is not perfectly realized by the experimental data. It is clear that, for forward proton angles, $\theta_p^{\text{CM}} = 15^\circ \div 45^\circ$, the data scale with a power of the total energy s lower than -11 according to the plot shown in Fig. 4.4. The data show a trend compatible with the CCR s^{-11} scaling roughly in the range of scattering angles $\theta_p^{\text{CM}} = 55^\circ \div 125^\circ$. Again, at backward angles, the

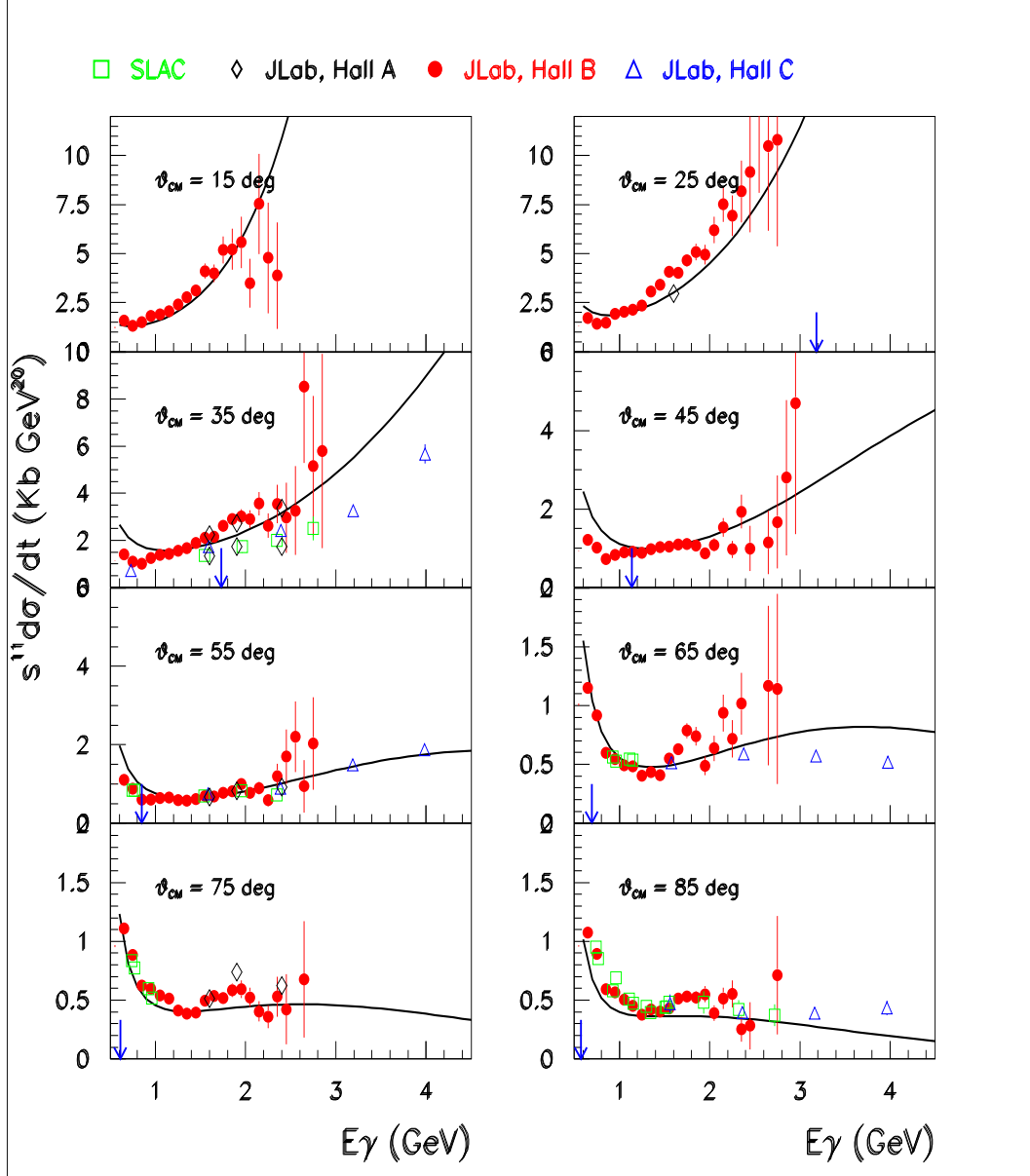


Figure 4.8: Deuteron photo-disintegration differential cross section expressed as $d\sigma/dt$ multiplied by s^{11} (being t the momentum transfer and s the total energy in the Mandelstam notation) in the angular range from $\theta_p^{\text{CM}} = 15^\circ$ up to $\theta_p^{\text{CM}} = 85^\circ$. The CLAS results are represented by the solid dots. Also shown are previously available data: SLAC [17, 18] data are represented by open squares, JLab Hall C [24, 25] data by open triangles, and JLab Hall A [26] data by open diamonds. The arrows in each panel, indicate the photon energies where the onset of the s^{-11} scaling is foreseen. This limit correspond to proton transverse momenta of 1 GeV/c. For the $\gamma d \rightarrow pn$ reaction the proton transverse momentum can be expressed $P_T^2 = \frac{1}{2} E_\gamma M_D \sin^2(\theta_p^{\text{CM}})$. According to the CCR, a constant behavior of the cross section as a function of the incident photon energy is expected when the limit for P_T is reached. The solid line represents the QGSM [31] non perturbative calculation for the cross section. This model, as discussed in the first Chapter of this thesis, gives a non perturbative description of the photo-disintegration cross section assuming that the scattering amplitude at very high energy is dominated by the exchange of three valence quarks in the t -channel.

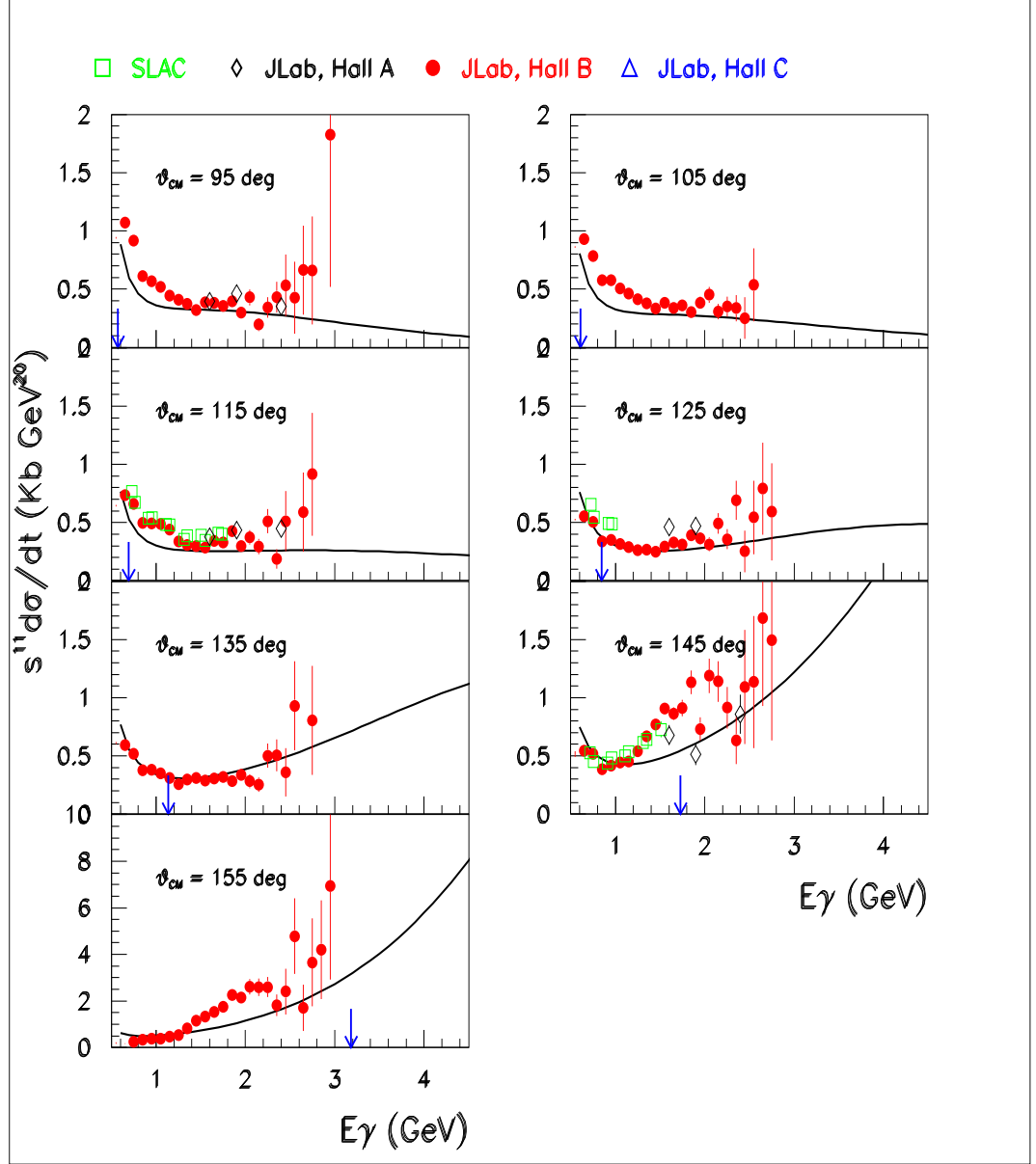


Figure 4.9: Deuteron photo-disintegration differential cross section expressed as $d\sigma/dt$ multiplied by s^{11} (being t the momentum transfer and s the total energy in the Mandelstam notation) in the angular range from $\theta_p^{\text{CM}} = 95^\circ$ up to $\theta_p^{\text{CM}} = 155^\circ$. The CLAS results are represented by the solid dots. Also shown are previously available data: SLAC [17, 18] data are represented by open squares, JLab Hall C [24, 25] data by open triangles, and JLab Hall A [26] data by open diamonds. The arrows in each panel, indicate the photon energies where the onset of the s^{-11} scaling is foreseen. This limit correspond to proton transverse momenta of 1 GeV/c. For the $\gamma d \rightarrow pn$ reaction the proton transverse momentum can be expressed by $P_T^2 = \frac{1}{2} E_\gamma M_D \sin^2(\theta_p^{\text{CM}})$. According to the CCR, a constant behavior of the cross section as a function of the incident photon energy is expected when the limit for P_T is reached. It can be seen that the asymptotic behavior for the cross section is well established from $\theta_p^{\text{CM}} = 75^\circ$ up to $\theta_p^{\text{CM}} = 125^\circ$ while at backward angles, the cross section dependence on the photon energy follows powers of s different from -11 as shown in Fig. 4.4. The solid line represents the QGSM [31], a non perturbative calculation for the cross section.

cross section dependence on the photon energy follows powers of s quite lower than -11 .

The observed deviation from the exact $n = -11$ prediction of plain pQCD for $P_T \geq 1$ GeV found for the exponent of the scaling power n may indicate that pQCD is not fully applicable in this energy region.

On the contrary, a non perturbative approach may be more effective in reproducing the behavior of the deuteron photo-disintegration cross section. This done by the non perturbative QGSM calculation for the cross section, which is shown as a solid line in Figs. 4.8 and 4.9. Again, it is seen that a good agreement with the data is found for the QGSM predictions at all proton scattering angles.

4.3 Summary and Conclusions

The aim of the present research project is the complete measurement of the deuteron photo-disintegration differential cross section in the few GeV region of incident photon energy.

This reaction is well suited for studying the interplay of nuclear and particle physics in order to find out how and at what energy the transition from the hadronic picture of the deuteron, established in the reaction at low energies (below 1 GeV), to the quark-gluon picture, takes place.

With respect to this goal, the physical motivation for such an investigation has been discussed, showing that the already published data do not fill the gap of knowledge on the physical mechanisms underlying the photo-disintegration process.

Different theoretical models have been developed to describe the deuteron photo-disintegration cross section. In particular, the QCD inspired models have been reviewed since there is common agreement on the fact that quark and gluons are more appropriate degrees of freedom for the description of the process in this energy region. The theoretical questioning is not on the use of QCD but, if perturbative QCD can be applied at this incident photon energies, or, on the contrary, non perturbative QCD must be necessarily used.

In order to answer the above question, the photo-disintegration cross section needs to be known with great statistical accuracy and over a broad angular range so to investigate its behavior in the most critical kinematic regions.

To this aim, the $\gamma d \rightarrow pn$ cross section has been measured with the CLAS large angle spectrometer at the Jefferson Lab Hall B, over a wide range of proton scattering angles ($15^\circ \leq \theta_p^{\text{CM}} \leq 155^\circ$) using a photon beam in the energy range from 0.55 up to 3.0 GeV.

This powerful investigation tool, combining the unique characteristic of a nearly 4π acceptance in conjunction with a tagged photon beam of high energy and intensity allowed the collection of a very high statistics and high quality dataset during the end of year 1999.

The analysis of this large amount of data constitutes the central part of this work and has been fully reported in the third Chapter of this thesis to illustrate the procedures and techniques used to extract the differential cross section data.

In the last part of the thesis, the new cross section data are discussed in order to contribute to the answering of the questions posed in the opening Chapter.

To this aim, the differential cross section is shown as a function of the total energy s . The new CLAS data add significant information to the previous scenario, allowing the study of the cross section decrease as s^n with an very good accuracy and over a wide angular range.

In addition, the different exponents n have been calculated over the complete range of proton scattering angles and an asymmetry is found between forward ($n = -9$) and backward angles ($n = -7$).

This result is reflected from the angular distributions of the cross section. The data measured at very forward and backward angles show that the photo-disintegration cross section exhibits a persistent asymmetry over the whole incident photon energy range.

For what concerns the theoretical interpretations, all cross section data (new and published) have been compared to the predictions of the available theoretical

models based on QCD degrees of freedom.

The conclusion is a clear indication that pQCD based models do not fully reproduce the data behavior in this region of incident photon energies. On the contrary, the non perturbative calculation provided by the Quark Gluon String Model has been able to well describe the overall data.

This result can be considered a further indication that a pQCD interpretation of the deuteron photo-disintegration process may not be adequate in the few GeV region and a complete non perturbative theory is needed.

4.4 Tabulated Data

E_γ	θ_p^{CM}	$d\sigma/d\Omega$	$\Delta(d\sigma/d\Omega)$	$d\sigma/dt$	$\Delta(d\sigma/dt)$
GeV	deg	nb/str	nb/str	kb/GeV ²	kb/GeV ²
0.55	15	780	23	7979	240
0.55	25	793	12	7958	122
0.55	35	682	8	6845	78
0.55	45	566	6	5679	61
0.55	55	610	6	6129	58
0.55	65	615	5	6174	52
0.55	75	585	5	5871	51
0.55	85	586	5	5884	49
0.55	95	574	5	5759	49
0.55	105	525	5	5271	48
0.55	115	393	5	3942	52
0.55	125	370	6	3207	46
0.55	135	372	5	3735	48
0.55	145	314	15	3154	146
0.55	155	119	16	1191	160
0.65	15	612	16	5022	131
0.65	25	633	9	5110	73
0.65	35	516	6	4161	45
0.65	45	447	5	3608	37
0.65	55	412	4	3322	31
0.65	65	426	4	3437	28
0.65	75	411	3	3319	27
0.65	85	399	3	3217	26
0.65	95	398	3	3211	27
0.65	105	345	3	2788	24
0.65	115	272	3	2198	22
0.65	125	233	3	1657	20
0.65	135	221	3	1780	23
0.65	145	203	4	1635	31
0.65	155	65	5	525	42

Table 4.1: Differential cross section data.

E_γ	θ_p^{CM}	$d\sigma/d\Omega$	$\Delta(d\sigma/d\Omega)$	$d\sigma/dt$	$\Delta(d\sigma/dt)$
GeV	deg	nb/str	nb/str	kb/GeV ²	kb/GeV ²
0.75	15	379	14	2586	94
0.75	25	322	8	2164	52
0.75	35	249	4	1674	28
0.75	45	230	4	1543	24
0.75	55	200	3	1345	20
0.75	65	208	3	1396	18
0.75	75	201	3	1352	17
0.75	85	203	2	1365	17
0.75	95	209	3	1403	17
0.75	105	178	2	1198	16
0.75	115	151	2	1010	14
0.75	125	140	4	772	13
0.75	135	118	2	794	15
0.75	145	118	3	792	21
0.75	155	57	5	385	32
0.85	15	266	8	1546	48
0.85	25	207	4	1186	25
0.85	35	144	2	823	13
0.85	45	102	2	581	9
0.85	55	84	1	484	8
0.85	65	85	1	486	6
0.85	75	89	1	507	6
0.85	85	84	1	480	6
0.85	95	87	1	495	6
0.85	105	82	1	469	6
0.85	115	70.3	1	402	6
0.85	125	52	1	273	5
0.85	135	58	1	307	6
0.85	145	54	1	311	7
0.85	155	46	3	263	15

E_γ	θ_p^{CM}	$d\sigma/d\Omega$	$\Delta(d\sigma/d\Omega)$	$d\sigma/dt$	$\Delta(d\sigma/dt)$
GeV	deg	nb/str	nb/str	kb/GeV ²	kb/GeV ²
0.95	15	168	5	846	27
0.95	25	172	3	855	16
0.95	35	111	2	553	8
0.95	45	74	1	369	6
0.95	55	54.3	0.9	270	4
0.95	65	48.8	0.7	243	3
0.95	75	53.3	0.7	265	3
0.95	85	50.9	0.7	253	3
0.95	95	50.8	0.7	253	3
0.95	105	51.6	0.7	257	3
0.95	115	44.2	0.6	220	3
0.95	125	35.7	0.8	156	3
0.95	135	36.8	0.9	170	3
0.95	145	37.1	0.8	185	4
0.95	155	34	2	170	8
1.05	15	112	5	497	22
1.05	25	116	3	509	13
1.05	35	80	2	350	7
1.05	45	51	1	226	5
1.05	55	36.9	0.8	162	4
1.05	65	28.4	0.6	125	3
1.05	75	31	0.6	136	3
1.05	85	29.1	0.6	128	2
1.05	95	30	0.6	132	2
1.05	105	29.1	0.6	128	3
1.05	115	28.1	0.6	124	2
1.05	125	21	0.7	80	2
1.05	135	22.7	0.8	89	2
1.05	145	25.4	0.7	111	3
1.05	155	21	1	94	6

E_γ	θ_p^{CM}	$d\sigma/d\Omega$	$\Delta(d\sigma/d\Omega)$	$d\sigma/dt$	$\Delta(d\sigma/dt)$
GeV	deg	nb/str	nb/str	kb/GeV ²	kb/GeV ²
1.15	15	70	4	277	14
1.15	25	80	2	313	9
1.15	35	53	1	210	5
1.15	45	34.1	0.8	134	3
1.15	55	24.7	0.6	97	3
1.15	65	18.1	0.5	71	2
1.15	75	19.2	0.4	75	2
1.15	85	16.9	0.4	66	2
1.15	95	16.7	0.4	66	2
1.15	105	17.4	0.4	68	2
1.15	115	16.5	0.4	65	2
1.15	125	12.8	0.5	42	1
1.15	135	12.8	0.5	45	2
1.15	145	17	0.6	67	2
1.15	155	18	1	70	4
1.25	15	86	5	311	17
1.25	25	58	2	206	7
1.25	35	39	1	137	4
1.25	45	21.8	0.7	78	2
1.25	55	14.5	0.5	52	2
1.25	65	10	0.4	35	1
1.25	75	10.2	0.3	36	1
1.25	85	9.3	0.3	33	1
1.25	95	10.1	0.3	36	1
1.25	105	10.2	0.3	36	1
1.25	115	8.4	0.3	30	1
1.25	125	6.5	0.3	23.1	1
1.25	135	7.2	0.4	23	1
1.25	145	13.4	0.5	48	2
1.25	155	13.1	0.8	46	3

E_γ	θ_p^{CM}	$d\sigma/d\Omega$	$\Delta(d\sigma/d\Omega)$	$d\sigma/dt$	$\Delta(d\sigma/dt)$
GeV	deg	nb/str	nb/str	kb/GeV ²	kb/GeV ²
1.35	15	49	3	160	11
1.35	25	51	2	165	6
1.35	35	27.6	1	89	3
1.35	45	16.1	0.6	52	2
1.35	55	9.6	0.4	31	1
1.35	65	7.2	0.3	23	1
1.35	75	6.4	0.3	20.8	0.9
1.35	85	7	0.3	22.5	0.9
1.35	95	6.2	0.3	20.1	0.8
1.35	105	6.3	0.3	20.3	0.8
1.35	115	5.1	0.2	16.4	0.8
1.35	125	4.4	0.2	14.4	0.7
1.35	135	5.7	0.4	16.1	0.8
1.35	145	11.2	0.5	36	1
1.35	155	13.8	0.9	45	3
1.45	15	39	3	116	9
1.45	25	39	2	115	5
1.45	35	21.5	0.9	64	3
1.45	45	11.7	0.5	35	1
1.45	55	7	0.4	21	1
1.45	65	4.6	0.3	13.7	0.8
1.45	75	4.5	0.2	13.3	0.7
1.45	85	4.6	0.2	13.5	0.7
1.45	95	3.6	0.2	10.8	0.6
1.45	105	3.8	0.2	11.2	0.6
1.45	115	3.4	0.2	10.1	0.6
1.45	125	2.8	0.2	8.4	0.5
1.45	135	3.9	0.3	10.4	0.6
1.45	145	8.7	0.4	26	1
1.45	155	13.1	0.8	39	2

E_γ	θ_p^{CM}	$d\sigma/d\Omega$	$\Delta(d\sigma/d\Omega)$	$d\sigma/dt$	$\Delta(d\sigma/dt)$
GeV	deg	nb/str	nb/str	kb/GeV ²	kb/GeV ²
1.55	15	42	4	115	10
1.55	25	32	2	87	4
1.55	35	16.4	0.8	45	2
1.55	45	8.2	0.4	22	1
1.55	55	5.5	0.3	14.9	0.9
1.55	65	4.3	0.3	11.8	0.7
1.55	75	3.9	0.2	10.6	0.6
1.55	85	3.3	0.2	9.2	0.6
1.55	95	3	0.2	8.3	0.5
1.55	105	3	0.2	8.2	0.5
1.55	115	2.2	0.2	6.1	0.4
1.55	125	2.3	0.2	6.3	0.5
1.55	135	2.7	0.3	6.2	0.5
1.55	145	7.1	0.4	19	1
1.55	155	10.3	0.7	28	2
1.65	15	25	2	65	6
1.65	25	22	1	56	3
1.65	35	11.7	0.7	30	2
1.65	45	6	0.4	15.2	1
1.65	55	3.7	0.3	9.5	0.7
1.65	65	3.4	0.3	8.7	0.6
1.65	75	2.9	0.2	7.5	0.5
1.65	85	2.8	0.2	7.1	0.5
1.65	95	2.1	0.2	5.3	0.4
1.65	105	1.8	0.1	4.7	0.4
1.65	115	1.9	0.1	4.8	0.4
1.65	125	1.8	0.1	4.5	0.4
1.65	135	1.7	0.2	4.2	0.4
1.65	145	4.7	0.3	12	0.8
1.65	155	8.3	0.6	21	2

E_γ	θ_p^{CM}	$d\sigma/d\Omega$	$\Delta(d\sigma/d\Omega)$	$d\sigma/dt$	$\Delta(d\sigma/dt)$
GeV	deg	nb/str	nb/str	kb/GeV ²	kb/GeV ²
1.75	15	26	3	62	7
1.75	25	18	1	43	3
1.75	35	10.1	0.7	24	2
1.75	45	4.2	0.3	10.1	0.8
1.75	55	3	0.3	7.1	0.6
1.75	65	3	0.2	7.2	0.6
1.75	75	2	0.2	4.7	0.4
1.75	85	2	0.2	4.9	0.4
1.75	95	1.4	0.1	3.3	0.3
1.75	105	1.4	0.1	3.3	0.3
1.75	115	1.3	0.1	3	0.3
1.75	125	1.2	0.1	2.9	0.3
1.75	135	1.2	0.1	2.9	0.3
1.75	145	3.5	0.3	8.3	0.6
1.75	155	6.8	0.6	16	1
1.85	15	15	3	33	6
1.85	25	14	1	31	3
1.85	35	8	0.7	18	1
1.85	45	2.9	0.3	6.5	0.7
1.85	55	2.2	0.2	5	0.5
1.85	65	2	0.2	4.5	0.5
1.85	75	1.6	0.2	3.6	0.4
1.85	85	1.4	0.1	3.2	0.3
1.85	95	1.1	0.1	2.4	0.3
1.85	105	0.8	0.1	1.9	0.2
1.85	115	1.2	0.1	2.6	0.3
1.85	125	1.1	0.1	2.4	0.3
1.85	135	0.8	0.1	1.7	0.2
1.85	145	3.1	0.3	6.9	0.6
1.85	155	6.2	0.6	14	1

E_γ	θ_p^{CM}	$d\sigma/d\Omega$	$\Delta(d\sigma/d\Omega)$	$d\sigma/dt$	$\Delta(d\sigma/dt)$
GeV	deg	nb/str	nb/str	kb/GeV ²	kb/GeV ²
1.95	15	11	2	24	4
1.95	25	10	1	21	2
1.95	35	6	0.6	12	1
1.95	45	1.7	0.2	3.6	0.5
1.95	55	2	0.2	4.1	0.5
1.95	65	1	0.2	2	0.3
1.95	75	1.2	0.1	2.5	0.3
1.95	85	1.1	0.1	2.3	0.3
1.95	95	0.59	0.1	1.2	0.2
1.95	105	0.8	0.1	1.6	0.2
1.95	115	0.59	0.1	1.2	0.2
1.95	125	0.7	0.1	1.5	0.2
1.95	135	0.7	0.1	1.4	0.2
1.95	145	1.5	0.2	3	0.4
1.95	155	4.2	0.5	9	1
1.95	165	5	3	10	7
2.05	15	14	3	28	7
2.05	25	9	1	18	2
2.05	35	4.2	0.5	8	1
2.05	45	1.6	0.2	3.1	0.5
2.05	55	1.1	0.2	2.2	0.4
2.05	65	0.9	0.2	1.8	0.3
2.05	75	0.8	0.1	1.5	0.2
2.05	85	0.56	0.1	1.1	0.2
2.05	105	0.65	0.1	1.3	0.2
2.05	115	0.54	0.09	1.1	0.2
2.05	125	0.45	0.08	0.9	0.2
2.05	135	0.41	0.09	0.8	0.2
2.05	145	1.7	0.2	3.4	0.4
2.05	155	3.8	0.5	7.5	0.9

E_γ	θ_p^{CM}	$d\sigma/d\Omega$	$\Delta(d\sigma/d\Omega)$	$d\sigma/dt$	$\Delta(d\sigma/dt)$
GeV	deg	nb/str	nb/str	kb/GeV ²	kb/GeV ²
2.15	25	8	1	15	2
2.15	35	3.8	0.5	7.1	1
2.15	45	1.6	0.3	3	0.5
2.15	55	0.9	0.2	1.8	0.3
2.15	65	1	0.2	1.9	0.3
2.15	75	0.43	0.09	0.8	0.2
2.15	85	0.55	0.1	1	0.2
2.15	95	0.21	0.06	0.4	0.1
2.15	105	0.33	0.07	0.6	0.1
2.15	115	0.31	0.07	0.6	0.1
2.15	125	0.53	0.09	1	0.2
2.15	135	0.27	0.07	0.5	0.1
2.15	145	1.2	0.2	2.3	0.3
2.15	155	2.8	0.4	5.1	0.8
2.15	165	1	0.8	2	2
2.25	15	3	1	5	2
2.25	25	5.5	0.8	10	1
2.25	35	2.1	0.4	3.7	0.7
2.25	45	0.8	0.2	1.4	0.3
2.25	55	0.5	0.1	0.8	0.2
2.25	65	0.6	0.1	1	0.2
2.25	75	0.28	0.08	0.5	0.1
2.25	85	0.44	0.09	0.8	0.2
2.25	95	0.27	0.07	0.5	0.1
2.25	105	0.28	0.07	0.5	0.1
2.25	115	0.4	0.08	0.7	0.1
2.25	125	0.28	0.07	0.5	0.1
2.25	135	0.4	0.08	0.7	0.1
2.25	145	0.7	0.1	1.3	0.3
2.25	155	2	0.3	3.6	0.6
2.25	165	2	1	4	2

E_γ	θ_p^{CM}	$d\sigma/d\Omega$	$\Delta(d\sigma/d\Omega)$	$d\sigma/dt$	$\Delta(d\sigma/dt)$
GeV	deg	nb/str	nb/str	kb/GeV ²	kb/GeV ²
2.35	15	12	4	21	6
2.35	25	4.8	0.9	8	2
2.35	35	2.1	0.5	3.5	0.8
2.35	45	1.1	0.3	1.9	0.4
2.35	55	0.7	0.2	1.2	0.3
2.35	65	0.6	0.2	1	0.3
2.35	85	0.15	0.06	0.3	0.1
2.35	95	0.26	0.08	0.4	0.1
2.35	105	0.2	0.07	0.3	0.1
2.35	115	0.11	0.05	0.19	0.08
2.35	135	0.3	0.08	0.5	0.1
2.35	145	0.4	0.1	0.6	0.2
2.35	155	1.1	0.3	1.8	0.5
2.35	165	3	2	6	3
2.45	25	4	1	7	2
2.45	35	1.3	0.7	2	1
2.45	45	0.4	0.3	0.7	0.4
2.45	55	0.8	0.3	1.2	0.5
2.45	75	0.2	0.1	0.3	0.2
2.45	85	0.13	0.09	0.2	0.1
2.45	95	0.2	0.1	0.4	0.2
2.45	105	0.11	0.08	0.2	0.1
2.45	115	0.2	0.1	0.4	0.2
2.45	125	0.11	0.08	0.2	0.1
2.45	135	0.16	0.09	0.3	0.1
2.45	145	0.5	0.2	0.8	0.4
2.45	155	1.1	0.4	1.7	0.7

E_γ	θ_p^{CM}	$d\sigma/d\Omega$	$\Delta(d\sigma/d\Omega)$	$d\sigma/dt$	$\Delta(d\sigma/dt)$
GeV	deg	nb/str	nb/str	kb/GeV ²	kb/GeV ²
2.55	15	106	44	165	68
2.55	25	4	1	6	2
2.55	35	1.1	0.6	1.7	1
2.55	55	0.7	0.3	1.1	0.5
2.55	105	0.2	0.1	0.3	0.2
2.55	125	0.2	0.1	0.3	0.2
2.55	135	0.3	0.1	0.5	0.2
2.55	145	0.4	0.2	0.6	0.3
2.55	155	1.6	0.5	2.5	0.8
2.65	25	3	1	4	2
2.65	35	2.2	0.8	3	1
2.65	45	0.3	0.2	0.4	0.3
2.65	65	0.3	0.2	0.4	0.3
2.65	75	0.2	0.1	0.3	0.2
2.65	95	0.17	0.1	0.3	0.1
2.65	115	0.15	0.09	0.2	0.1
2.65	125	0.2	0.1	0.3	0.2
2.65	145	0.4	0.2	0.6	0.3
2.65	155	0.4	0.3	0.6	0.4

E_γ	θ_p^{CM}	$d\sigma/d\Omega$	$\Delta(d\sigma/d\Omega)$	$d\sigma/dt$	$\Delta(d\sigma/dt)$
GeV	deg	nb/str	nb/str	kb/GeV ²	kb/GeV ²
2.75	25	2	1	3	2
2.75	35	1.0	0.6	1.5	0.8
2.75	45	0.3	0.2	0.5	0.3
2.75	55	0.4	0.2	0.6	0.3
2.75	95	0.13	0.09	0.2	0.1
2.75	115	0.2	0.1	0.3	0.1
2.75	125	0.12	0.08	0.2	0.1
2.75	135	0.16	0.09	0.2	0.1
2.75	145	0.3	0.2	0.4	0.2
2.75	155	0.7	0.4	1	0.5
2.85	25	5	2	7	2
2.85	35	0.9	0.6	1.2	0.9
2.85	45	0.4	0.3	0.6	0.4
2.85	155	0.7	0.3	0.9	0.4
2.95	45	0.6	0.4	0.7	0.5
2.95	155	0.8	0.5	1.1	0.6

Bibliography

- [1] R.J. Holt, *Phys. Rev.* **C41** 2400 (1990)
- [2] P. Rossi, E. De Sanctis *et al.*, *Phys. Rev.* **C40** 2412 (1989)
- [3] D.A. Jenkins *et al.*, *Phys. Rev.* **C50** 74 (1994)
- [4] H. Arenövel, M. Danos, and H.T. Williams, *Nucl. Phys.* **A162** 12 (1971)
- [5] P. Wilhelm and H. Arenövel, *Phys. Lett.* **B318** 410 (1993)
- [6] J.M. Laget, *Phys. Rep.* **I69** 493 (1981)
J.M. Laget, *Can. J. Phys.* **62** 1046 (1984)
J.M. Laget, *Phys. Lett.* **B 199** 493 (1987)
- [7] W. Jaus, D. Bofinger and W.S. Woolcock, *Nucl. Phys.* **A562** 477-500 (1993)
- [8] H.J. Arends *et al.*, *Nucl. Phys.* **A412** 509 (1984)
- [9] E. De Sanctis *et al.*, *Phys. Rev.* **C34** 413 (1986);
P. Levi Sandri *et al.*, *Phys. Rev.* **C39** 701 (1989)
- [10] MIT/BATES, <http://filburt.mit.edu>
- [11] P.A. Wallace *et al.*, *Nucl. Phys.* **A532** 617 (1991)
- [12] LEGS Data Release L1-3.0 (1994)
- [13] R. Crawford *et al.*, *Nucl. Phys.* **A603** 303-325 (1996)
- [14] K. Baba *et al.*, *Phys. Rev.* **C48** 286 (1983)
- [15] R. Ching and C. Schaerf, *Phys. Rev.* **141** 141 (1966)
- [16] P. Dougan *et al.*, *Z. Phys.* **A276** 55 (1976)
- [17] S.J. Freedman *et al.*, *Phys. Rev.* **C48** 1864 (1993)
- [18] J.E. Belz *et al.*, *Phys. Rev. Lett.* **74** 646 (1995)
- [19] Jefferson Lab Experiments E89-01 (1989) and E99-008 (1999)
- [20] Jefferson Lab Experiment E93-017 (1993)
- [21] Jefferson Lab Experiment E89-012 (1989) and E96-003 (1996)
- [22] S.J. Brodsky, G.R. Farrar, *Phys. Rev. Lett.* **31** 1153 (1998)
- [23] R. Gilman and F. Gross, *J. Phys. G.*, *Nucl. Part. Phys.* **28** R37 (2002)
R. Gilman and F. Gross, Review Article WM-01-113, JLAB-PHY-01-25 (2001)

- [24] C. Bochna *et al.*, *Phys. Rev. Lett.* **81** 4576 (1998)
- [25] E.C. Shulte *et al.*, *Phys. Rev. Lett.* **87** 102302-1 (2001)
- [26] E.C. Shulte *et al.*, *Phys. Rev.* **C** 0422011 (2002)
- [27] S.L. Brodsky, J.R. Hiller, *Phys. Rev.* **C28** 475 (1983)
- [28] S.J. Brodsky, B. T. Chertok, *Phys. Rev.* **D14** 3003 (1976)
 S.J. Brodsky, B. T. Chertok, *Phys. Rev. Lett.* **37** 269 (1976)
 S.J. Brodsky, C-R. Ji, G. P. Lepage, *Phys. Rev. Lett.* **51** 83 (1983)
 L.C. Alexa *et al.*, *Phys. Rev. Lett.* **82** 1374 (1999)
 D. Abbott *et al.*, *Phys. Rev. Lett.* **82** 1879 (1999)
- [29] L.L. Frankfurt *et al.*, *Phys. Rev. Lett.* **84** 3045 (2000)
 L.L. Frankfurt *et al.*, *Nucl. Phys.* **A663&664** 349 (2000)
- [30] A.E.L. Dieperink, S. I. Nagorny, *Phys. Lett.* **B456** 9 (1999)
- [31] V.Yu. Grishina *et al.*, *Eur. Phys. J.* **A10** 355 (2001)
- [32] M. Levin, *Sov. Phys. Usp.* **16** 600 (1973)
- [33] F. Close and N. Isgur, *Phys. Lett.* **B509** 81-86 (2001)
- [34] M. Mirazita, Proc. of *XL Internal Winter Meeting on Nuclear Physics*, Bormio, Jan. 21-26, 2002, hep/ph 0206213
 F. Ronchetti, Proc. of *Quark and Nuclear Physics 2002*, Jülich, Germany, Jun. 9-14 2002 in printing by *Eur. Phys. J. A*
 F. Ronchetti, Proc. of *IV Conference on Quark Confinement and the Hadron Spectrum*, Gargnano, Italy, Sept. 10-14 2002, in printing by World. Sci. Pub.
 P. Rossi, Proc. of *Electron-Nucleus Scattering VII*, Isola d'Elba, Italy Jun. 24-28 2002
- [35] M.M. Sargisan, Private Communication (2003)
- [36] G.P. Lepage, S.J. Brodsky, *Phys. Rev.* **D22** 2157 (1980)
 S.J. Brodsky, G.P. Lepage, *Phys. Rev.* **D24** 2848 (1981)
- [37] B.L. Ioffe and A.V. Smilga, *Nucl. Phys.* **B216** 373 (1983)
- [38] N. Isgur and C.H. Llewellyn Smith, *Phys. Lett.* **B217** 535 (1989)
 N. Isgur and C.H. Llewellyn Smith, *Phys. Rev. Lett.* **52** 1080 (1984)
- [39] A.V. Radyushkin, *Nucl. Phys.* **A 532**, 141 (1991)
- [40] I.G. Aznaurian, A.S. Bagdasarian, S.V. Esaibegian, and N.L. Ter-Isaakian, *Sov. J. Nucl. Phys.* **55** 1099 (1992)
- [41] K. Wijesooriya *et al.*, *Phys. Rev. Lett.* **86** 2975 (2001),
 and references therein.
- [42] V.Yu. Grishina *et al.*, Proc. of *Quark and Nuclear Physics 2002*, Jülich, Germany, June 9-14 2002 in printing by *Eur. Phys. J. A*
- [43] D.G. Grabb *et al.*, *Phys. Rev. Lett.* **65** 3241 (1990)
- [44] T. Gousset *et al.*, *Phys. Rev.* **D53** 1202 (1996)
 C. Carlson, M. Chachkhunashvili, *Phys. Rev.* **D45** 2555 (1992)

- [45] A. Afanasev *et al.*, *Phys. Rev.* **D61** 034014 (2000)
- [46] I.P. Auer *et al.*, *Phys. Rev. Lett.* **62** 2649 (1989)
- [47] F. Adamian *et al.*, *Eur. Phys. J.* **A8** 423 (2000)
- [48] M. Creutz, *Phys. Rev.* **D21** 2308 (1980)
M. Creutz, *Phys. Rev. Lett.* **45** 313 (1980)
M. Creutz, *Quarks, Gluons, and Lattice*, Cambridge U.P. (1983)
- [49] M.A. Shifman, A.I. Vainshtein, and V.I. Zakharov,
Nucl. Phys. **B147** 385, 448, 519 (1979)
- [50] G. 'tHooft, *Nucl. Phys.* **B72** 461 (1974)
- [51] G. Veneziano, *Phys. Lett.* **B52** 220 (1974)
G. Veneziano, *Nucl. Phys.* **B117** 519 (1976)
- [52] M. Ciafaloni, G. Marchesini, and G. Veneziano, *Nucl. Phys.* **B98** 472 (1975)
- [53] A. Casher, J. Kogut, and L. Susskind, *Phys. Rev.* **D10** 732 (1974)
- [54] A. Casher, H. Neuberger, and S. Nussinov, *Phys. Rev.* **D20** 179 (1979)
- [55] X. Artru and G. Menneiser, *Nucl. Phys.* **B70** 93 (1974)
- [56] B. Andersson, G. Gustafson, and C. Peterson, *Phys. Lett.* **B71** 337 (1977)
- [57] B. Andersson, G. Gustafson, and C. Peterson, *Z. Phys.* **C1** 105 (1979)
- [58] A.B. Kaidalov, *JTEP Lett.* **32** 474 (1980)
A.B. Kaidalov, *Sov. J. Nucl. Phys.* **33** 733 (1981)
- [59] L.A. Kondratyuk, E. De Sanctis *et al.*, , *Phys. Rev.* **C48** 2491 (1993)
- [60] A.B. Kaidalov, *Phys. Lett.* **B116** 459 (1982)
A.B. Kaidalov and K. Ter-Martirosyan, *Phys. Lett.* **B117** 247 (1982)
- [61] A.B. Kaidalov, *Z. Phys.* **C12** 63 (1982)
- [62] A.B. Kaidalov and P. Volkovitsky, *Sov. J. Nucl. Phys.* **35** 720, 909 (1982)
- [63] A.B. Kaidalov and K. Ter-Martirosyan, *Sov. J. Nucl. Phys.* **39** 979 (1984)
A.B. Kaidalov and K. Ter-Martirosyan, *Sov. J. Nucl. Phys.* **40** 135 (1984)
- [64] E.E. Zabrodin *et al.*, *Phys. Lett.* **B508** 184 (2001)
- [65] G.F. Chew and C. Ronzenzweig, *Phys. Rep.* **41** 26 (1978)
- [66] A.B. Kaidalov *Surv. High En. Phys.* **13** 265 (1999)
- [67] A. Capella *et al.*, *Z. Phys.* **C3** 329 (1980)
A. Capella and J. Tran Thanh Van, *Phys. Lett.* **B114** 450 (1982)
A. Capella *et al.*, *Phys. Rep.* **326** 225 (1994)
- [68] P.D.B. Collins and E.J. Squires, *Regge Poles in Particle Physics*,
Springer Tracts in Modern Physics **45** (1970)
- [69] J. Bjorken, SLAC Report, PUB-95-6949 (1995)
- [70] E. Segré, *Nuclei e Particelle*, Zanichelli, (1966)

- [71] M. Leon, *Particle Physics: an Introduction*, Academic Press (1973)
- [72] K.D. Born *et al.*, *Phys. Rev* **D40** 1653 (1989)
- [73] V.A. Lyubimov, *Sov. J. Nucl. Phys. Usp.* **20** 691 (1977)
- [74] A. Brandt and the UA8 Collaboration, *Nucl. Phys.* **B514** 3 (1998)
- [75] A.E. Inopin, hep/th 0012248
- [76] Z. Chikovani, L. Jenkowsky and F. Paccanoni, *Mod. Phys. Lett.* **A6** 1409 (1991)
- [77] A.B. Kaidalov, *Sov. Phys. Usp.* **14** 600 (1972)
- [78] A.B. Kaidalov, *Sov. Phys. Usp.* **53** 872 (1991)
- [79] C. Guaraldo, A.B. Kaidalov, L.A. Kondratyuk, Y.S. Golubeva, *Yad. Fiz* **59** 1896 (1996); *Phys. At. Nuclei* **59** 1832 (1996)
- [80] J.V. Allaby *et al.*, *Phys. Lett.* **B29** 198 (1969)
U. Amaldi *et al.*, *Lett. Nuovo Cimento* **4** 121 (1972)
H.L. Anderson *et al.*, *Phys. Rev.* **D3** 1536 (1971) - **D9** 580 (1974)
- [81] C. Bagalin *et al.*, *Nucl. Phys.* **B37**, 639 (1972)
A.J. Pawliki *et al.*, *Phys. Rev. Lett.* **31** 665 (1988)
C. Evangelista *et al.*, *Nucl. Phys.* **B131** 54 (1977)
- [82] R. Bizzarri *et al.*, *Lett. Nuovo Cimento* **2** 431 (1969);
G.A. Smith, in *The Elementary Structure of Matter*
ed. by J.M. Richard *et al.*, (Springer-Verlag, 219, Berlin (1988);
J. Reidleberger *et al.*, *Phys. Rev.* **C40** 2717 (1989);
M.P. Bussa, in *Proceedings of the Second Biennial Conference LEAP92*
ed. by C. Guaraldo, Courmayeur (1992);
A. Zenoni and F. Iazzi, *Nucl. Phys.* **A558** (1993)
- [83] M.M. Brisudova, L. Burakovsky, and T. Goldamn, *Phys. Rev.* **D** 61 054013 (2000)
- [84] A.B. Kaidalov, L.A. Kondratyuk, *et al.*, *Phys. od At. Nuclei* **63** 1395, 1409 (2000)
- [85] R.G. Arnold *et al.*, *Phys. Rev. Lett.* **57** 174 (1986)
- [86] T. Armstrong *et al.*, *Phys. Rev. Lett.* **70** 1212 (1993)
- [87] D. Bisello *et al.*, *Nucl. Phys.* **B** **411** 3 (1994)
- [88] C.J. Bebek *et al.*, *Phys. Rev. D* **13** 25 (1976)
- [89] D. Bisello *et al.*, *Phys. Lett. B* **220** 321 (1989)
- [90] J. Milana, S. Nussinov, and M.G. Olsson, *Phys. Rev. Lett.* **71** 2533 (1993)
- [91] I. Kobzarev *et al.*, *Sov. J. Nucl. Phys.* **45** 330 (1987)
- [92] H. Ito, *Progr. Theor. Phys.* **84** 94 (1990)
- [93] B.D. Anderson *et al.*, to be submitted to *Nucl. Instr. & Meth.* **A**
- [94] O.K. Baker *et al.* *Nucl. Instr. & Meth.* **A367** 92 (1995)
- [95] D.I. Sober *et al.*, *Nucl. Instr. & Meth.* **A440** 263 (2000)

- [96] N. Bianchi *et al.*, *Nucl. Instr. & Meth.* **A311** 172 (1992)
N. Bianchi *et al.*, *Nucl. Instr. & Meth.* **A317** 434 (1992)
- [97] T. Auger, PhD thesis, DAPNIA/SPhN-99-01T, (1999)
- [98] M.D. Mestayer *et al.*, *Nucl. Instr. & Meth.* **A449** 81 (2000)
- [99] D.S. Carman *et al.*, *Nucl. Instr. & Meth.* **A419** 315 (1998)
- [100] L.M. Qin *et al.*, *Nucl. Instr. & Meth.* **A411** 265 (1998)
- [101] G. Adams *et al.*, *Nucl. Instr. & Meth.* **A465** 414 (2001)
- [102] E.S. Smith *et al.*, *Nucl. Instr. & Meth.* **A432** 265 (1999)
- [103] M. Amarian *et al.*, *Nucl. Instr. & Meth.* **A460** 239 (2001)
- [104] M. Anghinolfi *et al.*, *Nucl. Instr. & Meth.* **A447**, 424 (2000)
- [105] S. Taylor *et al.*, *Nucl. Instr. & Meth.* **A462** 484 (2001)
- [106] P. Rossi *et al.*, *Nucl. Instr. & Meth.* **A381** 32 (1996)
- [107] M. Ripani *et al.*, *Nucl. Instr. & Meth.* **A406** 403 (1998)
- [108] P. Rossi *et al.*, JLab CLAS Note 2001-005, (2001)
- [109] G.P. Heath, *Nucl. Instr. & Meth.* **A278** 431 (1989)
- [110] D.C. Doughty Jr. *et al.*, *IEEE Trans. Nucl. Sci.* **NS-39** 241 (1992)
- [111] E. Jastrzembski *et al.*, Proc. of the *IEEE NPSS Real Time Conference* 538 (1999)
- [112] C. Witzig, *The DD system*, BNL Note, **510C** (1995)
- [113] CODA: CEBAF On Line Data Acquisition Manual, JLab Internal Report (1997)
- [114] V.H. Gyurjyan, <http://www.jlab.org/~gurjyan/dokumentations.htm>
S. Barrow, CODA 2.0, JLab Internal Report (1997)
- [115] V. Blobel *et al.*, The BOS System for the CLAS Detector, JLab Internal Report (1995)
- [116] E. Pasyuk, JLab Internal Report (2000)
- [117] E. Pasyuk and J. Ball, JLab Internal Report (2000)
J. Ball, <http://www.jlab.org/~jimball>
- [118] R. Schumacher, JLab CLAS Note, 2001-010 (2001)
- [119] H.D. Young, *Statistical Treatment of Experimental Data*,
McGraw-Hill Book Company, NY (1962)
- [120] K.Y. Kim *et al.*, JLab CLAS Note, 2001-18 (2001)
- [121] B. Mecking and the CLAS Collaboration, *The CLAS Detector*,
in printing by *Nucl. Instr. & Meth.* (2003)
- [122] D. Sober, <http://www.jlab.org/~sober/misc.html>

